UNIVERSIDADE FEDERAL DO PARANÁ

PAULO ANDRÉS QUEZADA POZO

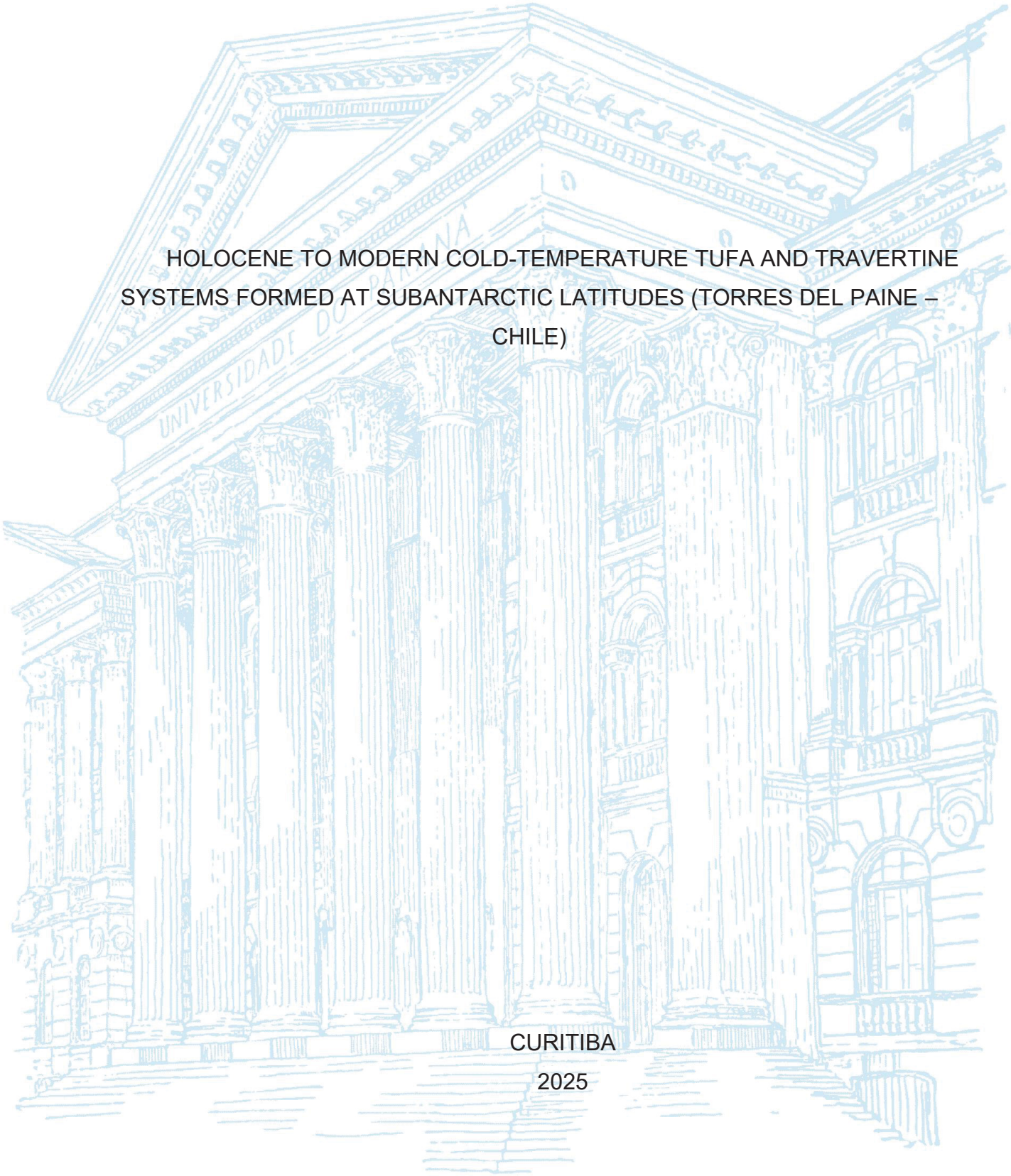

HOLOCENE TO MODERN COLD-TEMPERATURE TUFA AND TRAVERTINE SYSTEMS FORMED AT SUBANTARCTIC LATITUDES (TORRES DEL PAINE – CHILE)

CURITIBA

2025

PAULO ANDRÉS QUEZADA POZO

HOLOCENE TO MODERN COLD-TEMPERATURE TUFA AND TRAVERTINE SYSTEMS FORMED AT SUBANTARCTIC LATITUDES (TORRES DEL PAINE – CHILE)

Tese apresentada ao curso de Pós-Graduação em Geologia, Setor de Ciencias da Terra, Universidade Federal do Paraná, como requisito parcial à obtenção do título de Doutor em Geología.

Orientador: Prof. Dr. Leonardo Fadel Cury

Coorientador: Prof. Dr. Mauricio Calderón Nettle

CURITIBA

2025

DADOS INTERNACIONAIS DE CATALOGAÇÃO NA PUBLICAÇÃO (CIP)
UNIVERSIDADE FEDERAL DO PARANÁ
SISTEMA DE BIBLIOTECAS – BIBLIOTECA DE CIÊNCIA E TECNOLOGIA

Pozo, Paulo Andrés Quezada
Holocene to modern cold-temperature tufa and travertine systems formed at subantarctic latitudes (Torres del Paine – Chile) / Paulo Andrés Quezada Pozo. – Curitiba, 2025.
1 recurso on-line : PDF.

Tese (Doutorado) - Universidade Federal do Paraná, Setor de Ciências da Terra, Programa de Pós-Graduação em Geologia.

Orientador: Leonardo Fadel Cury
Coorientador: Mauricio Calderón Nettle

1. Hidrodinâmica. 2. Carbonatos. 3. Holoceno. 4. Radiação solar. 5. Torres del Paine (Chile). I. Universidade Federal do Paraná. II. Programa de Pós-Graduação em Geologia. III. Cury, Leonardo Fadel. IV. Nettle, Mauricio Calderón. V. Título.

Bibliotecário: Elias Barbosa da Silva CRB-9/1894

TERMO DE APROVAÇÃO

Os membros da Banca Examinadora designada pelo Colegiado do Programa de Pós-Graduação GEOLOGIA da Universidade Federal do Paraná foram convocados para realizar a arguição da tese de Doutorado de **PAULO ANDRÉS QUEZADA POZO**, intitulada: **HOLOCENE TO MODERN COLD-TEMPERATURE TUFA AND TRAVERTINE SYSTEMS FORMED AT SUBANTARCTIC LATITUDES (TORRES DEL PAINE CHILE)**, sob orientação do Prof. Dr. LEONARDO FADEL CURY, que após terem inquirido o aluno e realizada a avaliação do trabalho, são de parecer pela sua APROVAÇÃO no rito de defesa.

A outorga do título de doutor está sujeita à homologação pelo colegiado, ao atendimento de todas as indicações e correções solicitadas pela banca e ao pleno atendimento das demandas regimentais do Programa de Pós-Graduação.

CURITIBA, 30 de Maio de 2025.

Assinatura Eletrônica
03/06/2025 03:31:26.0
LEONARDO FADEL CURY
Presidente da Banca Examinadora

Assinatura Eletrônica
02/06/2025 23:53:03.0
CARLOS CONFORTI FERREIRA GUEDES
Avaliador Interno (UNIVERSIDADE FEDERAL DO PARANÁ)

Assinatura Eletrônica
27/06/2025 11:32:48.0
LUCAS VERÍSSIMO WARREN
Avaliador Externo (UNIVERSIDADE EST.PAULISTA JÚLIO DE MESQUITA FILHO/RIO CLARO)

Assinatura Eletrônica
26/06/2025 13:51:23.0
PAULO CÉSAR BOGGIANI
Avaliador Externo (UNIVERSIDADE DE SÃO PAULO)

Assinatura Eletrônica
04/06/2025 10:35:20.0
DANIEL ARIZTEGUI
Avaliador Externo (UNIVERSIDADE DE GENEBRA)

Documento assinado eletronicamente de acordo com o disposto na legislação federal Decreto 8539 de 08 de outubro de 2015.
Gerado e autenticado pelo SIGA-UFPR, com a seguinte identificação única: 456885
Para autenticar este documento/assinatura, acesse https://siga.ufpr.br/siga/visitante/autenticacaoassinaturas.jsp e insira o codigo 456885

A mi esposa e hijas

AGRADECIMENTOS

Esta pesquisa não teria sido possível sem o apoio da Sociedade Brasileira, que décadas atrás lançou as bases para que uma pequena parte de sua grande riqueza natural fosse investida no desenvolvimento de capacidades científicas e tecnológicas. Agradeço ao Programa de Pós-Graduação em Geologia da Universidade Federal do Paraná e ao Instituto LAMIR, que forneceram a infraestrutura e o financiamento para realizar este trabalho no âmbito dos projetos Diagenesis (UFPR/SHELL/ANP 20257/2) e GeoQI (UFPR/PETROBRAS/ANP SEI 23075039121/2022-97).

Agradeço aos meus orientadores, Prof. Leonardo Fadel Cury e Prof. Mauricio Calderon, por me convidarem a fazer parte deste caminho e pelo apoio ao longo dele. Assim como à Prof. Anelize Bahniuk Rumbelsperger, que estendeu sua ajuda sempre que foi solicitada.

Aos colegas do Instituto LAMIR — tanto aos que ainda estão presentes quanto aos que seguiram outros rumos —, àqueles que influenciaram diretamente este trabalho, seja com suporte técnico, administrativo ou por meio de discussões estimulantes, assim como aos que, no dia a dia, me presentearam com sua cordialidade e alegria. O tempo passará, mas sempre ficará algo de nós.

Ao Prof. Gustavo Athayde e o LPH por sua parceria e suporte com as análises de água.

Ao Prof. José Manuel Pérez-Donoso y Nicolas Bruna por sea parceria e suporte com as análises microbiológicas.

Também aproveito para estender minha admiração e gratidão ao Prof. Francisco Hervé, que exerceu uma profunda marca no meu desenvolvimento humano e profissional. Se não fosse pelo seu apoio desde o início, há já uns 13 anos atrás, as coisas teriam sido diferentes.

Por fim, mas não menos importante, à minha família, pelo apoio incondicional, e sua valentia, que nos permitiu embarcar nesta aventura; sem vocês, Pia, Agus e Alfis, o sal não salgaria e o açúcar não adoçaria. Com o mesmo carinho, agradeço aos meus pais Gabriel y Elisabeth, meus irmãos Manuel, Mario y Gabriel, é família, tio Mario e tia Paty, pelo amor, suporte, e pela incondicionalidade.

“*Hay dos panes.*
Usted se come dos. Yo ninguno.
Consumo promedio: un pan por persona”
Nicanor Parra (1914-2018),
antipoeta chileno.

RESUMO

Travertinos e tufas lacustres são carbonatos de água doce comum no Quaternário, importantes para estudos paleoambientais e como análogo de sistemas deposicionais antigos. Estudou-se aqui travertinos de baixa temperatura com exposição solar contrastante na Laguna Amarga, e extensivos acúmulos de tufa lacustre no Lago Sarmiento (Patagônia Chilena, 51°S). Esses sistemas se formam em um ambiente frio e ventoso, sobre depósitos turbidíticos cretáceos dominados por argilitos. Este estudo visa determinar os controles ambientais e bióticos na precipitação de carbonatos e suas feições deposicionais, além de investigar possíveis contribuições endógenas em sua formação, integrando petrografia, mineralogia e isotopia dos carbonatos; físico-química e isotopia das águas; e sequenciamento do gene 16S rRNA de tapetes microbianos do Lago Sarmiento. As águas das nascentes exibem características de travertinos formados por evasão de CO_2. Os depósitos apresentam variações similares em sedimentologia e composição $\delta^{13}C_{trav}$-$\delta^{18}O_{trav}$, resultantes de mudanças hidrodinâmicas ao longo do fluxo que influenciam efeitos bióticos e cinéticos na precipitação. Carbonatos esferulíticos de aragonita (calcita) formam-se em biofilmes nas nascentes do travertino exposto ao sol (sombreado), associados a bactérias redutoras de sulfato (fotossintéticas), enquanto dendritos cristalinos precipitam a jusante. Fontes comuns e profundidades rasas de infiltração são deduzidas a partir de análises isotópicas das águas das nascentes e dos carbonatos. O envolvimento de fontes profundas de CO_2 permanece incerto, embora os travertinos exibam $\delta^{13}C_{trav}$ na faixa de sistemas endogênicos; processos epígenos que poderiam explicar essas características são discutidos. Valores consistentemente mais baixos de $\delta^{13}C_{trav}$ no travertino sombreado sugerem controles microambientais nas assinaturas isotópicas, provavelmente devido à vegetação/solo mais espessa nesta margem. A mediação biótica é fundamental na deposição de tufas lacustres, com cianobactérias—especialmente Rivulariaceae—atuando como principais construtoras. Uma sequência multiestágio molda a mineralogia e microestrutura desses depósitos. A indução precoce dos substratos microbianos envolve a nucleação de nanopartículas ricas em Sr e Mg, precursores de aragonita e Mg-calcita, respectivamente. Segue-se um estágio construtivo de diagênese, caracterizado pela inversão de aragonita para Mg-calcita, aumento do tamanho dos cristais e cimentação por Mg-calcita. Com o declínio do nível do lago e a exposição dos depósitos à zona de arrebentação das ondas, uma fase destrutiva de diagênese, sob condições de maior energia, levou à micritização, dissolução/erosão da estrutura e sedimentação interna nos poros, apagando parcialmente as estruturas microbianas. Apesar das flutuações do nível do lago no Holoceno, impulsionadas por climas frios/úmidos e quentes/secos alternados, as composições $\delta^{13}C_{tufa}$-$\delta^{18}O_{tufa}$ exibem variabilidade limitada, consistentes com deposição sob condições relativamente frias (≤12°C) e estáveis. Este trabalho ressalta o potencial dos carbonatos de nascentes de baixa temperatura como proxies para rastrear flutuações de biomassa em escalas (sub-)bacinais. Também fornece critérios para identificar carbonatos microbianos depositados em ambientes lacustres antigos de alta energia—uma fácies pouco representada no registro geológico.

Palavras-chave: Hidrodinâmica; exposição solar; Organomineralização.

ABSTRACT

Travertine and lacustrine tufa are widespread freshwater non-marine carbonates in the Quaternary record, serving as valuable paleoenvironmental proxies and analogs for ancient depositional systems. This study examines two small low-temperature travertines with contrasting sun exposure at Laguna Amarga, and extensive lacustrine tufa build-ups featuring Lago Sarmiento (Chilean Patagonia, 51°S). These systems form in an unusual setting, developing under relatively cold and windy conditions in an area underlain by mudstone-dominated Cretaceous turbiditic deposits. The aim of this research is to constrain the environmental and biotic influence on carbonate precipitation and their depositional features, as well as to assess the potential role of endogenic processes in their formation. To achieve this, are integrate petrographic, mineralogical, and isotopic analyses of carbonates; physicochemical and isotopic analyses of spring and lake waters; and 16S rRNA gene sequencing of microbial mats from Lago Sarmiento. The spring waters exhibit typical features of travertines systems formed by CO_2 evasion. Both deposits exhibit similar longitudinal variations in sedimentology and $\delta^{13}C_{trav}$-$\delta^{18}O_{trav}$ composition, resulting from hydrodynamic changes along the stream that influence biotic and kinetic effects on precipitation. Spherulitic carbonates composed of aragonite (calcite) form within biofilms in the vents of the sun-exposed (sun-shaded) travertine in association with sulfate reducing bacteria (photosynthetic bacteria), while crystalline dendrites precipitate downstream. Common sources and shallow infiltration depths are deduced from isotopic analysis of spring waters and carbonate. The involvement of deep CO_2 sources remains unclear despite the travertines exhibit $\delta^{13}C_{trav}$ in the range of endogenic ones; possible epigean processes explaining these features are discussed. Consistently lower $\delta^{13}C_{trav}$ values in the sun-shaded travertine suggest microenvironmental controls on the $\delta^{13}C_{trav}$ signatures likely due to thicker vegetation/soil in this margin. Biotic mediation plays a fundamental role in lacustrine tufa deposition, with cyanobacteria–particularly *Rivulariaceae*–serving as the main framework builders. A multi-stage sequence shapes the mineralogy and microstructure of these deposits. Early induration of microbial substrates involves the nucleation of Sr- and Mg-rich nanoparticles, precursors to aragonite and Mg-calcite, respectively. This is followed by a constructive stage of diagenesis characterized by aragonite inversion to Mg-calcite, crystal size coarsening, and Mg-calcite cementation. As lake levels decline and deposits were exposed to the wave-breaking zone, a destructive diagenetic phase under higher-energy conditions led to micritization, dissolution/erosion of the framework, and internal sedimentation within pores, partly erasing the microbial structures. Despite Holocene lake-level fluctuations driven by alternating cold/wet and warm/dry climate, the $\delta^{13}C_{tufa}$-$\delta^{18}O_{tufa}$ compositions exhibit limited variability, consistent with deposition under relatively cold (≤12°C) and stable conditions. This work underscores the potential of cold-temperature spring carbonates as proxies for tracking biomass fluctuations at (sub-)basin scales. It also provides insights for identifying microbial carbonates deposited in ancient high-energy lake settings—a poorly represented facies in the geologic record.

Keywords: hydrodynamics; slope aspect; organomineralization.

FIGURE LIST

TABLE LIST

ABBREVIATIONS LIST

BSE	- Backscattering Electron
DIC	- Dissolved Inorganic Carbon
DO	- Dissolved Oxygen
EPS	- Extracellular Polymeric Substances
ORP	- Oxidation-Reduction Potential
SE	- Secondary Electron
SEM	- Scanning Electron Microscope
SWW	- Southern Westerly Winds
TDS	- Total Dissolved Solids
TdPB	- Torres del Paine Basin
VPDB	- Vienna Pee Dee Belemnite
VSMOW	- Vienna Standard Mean Ocean Water
XRD	- X-ray Diffraction

SYMBOLS LIST

δ - delta

‰ - per mil

SUMMARY

1 INTRODUCTION

Non-marine carbonates serve as valuable archives of paleoclimatic and paleohydrological proxies, offering insights into the evolution of ancient terrestrial environments (Andrews, 2006; Benson *et al.,* 1996; Pedley, 2009; Tanner, 2010). Their formation typically involves microbial mediation in mineralization processes (Dupraz *et al.,* 2009), making them suitable analogs for identifying biosignatures in Earth's early geological record (Riding, 2000) and potential reference models for its search in extraterrestrial materials and/or settings (Walter and Des Marais, 1993). Moreover, interest in non-marine carbonates has surged in recent decades following the discovery of giant hydrocarbon reservoirs in offshore basins of Brazil, Angola, and Congo (the "Presalt" deposits). These reservoirs are hosted in unusual carbonate associations deposited during the early stages of the Africa-South America rift (Terra *et al.,* 2010; Wright, 2012). These developments have drawn sedimentologists, geochemists, and microbiologists to study modern and Quaternary terrestrial environments, where the interactions between physical, chemical, and biotic factors driving carbonate accretion can be more directly investigated.

FIGURE 1 – MAIN DEPOSITIONAL ENVIRONMENTS OF NON-MARINE CARBONATES

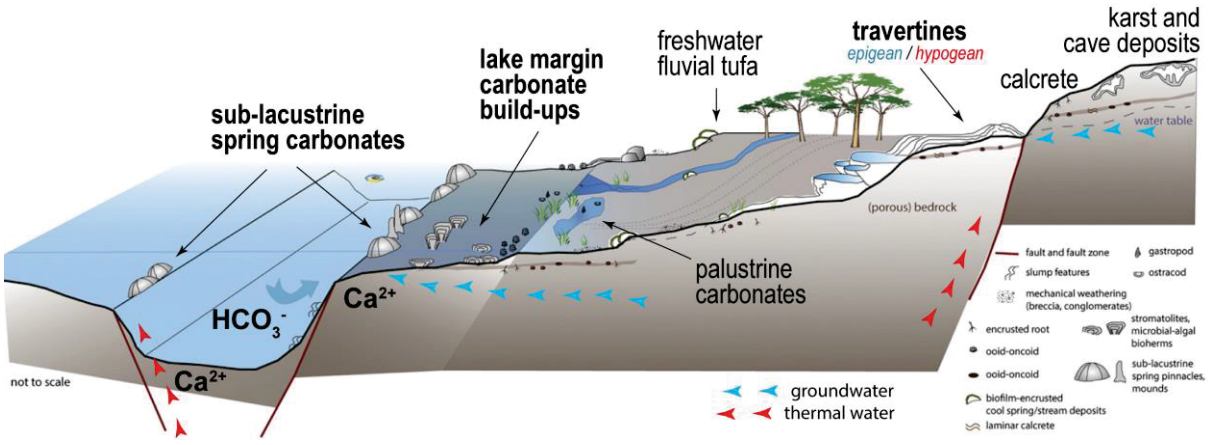

SOURCE: Modified from De Boever *et al.* (2017).

LEGEND: in bold letters are highlighted the environments of interest for this work.

Modern and fossil non-marine carbonate systems are associated with a range of settings, including closed or semi-closed lakes (lake-margin and sub-lacustrine build-ups), zones of groundwater or hydrothermal water discharge (travertines *sensu* Pentecost and Viles, 1994), rivers (freshwater fluvial tufa),

palustrine environments, calcretes, and caves (speleothems) (Fig. 1) (Della Porta, 2015). The intrinsic complexity of non-marine carbonates—driven by the interplay of biotic and abiotic processes during deposition as well as early diagenetic effects (De Boever *et al.,* 2017)—has led much of the scientific interest toward developing a process-based framework integrating sedimentology, petrology, microbiology, and geochemistry to decipher deposit features across scales, from microscopic to sedimentary-environmental (Arp *et al.,* 2010; Capezzuoli *et al.,* 2014; Della Porta, 2015; Ford and Pedley, 1996; Fouke, 2011; Fouke *et al.,* 2000; Gandin and Capezzuoli, 2014; Mercedes-Martín *et al.,* 2021; Okumura *et al.,* 2012; Pedley, 1990; Pentecost and Viles, 1994; Rogerson *et al.,* 2010; Shiraishi *et al.,* 2019, 2008a; Veysey *et al.,* 2008; Zeyen *et al.,* 2021). Among the cited depositional environments, those involving subsurface fluids and lacustrine settings are of interest for this work (Fig. 1).

Subsurface fluids, whether thermal waters or cold groundwater, play a fundamental role in the formation of certain types of non-marine carbonates. This is the case of travertines, which are physical-chemical carbonates precipitated in subaerial conditions at sites of bicarbonate-rich fluid discharge due to $CaCO_3$ supersaturation triggered by CO_2 degassing (Gandin and Capezzuoli, 2008; Pentecost, 2005). Similarly, distinctive carbonate build-ups (e.g., pinnacles and mounds) in lacustrine systems have been associated with subaquatic discharge of Ca^{2+}-rich fluids associated to cold or thermal sources. In these cases, precipitation occurs when such fluids mix with bicarbonate-rich lake waters (Della Porta, 2015; DeMott *et al.,* 2019; Rosen *et al.,* 2004). Although abiotic controls significantly promote carbonate accretion in these settings, mineralization is often associated with microbial substrates, including extracellular polymeric substances (EPS) secreted by the microbial consortia serving as nucleation sites (Brasier *et al.,* 2018; Della Porta *et al.,* 2022; DeMott *et al.,* 2021; Guo and Chafetz, 2012). Furthermore, the chemistry of these carbonates is influenced by local geology, the amount of fluid/rock interactions, and the hydrogeological pathway of subsurface fluids, different lithologies can supply ions to the involved "deep fluids" (Teboul *et al.,* 2016). As a result, these deposits can serve as valuable proxies for reconstructing ancient hydrothermal and groundwater dynamics.

While not a strict prerequisite, groundwater influences are reported in several Pleistocene to modern lacustrine microbial carbonate systems, with fundamental

roles however for microbial colonization in hypersaline settings (Warden *et al.,* 2019). In the case of freshwater lacustrine systems (*i.e.,* lacustrine tufa *sensu* Pedley, 1990) such environmental stressors for biota do not exist, and carbonate deposition often occurs in association with cyanobacteria, algae and higher plants. A topic debated has been under which conditions these biotic substrates are passively involved in deposition, *i.e.,* serving as templates for environmentally-driven precipitation, or actively inducing the mineralization through their metabolic activity (Dupraz *et al.,* 2009). While some studies argues that precipitation induced by photosynthetic activity of microbes is only effective when ambient waters have low amounts of dissolved inorganic carbon (DIC) and high concentrations of Ca^{2+} (Arp *et al.,* 2001; Chagas *et al.,* 2016), others have shown that photosynthesis is critical for surpassing the kinetic barriers leading to carbonate precipitation, even in highly supersaturated settings (Rogerson *et al.,* 2014; Shiraishi *et al.,* 2008a).

Most current knowledge about Quaternary lacustrine microbial carbonates and travertines derives from studies conducted in volcanic and/or karstic areas of semi-arid to humid Northern Hemisphere climates (Chagas *et al.,* 2016; Della Porta, 2015; Pedley, 2009). Notable Southern Hemisphere exceptions include Lagoa Vermelha (Brazil) (Vasconcelos and Mckenzie, 1997); Lake Clifton (Australia) (Moore and Burne, 1994); Lake Tanganyika (Africa) (Cohen and Thouin, 1987); and the Chilean-Argentinean Central Andes (Farías *et al.,* 2020; Mors *et al.,* 2022a), among others.

In contrast, late Quaternary to modern lacustrine carbonates systems occur sporadically east of the Patagonian Andes, Southern South America (41 to 53°S). These develop under the influence of the Southern Westerly Winds, a key agent modulating climate and evaporation in this relatively cold-temperature environment (Garreaud *et al.,* 2013). Studies on Patagonian microbial carbonates are not widespread, and although significant advances on understanding their sedimentological, geochemical and microbiological features have been performed in the last 15 years (Airo, 2010; Eymard *et al.,* 2021, 2020, 2019; Henríquez *et al.,* 2022; Osman *et al.,* 2020; Pacton *et al.,* 2015; Pollier *et al.,* 2024; Solari *et al.,* 2010), key questions remain about their formation processes and paleoenvironmental significance in this unique climatic setting. This is particularly true for freshwater systems, which represent early stages of endorheic basin evolution where

precipitation may occur under relatively lower supersaturation levels, raising important questions about biotic mediation and groundwater influences.

This doctoral research investigates non-marine carbonate systems in the Torres del Paine area (Chilean Patagonia, 51°S), a key region for Holocene to modern terrestrial carbonate development in southern South America. The study area includes two exceptional systems: (1) Laguna Amarga (Fig. 2), which hosts the only known travertines documented in southern Patagonia to date, and (2) Lago Sarmiento (Fig. 2), containing one of the most extensive lacustrine tufa systems in the Southern Hemisphere, with individual build-ups of <4 m tall.

1.1 STRUCTURE OF THE THESIS

This thesis is organized into six chapters.

Chapter 1 introduces the problem to be addressed and indicates the objectives of this work.

Chapter 2 provides a description of the study area, including its geological context, modern climate and its fluctuations during the Holocene.

Chapter 3 describes the materials and methods used in this work.

Chapter 4 studies the sedimentological, mineralogical and isotopic composition of two travertines located in Laguna Amarga, discussing the biotic and environmental controls on the microfacies and stable isotopes composition and the source of the fluids feeding the systems. This chapter was published in Sedimentary Geology (https://doi.org/10.1016/j.sedgeo.2024.106758).

Chapter 5 studies the bacterial composition and calcification of living and lithified microbial mats, respectively, together with the microstructure and stable isotope composition of fossil deposits in Lago Sarmiento, providing insights into the biotic and abiotic factors leading to tufa accretion, key mineralogical and textural modification from deposition to early diagenesis, and the local and wider paleoenvironmental significance of these deposits. This chapter is to be submitted.

Chapter 6 provides a synthesis on the main findings of this research.

1.2 PROBLEM TO BE ADDRESED AND JUSTIFICATIVE

The formation of two travertine deposits in Laguna Amarga, along with the extensive lacustrine tufa in Lago Sarmiento, occurs under unique environmental and geological conditions compared to similar deposits worldwide. The region's climate is characterized by relatively cold temperatures (annual average of ca. 7 °C) and strong winds, while the basin's bedrock consists predominantly of siliciclastic sedimentary rocks. Additionally, no significant limestone-rich units have been identified in the subsurface—at least to a depth of 2 km—and no thermal springs or recent volcanic activity are recorded in the area. The nearest active volcano lies approximately 60 km west, on the western slope of the Andes. This raises questions about whether carbonate deposition in Torres del Paine is controlled by endogenic (“deep”) processes and to what extent synergistic contributions from abiotic and biotic processes in the epigean (“shallow”) environment influence large-scale lacustrine tufa deposition in Lago Sarmiento.

To address this question, it is hypothesizing that endogenic contributions to carbonate precipitation are more easily discerned in the travertines of Laguna Amarga, whereas in a relatively large lake like Lago Sarmiento (ca. 9 km^3), their effects could be "diluted," allowing environmental and biotic influences on tufa deposition to dominate.

The coexistence of these systems in Laguna Amarga and Lago Sarmiento provides a natural laboratory to investigate low-temperature carbonate deposition. It also allows for an evaluation of the sedimentological, diagenetic, and geochemical responses of different depositional systems under similar climatic conditions—particularly the impact of wind on fluid hydrodynamics and, consequently, on precipitation. In this context, this research documents two understudied depositional settings: low-temperature travertines and lacustrine microbial carbonates deposited in wind-stressed, high-energy margins. The findings offer insights into their formation and significance for paleoenvironmental reconstructions.

1.3 OBJECTIVES

1.3.1 General objective

Determine key processes leading to cold-temperature carbonate deposition in the Torres del Paine area and assess their environmental significance.

1.3.2 Specific objectives

Characterize the sedimentological, petrographic, mineralogical, and geochemical features of the travertines in Laguna Amarga and the lacustrine tufa deposits of Lago Sarmiento.

Characterize the physiochemical and stable isotope composition of the spring waters in the travertines and the lake water of Lago Sarmiento, establishing their relationship with the respective precipitates.

Constrain the sources of the fluids and dissolved components forming the travertines of Laguna Amarga.

Elucidate the role of environmental factors and biotic processes on the formation of the travertines in Laguna Amarga and lacustrine tufa in Lago Sarmiento, and their expression on the sedimentological and geochemical features of the deposits.

2 STUDY AREA

2.1 LOCALIZATION

The study zone is in the Ultima Esperanza District – Region de Magallanes in southern Chile (51°S), about 80 km north of Puerto Natales city, and 40 km east of the Southern Patagonian Ice Field (SPI; Fig. 2). It comprises a low-lying mountainous area with steep slopes that harbors several endorheic alkaline lakes, from hereafter referred to as the Torres del Paine Basin (TdPB) (Fig. 3). Most of the TdPB is located inside the limits of the Torres del Paine National Park, under the administration of the Corporación Nacional Forestal de Chile (CONAF) (Fig. 2).

FIGURE 2 – LOCATION OF THE STUDY AREA

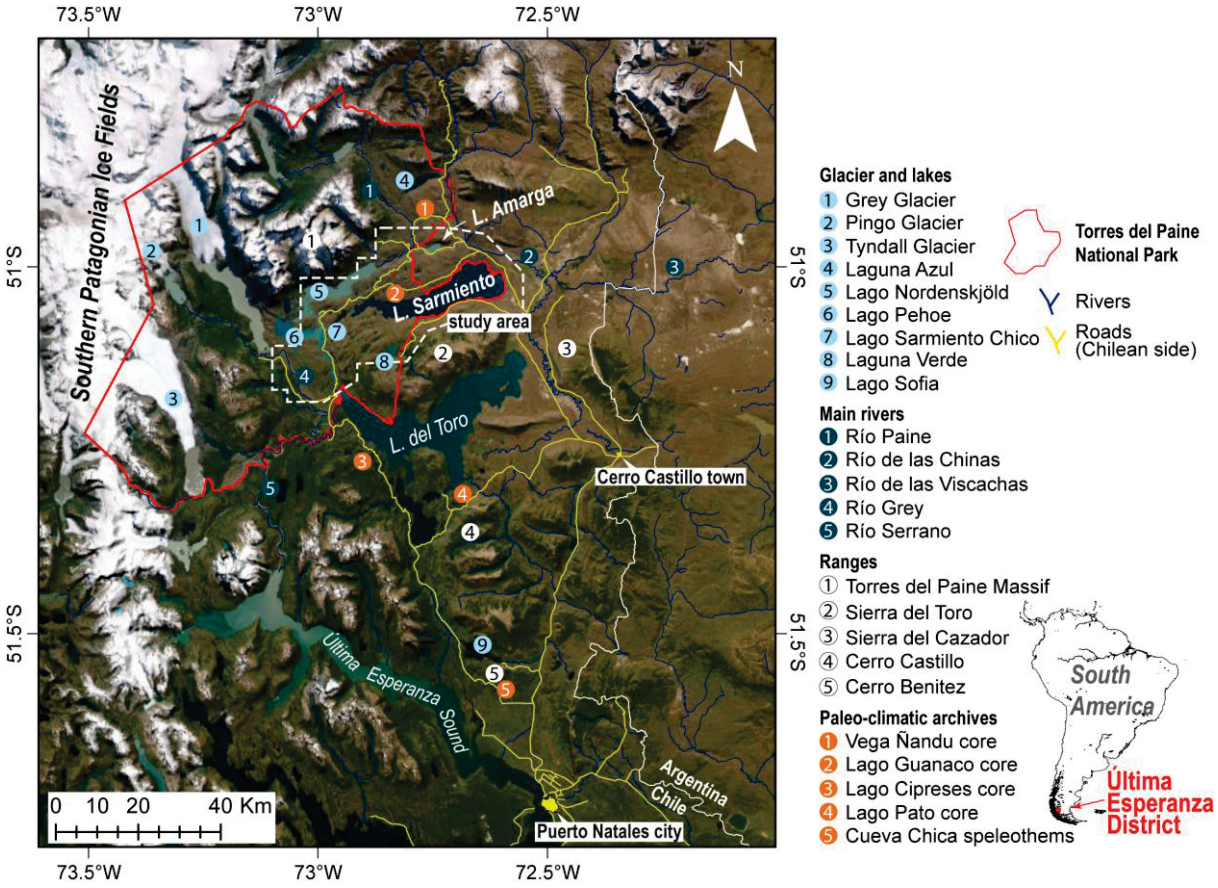

SOURCE: This work.

LEGEND: the limits of the Torres del Paine National Park and location of the nearest cities, access routes, main geographical features and paleo-climate archives are indicated.

2.2 GEOLOGICAL CONTEXT

The bedrock of the Torres del Paine Basin is composed by the Cerro Toro Formation, an Upper Cretaceous (Turonian to Campanian) deep-marine siliciclastic unit composed of black mudstone, sandstone, conglomerate, and minor marlstone, dolostones and carbonate concretion (Fig. 3) (Bernhardt *et al.,* 2011, 2012). The Cerro Toro Formation is deformed in gentle to tight folds with an approximately NNW-SSE strike, formed during the Upper Cretaceous to Miocene Andean orogenesis (Fosdick *et al.,* 2011; Ghiglione *et al.,* 2014) (Fig. 3). The folds are deformed by a subordinate NE-SW and WNW-ESE strike-slip faults with metric to decametric slips (Gonzales and Aydin, 2008a) (Fig. 3). This conjugated strike-slip system generated topographic depressions that host the endorheic lakes and control the current drainage system (Fig. 3) (Gonzales and Aydin, 2008b).

At regional scale, the geological units situated stratigraphically below the Cerro Toro Formation include, from top to bottom: 1) sand-rich turbidite deposits of the Punta Barrosa Formation (late Albian to Turonian), 2) pyrite-rich hemipelagic mudstone of the Zapata Formation (Tithonian to Barremian), and 3) acidic volcanic and volcaniclastic deposits of the Tobífera Formation (Middle-Upper Jurassic) (Katz, 1963; Wilson, 1991; SERNAGEOMIN, 2003; Fildani and Hessler, 2005; Fosdick *et al.,* 2011; Ghiglione *et al.,* 2014). These units crop out mostly to the west of the Torres del Paine Basin (Fig. 3), and the Zapata Formation is the only one with a relatively abundant carbonate content, present as calcareous mudstone and carbonate concretions in the lower half of the unit, and as bed-parallel calcite veins and cements in the siliceous mudstones of the upper half (Wilson, 1991). Log data from local wells (Toro-1B borehole, Fig. 3) indicate that, in the eastern portions of study area, the Cerro Toro Formation was deposited atop the Zapata Formation, with their contact located at ca. 70-75 m below the surface (Katz, 1963).

The magmatic rocks intruding the Cerro Toro Formation include Oligocene alkaline mafic dykes (K/Ar age; Altenberger *et al.,* 2003), early Miocene dykes (U-Pb in zircon; Fosdick *et al.,* 2011), and the bimodal intrusive suite of the Torres del Paine igneous complex, formed during the middle Miocene (Fig. 3) (U-Pb in zircon; Sánchez *et al.,* 2021 and references therein). Early Pleistocene (1-2 Ma; K/Ar ages) basaltic lavas crop out ca. 40 km north (Fleck *et al.,* 1972) and to the northeast, in the Meseta de las Vizcachas (Fig. 3). In comparison, the nearest Holocene volcano

is located ca. 60 km west, in the western slope of the Andes (cf. Ramírez de Arellano *et al.,* 2021).

FIGURE 3 – GEOLOGICAL AND GEOMORPHOLOGICAL MAP OF THE STUDY AREA

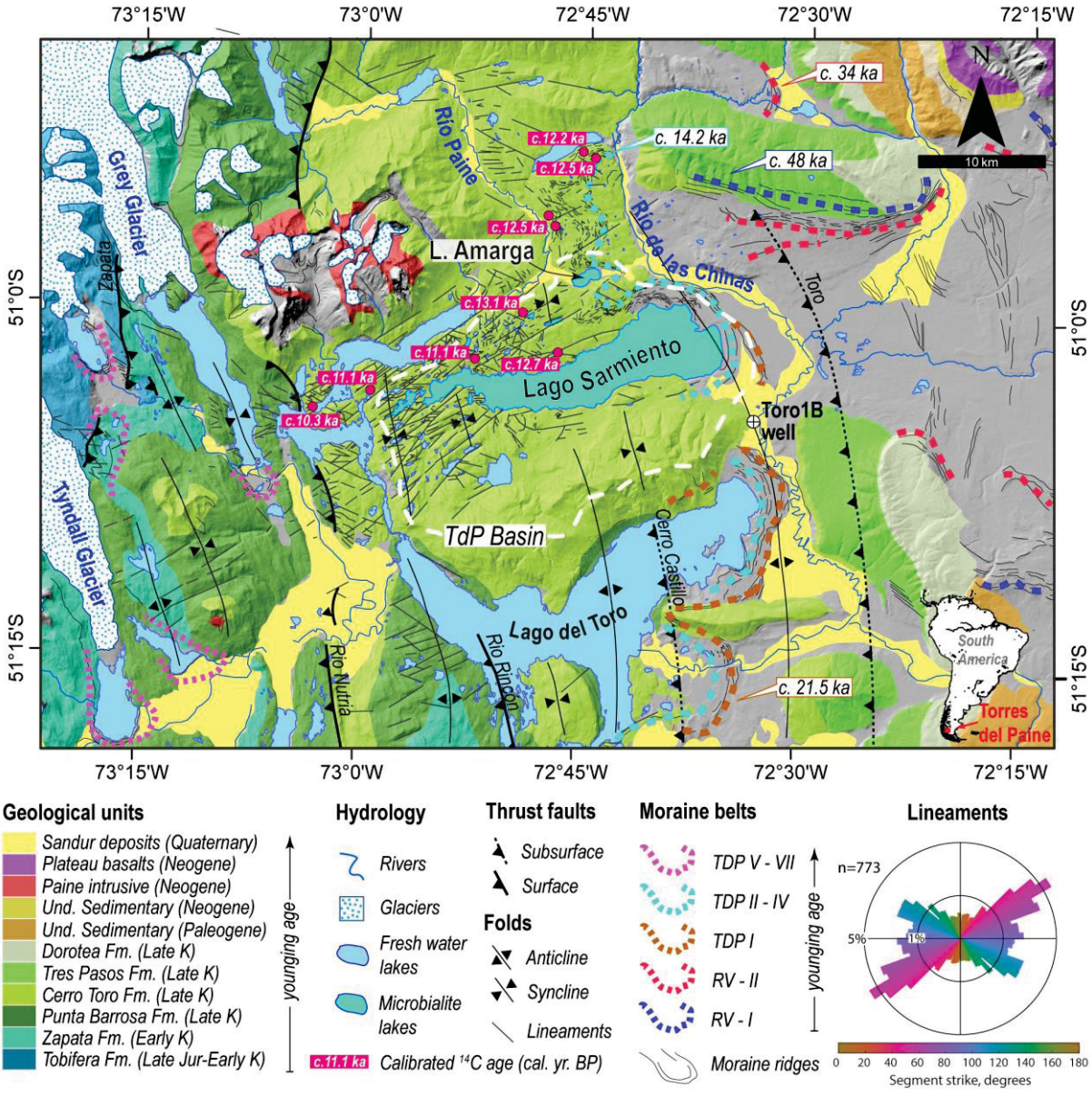

SOURCE: This work. Based on surface geology of Fosdick *et al.* (2011) and Ghiglione *et al.* (2014). Glacial geomorphology, ages of moraine arcs, and radiocarbon ages are taken from Garcia *et al.* (2014; 2020, and references therein). Microbial lakes after Solari *et al.* (2010).

LEGEND: White dashed line shows the approximated limits of the Torres del Paine Basin (TdPB). The radiocarbon ages demark ice-free conditions after the last glacial advance over Lago Sarmiento, demarked by moraines TDP II – IV. The tectonic lineaments were mapped using GIS. Note the location of Toro 1B well.

2.3 MODERN AND HOLOCENE CLIMATIC CONTEXT

The longitudinal climatic gradient in Southern South America is controlled by the orographic effect that exerts the Patagonian Andes over the moisture transported by the Southern Westerly Winds (SWW) from the Pacific Ocean to the continent (Garreaud *et al.,* 2013). This results in an hyper-humid and template climate in the western slope of the Andes, and a cold semi-arid climate extending from few kilometers east of the Andes towards the Atlantic coast (Garreaud *et al.,* 2013).

FIGURE 4 – MONTLY AVERAGES OF CLIMATIC PARAMETERS AND HOLOCENE PROXIES

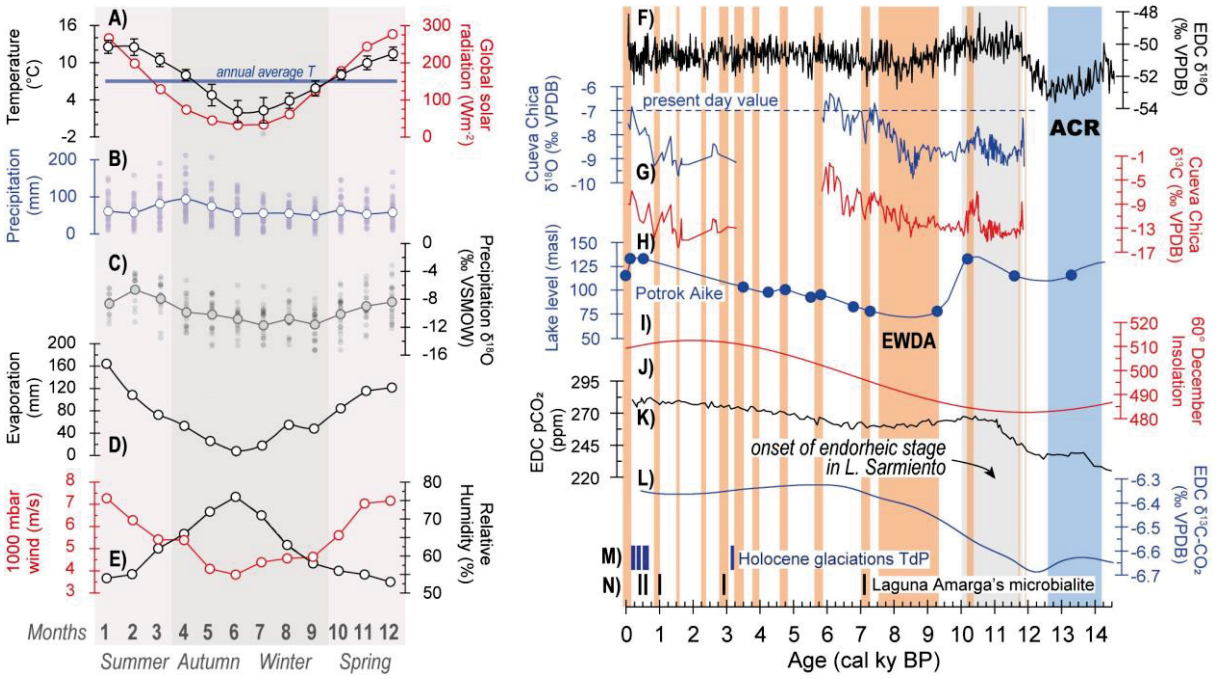

SOURCE: Elaborated by the author using published data. Air temperature in A) and precipitation in B) are from local meteorological data (Mesa Dabacens, 2016). Global solar radiation in A) is from Santana *et al.* (2010). Isotope composition in C) is from IAEA/WMO (2023). Data in D) and E) is from Moy *et al.* (2008) and Campos *et al.* (1994). Data from the Epica Dome Core (EDC) is from F) Landais and Stenni (2021), K) Monnin (2006) and L) Schmitt *et al.* (2012). Data in G) and H) is from Nehme *et al.* (2023). Data in I) is from Anselmetti *et al.* (2009). Data in J) is from Berger and Loutre (1991). Data in M) is from García *et al.* (2020) and in N) from Solari *et al.* (2010). Warm/dry and cold/wet periods after Moreno *et al.* (2018).

LEGEND: Compilation of local climatological data (left panel) and Holocene variation of local, regional and global archives (right panel). On the right panel the blue bar denotes the period when Lago Sarmiento was covered by ice, while the red and white bars denote warm/dry and cold/wet periods, respectively. Note the increase of $\delta^{18}O$, $\delta^{13}C$-CO_2, and pCO_2 following the Antarctic Cold Reversal (ACR), and correspondence between the lake-level minima in the Laguna Potrok Aike with the Early Warm-Dry Anomaly (EWDA).

Meteorological data (between the years 1985-2014) is available from a station located a few km southwest of Lago Sarmiento, in the Torres del Paine National Park

headquarters. During this period, the average monthly air temperatures varied between 2.1°C (June) and 12.5°C (January), with an annual average of 7.6°C (Fig. 4A), while the annual average precipitations were ca. 764 mm, the highest during April (ca. 94 mm) and the lower during September (ca. 51 mm) (Fig. 4B). The orographic effect generates large fractionations in the deuterium and oxygen stable isotope composition of rainfall between both sides of the Andes, reaching negative values of up to -115‰ for $\delta^{2}H$ and -15‰ for $\delta^{18}O$ in the eastern side (Mayr *et al.,* 2018; Smith and Evans, 2007). The lower isotopic composition of precipitation corresponds to autumn and winter (Fig. 4C), as observed in the nearest GNIP station, located ca. 260 km south, in Punta Arenas. Evaporation is positively correlated with wind speed throughout the year and inversely correlated with relative humidity (Fig. 4D-E). In average, the monthly wind velocity is higher during the afternoons of spring and summer (ca. 6-8 m/s) compared to autumn and winter (ca. 1-4 m/s) (Gómez-Fontealba *et al.,* 2022), although days with wind velocities larger than 27 m/s have been registered (Campos *et al.,* 1994a). At interannual scales, the amount of evaporation is higher than precipitation (Campos *et al.,* 1994a).

The TdPB was cover by outlet glaciers during the time of the Antarctic cold Reversal as evidenced by the ca. 14.2 ± 0.56 ka frontal moraines that bound Lago Sarmiento to the east (Fig. 3) (^{10}Be ages; García *et al.,* 2012). Based on lake and peat sediment core geochronology (calibrated ^{14}C ages), by ca. 12.5 ka the area was deglaciated (García *et al.,* 2014; Moreno *et al.,* 2009).

From early Holocene to the present, the climate in the area has fluctuated between cold/wet and warm/dry phases (Fig. 4), controlled by latitudinal shifts of the core of the SWW (Moreno *et al.,* 2018). Cold/wet periods prevailed when the core of the SWW migrated north of the study area (51°S), promoting the growth of glaciers, the expansion of closed-canopy forest and the rise in lake-levels, while the opposite responses are associated with warm/wet periods, when the SWW core migrated poleward (Moreno *et al.,* 2014). Most of these warm/dry periods lasted about 200 years, starting at ca. 10.3 ka (calibrated ^{14}C age; Moreno *et al.,* 2018), however, a large warm/dry period during Early to Middle Holocene is recognized in several paleo-climate archives in the area (EWDA in the right panel of Fig. 4). This period is constrained between: ca. 9.3-7.5 ka in the Lago Cipreses core (Fig. 2) (calibrated ^{14}C age; Moreno *et al.,* 2018), ca. 7.5-5.7 ka in the Lago Pato core (Fig. 2) (calibrated ^{14}C ages; Roberts *et al.,* 2022), 10.8-6.8 ka in the Vega Ñandú core (Fig. 2) (calibrated

^{14}C ages; Villa-Martínez and Moreno, 2007), and ca. 8.5-5.5 ka in the Cueva Chica speleothem (U-Th in calcite; Nehme *et al.,* 2023) (Fig. 2 and 4G-H). These dates partly overlap with the glacial chronology record (or its absence) northwards, in the Lago Argentino basin (ca. 50.25°S), were a long period of outlet glacier retraction spanning between ca. 12.2-7.7 ka is identified (^{10}Be ages; Strelin *et al.,* 2014), partly coinciding with the lake-level minima of Laguna Potrok Aike around 7-9 ka (calibrated ^{14}C ages; Anselmetti *et al.,* 2009) (Fig. 4I). Holocene glacial expansion at the latitude of the study area were restricted to the vicinity of the SPI (TDP V-VII in Fig. 3), occurring at an age of ca. 3.2 ka, and during the last millennia at ca. 700-500 yr. B.P., 400-300 yr. B.P., and 250-150 yr. B.P. (^{10}Be ages; García *et al.,* 2020) (Fig. 4I). The latter three glacial advances are synchronous with an hyperhumid phase that predates the modern warm/dry period that prevails since its establishment at 1890 CE (Moreno *et al.,* 2014).

2.4 HOLOCENE EVOLUTION OF LAGO SARMIENTO AND LAGUNA AMARGA

During the transition to ice-free conditions a large proglacial paleo-lake was formed in the study area, the Great Tehuelche Paleolake (Solari *et al.,* 2012), which connected Lago Sarmiento with Lago Toro, Lago Nordenskjöld and Laguna Amarga, among others (Fig. 3). The maximum altitude of this paleo-lake is inferred to be around 120 m.a.s.l., which is the height of the moraine arches damming the lake at its eastern end (TDP I to IV in Fig. 3). As inferred from the record of Lago Pato core (Fig. 2) (Roberts *et al.,* 2022), the Great Tehuelche Paleolake drained by ca. 11.7 ka (calibrated ^{14}C ages; Fig. 4), indicating that since early Holocene the TdPB has remained with an hydrological configuration similar to the modern one.

The lake-level fluctuations of Lago Sarmiento and Laguna Amarga during the Holocene are only partly constrained. Solari *et al.* (2012) performed a geomorphological survey in the area and described the occurrence of several terraces on Lago Sarmiento and Laguna Amarga sub-basins, which they interpreted as lake's paleo-shorelines. In Lago Sarmiento the terrace S2 (105-100 m.a.s.l.) may represent a shoreline of the Great Tehuelche Paleolake, while terrace S1 (85-90 m.a.s.l) formed once the lake had already become an endorheic systems. In Laguna Amarga, the older microbialites (ca. 7.1 Cal ka B.P.) (Solari *et al.,* 2010) formed at altitudes comparable to those of Lago Sarmiento's terrace S1 (ca. 90 m.a.s.l.),

indicating this sub-basin was articulated as an endorheic system by that time. Carbonate build-ups in Lago Sarmiento, on the other hand, are disposed below the S1 terrace, at altitudes between 75-85 m.a.s.l. The minimum age of these deposits is constrained by a gastropod shell collected from the top of the section, which yielded an age of ca. 1.2 Cal kyr B.P. (Solari *et al.,* 2010).

Lake-level variations during the last centuries are better constrained for Lago Sarmiento based on historical and aerial photography, which show a decrease of about 6 meters since 1929 (Airo, 2010). In Laguna Amarga, the age of the younger paleo-shoreline, over which the travertines are deposited, is constrained by a ca. 470 Cal yr. B.P. age obtained in the organic fraction of a microbialite collected just above paleo-shoreline (Solari *et al.,* 2010), thus representing a maximum age for this geomorphological marker.

3 MATERIALS AND METHODS

The materials studied in this work mostly correspond to carbonate rock samples together with spring and lake waters from the travertines of Laguna Amarga and the lacustrine tufa at Lago Sarmiento. Besides, to constrain possible sources of these systems, samples were collected from local reservoirs recognized in the area, including waters from lakes and rivers, and carbonate-bearing lithologies composing the bedrock. Also, one biological sample collected in the margin of Lago Sarmiento was studied to determine their bacterial composition.

The methods used in each matrix are described below, and the specific sampling sites and amount of analyzed samples will be indicated when corresponding in each of the following chapters.

3.1 WATER SAMPLES

Sampling of lake waters from Lago Sarmiento and spring waters from the travertines in Laguna Amarga were carried out along five campaigns, during 2017, 2018, 2022, 2023 and 2024, mostly between late September and early October, besides of February and April. Few local lakes and rivers were also sampled for comparison.

3.1.1 Physiochemistry and major element composition

In situ measurements of temperature, pH, electric conductivity (EC), salinity, dissolved oxygen (DO) and oxidation-reduction potential (ORP) were carried out with a Horiba multiparameter during the fieldwork. One liter of water was conditioned in plastic bottles to determine the major element composition. Ion concentrations of HCO_3^-, CO_3^{2-}, Ca^{2+} and Mg^{2+} were determined by titration method using BRAND® Titrette® digital bottle top burette, and the concentrations of Cl^-, SO_4^{2-}, NO_3^-, Na^+, K^+, Fe^{2+} and SIO_2 were determined by colorimetric method using a spectrophotometer MN® UV/Vis II. These analyses were conducted at the Hydrogeological Research Laboratory (LPH) of the Paraná Federal University (UFPR). The mineral saturation indexes and the pCO_2 were computed using PHREEQC Interactive version 3 with the phreeqc.dat thermodynamic data file (Parkhurst and Appelo, 2013).

3.1.2 $\delta^{2}H$, $\delta^{18}O$ and $\delta^{13}C$-DIC isotope composition

Water isotopic analyses of $\delta^{13}C$-DIC, $\delta^{18}O$ and $\delta^{2}H$ were performed in a Thermo® Fischer Scientific mass spectrometer model Delta V Advantage equipped with a Thermo® GasBench II (LAMIR Institute – UFPR). 0.2 mL of sample was used to determine the $\delta^{18}O$ and $\delta^{2}H$. The analyses were performed in two steps using standard methods based on the isotopic equilibrium exchange at a temperature of 25°C, which included 24 hours of isotopic exchange between CO_2-H_2O for $\delta^{18}O$, and 2 hours between H_2-H_2O for $\delta^{2}H$ determinations. The analyzed CO_2 and H_2 gases were calibrated against international standards (VSMOW2 and SLAP2) and internal standards of the LAMIR Institute (iLAMIR-1A and iLAMIR-2A). The internal standards and procedures are described in Mancini *et al.* (2022). The reproducibility is better than 2.5‰ for $\delta^{2}H$ and 1‰ for $\delta^{18}O$.

Duplicates of 0.2 mL and 0.5 mL of spring water were collected for the $\delta^{13}C$-DIC analysis. The water sample was introduced using a syringe into hermetically closed 12 mL vials containing H_3PO_4, which were previously flush-filled with He to eliminate atmospheric contamination. The measurement of the $\delta^{13}C$-DIC was performed at 25°C.

The isotope composition of the waters is expressed in “δ” notation in parts per thousand (‰) relative to Vienna Pee Dee Belemnite (VPDB) for the $\delta^{13}C$-DIC, and relative to the Vienna Standard Mean Ocean Water (VSMOW) for the $\delta^{2}H$ and $\delta^{18}O$.

The obtained $\delta^{2}H$-$\delta^{18}O$ data is compared with the Global Meteoric Water Line (GMWL) (Rozanski *et al.,* 1993), the Local Evaporation Line calculated for the area of Laguna Potrok Aike (Mayr *et al.,* 2007), available local data from ice cores, rivers, lakes, groundwater (Mayr *et al.,* 2018; Moy *et al.,* 2008; Nehme *et al.,* 2023; Shiraiwa *et al.,* 2002; Solari *et al.,* 2010), and the precipitation data between 1990-2017 from the Punta Arenas GNIP station (IAEA/WMO, 2023), which was filtered according to Xia *et al.* (2020).

3.2 ROCK SAMPLES

Hand samples collected in the field were cleaned and cuted for initial inspection in the laboratory. The selected samples for bulk-rock mineralogy and

geochemical analysis were crushed and powdered using a disk mill of tungsten carbide. Detailed sampling of specific facies/fabrics (subsamples) was performed using a hand drill with a diamond point, the obtained powder (< 0.2 g) was powdered using an agata mill.

3.2.1 Textures, fabrics, and mineralogy

The textures, mineralogy and microfabrics were studied on thin sections using a Zeiss Image A2m petrographic microscope. In addition, polished and unpolished rock fragments were analyzed using a JEOL model 6010LA scanning electron microscope (SEM) equipped with detectors for secondary electron (SE) and backscattering electron (BSE) imaging, and energy dispersive X-ray spectroscopy (model EX-94410T1L11). The operating conditions were set at 10 and 20 kV and 10 mm distance.

X-ray diffraction (XRD) analyses were performed in rock powders to determinate the mineralogical composition using a PANalytical X-ray diffractometer model Empyrean equipped with a X-Celerator detector using CuKα radiation at 40 kV and 30 mA and a reading scan rate of 0.5°/min. The subsamples powders were front-loaded in a stationary holder, and the bulk-rock powders were backloaded in a spinning holder. The X-ray diffractograms were processed using HighScore software to obtain semi-quantitative mineral content. The d-spacing of the 104 calcite peak was used to estimate the Mg content in calcite using the equation: mol % MgCO3 = -363.96x + 1104.5 (Arvidson and Mackenzie, 1999). All these analyses were carried out at the LAMIR Institute (UFPR).

3.2.2 $\delta^{13}C$ and $\delta^{18}O$ isotope composition of carbonates

The analyses were conducted in a Thermo® Fischer Scientific mass spectrometer model Delta V Advantage equipped with a Thermo® GasBench II (LAMIR Institute – UFPR). The $\delta^{13}C$ and $\delta^{18}O$ isotopic ratios were measured on the CO_2 released after the 2 hours of digestion of 0.4 mg of carbonate powder by orthophosphoric acid at 72°C. NBS18, NBS19, IAEA-CO-1, IAEA-CO-8, IAEA-CO-9 and IAEA-603 international standards were used as reference materials during the analytical sessions. The reproducibility is better than 0.01‰ for $\delta^{13}C$ and 0.25‰ for

$\delta^{18}O$. The isotopic compositions are expressed in “δ” notation in parts per thousand (‰) relative to Vienna Pee Dee Belemnite (VPDB).

3.2.3 LA-MC-ICP-MS in-situ $^{87}Sr/^{86}Sr$ isotopes of carbonates

Rock fragments of selected samples were mounted in epoxy and polished. The slabs were screened in SEM-BSD to select proper ablation zones. The LA-MC-ICP-MS analysis was performed in a Thermo® Fischer Scientific Neptune Plus coupled with a CETAC Teledyne Laser Analyte Excite Excimer (193 nm) at the LAMIR Institute (UFPR). The ablation was set in the line mode, with a 40 µm spot size, line longitude of 700 µm, scanning velocity of 5 µm s-1, beam frequency of 7 Hz and energy density of 6.26 J/cm2. Analytical helium gas was used as a carrier towards the mass spectrometer, with flows of MFC1=0.55 L min-1 and MFC2= 0.35 L m-1. For the measurement in the mass spectrometer were used X skimmer and Jet sample cones set with a radio frequency power of 1200W. Argon gas was used for the colling flux (16 L min-1), auxiliary flux (0.85-0.95 L min-1), and nebulization flux (1.08-1.14 L min-1). The analysis was performed in low resolution. The monitored masses were ^{83}Kr, 83.46 ($^{167}Er+2$), ^{84}Sr, ^{85}Rb, 85.47, ^{86}Sr, ($^{173}Yb+2$), ^{87}Sr and ^{88}Sr. The JCp-1 international standard ($^{87}Sr/^{86}Sr=0.70916$) (Krabbenhöft *et al.,* 2009) was measured 4 times during each of the analytical sessions.

3.3 BIOLOGICAL SAMPLES

A microbial mat from Lago Sarmiento was picked and placed in sterile bags by using gloves and sterilized utensils (scalpel and tweezers) and kept at 4°C until it was analyzed. DNA extraction from three layers of the microbial mat was performed in the Center for Bioinformatics and Integravie Biology of the Andrés Bello University (Chile) using the PowerSoil® DNA Isolation Kit (MO BIO Laboratories), following the manufacturer’s instruction (250 mg of soil). Qubit fluorometer (Invitrogen) was used to quantify the total DNA. Samples were sequenced in the Argonne National Laboratories using the Earth Microbiome Project barcoded primer set, adapted for the Illumina HiSeq2000 and MiSeq (Caporaso *et al.,* 2012, 2010). The data analysis was performed in R v4.0.3 and RStudio, using the DADA2 software package for paired-end fastq files (https://benjjneb.github.io/dada2/) (Callahan *et al.,* 2016). For

the analysis of the 16S rRNA gene, the V4 region was amplified using primers 515F (5'GTGCCAGCMGCCGCGGTAA3') and 806R (5'GGACTACHVHHHTWTCTAAT3'). The SILVA database (version 138) was used for taxonomic assignments (Quast *et al.,* 2013).

4 SIMILAR SOURCES BUT DISTINCT $\delta^{13}C$ SIGNATURES IN ADJACENT LOW-TEMPERATURE TRAVERTINES FROM LAGUNA AMARGA (SOUTHERN PATAGONIAN ANDES)

Paulo Quezada [a], Leonardo Fadel Cury [a], Mauricio Calderón [b], Carolina Henríquez [a], Luis Mancini [a], Joicy Micheletto [a], Gustavo Barbosa Athayde [c], Anelize Bahniuk Rumbelsperger [a]

[a]LAMIR Institute, Federal University of Paraná, Av. Cel. Francisco H. dos Santos 100, Curitiba, PR 81530-000, Brazil

[b] Centro C+, Facultad de Ingeniería, Universidad del Desarrollo, Av. Plaza 680, Santiago, Chile

[c] Hydrogeological Research Laboratory (LPH), Federal University of Paraná, Av. Cel. Francisco H. dos Santos 100, Curitiba, PR 81530-000, Brazil

ABSTRACT: This study examined the waters and carbonates from two cold spring travertines (ca. 13°C) located on the sun-exposed (north-facing travertine) and sun-shaded (south-facing travertine) margins of Laguna Amarga, an alkaline lake from the semiarid region of the eastern Patagonian Andes (51°S).

The travertines are composed of calcite + low-Mg calcite ± aragonite. Both exhibit similar sedimentological transitions along their longitudinal profiles. In the proximal zones, biologically-influenced carbonates form in wetland-like environments. Spherulitic calcite precipitates in association with extracellular polymeric substances in microbial biofilms containing cyanobacteria-like molds at the vent of the south-facing travertine, while aragonite spherulite formation at the north-facing travertine vent also involves sulfate-reducing bacteria, as indicated by their close association with framboidal pyrite. Downstream, in the intermediate and distal zones, crystalline dendrites predominantly precipitate due to increased turbulence-induced CO_2 degassing.

Both travertines share a similar range of carbonate $^{87}Sr/^{86}Sr$ composition (0.70720 – 0.70740) and isotopic signatures of the spring waters, including δ^2H (ca. -110‰ VSMOW), $\delta^{18}O_{water}$ (ca. -14‰ VSMOW) and $\delta^{13}C$-DIC (ca. -5‰ VPDB), suggesting common sources and processes influencing fluid composition. This points to the dissolution of carbonates from mudstone-rich marine units of the Lower

Cretaceous ($\delta^{13}C$ ca. -1‰ VPDB) and Upper Cretaceous ($\delta^{13}C$ ca. -10‰ VPDB) during shallow subsurface circulation of meteoric waters through the bedrock. The carbon isotopic composition of the deposits resembles those of endogenic travertines ($\delta^{13}C_{trav}$ -1.2 to 5.3‰ VPDB), with the highest $\delta^{13}C_{trav}$ values associated with carbonates from the vents. However, the involvement of deep CO_2 sources is unclear and epigenic processes capable of producing the observed ^{13}C enrichments are discussed.

Despite their common sources, similar sedimentological features and $\delta^{18}O_{trav}$ compositional range (-12.4 to -10.1‰ VPDB), the $\delta^{13}C_{trav}$ values are lower in the south-facing travertine (-1.2 to 1.9‰ VPDB) compared to the north-facing travertine (1.8 to 5.3‰ VPDB). This disparity is inferred to result from variations in local environmental conditions due to different levels of insolation, which favored the incorporation of soil-derived CO_2 in the south-facing travertine and likely increased photosynthetic productivity in the north-facing travertine, thereby shifting their $\delta^{13}C_{trav}$ signatures to lower and higher values, respectively. These relationships highlight the sensitivity of low-temperature spring carbonates to subtle environmental changes at basin scales.

Keywords: non-marine carbonates, slope aspect, organo-mineralization, hydrodynamics.

4.1 INTRODUCTION

Calcareous spring deposits typically precipitate under subaerial conditions from bicarbonate-rich waters due to passive CO_2 degassing, which enhances carbonate supersaturation during water flow (Chafetz and Lawrence, 1994; Ford and Pedley, 1996; Fouke *et al.,* 2000; Pentecost, 2005; Jones and Renaut, 2010; Luo *et al.,* 2022). However, these systems often harbor diverse microbial communities (Freytet and Verrecchia, 1998; Pentecost, 2005; Fouke, 2011; Okumura *et al.,* 2012; Peng and Jones, 2013; Shiraishi *et al.,* 2019; Della Porta *et al.,* 2022) capable of induce mineralization through metabolic activity or passively influence precipitation by providing templates for carbonate precipitation (Dupraz *et al.,* 2009). In this sense, Extracellular Polymeric Substances (EPSs) secreted by microbes have proven to significantly affect crystal (micro)fabrics (Chafetz and Guidry, 1999; Della Porta *et al.,* 2022; Folk, 1994; Guo and Riding, 1992; Jones, 2017a; Kandianis *et al.,* 2008;

Okumura *et al.,* 2012; Peng and Jones, 2013; Riding, 2000; Shiraishi *et al.,* 2019), though the role of biologically-induced precipitation in these calcium carbonate supersaturated systems remains debated (Arp *et al.,* 2010; Pentecost and Coletta, 2007; Rogerson *et al.,* 2014; Shiraishi *et al.,* 2008a).

Spring-related carbonate deposits are commonly classified as tufa or travertine based on their sedimentological features and the thermal state of the spring waters. Tufa forms from cooler waters, which support colonization by eukaryotic organisms (plants, microalgae and fungi, among others) that serve as substrates for predominantly microcrystalline calcite precipitation, resulting in poorly bedded, porous deposits (Capezzuoli *et al.,* 2014; Ford and Pedley, 1996; Gandin and Capezzuoli, 2008; Jones and Renaut, 2010; Pedley, 1990, 2009). In contrast, travertine typically consists of compact, well-laminated limestones formed by crystalline carbonate crusts that precipitate from deeply-cycled thermal waters (≥ 20 °C) (Ford and Pedley, 1996; Gandin and Capezzuoli, 2014; Jones and Renaut, 2010; Pedley, 2009). However, this classification scheme has limitations. Travertine can also precipitate from low-temperature fluids (Liu *et al.,* 2003), and tufa and travertine may represent a continuum in the distal portions of calcareous hot springs as the water cools (Mors *et al.,* 2022). Additionally, in ancient spring carbonates, determining paleo-fluid temperatures can be challenging (Brasier, 2011).

A distinction in the origin of CO_2 involved in tufa and travertine formation has been highlighted. Tufa-associated CO_2 typically derives from epigenic sources, such as vegetation, soil, or the atmosphere, while travertine-associated CO_2 originates from endogenic sources, often through limestone decarbonation or mantle outgassing (Panichi and Tongiorgi, 1976; Pentecost and Viles, 1994; Pentecost, 2005; Crossey *et al.,* 2006; Gandin and Capezzuoli, 2008; Kele *et al.,* 2011; Teboul *et al.,* 2016). Based on this criterion, Pentecost and Viles (1994) and Pentecost (2005) proposed using the terms meteogene travertine and thermogene travertine instead of tufa and travertine, respectively. In this work, a similar classification scheme is adopted, but the terms epigenic and endogenic are preferred over meteogene and thermogene (cf. Claes *et al.,* 2015). The contrasting isotope compositions of epigenic- and endogenic-derived CO_2 make the $\delta^{13}C$ signature of calcareous-spring deposits a valuable geochemical tracer for differentiating between epigenic travertines (typically $\delta^{13}C < -3‰$) and endogenic travertines (typically $\delta^{13}C >$

-1‰) (Pentecost and Viles, 1994; Pentecost, 2005; Gandin and Capezzuoli, 2008; Teboul *et al.,* 2016).

FIGURE 5 – LOCATION OF THE TRAVERTINES IN LAGUNA AMARGA

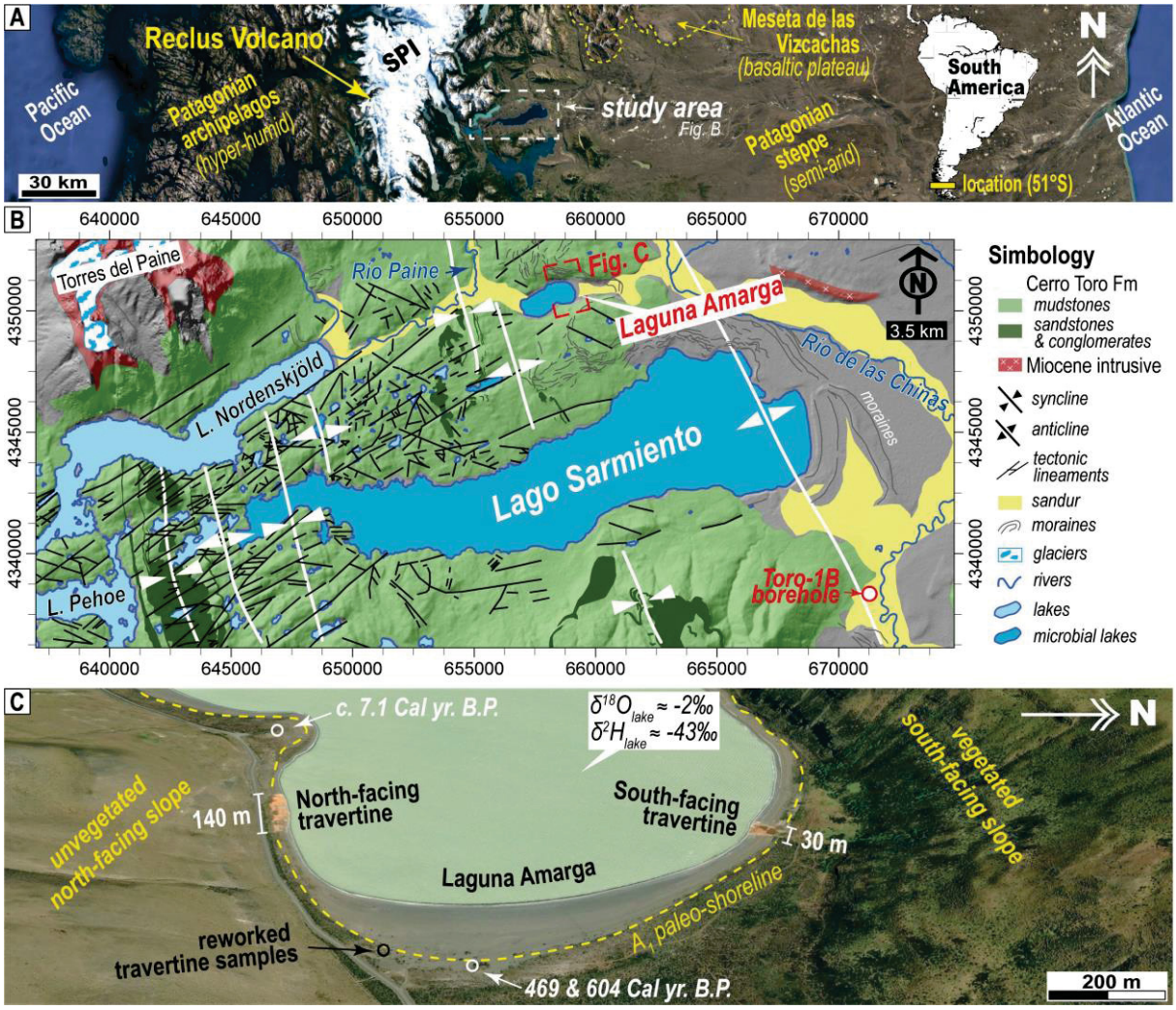

SOURCE: Quezada *et al.* (2024)

LEGEND: A) Google Earth satellite image showing the location of the study area, with the nearest late Pliocene to Quaternary volcanic units indicated. B) Geological map of the study area (modified from Ghiglione *et al.,* 2014), highlighting the locations of Laguna Amarga and the Toro-1B borehole. The glacial features are from Davies *et al.* (2020). C) 3-D view of the eastern side of Laguna Amarga (Google Earth satellite imagery). Radiocarbon ages and lake water isotope composition are sourced from Solari *et al.* (2010).

Increasing evidence shows that Quaternary travertine deposition is linked to climate oscillations, as observed at local, regional and global scales (Pentecost, 2005; Andrews, 2006; Bertini *et al.,* 2008; Ricketts *et al.,* 2019; Wang *et al.,* 2022; Harrison *et al.,* 2024; Mancini *et al.,* 2024). The carbon and oxygen isotope signatures of travertine are sensitive to seasonal variations in temperature and

precipitation, providing high-resolution records for tracing environmental changes (Liu *et al.,* 2010; Sun and Liu, 2010; Wang *et al.,* 2014). Carbon isotope signatures have also been used for paleoecological reconstructions, as spring fluids can incorporate carbon from the epigean environment during their flow (e.g., Prado-Pérez *et al.,* 2013). However, stable isotopic signals can be influenced by factors such as crystallization rates (Sun *et al.,* 2014), hydrodynamic setting (Yan *et al.,* 2012, 2021), metabolism of the involved microbes (Guo *et al.,* 1996; Fouke *et al.,* 2000) and the geological nature of substrate (Mohammadi *et al.,* 2019). Much of this understanding comes from integrative studies in active travertine systems, underscoring the importance of actualistic approaches to interpreting ancient travertine deposits.

This study compares two small, bedded travertines from a non-volcanic, semi-arid region of the Patagonian Andes (51°S), where limestone is largely absent in the bedrock (Fig. 5A-B). By integrating *in situ* physicochemical measurements with isotopic analysis of spring waters ($\delta^{2}H$, $\delta^{18}O$ and $\delta^{13}C$-DIC) and carbonates ($\delta^{13}C$, $\delta^{18}O$ and $^{87}Sr/^{86}Sr$), along with petrographic and X-ray diffraction studies, we constrained the biotic and abiotic factors influencing the sedimentological, mineralogical and isotopic features of both travertines. Our findings suggest that while similar source lithologies and processes contribute to their formation and characteristics, varying local environmental conditions, influenced by differences in sun exposure at the vents, differentially impact their carbon isotopic composition. The influence of this effect, known as slope aspect, is documented in ecological studies performed in mid-latitude regions. This work extends the discussion to its possible effects on the rock record of terrestrial spring-related carbonates.

4.2 STUDY SITE, MATERIALS AND METHODS

The studied travertines outcrop on the south-facing (50.9694°S/72.7346°W) and north-facing (50.9769°S/72.7378°W) margins of Laguna Amarga and are therefore referred to as the south-facing travertine (SFT) and north-facing travertine (NFT), respectively (Fig. 5C). Both travertines are primarily deposited below the A1 paleo-shoreline, which is located ca. 2 meters above the current lake level (67 m.a.s.l.) (Fig. 5C) (Solari *et al.,* 2012). Calibrated radiocarbon ages of the organic fraction from microbialite samples located just above the A_1 paleo-shoreline yield 469 and 604 Cal yr. B.P. (Fig. 5C) (Solari *et al.,* 2010) with the younger age interpreted

as the maximum age of the travertines. Access to the south-facing travertine was not always possible during different fieldwork campaigns due to the presence of a nearby den inhabited by *Puma concolor*.

The magnitude and direction of groundwater fluxes around Laguna Amarga remain unquantified. The lake is situated between the Río Paine and the Río de las Chinas (Fig. 5B), both of which are fed by the meltwater from perennial ice and seasonal snow accumulated in the high cordillera, respectively. Monthly average flow data from hydrological stations near Laguna Amarga (between 1985 and 2014) show that the average flow of the Río Paine is lower during autumn and winter (ca. 27 m^3/s) compared to spring and summer (ca. 72 m^3/s). The Río de las Chinas exhibits lower average flows from summer through winter (ca. 5.6 m^3/s) and higher flows in spring (ca. 16.7 m^3/s) (Meza Dabacens, 2016).

4.2.1 Water analysis

The physicochemical parameters of the travertine waters and the waters of Laguna Amarga were monitored during the field and the major element composition of three water samples from the north-facing vent were analyzed. The $\delta^{13}C$-DIC, $\delta^{18}O$ and $\delta^{2}H$ isotopic composition of 11 spring water samples were analyzed together with 4 local rivers and lakes. All the information is included in the Appendix 1.

4.2.2 Carbonate analysis

Samples of the south-facing travertine (n=8) and the north-facing travertine (n=7) were collected along their longitudinal profiles, covering the proximal, intermediate and distal depositional zones (Fig. 2A to C). These samples represent surface portions of the travertines (mostly < 2 cm depth) and are likely similar in age. Oncoids and loose calcite spherulites were collected from the intermediate and distal zone of the north-facing travertine. Two reworked samples were collected in the SE margin of the lake (Fig. 1C).

To investigate potential sources of the travertines, sedimentary carbonates from the Cerro Toro Formation including marlstones, calcite concretions and dolostones were sampled from outcrops in the area (n=8). Furthermore, calcite-bearing mudstones of the upper member of the Zapata Formation (hereafter referred

to as the Upper Zapata Formation) were sampled from depths of 75 – 460 m (n=9) in the Toro-1B well core (Fig. 5B).

Petrographic studies under SEM were performed in polished and unpolished rock fragments of 12 samples, and the textures of a few representative samples were examined under the petrographic microscope. XRD analyses were conducted on 45 samples to determine their mineralogical composition. A total of 64 carbonate samples were analyzed for $\delta^{13}C$ and $\delta^{18}O$ compositions, including 47 travertine samples/subsamples and 17 sedimentary/diagenetic carbonates of the bedrock. Finally, *in situ* $^{87}Sr/^{86}Sr$ analysis were performed in 7 travertine samples. All the information is included in the Appendix 2.

4.3 RESULTS

4.3.1 Field occurrence and morphology of the travertines

The studied travertines consist of bedded carbonate crusts of reddish to orange color (Fig. 6). The north-facing travertine is larger than the south-facing travertine in terms of lateral extension (ca. 140 m and 30 m, respectively) (Fig. 5C) and thickness (ca. 35 cm and 5 cm, respectively). The deposits of the south-facing travertine are more friable compared to those of the north-facing travertine, which consists of well-lithified carbonates.

The proximal zone is characterized by low-stand and vegetated plateaus situated approximately 2 meters above the current lake level. In this zone, bicarbonate-rich groundwater emerges through reworked sediments deposited over the bedrock, forming semi-continuous vents that produce unconsolidated carbonate deposits with a silt/mud size fraction (Fig. 6A-B). The pools in the south-facing travertine are shallower, with depths around 10 cm (Fig. 6D), compared to the north-facing travertine, where the pools reach depths of approximately 40 cm (Fig. 6E). The vents in the north-facing travertine are oriented parallel to the E-W lake shoreline (Fig. 5C), whereas in the south-facing travertine, groundwater upwelling occurs in two vegetated zones with a roughly NE-SW orientation, with the principal vent situated at a higher and outboard position relative to the lake (Fig. 6A).

An abrupt increase in slope (45°-60°) over a narrow zone of less than 0.5 meters marks the transition from the proximal zone to the intermediate zone (Fig. 6A-

B). The intermediate zone features a <10° slope and is characterized by a microterrace morphology (Fig. 6H). Here, carbonate precipitation occurs from a thin sheet of water, less than 1 cm thick, which flows from the vent toward the lake, resulting in a fan-like geometry of the deposits. Both travertines feature autobrecciated travertine sheets, though they are more prevalent in the south-facing travertine (Fig. 6B-F). White-colored botryoidal carbonates, formed by microstromatolites, grow in areas of sub-aerial exposure. In the south-facing travertine, these crusts appear as incrustations on the leeward sides of cobbles (Fig. 6F). In the north-facing travertine, they can be found stacked as microbial crusts (Fig. 6G) or as isolated mm-scale domal structures growing above the microterraces (Fig. 6H). Vegetation is minimal but persists as patches in the intermediate zone of the north-facing travertine (Fig. 6C). Oblate and minor prolate oncoids, ranging between 0.5 and 1 cm, are abundant in the intermediate zone of the north-facing travertine (Fig. 6I) but rare in the south-facing travertine. These oncoids are sometimes associated with biofilm remains (Fig. 6I).

The distal zone represents the transitional area between the Laguna Amarga foreshore and the intermediate zone of the travertine system. In the south-facing travertine, this zone is characterized by a narrow band where carbonates are deposited over reworked substrate sediments. In the north-facing travertine, the distal zone is broader and includes m-scale reworked fragments of travertine, evolving into an area where thin travertine crusts are deposited over partially cemented siliciclastic sediments near the modern lake margin (Fig. 6C). Locally, loose calcite spherulites (< 0.5 cm) and oncoids can be found in the transitional zone between the intermediate and distal areas of the north-facing travertine.

FIGURE 6 – FIELD PHOTOGRAPHS OF THE STUDIED TRAVERTINES

SOURCE: Quezada *et al.* (2024)

LEGEND: General views and sampling sites in the south-facing travertine (A) and north-facing travertine (B and C). D) Shallower vent of the south-facing travertine. E) Deeper vent of the north-facing travertine. F) Intermediate zone of the south-facing travertine, note the microbial crust on the wind-protected side of the boulders. In the north-facing travertine the microstromatolites can amalgamated conforming microbial crust (G), or isolated (H). I) Oncoids associated with biofilm remains on top of the microterraces in the intermediate zone of the north-facing travertine.

TABLE 1 – COMPARISON BETWEEN THE STUDIED TRAVERTINES

	South-facing travertine	North-facing travertine
Vent waters		
Temperature (°C)	12.8 – 13.9	12.8 – 17.8
pH	6.7 – 8.3	6.2 – 7.0
DO (mg/L)	12.8 – 41.4	8.3 – 28.18
Salinity (ppt)	0.6 – 1.9	0.8 – 1.7
$\delta^{18}O$ (‰ VSMOW)	ca. -13.6	ca. -14.4
d-excess (‰)	1.2 – 7	1.2 – 5
$\delta^{13}C$-DIC (‰ VPDB)	-5.3 – -3.4	-4.6 – -4.1 (up to 4.4)*
Travertine		
Mineralogy	calcite >> aragonite	calcite > aragonite
Oncoids	abundant	rare
$\delta^{13}C$ (‰ VPDB)**	-1.2 – 1.9	1.8 – 5.3
$\delta^{18}O$ (‰ VPDB)**	-12.1 – -10.5	-12.4 – -9.7
$^{87}Sr/^{86}Sr$ (mean)	0.70728 ± 3	0.70731 ± 3

**Samples without correlative sampling in the south-facing travertine during the same period*
**Microstromatolites analyses are not included

SOURCE: Quezada *et al.* (2024)

4.3.2 Spring water physiochemistry and isotope composition

The main physicochemical and isotopic characteristics of the spring waters from both vents are summarized in Table 1. The surficial waters at both springs have temperatures around 13°C, although temperatures of up to 18°C were measured at the north-facing travertine during warmer days. The spring waters are slightly brackish, with salinity ranging from 0.6 to 1.9 ppt, exhibit near-neutral pH values (mostly between 6.2 and 7), and are well-oxygenated (DO > 8.3 mg/L). During the 2018 fieldwork, the north-facing travertine vent emitted a hydrogen sulfide odor, indicating active sulfate reduction processes in its deeper section. This finding is consistent with the lower DO levels observed in the north-facing travertine compared to the south-facing travertine throughout the survey period (Table 1). A general trend observed as the spring waters flow from the proximal to the distal zones includes an increase in pH and ORP, along with a slight decrease in temperature (Fig. 7A).

The spring waters from the north-facing travertine vent are of the calcium bicarbonate type (Fig. 7B), exhibiting low Ca^{2+}/HCO_3^- molar ratios (0.25 – 0.44). Their Mg/Ca molar ratio are 0.31, 0.60, and 1.07. Total dissolved solids (TDS) range from

697 to 1,292 mg/L. The high Mg/Ca sample shows the highest concentrations of TDS, Na^+ (264 mg/L), SO_4^{-2} (176 mg/L), and Fe (15.96 mg/L), exhibiting a sulfur/iron molar ratio of 2.1, while having the lowest concentrations of Cl^- (1.4 mg/L) and HCO_3^- (450.9 mg/L). The calculated mineral saturation indexes (SI) for the low Mg/Ca samples are $SI_{aragonite}$: 0.04 and 0.62, and $SI_{calcite}$: 0.18 and 0.77. The high Mg/Ca sample is undersaturated with respect to calcium carbonate minerals ($SI_{aragonite}$: -0.28 and $SI_{calcite}$: -0.14) but supersaturated with respect to Fe-oxides and Fe-hydroxides (Appendix 1). The calculated log pCO_2 values range from -1.89 to -0.73, which are higher than the atmospheric levels (log pCO_2 = -3.44).

FIGURE 7 – SPRING WATER PHYSIOCHEMISTRY AND ISOTOPE COMPOSITION

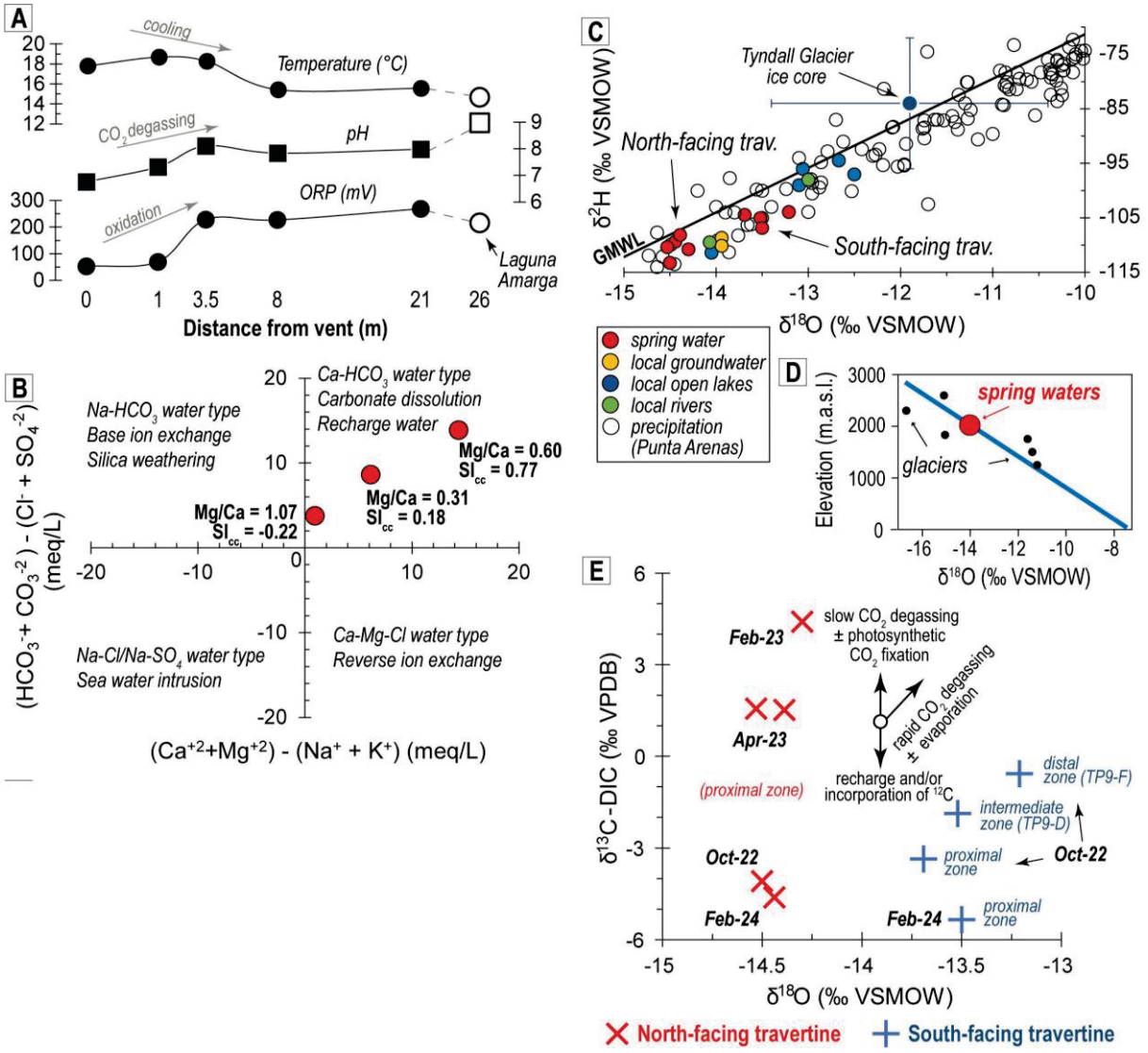

SOURCE: Quezada *et al.* (2024)

LEGEND: A) Variation of physical-chemical parameters along the longitudinal profile of the north-facing travertine. B) Modified Piper diagram (Chadha diagram) of water classification for samples from the north-facing travertine. The main processes explaining the chemical character for each water compositional field are also indicated (Chadha, 1999). C) $\delta^{2}H$-$\delta^{18}O$ isotope composition of the spring waters compared with local hydrologic reservoirs (Shiraiwa *et al.,* 2002; Moy *et al.,* 2008; Mayr *et al.,* 2018), and precipitation data from the Punta Arenas GNIP station (IAEA/WMO, 2023). D) Relation between $\delta^{18}O$ isotope composition of precipitation and elevation in the Patagonian Andes (Schwikowski *et al.,* 2013). E) $\delta^{18}O$ and $\delta^{13}C$-DIC of the spring waters. Note that no data is available for the south-facing travertine during February and April of 2023.

TABLE 2 – DESCRIPTION AND INTERPRETATION OF TRAVERTINE FABRICS

Fabric	***Description***	***Interpretation***
Aragonite spherulite (As)	Spherulites with diameters ranging between 100 – 500 µm, composed of needles of aragonite crystals (20 – 100 µm) radiating outwards from porous nuclei (10 – 100 µm in diameter) (Fig. 8B,C). In cases conform elongated arrays (Fig. 8J). The nuclei contains variable amounts of clotted micrite and/or calcified remnants of EPS and/or framboidal pyrite (<10 µm) (Fig. 8D,E,G). The aragonite crystals have euhedral external terminations but a transitional fabric to spheroidal nanocrystals in the portions adjacent to the nucleus (Fig. 8E,F,G,I). Calcified cyanobacteria-like microbes are sometimes preserved (Fig. 8K).	The occurrence of EPS remains in association with clotted micrite in the spherulite's nuclei suggest formation in a low energy environment, involving microbial mediation (Dupraz *et al.,* 2009). Similar fabrics have been reported in thermal travertines (e.g., Guo and Riding, 1992; Della Porta *et al.* 2022). The spherulites form through the aggregation of spheroidal nanocrystals (Fig. 8E,F), precipitated in association with microbial biofilms, leading to the progressive reduction of the micritic nuclei as the aragonite crystals growth inwards (Ge *et al.* 2021). The occurrence of framboidal pyrite (Fig. 8H) suggest reducing pore water conditions and the involvement of sulfate reducing bacteria in some step of mineralization (Dupraz *et al.* 2009; Pace *et al.,* 2016).
Feather-like calcite (Fc)	Partly symmetrical to asymmetrical branching calcite dendrites (Fig. 10A) growing perpendicular to the substrate. They compose laterally continuous layers (0.3 – 5 mm thick) (Fig. 10B) with intercrystalline porosity (Fig. 10A,B). The dendrites are crystalline (Fig. 10C) and may be variably coated by clotted micrite or have overgrowths of botryoidal aragonite crystals (<30 µm) (Fig. 10E), the latter only recognized in the NFT.	The formation of the feather-like calcite is attributed to abiotic precipitation from relatively fast-flowing, thin sheets of water under conditions of relatively high disequilibrium and supersaturation, promoted by turbulence-induced CO_2 degassing during the spring water flow (Jones and Renault, 1995; Guo and Riding, 1998; Chafetz and Guidry, 1999; Jones *et al.,* 2000; Gandin and Capezzuoli, 2014).
Spherulitic calcite (Sc)	Radially-organized spar calcite mesocrystals (30 – 500 µm) resulting in a spheroidal morphology (*ca.* 1 mm diameter) (Fig. 9A,B). These calcite crystals are embedded in abundant calcified EPS (Fig.9C) containing remains of encrusted cyanobacteria (Fig. 9D). Similar spherulitic calcite occurs as unlithified loose grains in the intermediate to distal zone of the south travertine (Fig. 9H). These grains have a high content of diatoms, lack of EPS, and exhibit extensive microboring of the calcite crystals (Fig. 9I).	The presence of cyanobacteria, diatoms and abundant calcified EPS in the calcite mesocrystals suggest that the spherulites formed through diffusion-related processes (*cf.* Jones 2017a) within relatively thick biofilm laminae (Dupraz *et al.,* 2009). Their formation is interpreted to be associated with low flow regimes, which favor the colonization of microorganism and consequently the generation of thicker microbial biofilm layers (Dupraz *et al.,* 2009; Okumura *et al.,* 2012; Shiraishi *et al.,* 2019).

Micro-laminated calcite (Mc)	Thin layers (0.2 – 2 mm thick) (Fig. 9A) composed of alternating syntaxial micro-laminated calcite spar/microspar (Fig. 10D). The calcite exhibits a dendritic-like microfabric (Fig. 9E) with intercrystalline porosity, partly filled with EPS threads variably encusted by micrite (Fig. 9F). Micritic microtubules and diatoms frustules, some of wich are encrusted by spar calcite, are common (Fig. 9G).	The relative abundance of microbial remains and EPS coated by micrite coexisting with spar calcite suggest a combination of physicochemical and microbially-mediated processes promoting the carbonate precipitation. Fabrics like the micro-laminated calcite has been observed associated with dendritic fabrics in several travertine systems (*cf.* Gandin and Capezzuoli, 2014), and it's interpreted as deposited in environments of lower energy compared to the feather-like calcite (*e.g.,* Mohamadi *et al.,* 2019).
Microstromatolite (St)	Microdomal structures (0.1 - 0.5 cm) (Fig. 11A) composed by micrometer-scale laminations of micrite interleaved with heteropachous bands of partly micritized spar calcite (Fig. 11B). Contain calcified remains of tingly packed and agglutinated filamentous structures of microbial origin (likely cyanobacteria) (Fig. 11D) associated with abundant diatoms and calcified EPS (Fig. 11E). Radially-organized aragonite-like needles < 20 µm are observed in microstromatolites from the NFT (Fig. 11F).	The microstromatolite are formed by biological mediation (Dupraz *et al.,* 2009) of photosynthetic microbes settle in subaerial exposure surfaces sporadically fed by waters due the effect of overflow, spraying, splashing or by capillarity action (cf. Luo *et al.,* 2022). During periods of larger water supply the spar calcite is formed due to abiotic processes.
Peloid (P)	Grains with sub-rounded, rodlike or ellipsoidal shapes and sizes between 10 - 200 µm (Fig. 10D) that are variably coated by clotted micrite (Fig. 10F). The nuclei are composed of calcite microspar or, most commonly, by aragonite arranged with spherulitic fabrics (Fig. 10G,H). Botryoidal aragonite can growth from the clotted micrite cortex (Fig. 10F).	The aragonite crystals with spherulite, fan-like and dumbbell fabrics, are interpreted to have formed within microbial biofilms (Peng and Jones, 2013; Jones 2017b), with the clotted micrite enveloped likely representing calcified EPS (Riding, 2000). The overgrowths of botryoidal aragonite suggest their formation after the peloid deposition.

SOURCE: Quezada *et al.* (2024)

The isotopic composition of the spring waters in the vents displays negative values for $\delta^{18}O$ (-14.5 to -13.2‰) and $\delta^{2}H$ (-113 to -104.4‰) (Fig. 3C), with positive d-excess values ranging from 1.2 to 7‰ (where d-excess = $\delta^{2}H - 8^{*} \delta^{18}O$; Dansgaard, 1964). The spring waters in the vents of the south-facing travertine had comparable negative $\delta^{13}C$-DIC values (-5.3 and -3.4‰) to those of the north-facing travertine (-4.6 and -4.1‰) in November 2022 and February 2024 (Fig. 7E). Positive $\delta^{13}C$-DIC compositions were exhibited by the vent waters of the north-facing travertine in February 2023 (4.4‰) and April 2023 (1.5‰) (Fig. 7E), however, no data is available for the south-facing travertine in this months. The $\delta^{13}C$-DIC values of the spring waters of the south-facing travertine increased 2.8‰ from the proximal zone to the distal zone (ca. 30 m), a variation that was accompanied by a negligible increase in the $\delta^{18}O$ values (0.5‰) (Fig. 7E) and decrease in d-excess (3.3‰) (Appendix 1).

4.3.3 Petrography and mineralogy

The XRD analysis (Appendix 2) indicates that the travertines are predominantly composed of calcium carbonates, with a content exceeding 97%. Calcite, followed by low-Mg calcite, are the major mineral components (> 92% in average), while aragonite is variably present. The mol % $MgCO_3$ content of the low-Mg calcite is mostly < 1.3. Aragonite is significant in the proximal zone of the north-facing travertine, reaching up to 57%, but its abundance decreases to around 7% in the intermediate to distal zones, except in certain fabrics (see Section 4.3.3.1 for details). In contrast, aragonite content in the south-facing travertine is negligible (< 2%). Some samples from the intermediate/distal zones contain minor amounts of detrital quartz (up to ca. 3%). No Fe-bearing minerals were identified in the XRD analysis, indicating that the iron causing the reddish color of the deposits is likely held in poorly crystalline or amorphous phases.

4.3.3.1 Fabrics and facies of the travertines

Six fabrics are recognized in the studied travertines: aragonite spherulites (As), feather-like calcite (Fc), spherulitic calcite (Sc), micro-laminated calcite (Mc), microstromatolite (St), and peloid (P). Their description and interpretation are summarized in Table 2. These fabrics are organized into five *in situ* precipitated facies, including F1) spherulite/dendrite boundstone, F2) spherulitic/laminated boundstone, F3) crystalline dendrite, F4) phyto-boundstone, and F5) microbial crust boundstone. Additionally, the F6) oncoid facies correspond to non-lithified grains.

FIGURE 8 – PETROGRAPHY OF SPHERULITE/DENDRITE BOUNDSTONE FACIES

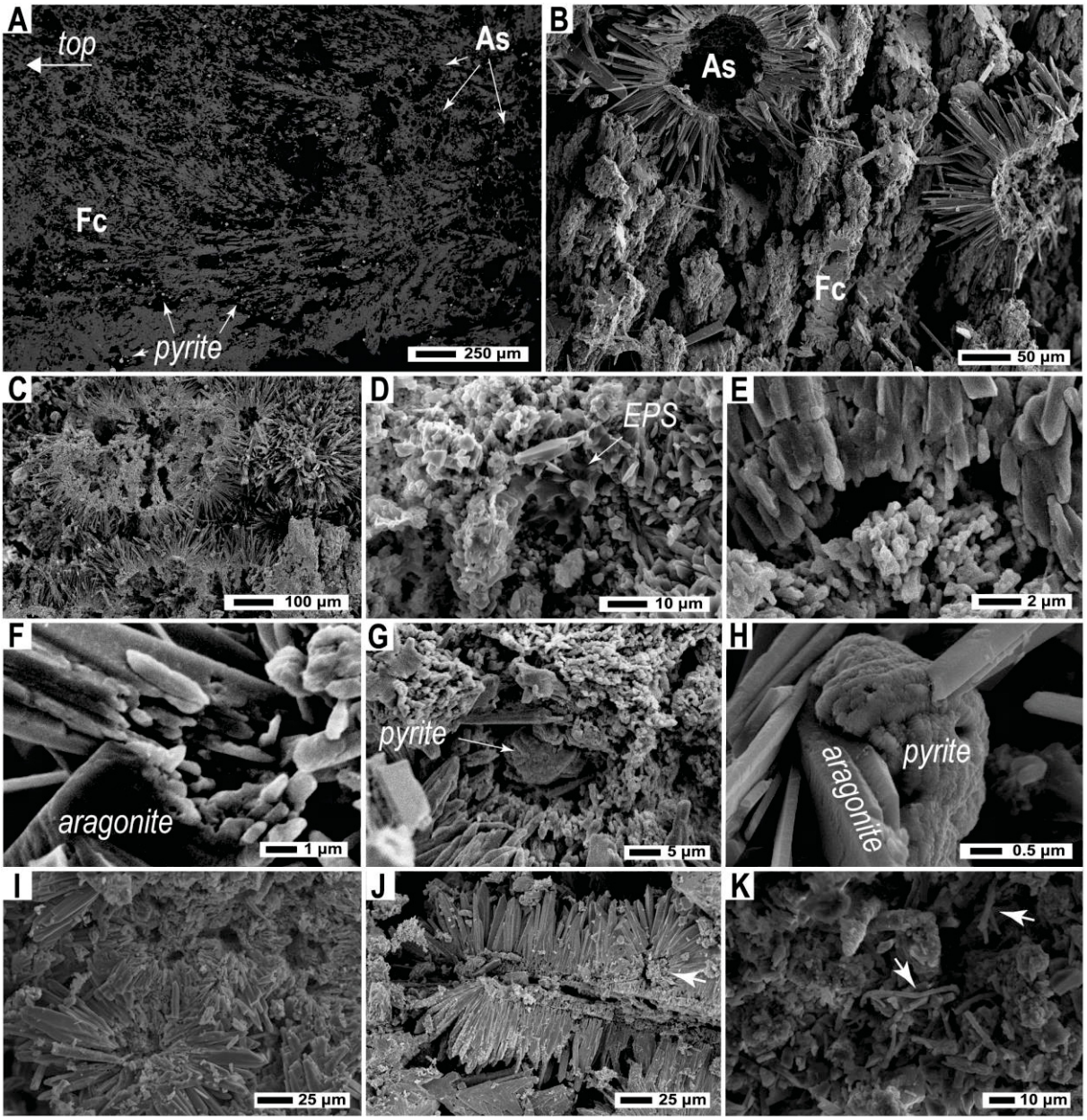

SOURCE: Quezada *et al.* (2024)

LEGEND: In situ (A to H) and reworked (I to K) samples. SEM-BSE image of a polished slab (A) and SEM-SE images of rock fragments (B to K). A) General view showing the relationship between feather-like calcite (*Fc*), aragonite spherulites (*As*), and pyrite crystals. B) Isolated *As* formed in the pore space between *Fc*. C) Laterally continuous horizon made of *As* with variable porosity in their nuclei. D) Remnants of EPS together with clotted micrite in the nucleus of an *As*. E) Fabric transition from clotted micrite to radially organized aragonite crystals in the nucleus of the *As*. F) Aragonite crystals growing from the aggregation of aragonite-like nanocrystals. G) Framboidal pyrite in the nucleus of an *As*, with clotted micrite (upper right) and aragonite crystals (lower left). H) Framboidal pyrite precipitated on aragonite crystals. I) Cluster of *As*. J) Aragonite crystals growing perpendicular to a tabular, or filamentous, pore, likely formed after organic matter degradation. Note the transitional fabric of the aragonite towards the center, similar to those observed in the *As*. The arrow indicates a botryoidal overgrowth of aragonite. K) Calcified, cyanobacteria-like, filamentous microbial remains immersed in micritic aggregates.

Spherulite/dendrite boundstone (facies F1) is formed by alternations of sub-centimetric layers of aragonite spherulites and feather-like calcite fabrics (Fig. 8A). The spherulites may form semi-continuous horizons (1–2 mm thick) or occupy the intercrystalline porosity between feather-like calcite layers (*ca.* 1 mm thick) (Fig. 8B-C). This facies are found *in situ* only in the proximal zone of the north-facing travertine, besides two reworked samples (Fig. 5C). It contains the highest amounts of aragonite in the studied systems (33 to 57%) and is the only facies where framboidal pyrite precipitates, associated with the aragonite spherulites (Fig. 8G-H).

FIGURE 9 – PETROGRAPHY OF SPHERULITIC/LAMINATED BOUNDSTONE FACIES

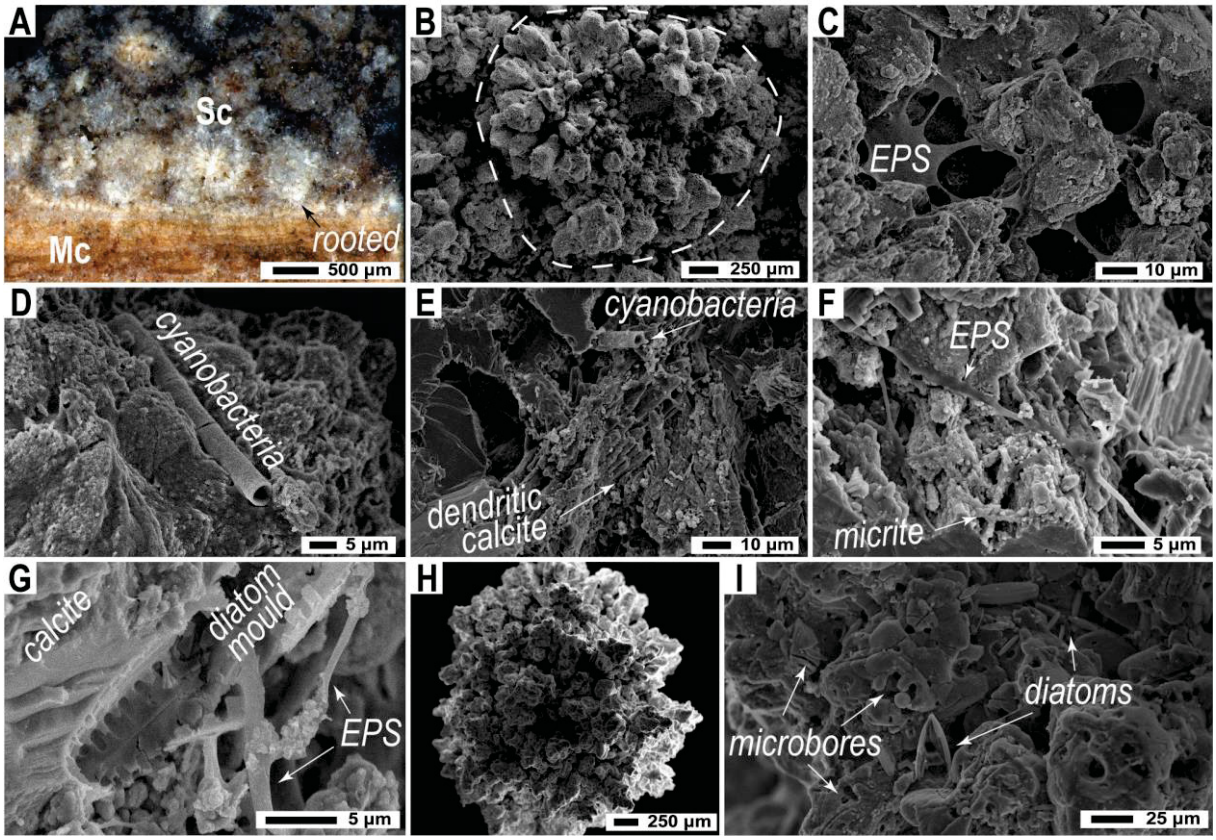

SOURCE: Quezada *et al.* (2024)

LEGEND: photograph of polished slab under magnifying glass (A) and SEM-SE images of rock fragments (B to I). A) Relationship between spherulitic calcite (*Sc*) and micro-laminated calcite (*Mc*) fabrics. Note that some *Sc* are rooted to the substrate. B) Individual *Sc* (dashed line) exhibiting a dendritic-like structure. C) Calcite mesocrystals forming the *Sc,* partially are embedded in EPS. D) Remains of calcified EPS sheets of cyanobacteria in the surface of the *Sc*. E) Calcite micro-spar with dendritic microfabric in the *Mc*, spatially associated with remains of encrusted cyanobacteria. F) Network of EPS encrusted by micrite forming the *Mc*. G) Mold of diatom frustule due to calcite microspar encrustation in the *Mc*. H) General view of loose spherulitic calcite, similar in morphology to the in situ spherulitic calcite shown in B). I) Close-up to the loose *Sc*, highlighting the abundance of diatom frustules and microbores with filamentous and spherical shapes.

Spherulitic/laminated boundstone (facies F2) is composed of a layer of spherulitic calcite (<3 cm thick) deposited on top of micro-laminated calcite (Fig. 9A). No alternation or cyclical repetitions of the two fabrics are observed. In some cases, spherulitic calcite is rooted to the micro-laminated calcite, exhibiting a pustular-like shrub morphology (Erthal *et al.,* 2017). This facies is restricted to the proximal zone and near-vent portions of the intermediate zone in the south-facing travertine.

Crystalline dendrite (facies F3) is the most representative facies in the intermediate and distal zones of both travertines, shaping the microterrace morphology (Fig. 6H). It is characterized by rhythmic layering of feather-like calcite (ca. 3-5 mm) and micro-crystalline calcite (<0.5 mm) (Fig. 10A-B). The micro-crystalline calcite is relatively thinner in the south-facing travertine. Sub-millimetric laminations of peloids delineate depositional surfaces active during the growth of crystalline dendrites in the north-facing travertine (Fig. 10C-D). Oncoids a few millimeters in size are also present (Fig. 10F to H). The aragonite content in this facies is relatively low, but larger in the north-facing travertine (0.5 – 7.1%) compared with the south-facing travertine (0 – 1.9%).

Phyto-boundstone (facies F4) corresponds to porous carbonates formed by stems and roots partially or totally encrusted by spar/microspar calcite (Fig. 11A-C). The vegetal tissues might be preserved or totally degraded, creating micro-moldic porosity in the latter case. In the proximal zone of the south-facing travertine, the deposits are thicker (ca. 5 cm), friable, and exhibit some overgrowth of microstromatolite. In the intermediate to distal zone of the north-facing travertine, this facies sporadically occur as patches in zones where the water supply is relatively constant. Includes a few oncoids baffled by plants in living position (Fig. 11A). In the distal zone of the north-facing travertine, gastropod shells are occasionally found in association with this facies, indicating a relatively prolonged contact with lake waters.

FIGURE 10 – PETROGRAPHY OF CRYSTALLINE DENDRITE FACIES

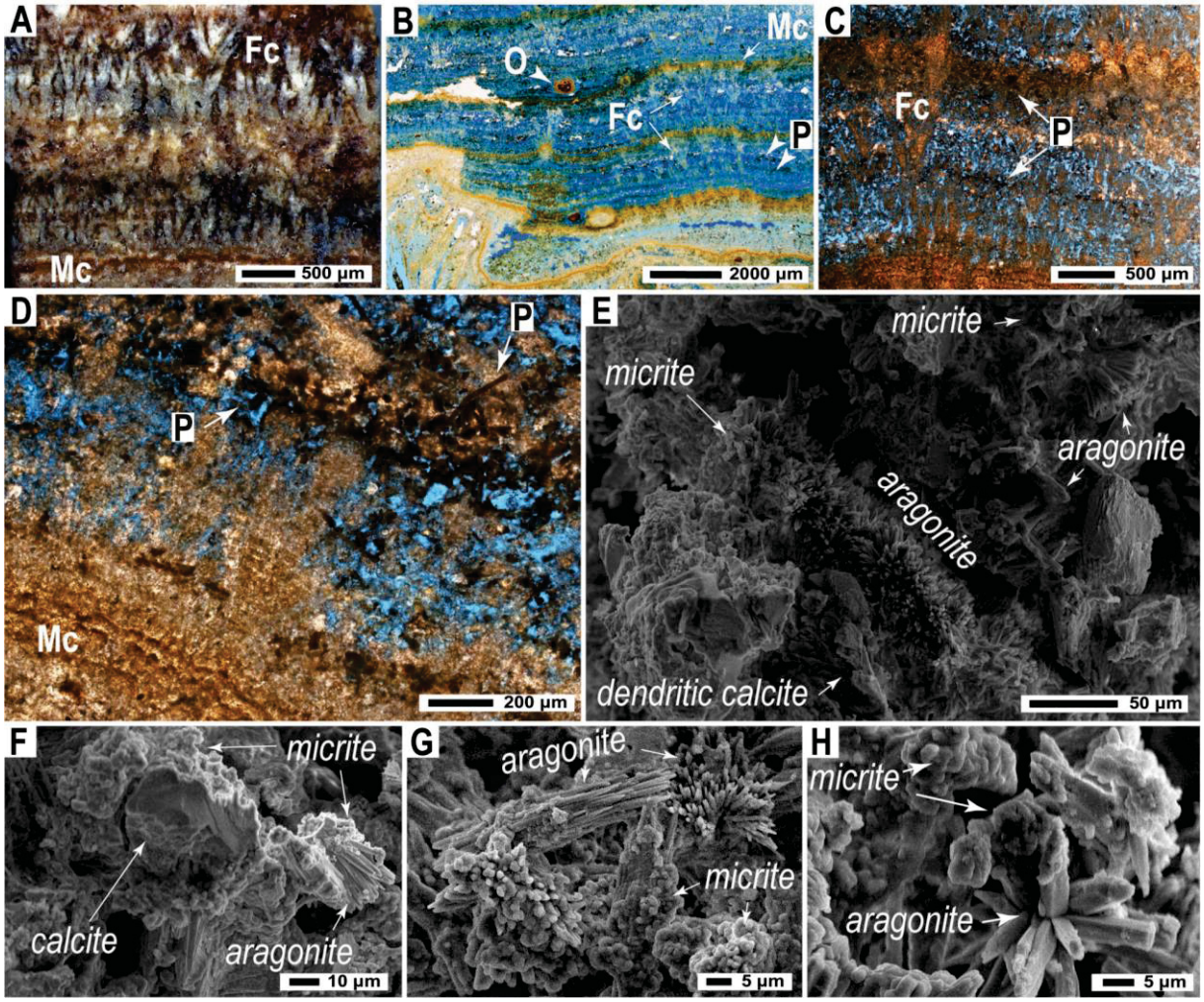

SOURCE: Quezada *et al.* (2024)

LEGEND: Photograph of polished slabs under magnifying glass (A), thin section photomicrography under unpolarized light (B and D), and SEM-SE images (C and E to H). A) Intercalations of micro-laminated calcite (*Mc*) and feather-like calcite (*Fc*) fabrics. Note the non-crystallographic branching of the *Fc*. B) *Fc* exhibiting more regular branching and intercrystalline porosity. Peloids (*P*) form continuous layers between the *Fc* and *Mc*. C) Dendritic microfabric of the *Fc*. D) Peloids (*P*) with sub-rounded and elongated shapes. Note the thin lamination of the *Mc*. E) Bundles of aragonite crystals radiating from elongated arrays (center) or displaying fan-like fabrics (upper right), partly embedded in micrite. F) Peloid conformed by a nucleus of calcite embedded in clotted micrite, overgrown with aragonite. G) Aragonite crystals with dumbbell microfabric partly embedded in clotted micrite. H) Aragonite with spherulitic fabrics in close relationship with clotted micrite.

Microbial crust boundstone (facies F5) is composed of amalgamated microstromatolites formed either in association with the phyto-boundstone facies in the north-facing travertine (Fig. 11A) or precipitated on the leeward side of boulders in the south-facing travertine (Fig. 6F). In both cases, their distribution is restricted to the intermediate zone, with thicker deposits near the vent area (<2 cm thick) compared to those located downslope (few millimeters thick) (Fig. 6H). In the south-

facing travertine the microstromatolites are composed of calcite while the north-facing travertine contains significant amounts of aragonite (between 7 and 72%).

FIGURE 11 – PETROGRAPHY OF MICROBIAL CRUST, ONCOID AND PHYTO-BOUNDSTONE FACIES

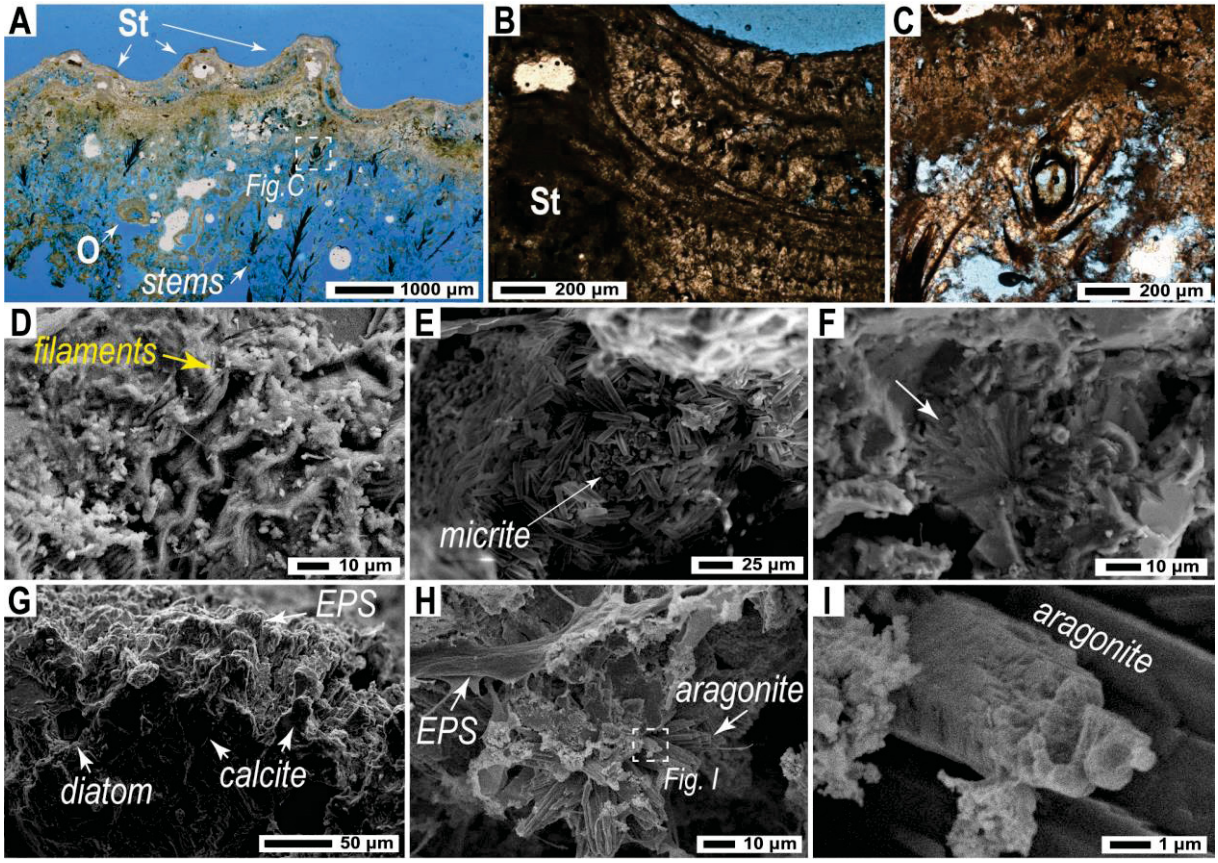

SOURCE: Quezada *et al.* (2024)

LEGEND: thin section photomicrography under unpolarized light (A to C). SEM-SE images of individual microstromatolite (A to F) and oncoid (G to I). A) Microstromatolites (*St*) formed on top of phyto-boundstone, note the oncoid (*O*) baffled by stems in living position. B) Close-up of a domal structure of a microstromatolite, showing micrite that grades laterally into alternating thin micritic laminae and partly micritized calcite spar. C) Stems encrusted by calcite. D) Filamentous microbial structures embedded in EPS. E) Diatom pockets around micrite in the inner portions of microstromatolite. F) Radially organized aragonite-like needles within the microstromatolite. G) Outer border of oncoid formed by dendritic calcite growing outward, with a thin EPS cover on the external surface. H) Botryoidal aragonite array precipitated in association with EPS in the oncoid's nucleus. I) Close-up of a growing aragonite crystal in the botryoidal array.

Oncoids (facies F6) predominantly exhibit oblate shapes and sizes between 0.5 and 1 cm. They are ubiquitous in the intermediate zone of the north-facing travertine but rare in the south-facing travertine (Fig. 6I). While they generally lack well-developed laminations, smaller oncoids (< 1 mm) observed in thin sections may display laminations (Fig. 11A). The nuclei of the oncoids are porous and contain

diatoms and EPS. In some oncoid cores, botryoidal aragonite crystals, less than 20 μm in length, are partially embedded in EPS (Fig. 11H), with smaller crystals showing incomplete outward terminations (Fig. 11I). The aragonite content can reach up to 27% in some nuclei. Toward the outer border, the abundance of EPS and aragonite decreases, and dendritic spar calcite is predominant (Fig. 11G).

4.3.3.2 Diagenesis

Mechanical weathering is the primary diagenetic modification observed, including fracturing caused by wave action in the distal zone (Fig. 6C) and the formation of autobreccias due to desiccation or frost weathering in the intermediate to distal zones (Fig. 6B-F). Fenestral porosity is also present in some crystalline dendrites, indicating partial dissolution. Cementation occurs locally as white spar calcite in some crystalline dendrite facies and is more commonly observed as small patches (< 1 mm) of calcite in the distal zone deposits of the north-facing travertine. Microbores and thin micritic bands are found in the microstromatolites (Fig. 11B).

4.3.4 Carbon and oxygen stable isotopes

There is a positive correlation between $\delta^{13}C$ and $\delta^{18}O$ in both systems, with higher $\delta^{13}C$ and $\delta^{18}O$ values associated with the bio-mediated carbonate facies of the proximal zone and more negative compositions in the crystalline dendrite facies of the intermediate to distal zones (Fig. 12A-B). The oxygen isotope composition of both travertines is overlapping the same range ($\delta^{18}O$ -12.4 to -10.1‰) (Fig. 12D). The carbon stable isotope composition of the south-facing travertine ($\delta^{13}C$ between -1.2 and 1.9‰) is lower compared to the north-facing travertine ($\delta^{13}C$ between 1.8 and 5.3‰) (Fig. 12D). The oncoids and the “loose” spherulitic calcite exhibit $\delta^{13}C$ values within the range of the *in situ* deposits of the north-facing travertine, but with slightly more positive $\delta^{18}O$ values (Fig. 12C). The aragonite/calcite cements from the lake/travertine mixing zone in the distal portion of the north-facing travertine (Fig. 12C) have $\delta^{13}C$ values like the travertines but show a more positive $\delta^{18}O$ composition.

The oxygen isotope compositions of the carbonates from the Upper Zapata Formation ($\delta^{18}O$ between -14.4 and -12.3‰) and the Cerro Toro Formation ($\delta^{18}O$

between -15.3 and -12.8‰) are similar. However, their carbon isotopic compositions are contrasting, with more positive values in the Upper Zapata Formation ($\delta^{13}C$ between -3.9 and 0.2‰, averaging -1.1‰) compared to the Cerro Toro Formation ($\delta^{13}C$ between -17.4 and -5.5‰, averaging -9.7‰) (Fig. 9).

FIGURE 12 – CARBON AND OXYGEN ISOTOPE COMPOSITION OF THE TRAVERTINES

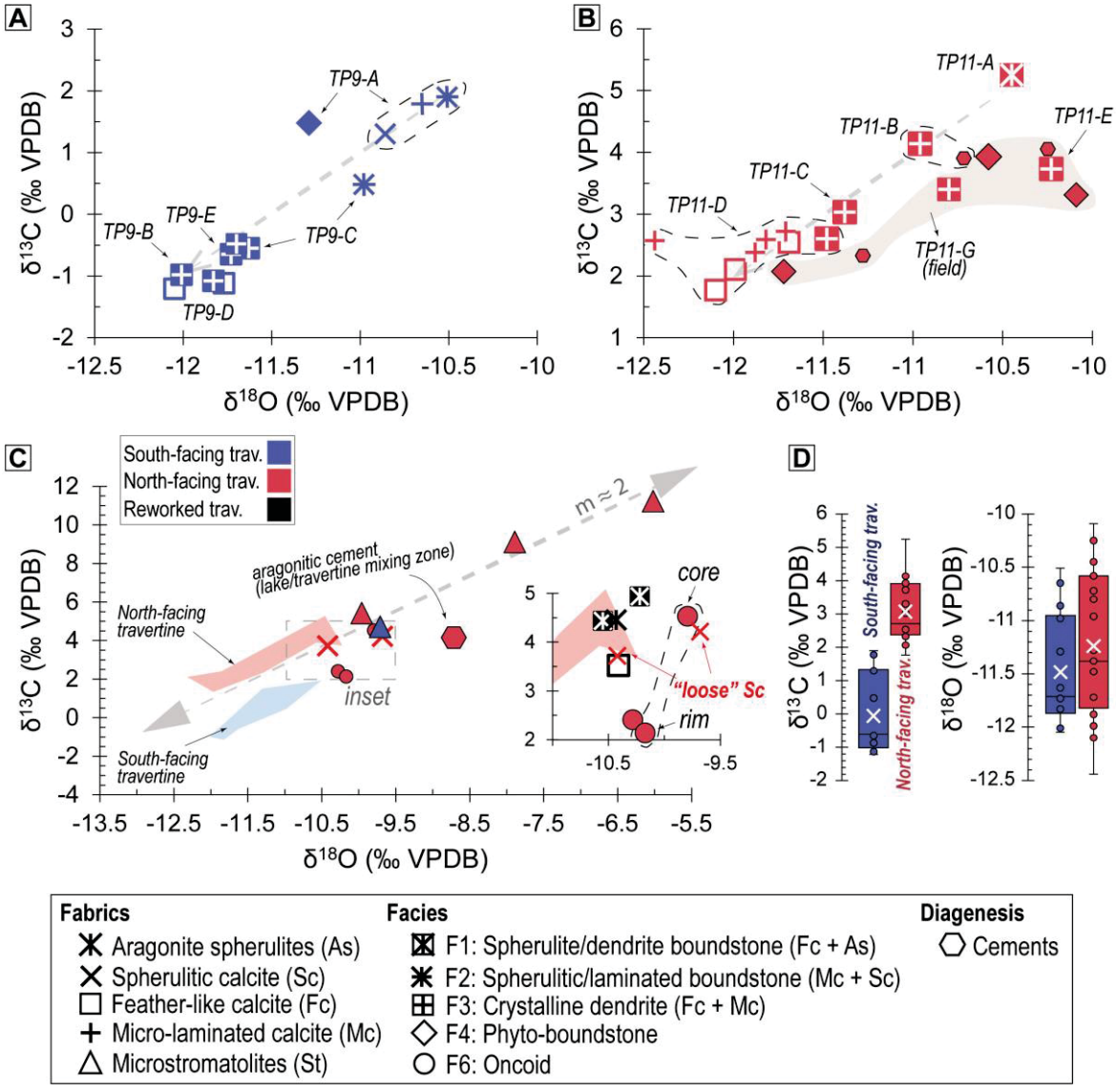

SOURCE: Quezada *et al.* (2024)

LEGEND: A) *In situ* carbonates from the south-facing travertine. B) In situ carbonates from the north-facing travertine. The grey dashed arrows highlight the similar range of internal variability in C-O isotope composition for both travertines. C) Comparison of the C-O isotopic composition across all analyzed samples. The inset highlights the composition of oncoids and loose spherulitic calcite. D) Boxplots comparing the range of carbon and oxygen isotopic compositions between the south-facing and north-facing travertines, excluding microstromatolites, oncoids, and loose calcite spherulites.

4.3.5 $^{87}Sr/^{86}Sr$ isotope composition of the travertines

The $^{87}Sr/^{86}Sr$ composition of the south-facing travertine varies between 0.70721 and 0.70736 (average of 0.70728). A similar composition is exhibited by the north-facing travertine, ranging from 0.70720 to 0.7040 (average of 0.70731) (Table 3). In both travertines, the carbonates from the proximal zone tend to have less radiogenic compositions compared to those from the intermediate zones (Table 3).

TABLE 3 – STRONTIUM ISOTOPE COMPOSITION OF THE TRAVERTINES

	Sample code	Facies	Sampling site	Fabric*	$^{87}Sr/^{86}Sr$	error (2σ)
South-facing travertine	040/22-126	spherulitic/laminated boundstone	TP9A	Sc	0.70721	2.E-05
				Mc	0.70729	3.E-05
	040/22-129	crystalline dendrite	TP9C	Fc	0.70727	3.E-05
				Fc	0.70727	3.E-05
	040/22-131	crystalline dendrite	TP9E	Fc	0.70736	2.E-05
				Fc	0.70729	3.E-05
			average		*0.70728*	*3.E-05*
North-facing travertine	060/18-01	spherulite/dendrite boundstone	TP11A	As	0.70728	2.E-05
	060/18-02	crystalline dendrite	TP11B	cement	0.70726	2.E-05
				Mc	0.70739	3.E-05
	060/18-03	crystalline dendrite	TP11C	Mc	0.70740	3.E-05
				Fc	0.70731	2.E-05
	060/18-04	crystalline dendrite	TP11D	Fc	0.70732	3.E-05
				Mc	0.70737	3.E-05
				Fc	0.70720	4.E-05
			average		*0.70731*	*3.E-05*

**Same acronyms as in Section 4.3.3.1*

SOURCE: Quezada *et al.* (2024)

4.4 DISCUSSION

4.4.1 Influence of abiotic and biotic factors on the sedimentological features of the travertines

The near-neutral pH (mostly 6.2 and 7) and above atmospheric log pCO_2 values (-1.89 to -0.73) of the spring waters at the vent, along with the in-stream rise in $\delta^{13}C$-DIC and fluid pH, are typical features of spring carbonates formed by CO_2

evasion (Chafetz and Lawrence, 1994; Pentecost, 2005; Fouke *et al.,* 2000; Kele *et al.,* 2011; Luo *et al.,* 2022, among many others).

Several factors can influence the fabric and facies types of evasive travertines. In the studied systems, topographic variation along the longitudinal profile of the travertines significantly affects the energy and regime of the spring water flow. Groundwater upwelling in the proximal zone occurs in a flat area, creating a wetland-like environment with a relatively tall column (> 10 cm) of slowly flowing water. This lower-energy environment allows the development of thicker microbial biofilms (Dupraz *et al.,* 2009; Shiraishi *et al.,* 2019), which acts as substrates for carbonate nucleation (Jones, 2017b; Della Porta *et al.,* 2022). Consequently, spherulitic carbonate fabrics are formed, with aragonite in the spherulite/dendrite boundstone facies of the north-facing travertine and calcite in the spherulitic/laminated boundstone facies of the south-facing travertine (Fig. 8 and 9). The fabric associations within each of these facies (Section 4.3.3) are interpreted to reflect variations in flow energy during precipitation (e.g., Mohammadi *et al.,* 2019; Table 2), likely in response to different rates of groundwater discharge (e.g., Rainey and Jones, 2009).

FIGURE 13 – STABLE ISOTOPE COMPOSITION OF POTENTIAL BEDROCK SOURCES

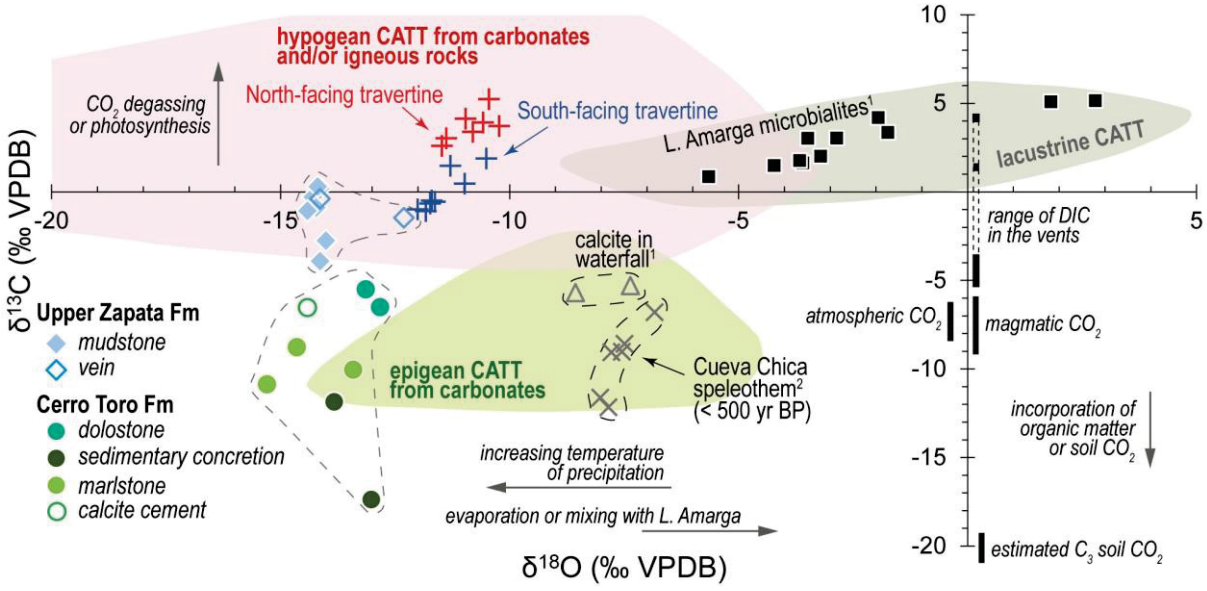

SOURCE: Quezada *et al.* (2024)

LEGEND: Carbon and oxygen isotope composition of bulk-rock travertines compared to potential bedrock sources (this study) and literature data from the area ([1]Solari *et al.,* 2010; [2]Nehme *et al.,* 2023). The compositional fields for calcitic and aragonitic travertine and tufa (CATT) are adapted from Teboul *et al.* (2016). The δ^{13}C-DIC range in the spring waters from the vents is indicated, along with

the composition of other typical carbon sources (modified from De Boever *et al.,* 2017). Note the marked difference in $\delta^{13}C$ composition between carbonates from the Upper Zapata Formation and the Cerro Toro Formation.

As the spring water reaches the intermediate zone, its flow velocity increases abruptly due to a higher topographic gradient. This less confined flow results in a reduced water column and increased turbulence due to the rougher substrate of microterraces. These hydrodynamic conditions promote CO_2 degassing and increase carbonate supersaturation (Liu *et al.,* 1995), leading to the widespread precipitation of crystalline dendrites (Jones and Renault, 1995; Guo and Riding, 1998; Chafetz and Guidry, 1999; Jones *et al.,* 2000; Gandin and Capezzuoli, 2014). Since the intermediate and distal zones are more exposed to westerly winds, seasonal variations in wind strength (Gómez-Fontealba *et al.,* 2022) can significantly impact the turbulence-induced CO_2 degassing and, consequently, carbonate supersaturation (Liu *et al.,* 1995; Zhang *et al.,* 2001; Chen *et al.,* 2004). This seasonality may contribute to the cyclic alternations observed in the crystalline dendrite facies, with feather-like calcite formed at higher precipitation rates and disequilibrium conditions due to increased turbulence driven by stronger winds (Jones and Renault, 1995; Jones, 2017b). Conversely, micro-laminated calcite fabrics form under lower turbulence and flow energy, in line with their relatively larger microbial component (Table 2).

The formation of *in situ* microbially-mediated carbonates in the intermediate and distal zones—such as isolated microstromatolites and microbial crust boundstone—is mostly restricted to sub-environments that are only sporadically in contact with the flowing waters. These include small topographic heights (Fig. 6G), surfaces on top of phyto-boundstones (Fig. 11A), or areas protected from the winds (Fig. 6F) (Section 4.3.3). It is inferred that the incorporation of biofilm into the spring water stream could lead to its mechanical fragmentation and encrustation, resulting in the formation of oncoids. The oblate shape of the oncoids suggests that their transport is primarily due to scrawling rather than rolling, and their lack of distinct lamination may indicate predominantly *in situ* growth (e.g., Hägele *et al.,* 2006). The greater prevalence of oncoids in the north-facing travertine compared to the south-facing travertine could be attributed to differing environmental conditions and/or microbial communities between the two systems, leading to increased biofilm formation in the former.

These relationships show that fluid hydrodynamics play a crucial role in the sedimentological features of the studied travertines. This is due to their influence on CO_2 degassing and, consequently, carbonate supersaturation (Liu *et al.,* 1995; Zhang *et al.,* 2001; Chen *et al.,* 2004). Additionally, hydrodynamics directly impact the ability of benthic microorganisms to settle (Dupraz *et al.,* 2009; Okumura *et al.,* 2012; Shiraishi *et al.,* 2019), thereby modulating the development of microbially-mediated fabrics.

4.4.2 Microbial mediation on the aragonite precipitation

The precipitation of aragonite in the north-facing travertine is unlikely to be related to physicochemical controls (cf. Jones, 2017b; Luo *et al.,* 2022). The spring waters have low temperatures (Section 4.3.2), and low Mg/Ca molar ratios (≤ 0.6 when $SI_{aragonite} > 0$; Section 4.3.2). Although our hydrochemical data are sparse, such Mg/Ca ratios are in good agreement with the mol % $MgCO_3$ in calcite exhibited by the travertines (4.3.3) (De Choudens-Sánchez and Gonzalez, 2009). Furthermore, the precipitation of calcite, rather than aragonite, is associated with higher rates of CO_2 degassing in the studied system (formation of feather-like calcite fabric; Section 4.4.1). Conversely, the presence of aragonite in fabrics or facies with a more predominant microbiological component (Section 4.3.3) suggests that the $CaCO_3$ polymorphism may be linked to precipitation in physicochemical microenvironments (e.g., Chafetz *et al.,* 1991), either modified by microbial metabolism (Dupraz *et al.,* 2009), or located within EPS secreted by such microbes (Decho, 2010). Moreover, depending on the EPS biochemical composition, the precipitation of aragonite over calcite can also be favored (Kawaguchi and Decho, 2002; Zhang *et al.,* 2021).

The smaller aragonite crystals with spherulitic, fan-like, and dumbbell fabrics associated with the peloids (Fig. 10E-H) resemble those formed in microdomains within microbial biofilms in hot-spring travertine systems, suggesting a similar origin (Jones, 2017a; Peng and Jones, 2013). Aragonite is also formed in the inner portions of microstromatolites and within cores of some oncoids, where it precipitates partly isolated from direct contact with the spring waters (Fig. 11F) and in association with photosynthetic microbes and EPS (Fig. 11D-E). The pore water in these restricted microenvironments might be more susceptible to physicochemical changes driven by photosynthetic microbial activity. By removing CO_2, these microbes could effectively

increase the CO_3^{2-}/Ca^{2+} activity ratio (Dupraz *et al.,* 2009), thereby enhancing aragonite supersaturation (e.g., Given and Wilkinson, 1985). The higher $\delta^{13}C$ values observed in the oncoid core compared to the rim support this (Fig. 8C). However, in addition to biotic effects, evaporation and CO_2 degassing might also contribute to increased aragonite supersaturation in the microstromatolite, as indicated by their positive $\delta^{18}O$ and $\delta^{13}C$ covariance (Fig. 12C).

The larger amounts of aragonite are formed in the vent of the north-facing travertine, within the spherulite/dendrite boundstone facies (Fig. 8; Section 4.3.3). Petrographic observations reveal that aragonite exhibits a spherulitic fabric whose growth is interpreted to occur through the aggregation of nanocrystals initially precipitated in biofilms composing the spherulite nuclei (Fig. 8D-E-F) (Ge *et al.,* 2021). Similar growth mechanisms of the aragonite spherulites is described near the vent of the Bagni San Filipo travertine and in the microbial bioherms of Great Salt Lake (Table 2) (Ge *et al.,* 2021). In these contrasting depositional environments, aragonite precipitation depends on different controlling factors; water temperature (>40°C) in the Bagni San Filipo travertine (Folk, 1994; Della Porta *et al.,* 2022), and the metabolic activity of sulfate-reducing bacteria in the Great Salt Lake bioherms (Pace *et al.,* 2016). The presence of framboidal pyrite (Fig. 8G-H) in the studied aragonite spherulites points to the participation of sulfate-reducing bacteria (Dupraz *et al.,* 2009), as well as the odorant gases expelled by the vent (Section 4.3.2). Pace *et al.* (2016) provided evidence linking aragonite nucleation and growth to microdomains created by the degradation of cyanobacteria and extracellular organic matrixes due to the activity of heterotrophic microbes, including sulfate-reducing bacteria. The high $\delta^{13}C$ values (> 4.4‰) (Fig. 12B-C) of the spherulitic/dendritic boundstone suggest that the contribution of alkalinity from the decay of organic matter to the DIC pool is minor. Thus, even though aragonite mineralization may be influenced by the heterotrophic degradation of exopolymers (Arp *et al.,* 2012; Pace *et al.,* 2016), the primary source of alkalinity is the spring waters.

The combined influence of strong photosynthetic activity and significant inhibitory effects of EPS on carbonate crystallization has been proposed as mechanism for forming aragonite spherulites precipitating from microcrystalline aggregates in microbial mats within sea-water fed lakes (Arp *et al.,* 2012). Also, microbial photosynthesis has been interpreted as the driving force behind the formation of micritic laminae of aragonite spherulites associated with dendritic calcite

in thermal travertine (Guo and Riding, 1992). By stimulating EPS production, photosynthetic microbial activity has been linked to enhanced aragonite precipitation (Kawano and Obokata, 2007; Kandianis *et al.,* 2008; Okumura *et al.,* 2013). In the case under study, elevated rates of photosynthesis could explain the high $\delta^{13}C$ values observed in the carbonates (> 4.4‰; Fig. 12C) and in the $\delta^{13}C$-DIC of spring water from the vent (up to 4.4% in some periods, as discussed in Section 4.4.4.1) (Fig. 7E), despite the activity of heterotrophic bacteria.

While there are similarities with the cited examples, the available data does not allow us to determine the controlling factors on aragonite precipitation in the north-facing travertine beyond suggesting a link to EPS-mediated mineralization. However, the absence of framboidal pyrite in the spherulitic calcites from the south-facing travertine vent suggests that, in addition to the likely influence of photosynthetic microbes, sulfate-reducing bacteria may play a significant role in the stabilization of aragonite over calcite in the vent of the north-facing travertine.

4.4.3 Sources of the fluids and dissolved compounds forming the travertines

Besides mechanical weathering, the effects of diagenesis are reduced (Section 4.3.3.2), with sparse cementation and formation of micrite outlines, likely due to sparmicritization (Fig. 11B) (Kahle, 1977). The subtle increase in $\delta^{18}O$ values in the distal zone of the north-facing travertine (Fig. 12B) likely results from mixing with evaporated lake waters ($\delta^{18}O$: ca. -2‰ VSMOW; Solari *et al.,* 2010) (Fig. 13), consistent with the gastropods found in phyto-boundstone (Section 4.3.3.1) and higher $\delta^{18}O$ in carbonates from the modern lake-water mixing zone ($\delta^{18}O$ of -8.7‰; Fig. 6C and 12C). Therefore, the $\delta^{13}C$ and $^{87}Sr/^{86}Sr$ values of carbonates in the proximal and intermediate zones are more likely to reflect those of the spring waters.

Both studied travertines exhibit $\delta^{13}C$ values that are consistent with those typically found in endogenic travertines ($\delta^{13}C$ > -2‰) (Fig. 13) (Pentecost, 2005; Gandin and Capezzuoli, 2008; Teboul *et al.,* 2016). However, considering the non-volcanic nature of the local setting, the reduced size of the deposits and the low temperature of the spring waters, the contribution of endogenic CO_2 must be evaluated by considering the sources and processes involved in the formation of the travertines.

The $\delta^{2}H$, $\delta^{18}O$ and d-excess values of the spring waters are similar to those exhibited by open lakes and rivers in the area, suggesting a common origin (Section 4.3.2; Fig. 7C). Compared with the $\delta^{18}O$ vs. altitude precipitation curve proposed for the Patagonian Andes, it is inferred that the aquifer feeding the travertines is recharged by meteoric waters derived from the ablation of snow and/or ice precipitated at altitudes of ca. 2000 meters (Schwikowski *et al.,* 2013) (Fig. 7D). After infiltration, these waters dissolve both carbonate-rich and silicate-rich lithologies in the subsurface. This is inferred from the Ca^{+2}/Na^{+} vs HCO_3^{-}/Na^{+} meq ratios exhibited by the spring waters (Gaillardet *et al.,* 1997) (Appendix 1).

FIGURE 14 – STRONTIUM ISOTOPE COMPOSITION OF THE TRAVERTINES

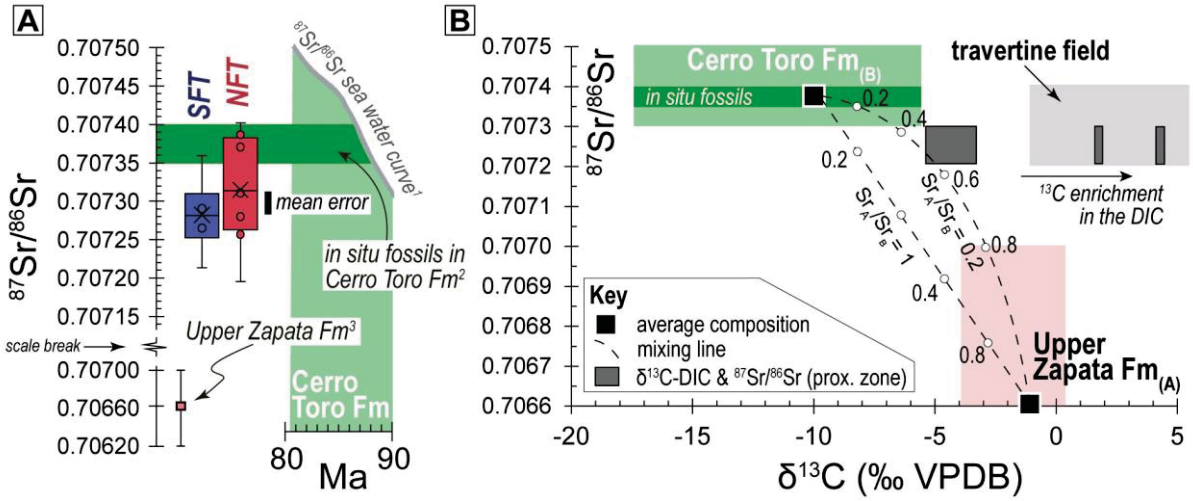

SOURCE: Quezada *et al.* (2024)

LEGEND: A) Boxplot showing the Sr isotope composition of the south-facing travertine (SFT) and the north-facing travertine (NFT), compared to global ([1]McArthur *et al.,* 2020), and local ([2]Bernhardt *et al.,* 2012; [3]Fildani and Hessler, 2005) literature data. B) Mixing model between Cerro Toro Formation and Upper Zapata Formation, using Sr isotope data from literature and carbon isotope data from this study. The Sr isotope composition of the dark grey boxes represents the range of values from samples in the proximal zones of both travertines. The Sr_A/Sr_B ratios in the mixing model are arbitrary.

The $^{87}Sr/^{86}Sr$ signature of the travertines reflects the isotopic composition of the precipitating spring waters and can be used to constrain the parent rocks that interacted with the meteoric waters during their hydrogeological pathway (e.g., Crossey *et al.,* 2006). The average $^{87}Sr/^{86}Sr$ values of the south-facing travertine (0.70728) and north-facing travertine (0.70731) are identical within the analytical error (0.00003), indicating similar sources for both travertines (Fig. 14A). These values are lower than the $^{87}Sr/^{86}Sr$ composition of *in situ* fossils in the Cerro Toro

Formation (Bernhardt *et al.,* 2012) and are at the lower end of the expected values for marine carbonates with ages in the range of the Cerro Toro Formation (Fig. 14A) (McArthur *et al.,* 2020). The less radiogenic signatures exhibited by the travertines ($^{87}Sr/^{86}Sr$ 0.70720 – 0.70729) are mainly restricted to samples from the vents or near them (Table 3) and are interpreted as more representative of the fluid composition in subsurface, while the higher $^{87}Sr/^{86}Sr$ values downstream might reflect in-stream incorporation of more radiogenic Sr. This suggests that, in addition to Cerro Toro Formation, Sr is also being supplied by a less radiogenic source. The most likely candidate is the Upper Zapata Formation, whose (present-day) mean Sr isotopic composition is 0.7066 ± 0.0004, as reported in mudstones cropping out at the latitudes of the study area (Fig. 14A) (Fildani and Hessler, 2005). The participation of geological units located stratigraphically below the Upper Zapata Formation is unlikely due their more radiogenic (present-day) $^{87}Sr/^{86}Sr$ composition (> 0.7100) (Fildani and Hessler, 2005; Calderón *et al.,* 2007 and references therein). This suggests that the infiltration of meteoric waters did not exceed depths greater than ca. 450-500 m, which is the depth of the bottom of Upper Zapata Formation in the Toro-1B borehole (Katz, 1963), consistent with the low temperature of the spring waters (ca. 13°C).

The involvement of endogenic CO_2 is difficult to reconcile with the shallow aquifer feeding the travertines. CO_2 originating from thermal decarbonation of limestone or magma degassing would need to either be transported in solution to the surface via deep-seated faults (e.g., Crossey *et al.,* 2006; Ring *et al.,* 2016), which seems implausible given the $^{87}Sr/^{86}Sr$ composition of the travertines, or be introduced as a dry gas phase into the aquifer. CO_2 discharge through dry gas vents or zones of diffuse degassing are far more common in regions with abnormally high heat flow (above 100 mW/m^2), usually associated with zones of crustal stretching or major lithospheric fault zones with active seismicity, where thermal springs are typically abundant (e.g., Kerric, 2001; Faulds *et al.,* 2004; Minissale, 2004; Tamburello *et al.,* 2018; Vannoli *et al.,* 2021). At the latitudes of the study area (ca. 51°S), hot springs are notably scarce compared to the Patagonian Andes north of 48°S (Hauser, 1997), where heat flow is higher (>100 mW/m^2) due to active ridge subduction (Avila and Dávila, 2018). Additionally, although the area is seismically active, the intensity and abundance of seismic events are much greater north of 46°S (Suárez *et al.,* 2021). The involvement of endogenic CO_2 is not clear even in tufa deposits within

Pleistocene basaltic maars located ca. 200 km SE of Laguna Amarga (Henriquez *et al.,* 2022). Therefore, it seems reasonable to discuss other possibilities.

The sulfur/iron molar ratio (S/Fe = 2.1) in the high Mg/Ca spring water sample suggests that these elements are derived from pyrite (FeS_2) oxidation, following the reaction: $FeS_2 + 7/2O_2 + H_2O \rightarrow Fe^{2+} + 2SO_4^{2-} + 2H^+$. Although our hydrochemical data are sparse, the reddish color of the travertines, indicative of their iron content, suggests a rather continuous availability of dissolved Fe in the spring waters over time. It is thus possible that pyrite breakdown, which is an abundant mineral in the Zapata Formation (Wilson, 1991), might be influencing the spring water chemistry in the long-term. Chemical weathering of carbonate rocks by sulfuric acid derived from pyrite oxidation can be significant in regions rich in black shales, like the studied one (Calmels *et al.,* 2007; Li *et al.,* 2008). Since this process does not involve the participation of other CO_2 sources, the resulting carbon isotope composition of the fluid is similar to the $\delta^{13}C$ values of the source rocks (Aucour *et al.,* 1999; Li *et al.,* 2008). Carbonate dissolution within the $CaCO_3$–H_2O–CO_2 system cannot be ruled out, however, in this case, it would need to occur primarily under closed system conditions (Buhmann and Dreybrodt, 1985). Otherwise, the $\delta^{13}C$ composition of the dissolved bicarbonate would shift to more negative values, buffered by the soil $\delta^{13}C$ composition (Deines *et al.,* 1974), resulting in compositions similar to those exhibited by a local speleothem ($\delta^{13}C$ ca. -9.5‰ for overgrowths < 500 yr. BP) (Nehme *et al.,* 2023), which is comparable to typical epigenic travertines (Pentecost, 2005; Teboul *et al.,* 2016; Fig. 13). A simple mixing model considering the closed system dissolution of carbonates of the Cerro Toro Formation ($\delta^{13}C$ ca. -10‰) and the Upper Zapata Formation ($\delta^{13}C$ ca. -1‰) (Fig. 13) reproduces $\delta^{13}C$-DIC compositions like the exhibited by the spring waters (ca. -5‰) if over 50% of the DIC is supplied by carbonates from the Upper Zapata Formation, with the remainder coming from the Toro Formation (Fig. 14B).

In summary, although we acknowledge that cryptic contributions of endogenic CO_2 might be involved in the formation of the travertines, epigenic processes could also explain their characteristics. Their relatively high $\delta^{13}C$ values (> -2‰) might result from closed system carbonate dissolution involving variable amounts of sulfuric acid sourced by pyrite breakdown, followed by $^{13}C/^{12}C$ fractionation by abiotic and/or biotic processes in the epigean environment (discussed in Section 4.4.4.1). High rates of wind-induced CO_2 degassing in these

systems, as inferred from the rapid in-stream δ^{13}C-DIC increase (ca. 3‰ over 30 meters), could elevate calcium carbonate supersaturation levels sufficiently to precipitate facies typically found in endogenic travertines, such as crystalline dendrites (Gandin and Capezzuoli, 2014). In this sense, branching calcite spar, comparable in size to those in the studied crystalline dendrites, forms in high-energy sub-environments of (epigenic) calcareous tufa systems (e.g., Gradziński, 2010).

4.4.4 Influence of intrinsic factors on the carbon and oxygen isotopes

The higher δ^{13}C and δ^{18}O values exhibited by the carbonates from the proximal zone, compared to those in the intermediate to distal zones, represent atypical features for evasive travertines (Fig. 12A-B) (Chafetz and Lawrence, 1994; Pentecost, 2005; Fouke *et al.,* 2000; Kele *et al.,* 2011; Teboul *et al.,* 2016). Notably, these characteristics are observed in both travertines, suggesting that they result from common intrinsic processes, as discussed below.

4.4.4.1 Carbon isotopes

During February and April 2024, the spring waters in the vent of the north-facing travertine exhibited positive excursions in δ^{13}C-DIC (ca. 4.4 and 1.5‰, respectively), with negligible changes in the δ^{18}O values (Fig. 7E). This differs from the coupled seasonal shifts in the carbon and oxygen isotopes observed in calcareous spring systems (e.g., Liu *et al.,* 2010; Yan *et al.,* 2017), and it is unlikely to result solely from evaporative processes during the summer season. If evaporation were the cause, some degree of δ^{13}C-DIC and δ^{18}O covariance would be expected (Horton *et al.,* 2016) (Fig. 7E), as well as with rapid CO_2 degassing (Asta *et al.,* 2017).

The increase in δ^{13}C-DIC (Fig. 7E) could be associated with slow CO_2 degassing, along with variable contributions from photosynthetic uptake of ^{12}C by microbes (Guo *et al.,* 1996) and vegetation (Coletta *et al.,* 2001). This interpretation is consistent with the predominance of biologically-mediated carbonates exhibiting high δ^{13}C values in both vents (Fig. 12A-B), indicating that ^{13}C enrichment of the spring waters is a recurrent process in the proximal zone. This may explain the high δ^{13}C values of the DIC and carbonates in the vents, but not the lower δ^{13}C values of

the carbonates in the intermediate to distal zones, which would be expected to precipitate from fluids with higher δ^{13}C-DIC due to in-stream CO_2 degassing (Fig. 7E). Kinetic effects associated with pH-dependent DIC speciation reactions (cf. Watkins and Hunt, 2015; Sade *et al.,* 2020) or hydrodynamic influences (Yan *et al.,* 2021) on carbon isotope fractionation are smaller than the in stream δ^{13}C-DIC rise (ca. 3‰; Fig. 7E) and thus unlikely to account for the observed δ^{13}C variations within each travertine (up to ca. 3‰; Fig. 12A-B). Additionally, considering a 1‰ calcite-DIC δ^{13}C fractionation factor (Romanek *et al.,* 1992), the δ^{13}C values of the carbonates from the intermediate/distal zone of the south-facing travertine (-1.2 to 0.5‰; Fig. 12A) can be explained by the measured δ^{13}C-DIC of the spring waters (-1.9 to -0.6‰; Fig. 7E). These observations suggest that precipitation occurs diachronically between the proximal and intermediate/distal zones. A likely explanation could be linked to variations in groundwater discharge rates, as inferred from the fabric associations in the vents (Section 4.3.3.1). In such a case, during periods of lower discharge and consequently longer residence times of the spring waters in the vents, CO_2 degassing and photosynthetic CO_2 uptake would raise the δ^{13}C-DIC and increase the CO_3^{2-}/Ca^{2+} activity ratio, resulting in the precipitation of biologically-influenced carbonates enriched in ^{13}C in the vents (Fig. 12A-B). Conversely, during periods of higher groundwater discharge, the δ^{13}C-DIC in the vents would be buffered by groundwater composition (ca. -5‰; Section 4.4.3), and carbonate supersaturation would primarily be driven by passive CO_2 degassing along the stream. This process would lead to more extensive carbonate precipitation in the intermediate and distal zones, but with lower δ^{13}C values compared to those in the proximal zone. Higher-resolution monitoring is necessary to evaluate this hypothesis.

4.4.4.2 Oxygen isotopes

The observed differences in δ^{18}O between the proximal and the intermediate/distal zones may result from variations in the δ^{18}O composition of the spring waters or differences in precipitation temperatures (e.g., Kele *et al.,* 2011 and references there cited). The impact of these variables was estimated on the south-facing travertine, which exhibited stable vent temperature (ca. 13°C) and negligible aragonite content (i.e., no mineralogical influence on δ^{18}O). For this, theoretical

calculations were performed using oxygen isotope fractionation factors suited for low-temperature spring carbonates:

1) the bicarbonate-water curve of Halas and Wolacewicz (1982) (1000 $\ln\alpha(HCO_3^-\text{-}H_2O) = 2{,}920{,}000/T^2 - 2.66$), following Kele *et al.* (2011), and

2) the $CaCO_3$-water curve proposed by Kele *et al.* (2015) for travertine, tufa and cave carbonates (1000 $\ln\alpha(CaCO_3\text{-}H_2O) = 16.8 \times 1000/T - 26$).

Our estimates suggest that temperature does not control the $\delta^{18}O$ values of the carbonates, as an in-stream temperature rise of about 3 to 7°C would be required (Fig. 14), which seems implausible given the observed temperature trends (Fig. 7A). Variations in fluid compositions (by 1.5‰ towards more negative values) could explain the $\delta^{18}O$ shift (Fig. 15), although such large variations were not detected during the study period (Fig. 7E).

FIGURE 15 – THEORETICAL CALCULATIONS OF THE OXYGEN ISOTOPE COMPOSITION

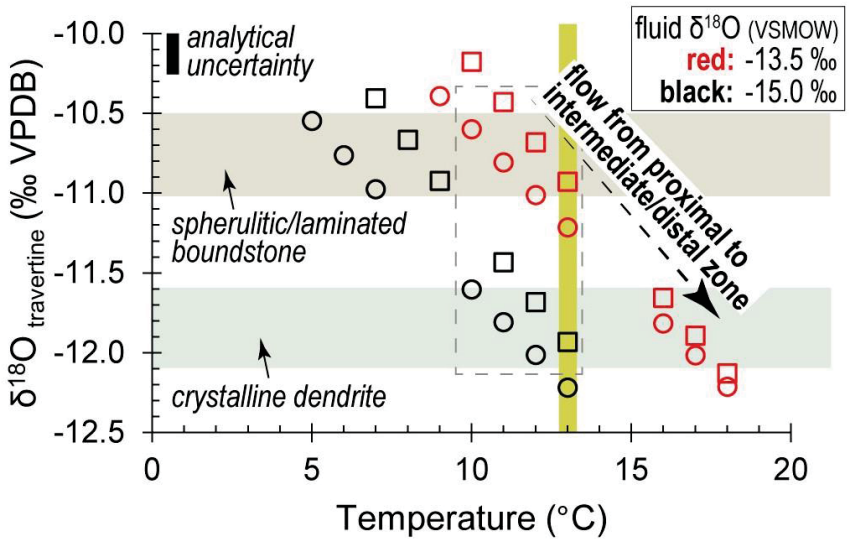

SOURCE: Quezada *et al.* (2024)

LEGEND: Theoretical calculations of the oxygen isotope composition for the south-facing travertine based on the fractionation factors proposed by Kele *et al.* (2011) (in squares) and Kele *et al.* (2015) (in circles). Details in the main text. The grey dashed rectangle indicates the best fit, considering the measured vent temperature (highlighted in yellow). Note that instream warming is needed to reproduce the observed $\delta^{18}O$ values of the spherulitic/laminated boundstone (proximal zone) and the crystalline dendrite (intermediate/distal zone), regardless of the initial fluid composition.

Alternatively, the $\delta^{18}O$ difference might arise from non-equilibrium isotope fractionation due to the contrasting hydrodynamic setting of calcite precipitation between the proximal and intermediate/distal zones (Yan *et al.,* 2012). In this sense,

if the parent waters have similar $\delta^{18}O$ isotope values, increasing precipitation rates would result in calcites with lower $\delta^{18}O$ values (Coplen, 2007; Dietzel *et al.,* 2009). This process is likely occurring in both travertines. The lower $\delta^{18}O$ values are associated with the crystalline dendrite facies (Fig. 12A-B), which are interpreted to have formed under higher precipitation rates and CO_2 degassing (Section 4.4.1) (Yan *et al.,* 2012). In contrast, the higher $\delta^{18}O$ values correspond to carbonates formed in a lower energy environments in the vents (Fig. 12A-B) (Section 4.4.1) (Sun *et al.,* 2014; Kele *et al.,* 2015).

Kinetic-isotope effects associated with pH variations can also be a relevant factor in the studied systems. When the DIC and the H_2O are in disequilibrium, the $\delta^{18}O$ composition of the precipitated carbonate will be influenced by the relative proportions of the dissolved carbon species, due to the large $\delta^{18}O$ fractionation among them ($\delta^{18}O$ composition of CO_2 > HCO_3^- > CO_3^{2-}) (Beck *et al.,* 2005). Thus, carbonates formed at higher pH (e.g., in the intermediate/distal zones; Fig. 7A) will tend to be depleted in ^{18}O compared to those formed at lower pH (e.g., in the proximal zone) (Zeebe, 1999; Dietzel *et al.,* 2009; Watkins *et al.,* 2013, 2014). The time required to reach oxygen isotopic equilibrium between H_2O and DIC in fluids like the spring waters (with neutral pH and temperatures of ca. 13°C) is in the order of a few minutes (cf. Watkins *et al.,* 2013 and references therein). This time frame is similar to the time it takes for the spring waters to travel from proximal to the distal zones, suggesting that once the waters flow out from the vents, they no longer will achieve oxygen isotopic equilibrium with the DIC. Experimental work shows that this phenomenon can generate variations >2‰ towards lower $\delta^{18}O$ compositions in the precipitated calcite (Watkins *et al.,* 2014). Thus, this effect might contribute to counteract the negligible impact of along-stream CO_2 degassing and evaporation on the $\delta^{18}O$ composition of spring water (increase of ca. 0.5‰; Fig 7D) and generate the ca. 1.5‰ variations towards lower $\delta^{18}O$ values in the carbonates of the intermediate/distal zones compared to those in the proximal zone (Fig. 12A-B).

4.4.5 Effects of local environment on the $\delta^{13}C$ isotopic signature

The difference in the compositional range of $\delta^{13}C$ among the travertines (averaging 3‰ higher in the north-facing travertine; Fig. 12D) is unlikely to be due to source variations (Section 4.4.3) or different intrinsic processes (Section 4.4.4.1).

When comparing similar fabrics or facies among the travertines (e.g., spherulitic calcite or crystalline dendrite), the $\delta^{13}C$ values in the north-facing travertine are consistently higher than those in the south-facing travertine (Fig. 16). Furthermore, the preferential formation of aragonite in the north-facing travertine cannot account for such significant $\delta^{13}C$ difference, as the aragonite-calcite carbon isotope fractionation is relatively small (1.7 ± 0.4‰) (Romanek *et al.,* 1992), and aragonite is not a predominant mineral component in most of the carbonates from this travertine (Fig. 16). These conditions suggest that distinct environmental (extrinsic) factors are influencing the carbon isotope composition of the travertines. It is proposed that such factors are modulated by the different levels of solar irradiance between the two springs, as discussed below.

FIGURE 16 – RELATIONSHIP BETWEEN MINERALOGY AND CARBON ISOTOPE COMPOSITION

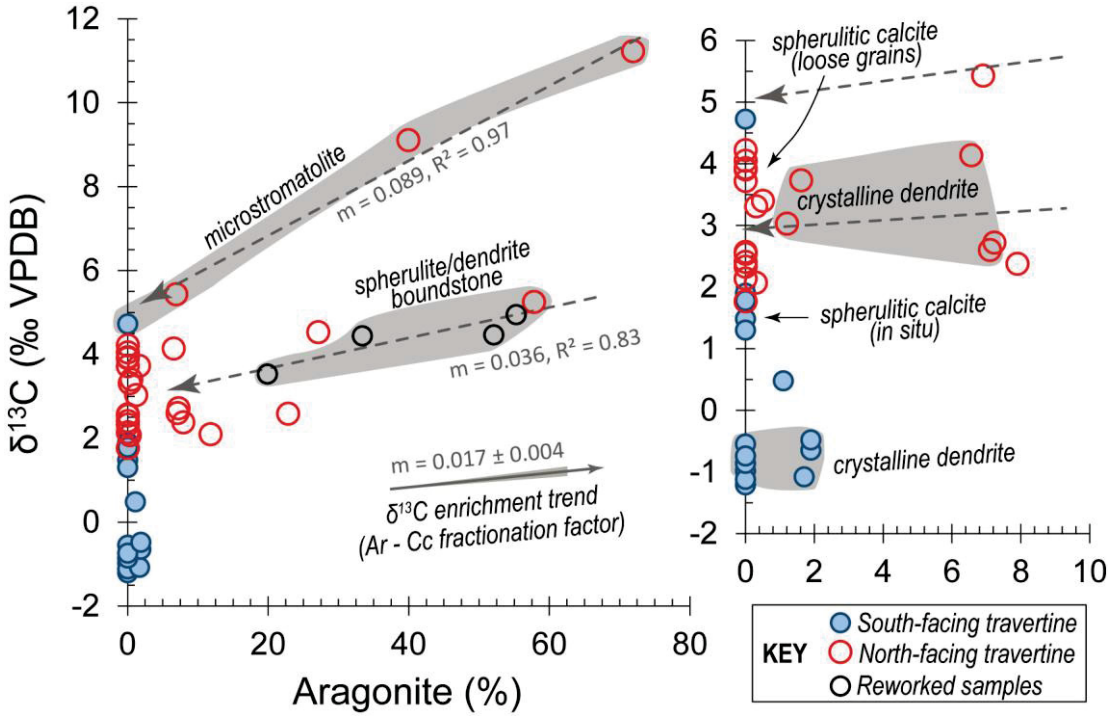

SOURCE: Quezada *et al.* (2024)

LEGEND: Relationship between the carbon isotopic composition of the travertine samples and their aragonite content. The right panel is a zoom of the left panel. The grey fields highlight samples of the same fabric or facies. The $\delta^{13}C$ enrichment trend corresponds to the aragonite-calcite fractionation factor of Romanek *et al.* (1992). Samples from the north-facing travertine exhibit higher $\delta^{13}C$ values compared to those with similar fabrics or facies from the south-facing travertine. The slope of the linear regressions exceeds the $\delta^{13}C$ enrichment trend associated with increasing aragonite content, suggesting additional processes influencing the carbon isotopic composition.

In mid-latitude mountainous regions of the Southern Hemisphere, north-facing slopes receive greater sun exposure than south-facing slopes (Segal *et al.,* 1987). This effect creates microclimatic zonation among adjacent areas, particularly in semi-arid regions (Cantlon, 1953). Variations on insolation influence surface temperature and evaporation/evapotranspiration rates—higher on sun-exposed areas—while shaded areas typically have higher soil moisture, greater vegetation cover, and increased soil organic carbon content (Cantlon, 1953; Holland and Steyn, 1975; Segal *et al.,* 1987; Geroy *et al.,* 2011; Moeslund *et al.,* 2013; Nahidan *et al.,* 2015; Yang *et al.,* 2020).

In the studied area, this geographic effect results in a denser vegetation canopy on the south-facing slope compared to the north-facing slope of the Laguna Amarga basin (Fig. 5C). Additionally, it affects the amount of solar radiation received by the travertine vents, which is greater in the north-facing travertine compared to the south-facing travertine throughout the year (Fig. 17A), particularly during autumn and winter when insolation is at its minimum (Santana *et al.,* 2010). Consistent with this, measurements taken during the study period showed that spring water temperatures at the vents were 1–5°C higher in the north-facing travertine than in the south-facing travertine, and lake waters near the north-facing travertine were 2–3.1°C warmer compared to those near the south-facing travertine (Appendix 1).

It is inferred that these factors can be modulating the $\delta^{13}C$ of the travertines. The lower temperatures, larger vegetational cover and higher moisture levels prevailing in the sun-shaded margin of Laguna Amarga favor the retention of soil-respired CO_2 (Hashimoto and Komatsu, 2006; Sánchez-Cañete *et al.,* 2018). This would increase the availability of light carbon, which could be incorporated by the spring waters of the south-facing travertine as they flow through the soil layer (Sánchez-Cañete *et al.,* 2018). The $\delta^{13}C$ composition of the soil-derived CO_2 in the area is expected to be very negative, since vegetation is mostly mixed C3/C4 types in open grasslands in South Patagonia (Cerling and Quade, 1993). This is consistent with the low $\delta^{13}C$ values (ca. -15‰) exhibited by modern calcites precipitating in the Cueva Chica speleothem (Nehme *et al.,* 2023). Thus, even small amounts of soil-derived CO_2 incorporated into the spring waters can significantly lower the $\delta^{13}C$ signature of the precipitating carbonate.

Conversely, the relatively greater sunlight availability and higher temperatures in the north-facing travertine vent may promote photosynthetic

productivity, resulting in greater enrichments of δ^{13}C-DIC in the spring waters. Photosynthesis is a complex process influenced by various factors, including environmental variables and intrinsic characteristics of the photosynthetic organisms (Ooms *et al.,* 2016 and references there cited). However, positive relationships between irradiance, temperature and microbial photosynthesis have been demonstrated under experimental conditions comparable to those prevailing in Laguna Amarga (e.g., Sánchez Zurano *et al.,* 2021). Although it is currently difficult to estimate the relative contributions of soil CO_2 versus photosynthetic CO_2 uptake, their combined effects are consistent with the significant differences in δ^{13}C composition observed among the travertines (Fig. 17B).

FIGURE 17 – RELATIONSHIP BETWEEN INSOLATION AND CARBON ISOTOPES

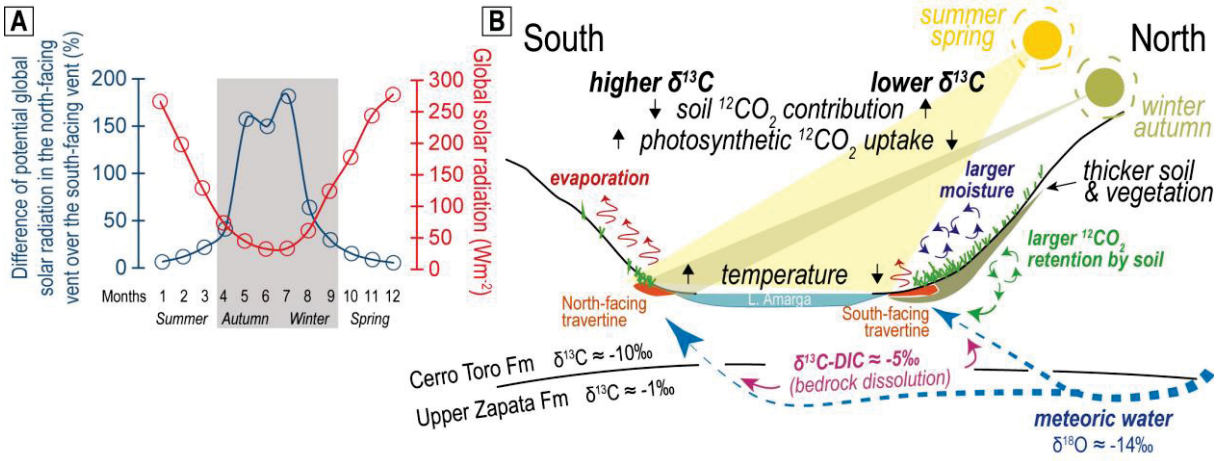

SOURCE: Quezada *et al.* (2024)

LEGEND: A) Graphic illustrating that over the year the potential global solar radiation (direct plus diffuse radiation) is larger on the north-facing vent compared to the south-facing vent. Monthly averages of global solar radiation (Wm^{-2}) correspond to high-resolution measurements performed over the year 2008 in the Patagonia steppe (ca. 52.25°S) (Santana *et al.,* 2010). The difference in solar irradiation between the travertines was estimated using the potential incoming solar radiation module of the SAGA GIS environment (Conrad *et al.,* 2015) and the ALOS-PALSAR Digital Elevation Model (12.5 m resolution) as input parameter. B) Conceptual model illustrating the sources and environmental conditions influencing the carbon isotopic characteristics of the travertines (details in the text).

4.5 CONCLUSION

A comparative study of spring waters and carbonates was conducted to constrain the sources and processes involved in the formation of two adjacent cold-temperature travertines. Both travertines display similar trends in sedimentological

features and stable isotope compositions but differ in their $\delta^{13}C$ ranges and mineralogy, despite having similar sources.

Their similarities are attributed to common along-stream processes driven by variations in spring water flux. This led to the development of depositional sub-environments (proximal vs. intermediate/distal zones) with distinct flow energy (lower vs. higher) where carbonates precipitated under varying influences of biotic activity (higher vs. lower) and kinetic effects (lower vs. higher), resulting in an atypical carbon and oxygen isotopic trend, with higher values in the proximal zone. Together, these features underscore the impact of fluid hydrodynamics in modulating the sedimentological and isotopic characteristics of cold-temperature carbonate spring systems.

The marked difference in their $\delta^{13}C$ compositional range, with the north-facing travertine averaging 3‰ higher, is inferred to be influenced by microclimatic zonation between the two depositional sites due to varying solar irradiance (Fig. 17). Increased sunlight and higher temperatures in the north-facing travertine promote photosynthetic productivity, while higher moisture levels and thicker vegetation/soil in the south-facing travertine favor the incorporation of soil-derived CO_2. The influence of sun exposure on the carbon isotope composition of travertines were intuited by Pentecost (2005), but to our knowledge, this is the first study providing information on this subject. These findings suggest that the carbon isotope composition of equatorward-facing and poleward-facing spring-related carbonates might be used as proxies to track biomass fluctuations at (sub-)basin scales in mid-latitude semi-arid ecosystems, which are highly sensitive to hydroclimate oscillations.

Finally, EPS-influenced aragonite mineralization is predominantly restricted to the north-facing travertine, where it largely precipitates in close association with the activity of sulfate-reducing bacteria. The occurrence of aragonite in this low-temperature freshwater environment is intriguing and warrants further investigation to uncover the mechanisms behind its formation.

5 RECORD OF COLD-TEMPERATURE TUFA THROMBOLITE IN WIND-STRESSED LACUSTRINE ENVIRONMENTS: INSIGHTS FROM LAGO SARMIENTO, SOUTHERN PATAGONIAN ANDES

ABSTRACT: Lago Sarmiento transitioned from ice-covered conditions to hosting the Southern Hemisphere's largest extratropical microbial carbonate system within 14000 years. Fossil tufa thrombolite build-ups (<4 m-tall) and minor crusts featuring the lake-margin developed under persistent windy conditions during Holocene, providing the opportunity to fill the gaps between processes leading to freshwater carbonate accumulation in high-energy lacustrine systems and their products. This work integrates genetic characterization of microbial mats with petrologic studies of modern and fossil deposits to understand their genesis and early diagenesis, and stable isotope geochemistry in water and carbonate to constrain the conditions facilitating extensive tufa deposition. Calcified filaments in fossil deposits and 16S rRNA sequencing of living microbial mats identify cyanobacteria—particularly Rivulariaceae—as the primary framework builders. Modern microbial substrates undergo early induration through Extracellular Polymeric Substances-mediated nucleation of Sr- and Mg-rich nanoparticles that evolve into aragonite and Mg-calcite microspar. Fossil deposits, however, preserve only remnants of these early products due to diagenetic overprinting. An initial *constructive diagenetic* phase, under conditions favoring Mg-calcite precipitation, promoted aragonite inversion, crystal coarsening, and cement fringe formation, stabilizing the organosedimentary structures while preserving biogenic microstructures. Subsequent lake-level decline exposed deposits to wave action, triggering *destructive diagenesis* marked by micritization and partial dissolution/erosion of the framework, nearly obliterating microbial textures and filling the secondary pores with internal sediments (mostly terrigenous grains, intraclasts and peloids). Wind-driven lake-atmosphere CO_2 exchange and stable evaporation/inflow ratios explains the narrow variability of $\delta^{13}C_{tufa}$ (mostly 3.9 to 5.3‰ VPDB) and $\delta^{18}O_{tufa}$ (mostly -2.2 to -0.7‰ VPDB), consistent with precipitation at ≤12°C. Lago Sarmiento likely acted as a resilient ecosystem across Holocene cold/wet-warm/dry climate transitions, sustaining favorable conditions for Rivulariaceae-dominated mats colonization and carbonate precipitation. This work

provides insights into freshwater microbial carbonate deposition in high-energy lacustrine settings and their identification in the geologic record.

Keywords: organomineralization; fetch; oligotrophic; high-magnesium calcite; eodiagenesis; Southern Westerly Winds; hydrodynamics

5.1 INTRODUCTION

Organosedimentary deposits accreted due particle agglutination and/or mineralization of benthic microbial communities are known as microbialites (Burne and Moore, 1987), and comprise the most extensive record of organism-environment interactions. Among these, thrombolites represent a non-laminated variety characterized by mm- to cm-scale polylobate mesoclots (Aitken, 1967; Shapiro, 2000). While thrombolites appeared in the Proterozoic (Aitken and Narbonne, 1989), their rise to dominance in marine environments coincided with the emergence of calcified cyanobacteria and metazoan radiation in the Cambrian (Kennard and James, 1986; Riding, 2000), a pattern suggesting microbial evolutionary adaptation (Kennard and James, 1986; Shiraishi *et al.,* 2017). However, diverse processes can influence their formation (Chacón-Baca *et al.,* 2024; Riding *et al.,* 1991; Warden *et al.,* 2019), including diagenetic modifications (Aitken, 1967; Planavsky and Ginsburg, 2009; Walter and Heys, 1985) and calcification of coccoid-dominated (Graham *et al.,* 2014; Kennard and James, 1986) or filamentous-dominated communities (Burne and Moore, 1987; Riding, 2000).

By a combination of factors, including among others increased eukaryote competition and lower carbonate supersaturation, the abundance of marine microbialites declined episodically since mid-Ordovician (Arp *et al.,* 2001; Fisher, 1965; Riding, 2000; Riding *et al.,* 2019), and is currently restricted to local settings (Reid *et al.,* 2024 and references therein). In contrast, microbial carbonates flourish in diverse terrestrial setting, including freshwater to hypersaline lakes, hot and cold calcareous springs, palustrine and fluvial environments (Alonso-Zarza and Wright, 2010; Arenas-Abad *et al.,* 2010; Della Porta, 2015; Ford and Pedley, 1996; Jones and Renaut, 2010; Pedley, 1990; Pentecost, 2005; Riding, 2000). This makes them valuable paleoenvironmental proxies (Tanner, 2010), besides allowing to assess the impact of abiotic factors (*e.g.,* carbonate supersaturation, CO_2 degassing, etc) and organomineralization processes (sensu Dupraz *et al.,* 2009) on carbonate

precipitation under diverse physical, chemical and ecological conditions, including cases analogous to early Earth or extraterrestrial environments (e.g., Walter and Des Marais, 1993). Debated topics are how microbial metabolism promotes precipitation (biologically-induced mineralization) and the role of extracellular polymeric substances (EPS)—secreted by the microorganism—in governing the nucleation, mineralogy and morphology of the deposits (biologically-influenced mineralization) (Arp *et al.,* 2010, 1999; Bissett *et al.,* 2008a; Chagas *et al.,* 2016; Della Porta *et al.,* 2022; Jones, 2017a, 2017b; Merz-Preiß and Riding, 1999; Merz, 1992; Pedley and Rogerson, 2010; Shiraishi *et al.,* 2020, 2008a).

At the microscale non-marine thrombolites can be highly heterogeneous, reflecting multiphase construction under varying microbial mediation and environmental conditions, besides of early diagenetic modifications (Bosence and Gallois, 2022). Those deposited in freshwater streams and lakes (tufa thrombolite *sensu* Riding, 2000) often form via filamentous cyanobacteria calcification, resembling Cambro-Ordovician marine examples (Aitken, 1967; Kennard and James, 1986; Riding, 2011). Calcification can involve carbonate nucleation within the EPS sheath embedding the trichomes (impregnation) and/or in their outer surface (encrustation) (Riding, 1977). Although debated (Shiraishi *et al.,* 2008b), the first has been commonly linked to photosynthetically-induced precipitation in slightly supersaturated waters ($SI_{calcite}$ 0.2-0.3) (Merz, 1992), while the latter to physiochemically-driven precipitation in agitated waters ($SI_{calcite}$ >0.8) (Merz-Preiß and Riding, 1999).

Microbialites sporadically develop east of the Patagonian Andes in Southern South America (41-53°S). In this region, modern and Holocene climate is mainly modulated by the Southern Westerly Winds (SWW) (Garreaud *et al.,* 2013; García *et al.,* 2020; Moreno *et al.,* 2018, 2014; Nehme *et al.,* 2023; Roberts *et al.,* 2022) and microbialites develop under wind-stressed conditions in hypersaline to freshwater lacustrine setting (Airo, 2010; Eymard *et al.,* 2020, 2019; Henríquez *et al.,* 2022; Pacton *et al.,* 2015; Pollier *et al.,* 2024; Solari *et al.,* 2010). The largest occur in Lago Sarmiento (surface of 83 km²) (Fig. 18), where <4-m-tall fossil tufa thrombolites record extensive microbial colonization and calcification during Holocene, starting sometime after the area became ice-free (ca. 12.5 ka; García *et al.,* 2014). This study integrates microbiological, petrographic, mineralogical and isotopic analysis with previous work in Lago Sarmiento to investigate the biotic/abiotic contributions to the

genesis of tufa thrombolites and the environmental influences on their diagenesis, providing insights into deposition of microbial carbonates in lacustrine high-energy systems.

FIGURE 18 – GENERAL AND LOCAL CONTEXT OF LAGO SARMIENTO

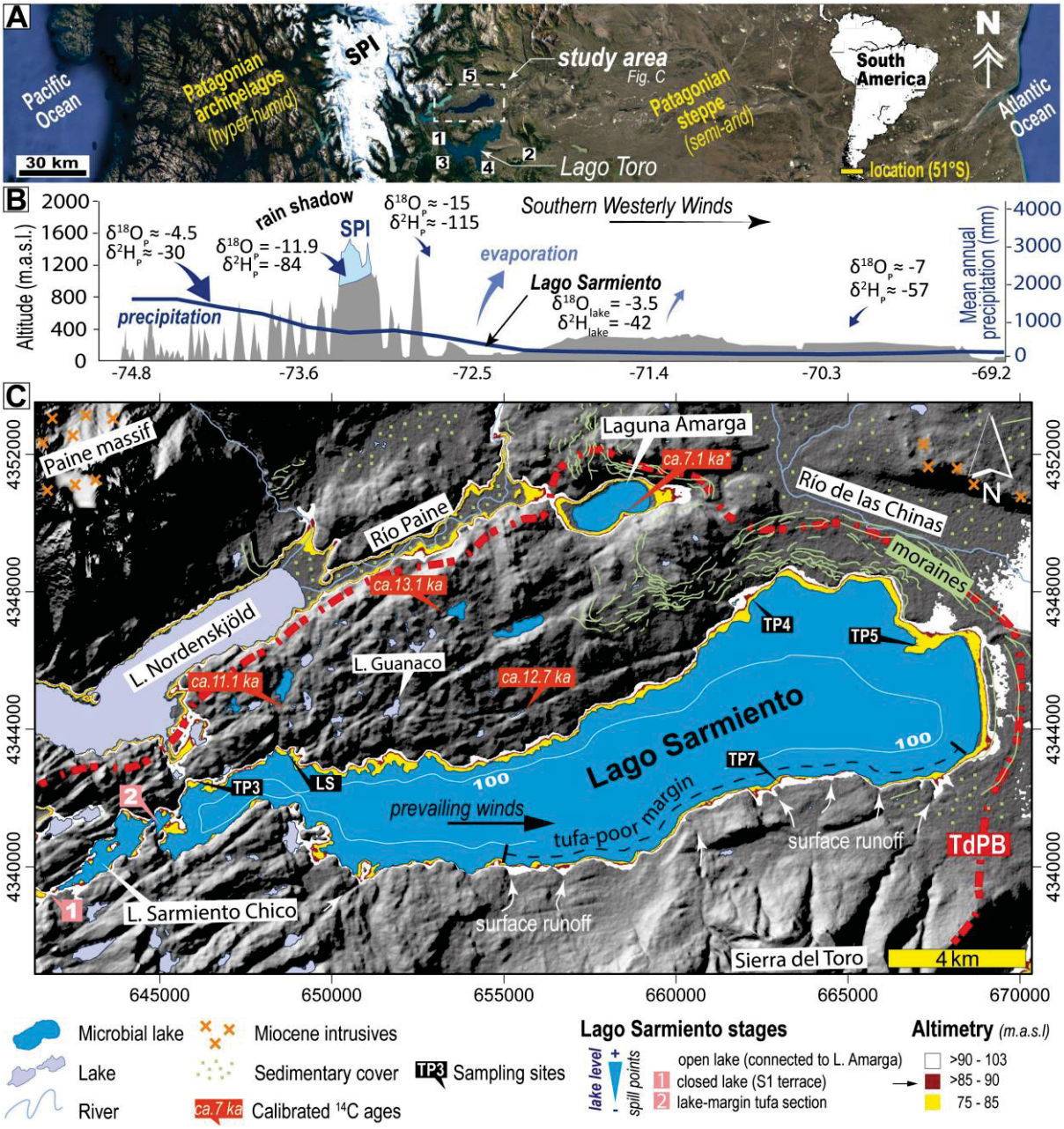

SOURCE: This work.

LEGEND: A) Continental-scale Google satellite image of Southern South America at the latitude of 51° showing the general geographical context of the study area. Localization of meteorological stations (1: Torres del Paine; 2: Cerro Castillo) and paleo-climate archives (3: Lago Cipreses; 4: Lago Pato; 5: Vega Ñandú) referred in the text are indicated. B) Topographic profile (51°S) showing the west-east variations of the mean annual precipitation (Almonacid *et al.,* 2021) and reference values of the isotopic composition of precipitation (Mayr *et al.,* 2018; Shiraiwa *et al.,* 2002) in comparison with those of Lago Sarmiento (this study). C) Digital elevation map showing the main geological,

geomorphological, and hydrological features of the Torres del Paine Basin (TdPB) and Lago Sarmiento, together with the location of the main sampling sites. The 100 m-depth bathimetric contour is bases on Campos *et al.* (1994b). The distribution of the glacial deposits is from Davies *et al.* (2020). The bedrock of the TdPB is composed of the Cerro Toro Formation (not demarked). The microbialite's radiocarbon age at Laguna Amarga and the distribution of tufa-bearing lakes is from Solari *et al.* (2010). The radiocarbon ages of peat deposits signaling the minimum ages of ice-free conditions in the area are indicated (cf. García *et al.,* 2014 and references therein).

5.2 LAGO SARMIENTO DEPOSITIONAL SYSTEM

Lago Sarmiento is a relatively large (9 km³ volume) and deep (312 m) E-W-oriented lake fed by rainfall, restricted surface runoff, and most likely groundwater (Campos *et al.,* 1994a; Solari *et al.,* 2010). Modern lake level is at 75 m.a.s.l., while it was about 6 meters higher by 1929 based on photographic record. The lake has a sodium-bicarbonate composition (Campos *et al.,* 1994a), and is cataloged as a nitrogen-deficient oligotrophic system with low zooplankton biomass (De los Ríos and Soto, 2009 and references therein).

A *ca.* 10-m thick fossil tufa section underlies the S1 terrace (85–90 m.a.s.l) (Fig. 19-20-21), formed after lake level fell below the spill point west of Lago Sarmiento Chico (Fig. 18C) (Solari *et al.,* 2012). The deposits consist of isolated to variably amalgamated build-ups (<4 m-tall) with mounded, tabular, columnar, domical and V-shaped (cauliflower-like) morphologies and minor cm-thick crusts (Fig. 19-20-21). A 1215 Cal yr BP radiocarbon age in a gastropod shell form the top of the section constraint the minimum age of the deposits, while the oldest microbialite in the area (7112 Cal yr BP) is located at ca. 90 m.a.s.l. near Laguna Amarga (Fig. 18C) (Solari *et al.,* 2010). Microbial carbonate accretion is currently active, and meter-scale build-ups are described up to depths of 20 meters within Lago Sarmiento (Airo, 2010).

5.3 MATERIALS AND METHODS

This work mostly focuses on 5 sites where fossil tufa build-ups (TP3, TP4, TP5 and TP7 sites) and crusts (LS site) are well exposed (Fig. 18C). In situ measurements of physicochemical parameters and sampling of waters for stable isotope determinations of $\delta^{2}H$-$\delta^{18}O$ (n=7) and $\delta^{13}C$-DIC (n=2) were performed in

these sites, or near them (Appendix 3). Also, the $\delta^{2}H$-$\delta^{18}O$ and $\delta^{13}C$-DIC composition of three nearby lakes is reported for comparison.

FIGURE 19 – FIELD PHOTOGRAPHS OF TUFA CRUST AND MICROBIAL MATS

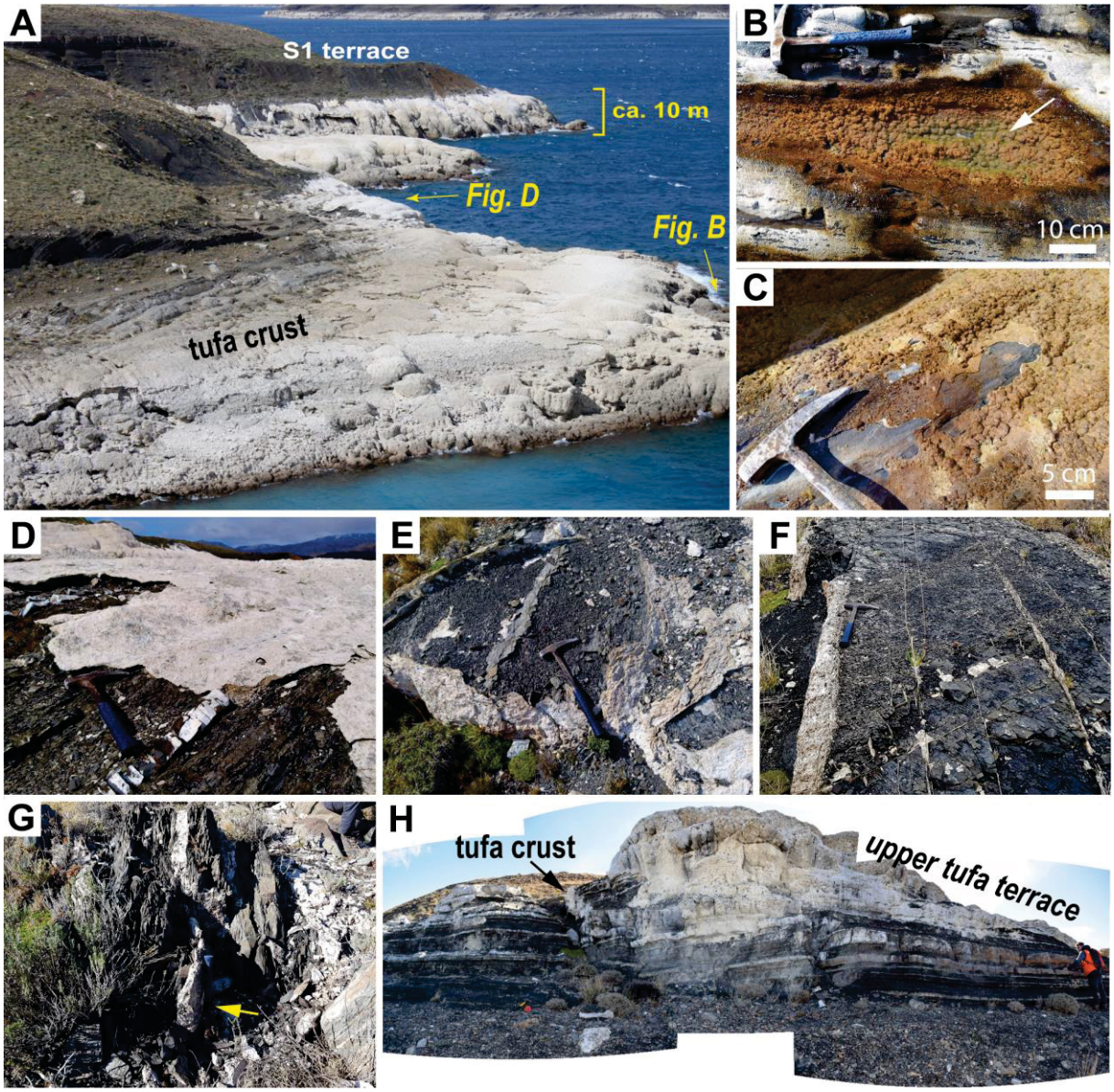

SOURCE: This work.

LEGEND: A) General view of the LS site. Note the S1 terrace and the crust capping the tufa build-ups. B) "Living" microbial mat sampled in the splash zone at the LS site. C) Calcified microbial mat next to the living counterpart. D), E) and F) Tufa crust capping the bedrock, few meters above the upper tufa build-up level. Note the carbonates deposited inside fractures in F). G) Tufa crust deposited inside the fractures of a boulder sampled west of the TP3 site, on an area with sparse relicts of tufa deposits. H) Sampled tufa crust capping the walls of a normal fault, located 2 kms west of the TP4 site. Note that only the upper tufa terrace is developed in this locality.

FIGURE 20 – FIELD PHOTOGRAPHS OF TUFA BUILD-UPS IN SITES TP3 AND TP4

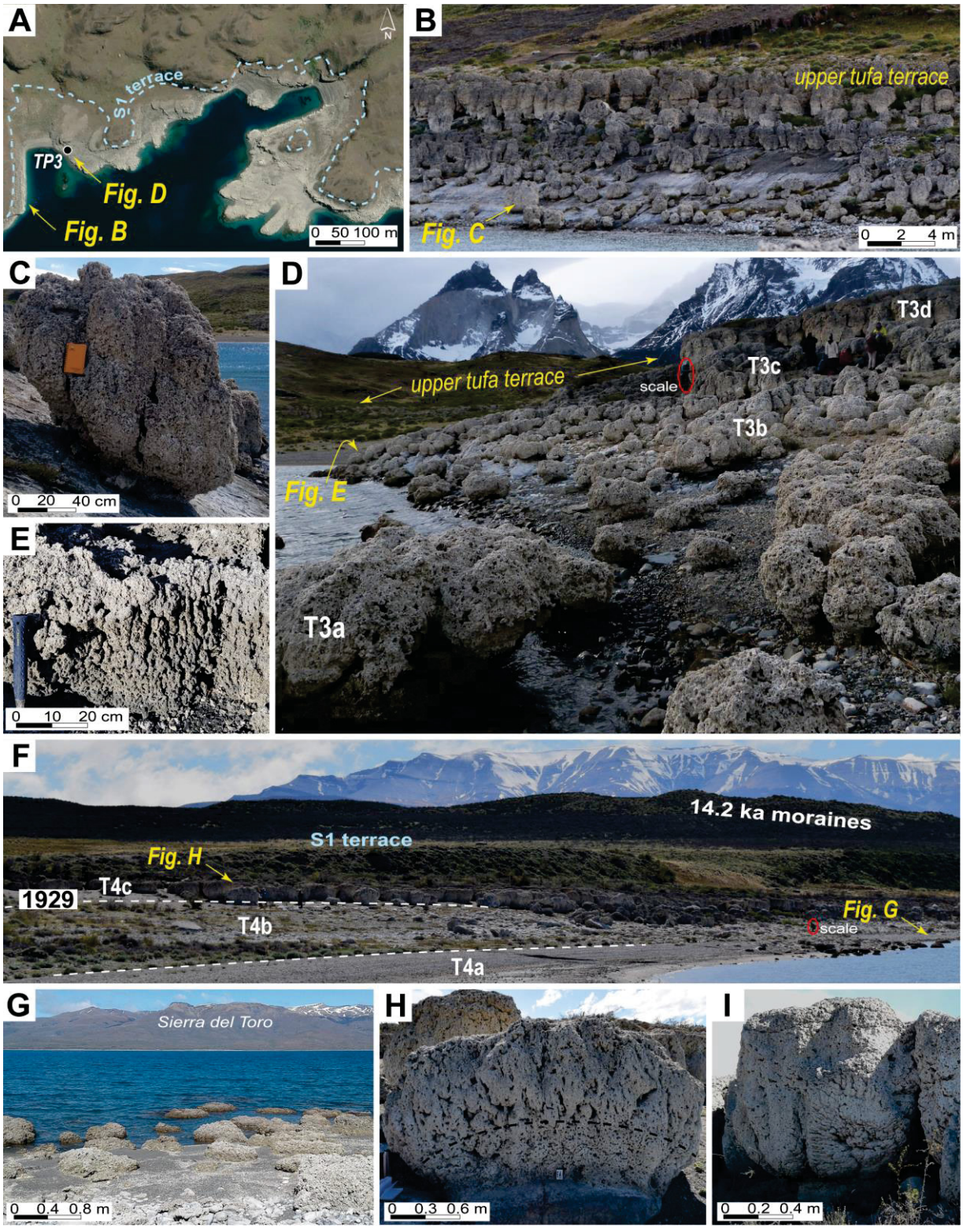

SOURCE: This work.

LEGEND: Google satellite image of the northwestern part of Lago Sarmiento highlighting the S1 terrace and location of the TP3 sampling site. Note the tectonically controlled morphology of the lake margin. B) Section of fossil tufa build-ups developed on inclined slope in front of the TP3 site showing the greater height and degree of amalgamation of the build-ups in the upper terrace compared to those below. C) Isolated build-ups composed by linked columns develop in the lowermost, and poorly developed, tufa terrace. D) TP3 sampling site. The geologist serving as scale is ca. 1.8 m tall. E) Tufa

with well-developed branched fabric. F) General view of the TP4 sampling site, located in the northeastern margin of the lake. The approximate lake level in 1929 is based on historical photographic record in the same site. Note the increasing degree of amalgamation and height of the build-ups from T4a to T4c, and the unconsolidated sediments composing the substrate. G) Low-relief mounds with convex tops developed on terrace T4a. H) Columnar build-ups developed atop of a boulder in the T4c terrace. Note the variation in pore morphology from the base (subrounded) to the top (elongated), reflecting increasing branching development. I) Columnar build-up of the T4c terrace exhibiting an internally branched fabric.

In the LS site (Fig. 19A) a living pustular microbial mat growing in a shallow pond alongside the lake (Fig. 19B), and its lithified counterpart in desiccated areas (Fig. 19C), were sampled to study their microbial composition and calcification, respectively. The biological sample was collected with sterile tools and stored at 4°C. In the lab, the internal structure of the microbial mat was inspected under magnifying glass and DNA extraction for 16S rRNA sequencing was performed in three layers of the mat. SEM and XRD analysis were performed in the calcified mat to study its microfabric and mineralogy, respectively.

Rock samples of the tufa were collected at different levels on the study sites, including tufa crusts (Fig. 19D to H) and build-ups (Fig. 20 and 21). Besides, powders (<0.2 g) were obtained every 20 cm along a vertical profile using diamond-head hand drilling at the TP3 site (Fig. 20D). The textures and microfabrics of the deposits were studied in thin sections under the petrographic microscope (n=26) and rock fragments under the SEM (n=19). X-ray diffraction (XRD) and stable isotope ($\delta^{13}C$, $\delta^{18}O$) analyses of the carbonates were performed in bulk-rock samples (n=41) and subsamples from the TP3 profile (n=38) (Appendix 4).

FIGURE 21 – FIELD PHOTOGRAPHS OF TUFA BUILD-UPS IN SITES TP5 AND TP7

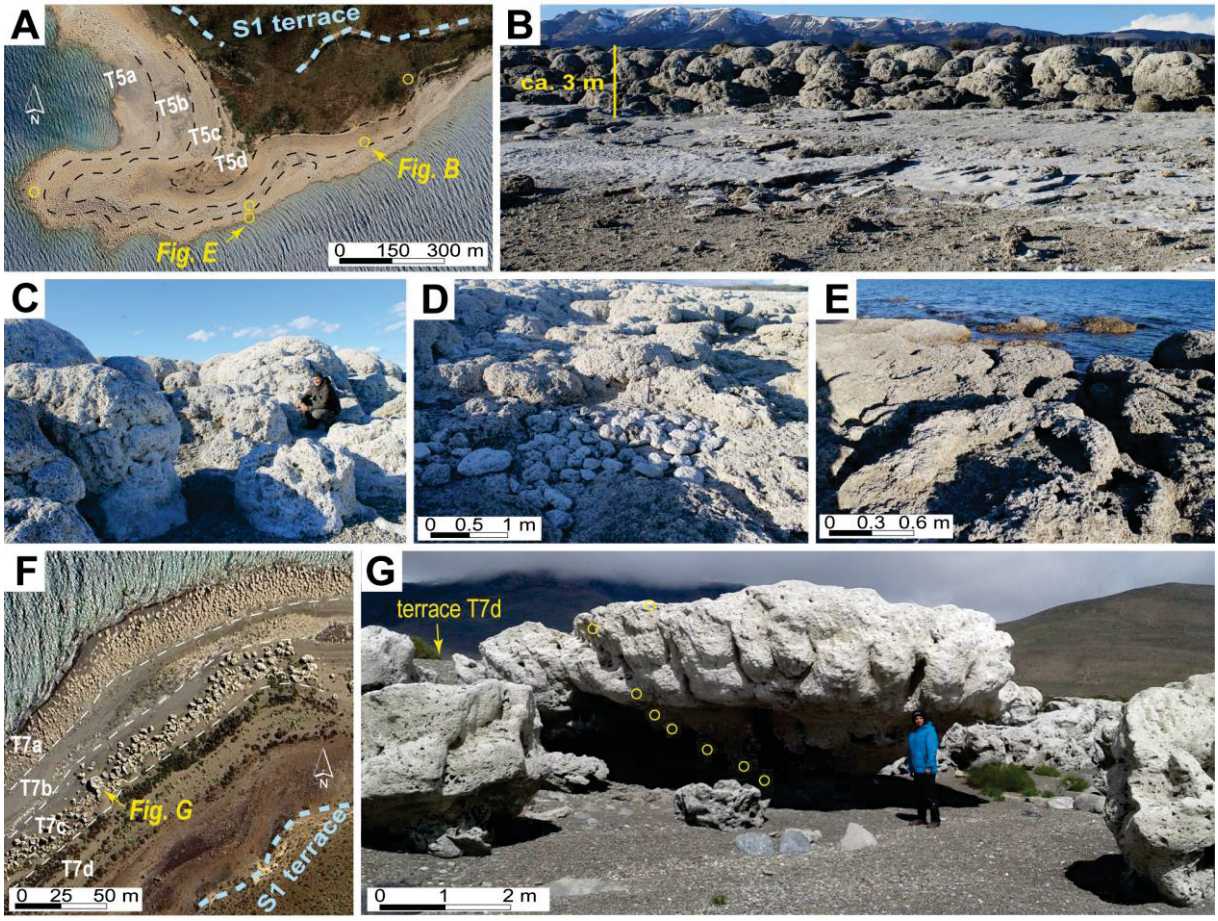

SOURCE: This work.

LEGEND: A) Google satellite image of the eastern margin of the lake (TP5 site). The yellow circles show the sampling sites. Note the abundant development of tufa deposits in the T5a to T5c terraces compared to the T5d terrace. B) Amalgamated domes of metric sizes composing the T5c terrace. C) Close up to the domes. These exhibit subrounded to irregular surfaces and lower porosity compared to the low-relief build-ups found elsewhere. D) Cobbles and boulders of reworked tufa are surrounded by amalgamated, tabular to mounded, low-relief build-ups in the T5b terrace. E) Amalgamated low-relief build-ups in the T5a terrace, note the hammer in the concave top. F) Google satellite image of the southeastern margin of the lake (TP7 site). Low-relief build-ups are restricted to the T7a and T7b terraces, while tall build-ups (> 2 m) are restricted to the T7c terrace. G) The yellow circles show the sampled portions of the V-shaped build-up. Note that the build-up was built atop of a boulder, and its top is at a similar altitude to that of T7d terrace.

5.4 RESULTS

5.4.1 Distribution and morphology of the fossil tufa deposits

The development of fossil crusts is exceptional at the LS site, where they cover flat-to-step bedrock walls (Fig. 19D to F) and the build-ups (Fig. 19A), supporting a younger age than the latter. Although sparse, similar crusts are

deposited along the north margin, west of the TP3 (Fig. 19G) and TP4 sites (Fig. 19H), and usually located at similar or higher altitudes than the uppermost level of tufa build-ups.

The tufa build-ups primarily form on flat-to-stepped bedrock surfaces in the western lake sector (e.g., TP3; Fig. 20A-E) and on gentle sediment slopes in eastern areas (TP4, TP5, TP7; Fig. 20-21). Paleo-shorelines are more pronounced in eastern sites (Fig. 20F, 21A-F) than western ones (Fig. 20A-B-D), displaying a consistent shore-perpendicular trend of increasing buildup size and abundance with distance from the lake (Fig. 20B-D-F, 21). Despite this general trend, site-specific variations in terms of build-up morphology and abundance are evident among the studied sites.

Near-shore deposits comprise low-relief (0.2-1 m) mounded, columnar, and tabular build-ups, occurring either isolated (TP3a, TP4a, TP7a; Fig. 20B-D-F-G, 21F) or amalgamated (TP5a; Fig. 21A-E), with rare taller edifices (Fig. 3B-C). Mid-section build-ups show similar morphologies but greater vertical/lateral development within sites (Fig. 20B-D-F, 4D), except at TP7 where they are sparser (TP7b; Fig. 21F). The uppermost section contains the tallest (1.2-3.7 m), closely spaced to amalgamated build-ups (columnar: T3d, T4c; domical: T5c; V-shaped: T7c; Fig. 20B-F-H-I, 21B-C-F), forming the most continuous tufa terrace along the lake margin. Besides the tufa crust previously described, only rare domes develop above this upper tufa terrace (T5d; Fig. 20A).

Mesoclots form the fundamental architectural units of all the deposits, producing irregular (Fig. 20C-D) to branched (Fig. 20E-I) internal structures, sometimes coexisting within single build-ups (Fig. 20H). Reworked deposits are more abundant in the eastern areas of the lake (Fig. 21D).

5.4.2 Water analysis

The range of temperature, pH, and conductivity at 25°C (Table 1) are similar to previous studies (Campos *et al.,* 1994a). The TDS (0.63 and 0.89 g/L) and the calculated salinity (avg. 1.04 g/L) signal near freshwater conditions. The concentrations of DO (Table 1) indicate oversaturation conditions. Lago Sarmiento exhibit narrow $\delta^{2}H$ (avg. -41‰), $\delta^{18}O$ (avg. -3.6‰), and $\delta^{13}C$-DIC (1.4 and 1.6‰)

compositions, more positive than the analyzed open lakes (δ^2H -112 to -67‰; $\delta^{18}O$ -14.3 to -6.8‰; $\delta^{13}C$-DIC -3 to -1‰) (Fig. 22).

TABLE 4 – LAGO SARMIENTO WATERS

Temperature (°C)	5.7 - 10.1
pH	8.1 - 8.8
DO (mg/L)	17.8 - >50
Conductivity (µS/cm)	1300 - 1493
Salinity* (g/L)	0.96 - 1.18
$\delta^{18}O$ (‰ VSMOW)	-4.3 to -3.1
δ^2H (‰ VSMOW)	-47 to -37
$\delta^{13}C$-DIC (‰ VPDB)	1.4 and 1.6

*Calculated using measured temperature and conductivity at 25°C (Aminot and Kérouel, 2004)

SOURCE: This work.

5.4.3 Living and calcified microbial mat

The pustular microbial mat (<1 cm-thick) (Fig. 19A) is composed of an external EPS-rich layer (<1-mm) covering a 2 mm-thick green layer, and a beige internal portion of 5 mm-thick (Fig. 23A). Diatoms are common in the external layer while filamentous cyanobacteria and carbonate grains are ubiquitous in the green (Fig. 23B) and beige layers (Fig. 23C).

FIGURE 22 – WATER STABLE ISOTOPES OF LAGO SARMIENTO

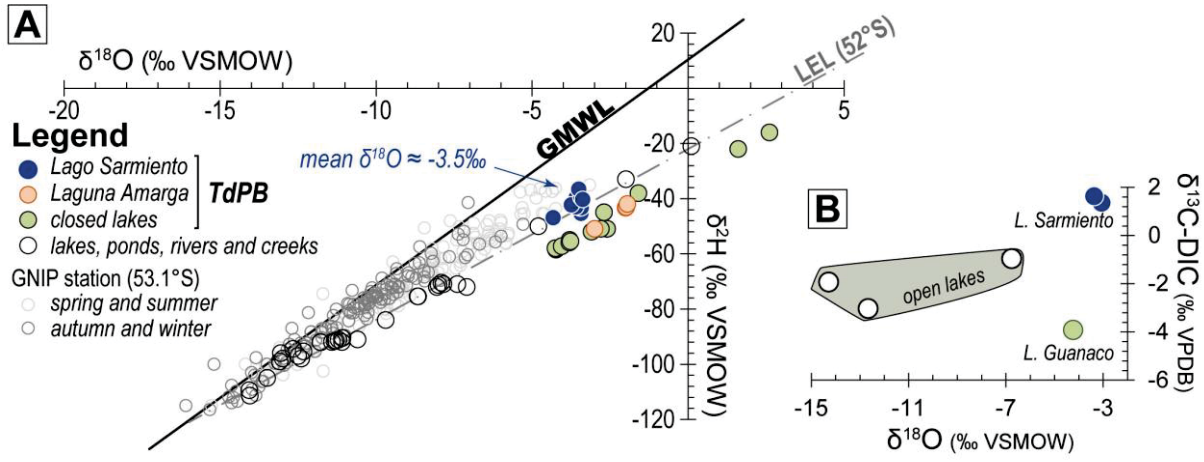

SOURCE: This work.

LEGEND: $\delta^{2}H$ and $\delta^{18}O$ isotope composition of Lago Sarmiento (this work; Solari *et al.,* 2010; Mayr *et al.,* 2018) in comparison with other water reservoirs in the area (Mayr *et al.,* 2018; Moy *et al.,* 2008; Nehme *et al.,* 2023; Solari *et al.,* 2010), and the precipitation data between years 1990-2017 from the Punta Arenas GNIP station (ca. 53.1°S) (IAEA/WMO, 2023) filtered following Xia *et al.* (2020). The Global Meteoric Water Line (GMWL) is from Rozanski *et al.* (1993) and the Local Evaporation Line (LEL) is the calculated by Mayr *et al.* (2007) for the extra-Andean Patagonia at 52°S. B) $\delta^{13}C$-DIC and $\delta^{18}O$ isotope composition of Lago Sarmiento in comparison to open and closed lakes of the area. The data of Lago Guanaco is from Moy *et al.* (2008).

The 16s rRNA gene analysis shows dominant occurrence of Cyanobacteria with a relative abundance between 34 and 70% depending on the layer (Fig. 23D). Another abundant phylum corresponds to Proteobacteria (18-39%), Bacteroidota (6 to 22%), and Verrucomicrobiota (2-9%) (Fig. 23D). Planctomycetes are present in the three layers but with lower relative abundances (1-2%). Among Cyanobacteria, the nitrogen-fixating filamentous bacteria from the Rivulariaceae family (order Nostocales) are the most abundant (>50%), including the genus *Rivularia* and *Calothrix* (Fig. 23E). Other filamentous cyanobacteria correspond to genus *Leptolyngbya*, while genus *Aliterella* is the only identified cyanobacteria with coccoid morphology (Fig. 23C). Bacteria with aerobic heterotrophic metabolisms are abundant among Proteobacteria and in some Bacteroidota, including among the latter genus *Lewinella* (family Saprospiraceae), which is particularly abundant in the green layer (13%).

FIGURE 23 – LIVING MICROBIAL MAT COMPOSITION

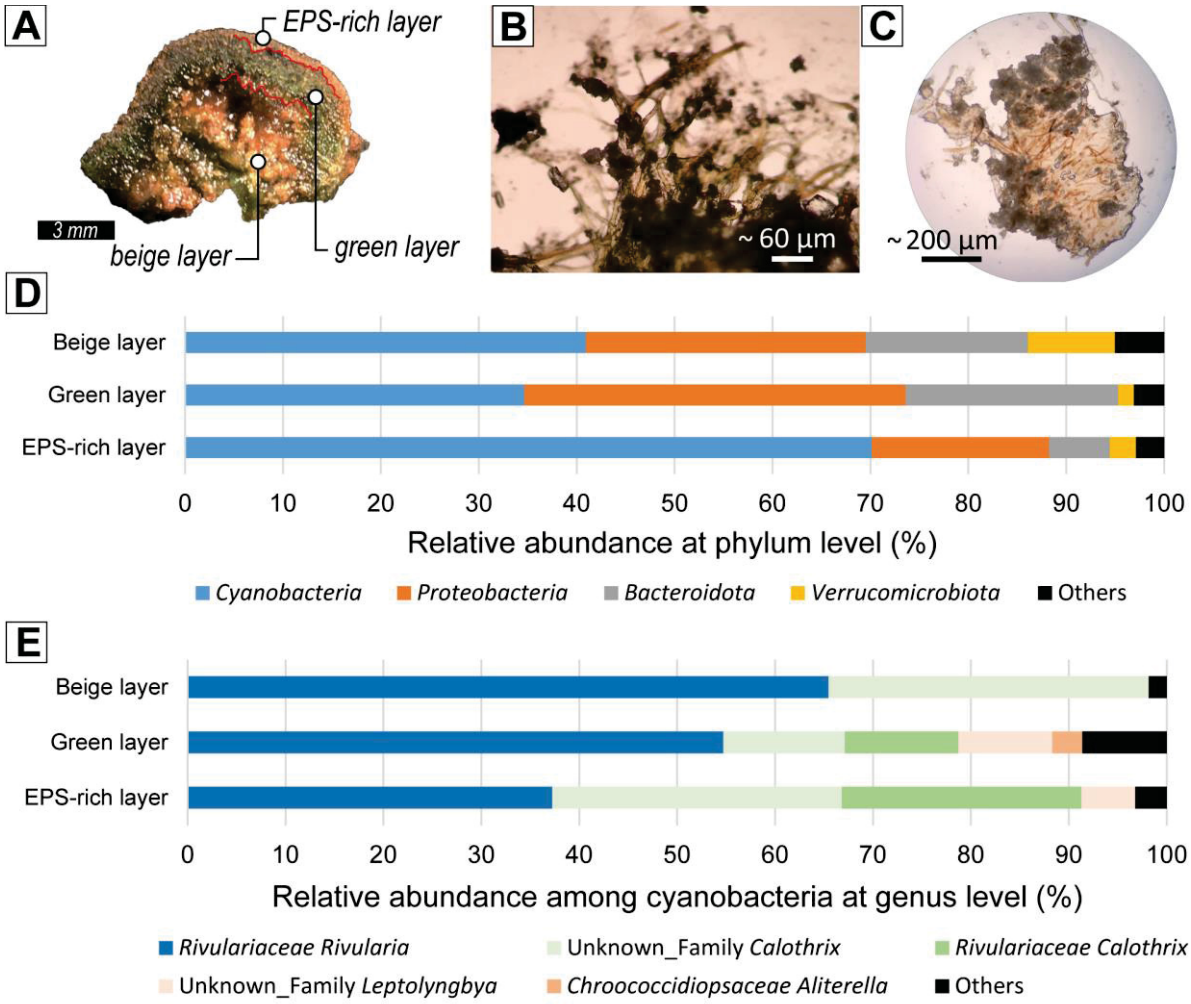

SOURCE: This work.

LEGEND: A) Structure of the “living” microbial mat collected in the LS site. Photomicrographs under the magnifying glass showing the abundant present of filamentous cyanobacteria, and their association with carbonate minerals, in the green (B) and beige (C) layers. D) Relative abundances of 16S rRNA sequences of bacteria at phylum level. E) Relative abundances of 16S rRNA sequences of cyanobacteria at genus level.

FIGURE 24 – SEM IMAGES OF CALCIFIED MICROBIAL MAT

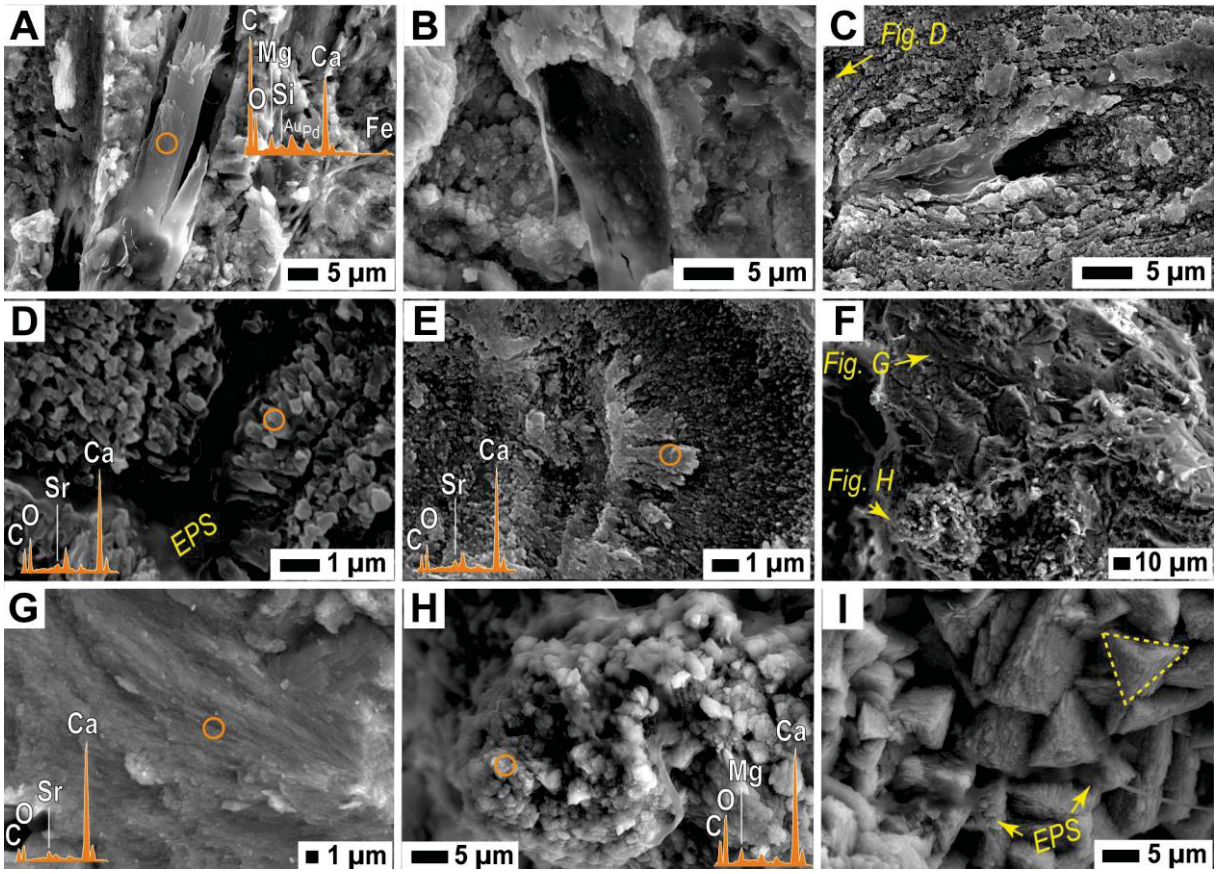

SOURCE: This work.

LEGEND: Secondary electron SEM images and punctual EDS analysis of the calcified microbial mat from LS site. A) Filamentous cyanobacteria sheath with basal heterocyst impregnated by amorphous carbonates and Mg-Fe-bearing silicate phase and encrusted by micrite-grade carbonate grains. B) Impregnated EPS sheath encrusted by globular subhedral grains (<1 µm). C) EPS sheath impregnated by an amorphous carbonate phase. The porous interior formed after the decay of the cyanobacterial cells is partly occluded by micrite-grade carbonate precipitation. D) and E) Close-up to Sr-rich, submicron-sized anhedral grains with elongated to ellipsoidal morphologies radiating from the mucilaginous sheath of cyanobacteria. F) Microscale relationship between an internal microdomain composed of Sr-rich carbonate crystal with acicular morphology (G) and an external microdomain composed of Mg-rich subhedral carbonates nanoaggregates precipitated embedded in EPS (H). I) Trigonal mesocrystals of Mg-calcite microspar associated with EPS.

Encrusted filaments (diameter 5–15 µm) and calcified EPS sheaths of filamentous cyanobacteria (diameter 5–12 µm) with internal tubular pores (diameter 3–8 µm) are ubiquitous in the calcified microbial mat (Fig. 24A-B-C). Some exhibit basal heterocyst and false branching pattern of *Rivularia*-like cyanobacteria (Fig. 24A). The EPS sheath is impregnated with an unknown Fe-Mg-Si phase, presumably some type of clay (Fig. 24A), and amorphous carbonates with unknown ultrastructure (Fig. 24B). The carbonates formed at the outer surface of the filamentous EPS sheaths can consist of globular to subhedral nanoparticles (Fig. 24B) or radially

organized, Sr-rich, nano-to-micritic grains with spheroidal to elongated morphologies associated with EPS (Fig. 24C-D). The aggregation of these nanograins produces radiating (fan-like) microstructures (Fig. 24E). Microdomains composed of micrite-to-microspar grade, Sr-rich, acicular crystals, and micrite-grade aggregates composed of smaller (≤1 μm) subhedral Mg-rich carbonates embedded in EPS (Fig. 24F-G-H) are distinguished between the filaments. Larger mesocrystals (5-10 μm) with triangular terminations form partly embedded in EPS (Fig. 24I). The XRD analysis indicates that the Sr-rich acicular crystals correspond to aragonite (25%) and the mesocrystals to Mg-calcite (75%; 7.3 mol % of $MgCO_3$).

5.4.4 Fossil tufa deposits

The deposits consist predominantly of Mg-calcite (≥90%; 5.1–11.6 mol% $MgCO_3$, avg. 8.3). Minor aragonite (≤10%) occurs sporadically, with trace dolomite and monohydrocalcite (≤5%) in two samples. Terrigenous grains (quartz > plagioclase ≫ pyroxene, micas, amphibole) are ubiquitous but more abundant in build-ups (avg. 10%).

5.4.4.1 Textural components

Similar *in situ* and granular components constitute the tufa crust and build-ups, and their description and interpretation are summarized in Table 1. The *in situ* components are mostly constituting the rock framework and can be either depositional or diagenetic features, though this division is in cases diffuse (Table 1). The granular components are authigenic and non-authigenic grains disposed into a micritic matrix and conform microdomains referred as “internal sediments” (Bosence and Gallois, 2022; Rainey and Jones, 2007). The internal sediments were mostly attached during diagenesis and fill secondary pores or enlarged growth framework pores.

TABLE 5 – MAIN COMPONENTS OF THE FOSSIL TUFA DEPOSITS

Components	Description	Occurrence	Interpretation
In situ			
Shrub (*Fig. 25, 26, 27)*	Radiating microstructures (0.5 to <3 mm) composed of filamentous microbes (diameter <20 µm) encrusted by fascicular-optic spar, mixed micrite/microspar, or, exceptionally, micrite. The filaments can be hollow or permineralized by an undetermined clay-like phase.	Forming domains of the framework. Typically grading into zones of mixed micrite/microspar and clotted micrite.	Depositional feature formed by calcification of Rivularia colonies (Freyret and Verrecia, 1999). Variably degraded to micrite during early diagenesis.
Calcified filament *(Fig. 27A-B-C-J, 28D)*	Microbial filaments (diameter <20 µm) coated by micrite and encrusted by spar/microspar. The filaments are arranged in parallel or as radiating bundles.	Forming domains of the framework with radiating morphology	Depositional feature. Organomineralization of filamentous cyanobacteria (micrite) and abiotic precipitation (spar). Variably degraded to micrite during early diagenesis.
Microstromatolite *(Fig. 25B-J)*	Dome-shaped microstructures (<0.5 mm) with limited lateral extension, composed of finely laminated micrite layers, in some cases interbedded with spar.	Minor component of the framework. Growing from shrubs, syntaxial spar, or terrigenous grains.	Depositional feature formed by microbially mediated precipitation.
Clotted micrite *(Fig. 25A-K-L, 27D, 28A-D)*	Amalgamated clots of peloidal micrite (20–100 µm) with globular to irregular morphologies, usually within a spar matrix.	Mainly forming the framework as patches around shrubs and/or zones of mixed micrite/spar. In some cases, as poorly defined laminations.	Diagenetic product following framework degradation (Flügel, 2010) or a depositional feature formed by EPS calcification (Riding, 2000).
Mixed micrite/microspar *(Fig. 25B-G-M, 27K, 28B-E)*	Structureless arrays of micrite and microspar with no preservation of filamentous microbial structures.	Irregular domains within the framework. Spatially associated with shrubs and clotted micrite	Early diagenetic feature formed by degrading recrystallization of spar/microspar.
Massive micrite *(Fig. 25G, 27K, 28E-F)*	Homogenous and structureless micrite	Coating the rock framework, around shrubs, or as matrix of granular components	Diagenetic micrite (pseudomicrite; Flugel, 2010).

Interlayered micrite/spar *(Fig. 26G, 28B)*	Isopachous bands (<0.5 mm thick) with convex shapes composed of micrite and fibrous spar couplets.	Coating the external portions of the framework. In cases overgrown by spar fringes	Early cement. Alternating modes between abiotic (spar) and microbially mediated (micrite) precipitation, likely due to changes in extrinsic parameters (Flügel, 2010).
Spar *(Fig. 25B-F-K. 28I)*	Clean to dirty crystals with variable fabrics (acicular, radiaxial fibrous, dogtooth, and granular) and sizes (<0.3 mm).	Linning or within the framework.	Primary or secondary origin (see text for details)
Granular			
Skeletal (*Fig. 26A-F, 28E-F)*	Variably preserved shells (0.25–2 mm) of unidentified gastropods and presumably ostracods.	Common, yet not abundant. Mostly attached to the external portions of the framework, or filling the secondary porosity.	Low abundance due to oligotrophic conditions. Some are depositional, but most were incorporated during early diagenesis.
Peloid (*Fig. 28A-F-I)*	Subrounded and structureless micritic grains with diameters < 100 µm.	Filling framework porosity and secondary pores	Mostly formed by abrasion of micritized tufa framework. Some are fecal pellets. Incorporated during early diagenesis.
Ooid *(Fig. 28H)*	Spheroidal grains (<0.5 mm) with terrigenous or calcareous nuclei coated by thin (<0.1 mm) regular laminae with tangential, and in some cases radial, fabrics.	Common, yet not abundant. Filling framework porosity and secondary pores	Formed in agitated low-energy (fibro-radial) to high-energy (tangential) waters (Flugüel, 2010)
Intraclast *(28E-H)*	Fragments of tufa and rare ooidal and peloidal aggregate grains. Sizes range from 0.1–2 mm, generally with a thin, structureless micrite envelope.	Common, in cases abundant. Filling framework porosity and secondary pores	Mechanical reworking of the tufa deposits. Incorporated during early diagenesis
Terrigenous grain *(Fig. 25A-N, 26C-D-H, 27I-J, 28G)*	Mostly subrounded grains of mudstones and sandstones, and individual crystals of quartz and plagioclase, among others. Sizes range from 0.03–2 mm, generally with a thin, structureless micrite envelope.	Ubiquitous. Filling framework porosity and secondary pores.	Reworking of local and glacial deposits. Micrite envelopes may represent calcified biofilms (Riding, 2000). Mostly incorporated during early diagenesis. In some cases, in situ.

SOURCE: This work.

FIGURE 25 – PETROGRAPHY OF FOSSIL TUFA CRUST

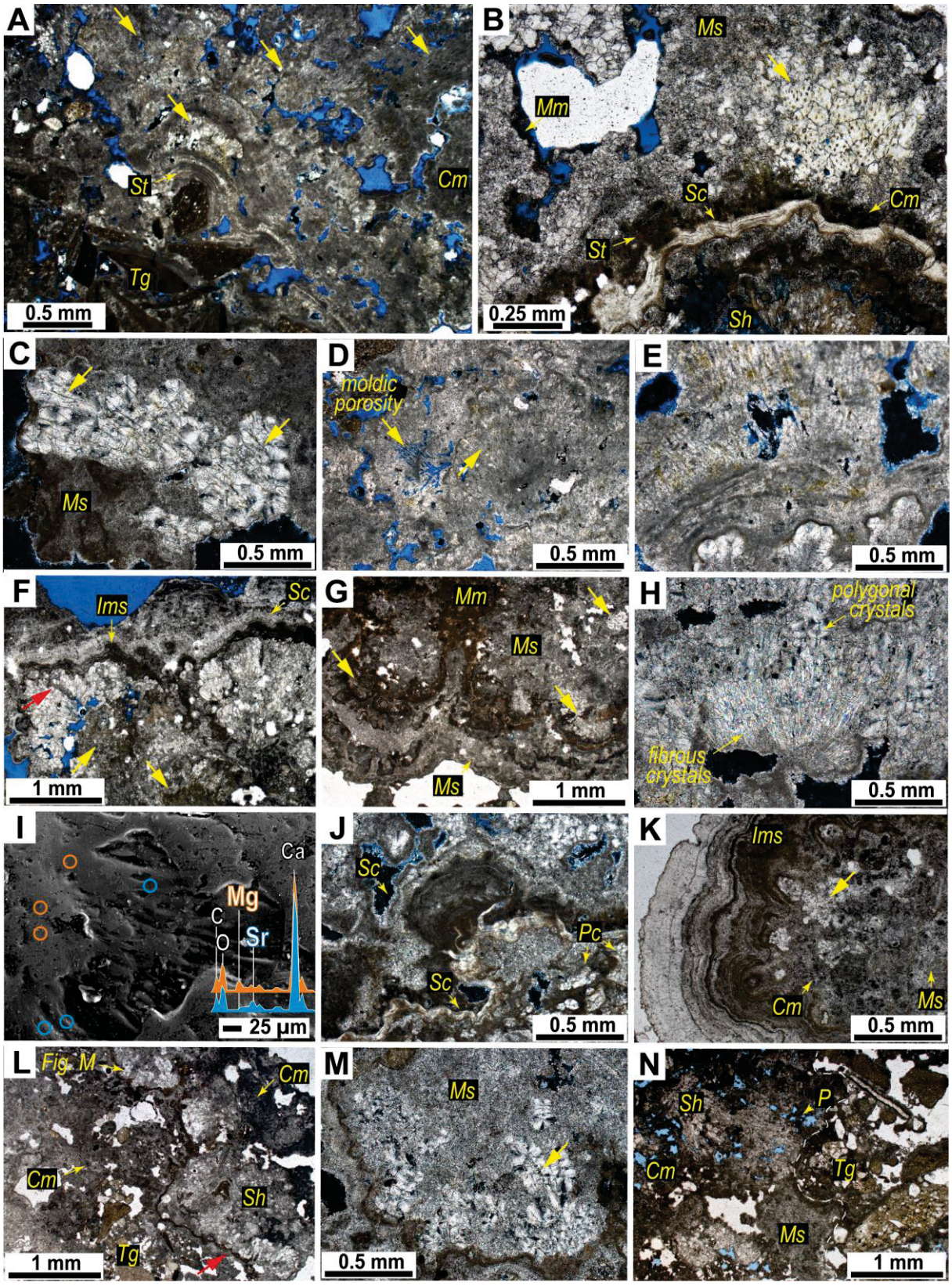

SOURCE: This work.

LEGEND: Photomicrographs under polarized (A, B, F, G, K, L and N) and unpolarized (C to E, H, J and M) transmitted light microscopy of the fossil tufa crust showing the relationships among their textural components. The thick yellow arrows point to variably preserved filamentous cyanobacteria

structures, in cases with formation of clay-like minerals (E). Shrubs (Sh) are the main framework component (A, B, D to G), and their stacking developed with intermittent microstromatolite deposition (St) and isopachous spar (Sc) cementation (B and J). Polygonal and fibrous domains within individual shrubs are composed of Mg- and Sr-rich carbonates as shown by punctual SEM-EDS analysis in the SEM-BSE image at (I). Some micritic domains preserve calcified filaments (top-right in A), however they are generally absent in domains of mixed micrite/microspar (Ms), massive micrite (Mm) and clotted micrite (Cm) developed around or within shrubs (B-C, G, K, M). Note that micrite formation at expenses of shrubs can be selective (red arrow in F) or not selective (C). Masive micrite and clotted micrite also develop around the framework (B and L-M). Cements mostly consist of isopachous fringes around the framework, including interlayered micrite/spar (Ims), acicular spar and fibrous radiaxial spar (Sc) in (F-G) and thin rinds of dog tooth microspar (J). Note that locally terrigenous grains (Tg) are in situ, serving as substrate for deposition (A), but more commonly conform internal sediments (L and N), in cases with sparce peloids (P). The dashed line in (N) demarks the limit between the framework (left) and internal sediments (right).

5.4.4.2 Tufa crust

Spar/microspar encrusted filamentous cyanobacteria cementstone exhibiting a continuous framework mostly composed of shrubs that grade to irregular microdomains of clotted micrite and mixed micrite/microspar (Fig. 25A-B). The shrubs are composed of microspar (Fig. 25A) or by fascicular spar mosaics with sutured margins encasing cyanobacteria filaments (Fig. 25B-C). Such filaments can be degraded, leaving a moldic porosity (Fig. 25D), or be mineralized by an undetermined clay-like mineral phase (Fig. 25E). Commonly, the shrubs are stacked due to repeated cycles of deposition (Fig. 25A-D-F), occasionally overgrowth by radiating concentric irregular bands (0.2 mm-thick) due to successive periods of accretion (Fig. 25G), or form directly over microstromatolites (Fig. 25A-E). Fibrous domains coexisting with fascicular optic polygonal spar crystal are preserved within individual shrubs (Fig. 25H); SEM-EDS analysis shows these are enriched in Sr and Mg, respectively (Fig. 25I). Microstromatolites are a minor component (Fig. 25A-B), and in cases their deposition was synchronous with cementation as evidenced by deflected bands of acicular Mg-calcite in zones of microstromatolite accretion (Fig. 25J). Irregular layers (< 0.1 mm thick) of clotted micrite occasionally developed next to the microstromatolite (Fig. 25B). The rock framework can be coated by a continuous band of interlayered micrite/spar overgrown by spar fringes of Mg-calcite (Fig. 25F-K).

FIGURE 26 – PETROGRAPHY OF TUFA BUILD-UPS: GENERAL VIEW

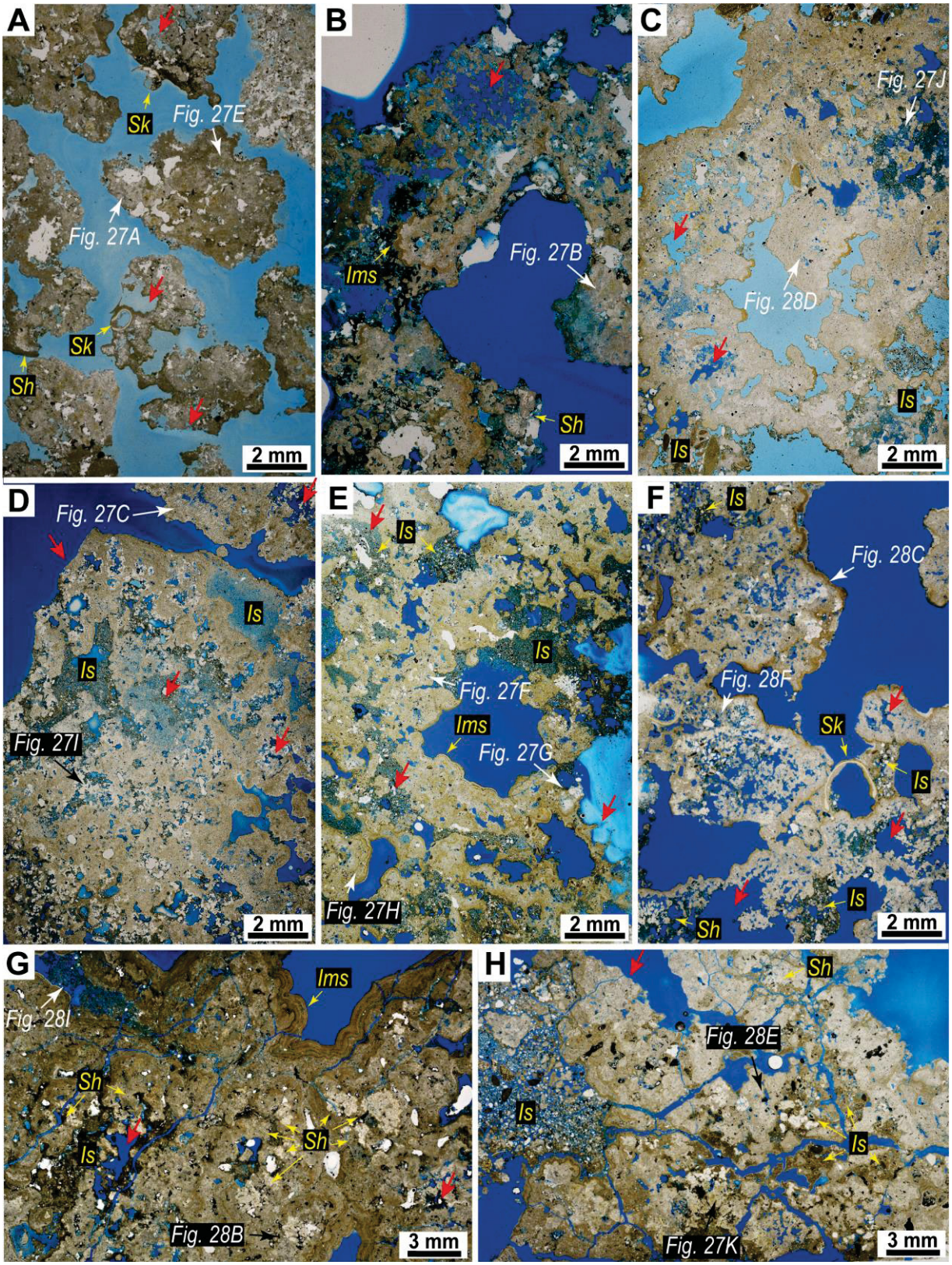

SOURCE: This work.

LEGEND: Photomicrographs of the fossil tufa build-ups under unpolarized transmitted light microscopy. A general trend of increasing framework connectivity is distinguishable among the fossil tufa build-ups, from the low-relief mounds (A-B), towards those with columnar (C), V-shaped (D-E) and dome (F-G-H) morphologies and metric sizes. The red arrows indicate dissolution/erosion features.

Note the ubiquitous presence of internal sediments (Is) filling the primary and secondary porosity and the *in situ* brecciation of the domes (G-H). Note that skeletal grains (Sk) are mostly attached to the outer border of the framework (A and F) and the interlayered micrite/spar (Ims) is typically an isopachous band rimming the framework, although with variable thickness among samples (B, E and G). For details the reader is referred to the main text. Abbreviations are the same as in Fig. 25.

Generally, the domains composed of mixed micrite/microspar, clotted micrite, and massive micrite lack filamentous structures, even when forming around or within shrubs (Fig. 25A-B-C-G-K-M). The contact between these micritic microfabrics and the shrubs is transitional (Fig. 25B-F), with the first generally forming micro-embayment or irregular overgrowths into the spar (Fig. 25C). Occasionally mixed micrite/microspar selectively form within shrubs along spar crystal boundaries. These textural relationships unequivocally indicate that the micritic microfabrics are forming at the expense of the shrubs and are therefore post-depositional features.

In a few crust samples (*e.g.,* Fig. 19H) the framework is disrupted by concave dissolution/erosion surfaces, which can be coated by a thin layer of massive micrite (Fig. 25L-N). These surfaces separate framework domains composed of poorly preserved shrubs of domains of internal sediments. The latter composed of terrigenous grains with micrite envelopes immersed in a matrix of clotted micrite with occasional peloids (Fig. 25L-N).

5.4.4.3 Tufa build-ups

Porous and heterogeneous deposits with abundant dissolution/erosion surfaces and internal sedimentation within primary/secondary pores (Fig. 26). Their framework consists of micrite/microspar encrusted filamentous cyanobacteria boundstone that grade to domains of micrite/microspar and/or clotted micrite and/or massive micrite, the latter with poor preservation of cyanobacteria filaments, or lacking them (Fig. 27). Framework connectivity increases from the low-relief build-ups (Fig. 26A-B) to the taller columns (Fig. 26C), V-shaped (Fig. 26D-E) and domes (Fig. 26G-H), although isolated domes in terrace T5d (Fig. 21A) exhibit greater secondary porosity (Fig. 26F).

FIGURE 27 – PETROGRAPHY OF TUFA BUILD-UPS: MICROBIAL TEXTURES

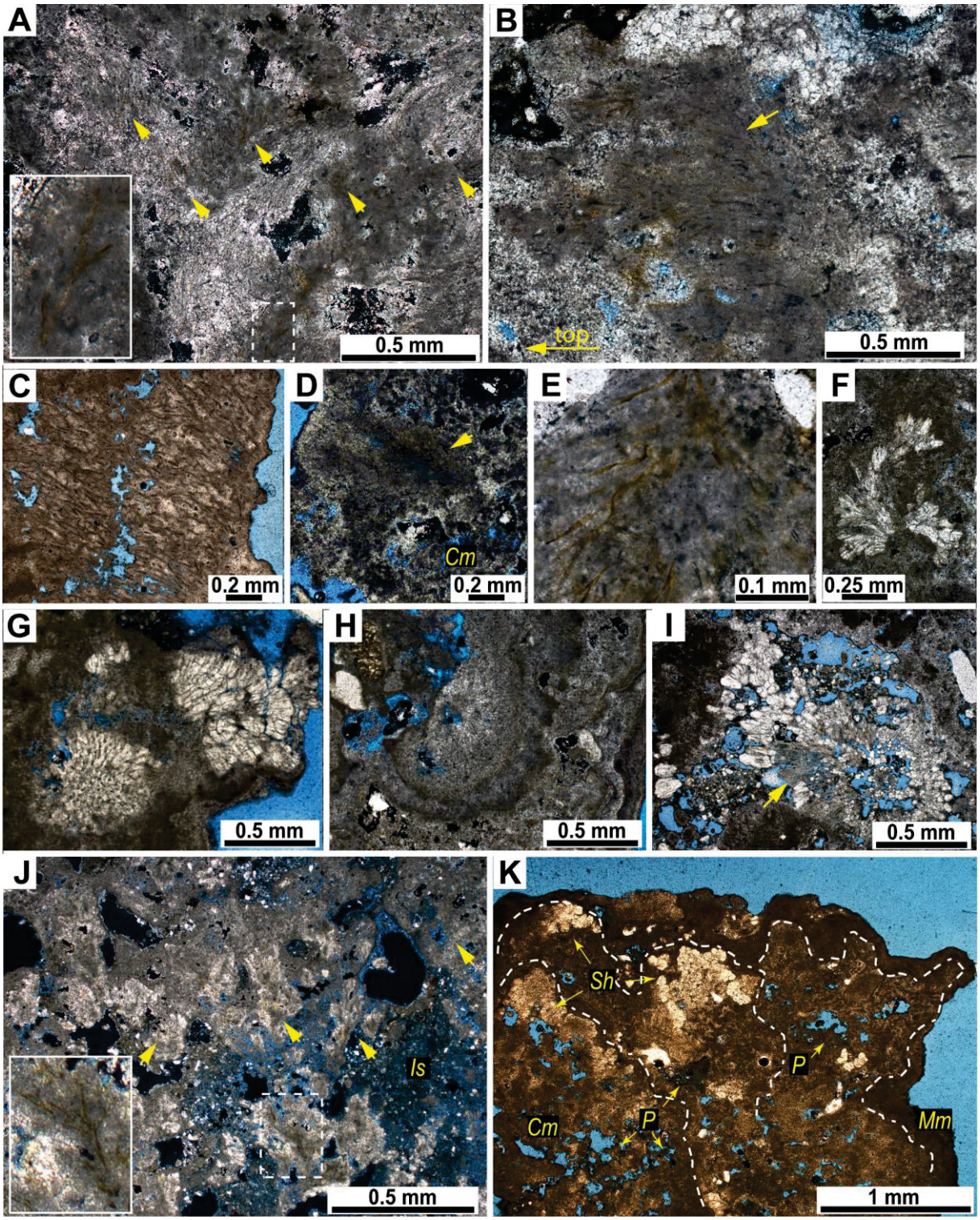

SOURCE: This work.

LEGEND: Photomicrographs under polarized (A-B and J-K) and unpolarized (C to I) transmitted light microscopy of the fossil tufa build-ups highlighting their microbial components. The microscale context of each photomicrographs within the tufa framework is indicated in Fig. 26, except for (D). The thick yellow arrows, as well as the insets, highlight poorly preserved cyanobacteria filaments composing micritic domains of the framework surrounded by spar or within shrubs. Radiating bundles of cyanobacteria filaments composing the shrubs (Sh) can be partially to totally erased due to micritization and dissolution/erosion (D to I). The secondary pores filled with internal sediments (H to

J). Note the non-isopachous fringes of mixed micrite/microspar overgrowth on the shrubs (G-H). In (K) the dashed line demarks cyclic irregular overgrowths composed of sparitic shrubs borders that grades to porous domains of clotted micrite (Cm) with peloids (P) infilling the pores. For details the reader is referred to the main text.

FIGURE 28 – PETROGRAPHY OF TUFA BUILD-UPS: DIAGENETIC FEATURES

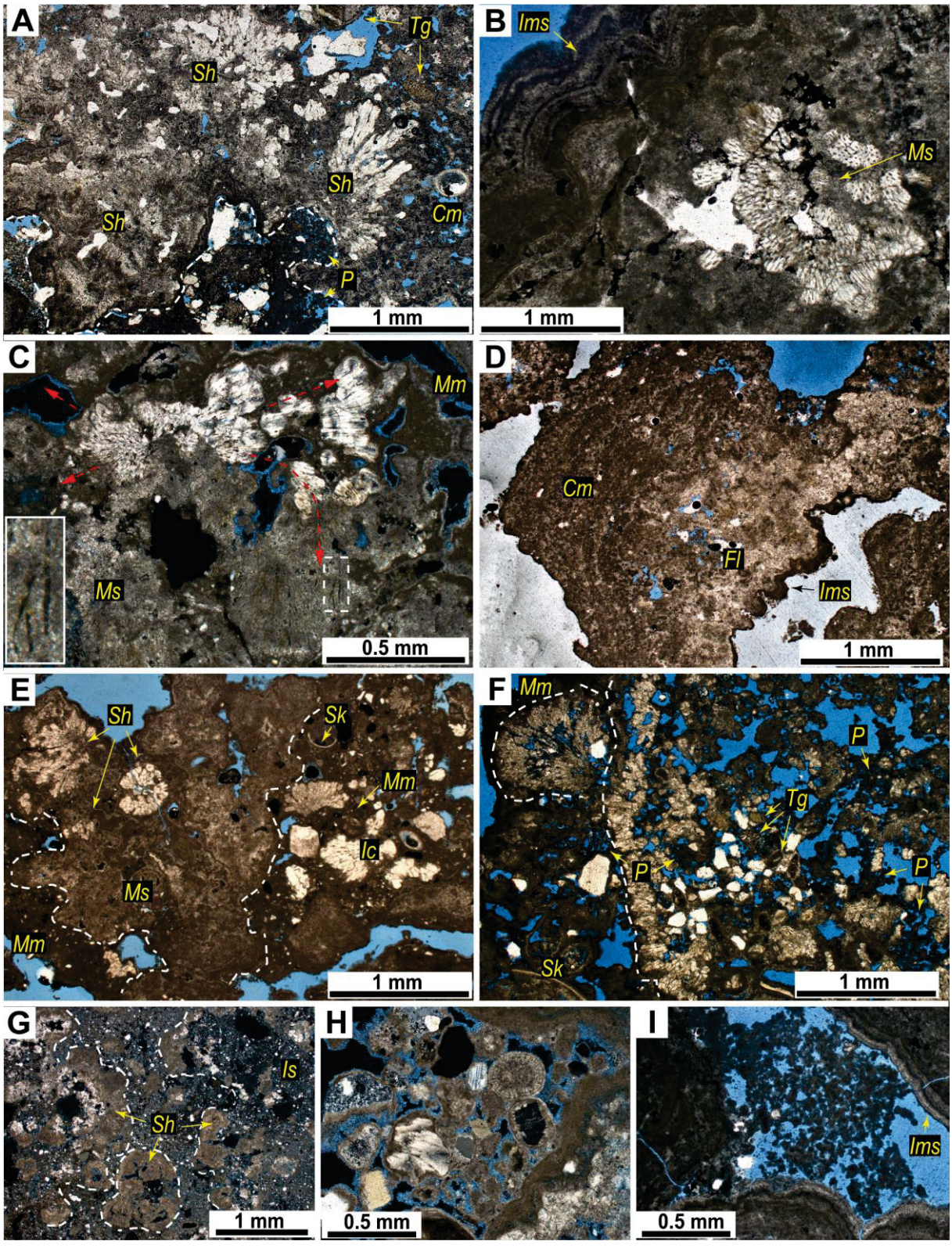

SOURCE: This work.

LEGEND: Photomicrographs under unpolarized (A to F and I) and polarized (G and H) transmitted light microscopy showing the heterogeneity of fossil tufa build-ups at microscales, and the relationships between their textural components. The microscale context of (B to F) and (I) photomicrographs within the tufa framework is indicated in Fig. 26. Note the formation of clotted micrite (Cm), mixed micrite/microspar (Ms), and massive micrite (Mm) after the degradation of the sparitic shrubs (Sh) in (A), (B) and (C). The red arrows in (C) highlight the growth direction of the cyanobacteria filaments and the inset its preservation within the Ms domain. In (D) poorly preserved calcified filaments (Fl) within domains of spar with micritic patches grade to clotted micrite exhibiting faint laminations. In (E) the segmented line demarks the limit between framework domains composed of Ms and partly preserved shrubs with internal sediments composed of skeletals (Sk) and intraclasts (Ic) in a matrix of massive micrite (Mm). In (A), (F) and (G) the segmented line highlights the limit between dissolved/eroded framework domains and internal sediments (Is), including terrigenous grains (Tg) and peloids (P); note that these grains also infill secondary pores. Note that shrubs are partly to totally micritized in (G). A closer view to ooids, peloids, and the micrite envelop in terrigenous grains and intraclast is shown in (H) and (I). Note that the interlayered micrite/spar (Ims) rimming the framework can exhibit irregular (B) or regular lamination (I), in cases with limited lateral extension (D). For details the reader is referred to the main text.

Cyanobacterial microstructures are preserved as calcified filaments in diffuse framework domains or within the shrubs. The calcified filaments are usually contained in micritic micro-domains immersed in spar matrix and their preservation tends to be lower in the low-relief build-ups (Fig. 27A-B-E) compared to the larger columns (Fig. 27J). Similar micrite-spar association is exceptionally well-preserved in filaments at the basal portions of V-shaped build-up (Fig. 27C). The shrubs consist of radiating microstructures with arborescent, fan-like or sub-spherical shape composed of spar and/or microspar and in cases micrite (Fig. 27D to H and Fig. 28A to G). They are a ubiquitous component in all the deposits (Fig. 26), though their preservation is greater in the tufa domes (Fig. 26G).

The organization of the filament-related components is the main control on the framework growth. The calcified filaments shape radiating structures of a few millimeters that compose irregular mesoclots (Fig. 26A), or larger domains with more continuous framework (Fig. 26B-C-D). The shrubs can define radiating protrusion with bumpy shapes due to their irregular stacking (Fig. 27K and 28A) or coalesce at variable degrees to structure irregular to rounded botryoids which are overgrowth by concentric and non-isopachous bands of mixed micrite/microspar (<0.5 mm-thick) (Fig. 26E-G, 27H). The framework is also lined by a syntaxial band of interlayered micrite/spar (Fig. 26G and 27B).

The depositional features of the build-ups are partly obscured by early diagenetic processes as evidenced by the transitional textures between sparitic shrub and micritic microfabrics (Fig. 27F-G and 28A-B), and by the ubiquitous

dissolution/erosion features in domains composed of shrubs and calcified filaments (Fig. 26, 27H-I-J and 28A). Generally, the filamentous structures within the shrubs are not preserved when replaced by peloidal micrite (Fig. 27K and 28A), mixed micrite/microspar (Fig. 28B) and massive micrite (Fig. 28C), although in cases they can be continuously tracked towards domains of mixed micrite/microspar (Fig. 28C). Less commonly the domains of clotted micrite exhibit diffuse microlaminations (Fig. 28D). Granular components (terrigenous grains > intraclast > peloids, and minor skeletals and ooids), are filling the framework porosity (Fig. 26G and 28H-I), the secondary porosity (vugs and intercrystalline porosity) (Fig. 28A-F) or both (Fig. 28G). These internal sediments are contained in a micritic matrix, and their attachment occurred after the micritization of the framework (Fig. 28E). Late-stage pseudo-breccia texture with unrotated angular fragments is developed in the tufa domes (Fig. 26G-H).

5.4.4.4 Microfabrics of calcified filaments

Tubular microfabrics (5–20 μm) with hollow interiors (ca. 2–15 μm) result from the sheath impregnation of filamentous cyanobacteria (Fig. 29A-B-C-D). The ultrastructure of the amorphous carbonate within the sheaths was not possible to be determined (Fig. 29E-F), although in cases globular nanoparticles (≤1 μm) were observed (Fig. 29G-H). Similar nanoparticles form around filaments (Fig. 29E-H), defining radiating structures (Fig. 29F) comparable to those of acicular microspar encrusting filaments in tufa crust (Fig. 29G). A marked compositional difference is detected in cases, with Sr-rich carbonate forming within shrubs and Mg-rich carbonates in the surrounding matrix, the latter typically containing abundant filamentous remains (Fig. 29I). Subhedral micrite-grade carbonates around filaments can grade to microspar and spar, the latter exhibiting subrounded hollow cavities (<3 μm) and in cases encrusting smaller filaments (diameter of 1–2 μm; Fig. 29J). Tubular microstructures formed by carbonate precipitation inside calcified EPS sheaths (“sheath casts” *sensu* Rainey and Jones, 2010) can coexist within a few micrometers with hollow impregnated sheaths, pointing to heterogeneous conditions among microdomains (Fig. 29K).

FIGURE 29 – SEM IMAGES OF CALCIFIED CYANOBACTERIA IN FOSSIL DEPOSITS

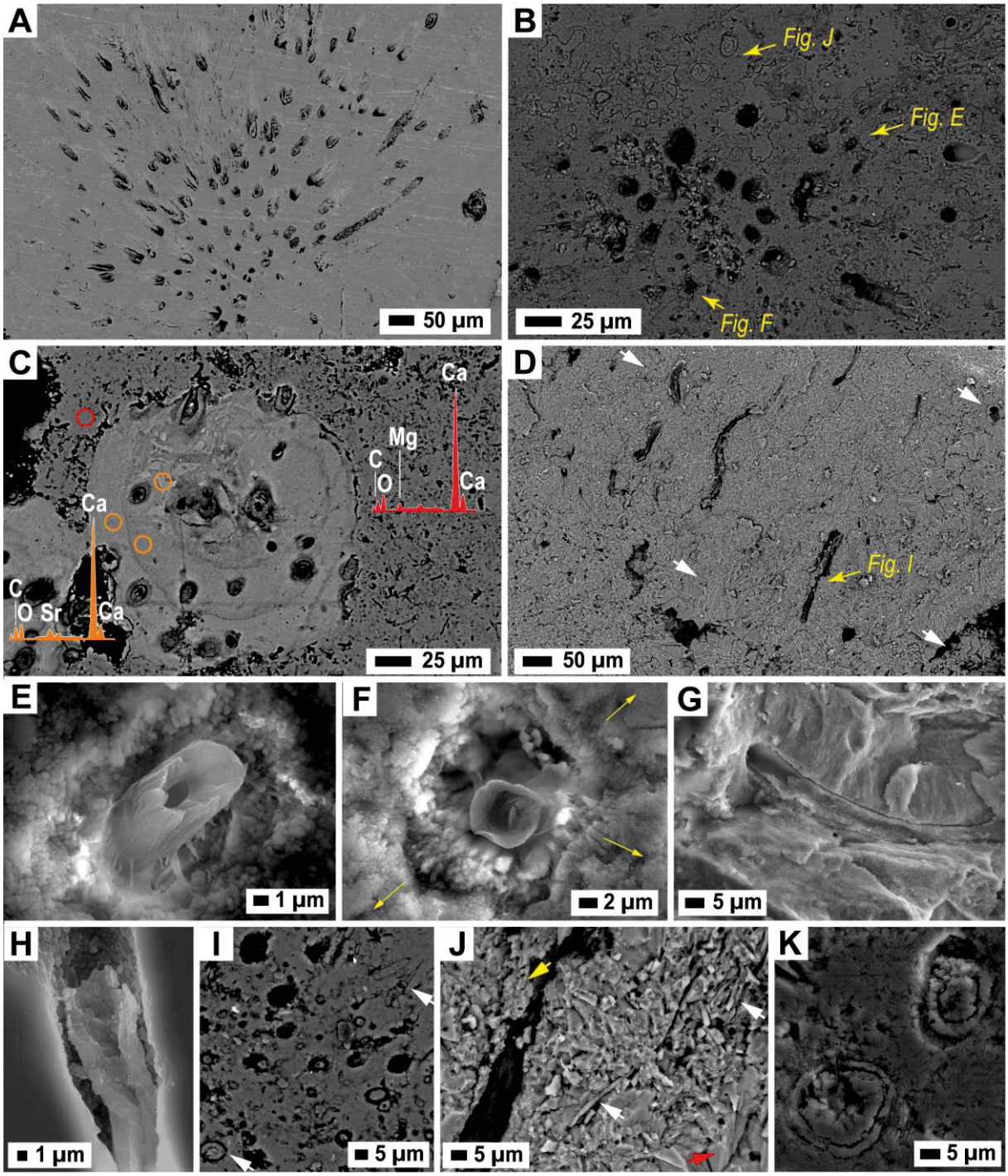

SOURCE: This work.

LEGEND: SEM-BSE images (A to D and I to K) and SEM-SE images (E to H) of calcified filamentous cyanobacteria in the fossil tufa crust (A-G) and build-ups (rest of them). Cross-view (A to C) and lateral view (D) of cyanobacteria colonies and individual cyanobacteria filaments (E to H and J-K). Note that typically the filaments are impregnated by amorphous carbonate with either unknown ultrastructure (E-F) or globular morphology (G-H). The carbonates formed around the filaments can be globular particles <1 µm (E-F-H) or fibrous crystals (G). In (J) smaller carbonates grains (<1 µm) form in the outer sheath surface (yellow arrow) while fringes of scalenohedral microspar/spar with hollow pores forms outwards (red arrow), also encrusting smaller filaments (white arrow). The white arrow in (D) also points to the spar fringes. Punctual analysis of SEM-EDS shows chemical variations between shrubs (Sr-rich) and the matrix that contains them (Mg-rich) (C). The latter is composed of abundant

microbial remains, including filamentous cyanobacteria (I). In cases the tubular pores leave after sheath impregnation and trichome decay is filled by carbonate (K).

5.4.5 Tufa stable isotope composition

The build-ups show homogeneous isotopic composition among the sites ($\delta^{13}C$ 4.0–4.8‰; $\delta^{18}O$ -1.9 to -1.0‰; Fig. 30A), while in the TP3 profile are slightly more variable ($\delta^{13}C$ 4.0–5.5‰; $\delta^{18}O$ -1.9 to -0.7‰; Fig. 30B). Tufa crusts share similar $\delta^{13}C$ (4.1–5.0‰) but lower $\delta^{18}O$ (-2.2 to -1.4‰) compared to the build-ups. The calcified microbial mat match $\delta^{18}O$ (-1.4‰) but have higher $\delta^{13}C$ (5.6‰). No significant $\delta^{13}C$-$\delta^{18}O$ covariation exists except in the upper interval of the TP3 profile (Fig. 30C).

5.5 DISCUSSION

5.5.1 Microbial and environmental influences on tufa accretion

The ubiquitous presence of cyanobacteria filaments in the fossil deposits indicates that organomineralization processes (Dupraz *et al.,* 2009) played a significant role in the precipitation. While similar diameters, morphology and calcification between preserved cyanobacteria sheaths in the fossil deposits (Fig. 12) and those in the calcified mat (Fig. 7) suggest comparable microbial consortia.

The pustular mat at LS site (Fig. 2B) exhibits similar green/beige layering (Fig. 23A) and phylum-level composition (Fig. 23D) to mats colonizing submerged tufa build-ups (up to 10 m-depth) (Airo, 2010), suggesting its representativeness of benthic microbial mats developing within the lake. Both are dominated by Cyanobacteria, followed by Proteobacteria, Bacteroidota and Verrucomicrobia (this work; Airo, 2010). Similar composition is reported by Osman *et al.* (2020) in a sample collected from the wave-breaking zone at the TP5 site, though with increased Planctomycetes and reduced Cyanobacteria. These phylum-level similarities are consistent with stable lake physiochemical conditions (e.g., pH, salinity and dissolved oxygen), while observed variations may reflect seasonal differences between late summer (Osman *et al.,* 2020) and early spring (this study) sampling (Petryshyn *et al.,*

2021), as no major environmental shifts have occurred recently (e.g., Eymard *et al.,* 2021).

Cyanobacteria of the order Nostocales (genus *Rivularia* and *Calothrix,* family Rivulariaceae) dominate the studied microbial mat (Fig. 23E), consistent with the abundant presence of Nostocales (genus *Rivularia)* in the submerged mats (Airo, 2010). Their prevalence is likely linked to their ability to fix nitrogen (Mateo *et al.,* 2015), a competitive advantage in Lago Sarmiento's oligotrophic, nitrogen-limited waters (De los Ríos and Soto, 2009 and references therein), suggesting rivulariaceans play a critical ecological role in sustaining the microbial consortia of benthic mats in Lago Sarmiento.

Marine calcified rivulariaceans are abundant in pre-Cenozoic deposits (Liu *et al.,* 2016), while Neogene-to-modern carbonate precipitation by *Calothrix* and *Rivularia* occurs primarily in freshwater systems (Caudwell *et al.,* 2001; Hoppert *et al.,* 2023; Pentecost, 1989; Pentecost and Franke, 2010; Pentecost and Talling, 1987; Willmer and Rasser, 2022), with rare marine exceptions (Golubic and Campbell, 1981; Kershaw and Guo, 2003; Portman *et al.,* 2005). Despite morphological similarity (Berrendero *et al.,* 2008), their calcification pattern differ due to colony organization and EPS production; *Rivularia* filaments are typically organized into subspherical to hemispheric radiating mucilaginous colonies, while *Calothrix* grows as individual or poorly ordered sheathed filaments lacking interstitial EPS (Casamatta and Hašler, 2016; Whitton and Mateo, 2012). This suggests the shrubs exhibiting non-crystallographic and upward diverging growth in the fossil tufa correspond to calcified *Rivularia* colonies (Fig. 26-27-28) (Freytet and Verrecchia, 1998), while those unorganized calcified filaments in the matrix that contains the shrubs could be cyanobacteria of genus *Calothrix (Fig. 29K)* (Pentecost, 1989). The smaller sheathed filaments in the shrubs could represent the apical zone of *Rivularia*, which depending on the species it can reach widths as small as 1-2 μm (Sihvonen *et al.,* 2007; Singh and Kumar, 2009). Those encrusted filaments <3 μm lacking sheaths may correspond to genus *Leptolyngbya* (Shiraishi *et al.,* 2020). The new data agrees with previous works (Airo, 2010) supporting cyanobacteria, and particularly rivulariaceans, are the main framework builders in Lago Sarmiento.

The early induration of the deposits involved the EPS-mediated nucleation of globular to subhedral particles with sizes $\leq$1 μm within or in the outer surface of cyanobacteria sheaths and interstitial EPS (Fig. 24 and 29). These nanoparticles

resemble the amorphous calcium carbonate (ACC) precipitating in biofilms from ambient temperature, freshwater carbonate systems (Broughton, 2023; Perri *et al.,* 2012; Rainey and Jones, 2010; Shiraishi *et al.,* 2020; Zeyen *et al.,* 2021), controlled experiments (Obst *et al.,* 2009; Pedley, 2014; Pedley *et al.,* 2009; Shiraishi *et al.,* 2020), and associated with calcified *Rivularia* in ancient freshwater microbialites (Willmer and Rasser, 2022). Sheat impregnation involves mineralization of an unknown clay-like phase (Fig. 24A, 25E) resembling those described in microbialites from alkaline lakes (Kremer *et al.,* 2012), however its significance is not addressed here as its study requires more sophisticated methods due its low abundance.

The nucleation of ACC at intra-EPS sites occurs when the amount of Ca^{2+} ions bound to acidic macromolecules exceeds the EPS capacity of inhibiting precipitation (Arp *et al.,* 1999; Decho, 2010; Tomohiro Kawaguchi and Decho, 2002). This process has been signaled as a relevant factor favoring crystal nucleation in tufa-depositing systems (Pedley, 2014; Rogerson *et al.,* 2008; Shiraishi *et al.,* 2008a), although it may not be the main factor controlling the Ca^{+2}-fluxes and, consequently, the amount of carbonate precipitation (Shiraishi *et al.,* 2008a). Conversely, daily fluxes in pH, DO, Ca^{2+} and CO_3^{2-} in biofilms, signaling to carbonate precipitation and dissolution under light and dark, respectively (Bissett *et al.,* 2008a, 2008b; Rogerson *et al.,* 2010; Shiraishi *et al.,* 2008b), suggest photosynthesis plays a relevant role in the precipitation. This could explain the frequent observation that precipitation only occurs in the presence of microbial substrates, despite relatively high carbonate supersaturation levels (Arp *et al.,* 2010; Pedley *et al.,* 2009; Shiraishi *et al.,* 2008a, 2008b). Works quantifying the impact of photosynthesis in the amount of precipitated carbonates under conditions comparable to those in Lago Sarmiento have estimated that biologically induced precipitation is relatively minor (around 10 to 20%) in comparison to physiochemical precipitation (Arp *et al.,* 2010; Pentecost and Franke, 2010; Shiraishi *et al.,* 2008b; Spiro and Pentecost, 1991), however, its role seems to be critical for surpassing the kinetic barriers for carbonate precipitation (Rogerson *et al.,* 2014; Shiraishi *et al.,* 2008a).

FIGURE 30 – CARBON AND OXYGEN STABLES ISOTOPES OF CARBONATES

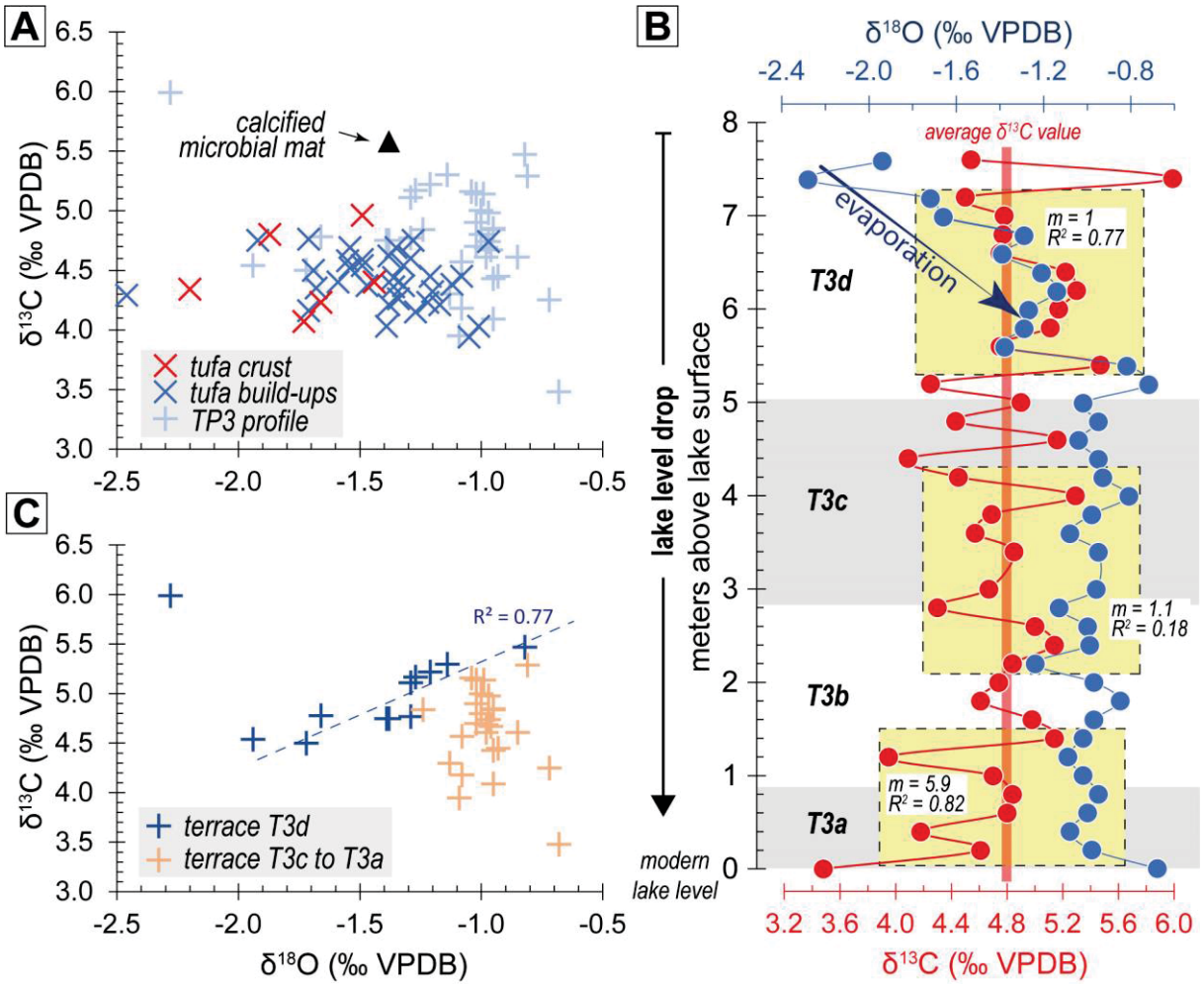

SOURCE: This work

LEGEND: Carbon and oxygen isotopes of the studied deposits. A) Binary plot of all the data. B) Variation along the TP3 profile. C) Binary plot of TP3 profile data highlighting the strong positive covariance in the T3d terrace. Note that $\delta^{18}O$ variation in the T3d terrace is comparable to that in the whole dataset.

The extensive tufa outcrops in Lago Sarmiento signal that carbonate precipitation in the littoral zone is mostly restricted to microbial substrates despite, at least periodically, high carbonate supersaturation levels ($SI_{calcite}$ of 0.93 and 1.01; Osman *et al.,* 2020). This suggests biotic mediation is key for triggering precipitation (Shiraishi *et al.,* 2008a), either involving EPS-influenced nucleation of ACC-like particles though diffusion-driven processes within communal EPS secreted by the microbial consortia (Pedley, 2014) and/or sheath impregnation, likely reflecting photosynthetically-induced precipitation (Merz, 1992). Following nucleation, lower carbonate supersaturation levels would be needed for the stabilization and further growth of the organosedimentary structures as heterogeneous precipitation in

freshwater systems is estimated to occur at $SI_{calcite}$ around 0.48 (Pentecost, 2005). In addition to favorable thermodynamic conditions for carbonate precipitation, similar to those estimated for cyanobacteria encrustation ($SI_{calcite}$ between 0.8 to 1) (Arp *et al.,* 2001; Kempe and Kazmierczak, 1990; Merz-Preiß and Riding, 1999), kinetic factors associated with turbulence-induced CO_2 degassing stimulated by the wind effects may also promote precipitation (Dreybrodt and Buhmann, 1991; Liu *et al.,* 1995; Pedley and Rogerson, 2010; Zhang *et al.,* 2001). This is supported by the ubiquitous presence of (micro)spar cements in the studied deposits (Fig. 25 and 27), a feature more characteristic of freshwater microbial carbonates deposited in high-energy settings (Gradziński, 2010). Therefore, it is deduced that large-scale tufa deposition in Lago Sarmiento reflects optimal biotic-abiotic interplay, mirroring positive feedback between lithification, build-up size, and energy regime in marine settings (Suosaari *et al.,* 2019).

5.5.2 Syn-depositional to early diagenetic mineralogical and textural progression

Integration of modern and fossil deposits reveals key mineralogical/textural modifications from initial microbial calcification to subaerial exposure. Three stages are identified: (1) early mat induration, (2) constructive diagenesis stabilizing the organosedimentary structures, and (3) late destructive diagenesis partially erasing microbial textures. While stages 1-2 occurred near simultaneously in phreatic conditions, stage 3 developed in the eulittoral zone under wave influence as the lake-level diminished, implying that individual build-ups could have been repeatedly subjected to these stages depending on water-level oscillations.

5.5.2.1 Early induration

The remnants of ACC-like particles in the fossil deposits (Fig. 29E to H) indicates that early mineralization follows a non-classical crystallization pathway (De Yoreo *et al.,* 2015), while the coexistence of Sr-rich and Mg-rich ACC-like particles associated with EPS within the calcified microbial mat (Fig. 24) suggests these are precursor phases for aragonite and Mg-calcite identified in the XRD analysis.

The Sr-rich ACC-like particles in the calcified microbial mat tend to form radiating microfabrics (Fig. 24B) resembling some hot and cold calcareous spring deposits and lacustrine microbialites, where aragonite forms through the aggregation of ACC-like particles (e.g., Peng and Jones, 2013; Ge *et al.,* 2021; Quezada *et al.,* 2024). A comparable growth mechanism for the acicular aragonite crystals in the calcified microbial mat (Fig. 24G), and those preserved in fossil crusts (Fig. 29G) is interpreted. Conversely, the Mg-calcite mesocrystals with triple face junctions (< 10 µm) in the calcified microbial mat (Fig. 24I) are inferred to form partly embedded in EPS through oriented attachment of subhedral to anhedral Mg-rich nanoparticles (Fig. 24H) (De Yoreo *et al.,* 2015; Jones, 2017a), although it remains unclear whether the latter correspond to Mg-rich ACC or nanocrystals of Mg-calcite. Tentatively, EPS-chemoselectivity of Ca^{+2} and Sr^{+2} against Mg^{+2} in freshwater systems (Rogerson *et al.,* 2008) could explain the formation of chemical microgradients leading to the compartmentalized formation of aragonite and Mg-calcite.

Modern microbialites in Mexican subsaline lakes (<3 g/L) display a mineralogical progression where ACC transform into monohydrocalcite before converting through dissolution-precipitation process into Mg-calcite and/or aragonite depending on the Mg/Ca molar ratio of the lake water (Zeyen *et al.,* 2021). These transitions occur within certain thresholds: both Mg-calcite and aragonite form when 3<Mg/Ca<10, while Mg-calcite dominates at ratios <3. The mineral assemblage in the calcified microbial mats (Mg-calcite and aragonite) aligns well with Lago Sarmiento's Mg/Ca ratios (1.6-7.1, avg. 3.4; Campos *et al.,* 1994a). However, the potential role of monohydrocalcite in the system remains uncertain as it appears only as a trace component in one fossil sample and is absent in the studied mat. This warrants further investigation of submerged build-ups considering this phase has been suggested to play a pivotal role in microbialite formation (Caumartin *et al.,* 2023).

5.5.2.2 Constructive stage

The induration of the microbial mats was followed by neomorphism (Folk, 1965) and cementation under favorable conditions for Mg-calcite precipitation. This stage includes the inversion of aragonite to Mg-calcite, as suggested by the relict

textural relationships within some shrubs, with Mg-rich fascicular-optic crystals forming at the expense of Sr-rich, aragonite-like fibrous crystals (Fig. 25H-I). This interpretation is consistent with the relatively abundant occurrence of aragonite in the calcified microbial mat (25%) and its near absence in the fossil tufa deposits. Mineralogical stabilization, *i.e.,* transformation into a thermodynamically more stable mineral phase, is likely the driving force behind the aragonite inversion. As a consequence, this suggests that in the long-term the lake waters have prevailed mostly with Mg/Ca >2 (Müller *et al.,* 1972), similar as in modern times (Campos *et al.,* 1994). The aragonite inversion was accompanied by grain-size coarsening (aggradation) of the Mg-calcite, resulting in the formation of polygonal spar composing the shrubs (Fig 25B) and likely the dirty spar preserving relicts of calcified filaments (Fig. 27A-B-J). This likely result due Ostwald ripening processes, which promotes the growth of larger crystals at the expense of smaller, thermodynamically less stable crystals (Armenteros, 2010).

Neomorphic transformations were accompanied by early cementation, forming spar fringes around cyanobacterial filaments (Fig. 27C) and lining shrubs (Fig. 25B-F). Competitive growth between microstromatolite accretion and isopachous cements demonstrates a deposition-diagenesis continuum. Some micrite/microspar fringes show ambiguous origins: their non-isopachous distribution and relict structures suggest microbial mediation (Fig. 27G), while featureless examples may represent early cements (Fig. 27H). The framework also contains rhythmically layered micrite/spar (Fig. 26B-G) with either regular (Fig. 25K) or disrupted (Fig. 28B) textures, including protrusions (Fig. 25F) and wrinkled laminations (Fig. 28B). These patterns likely reflect cyclic controls on alternating abiotic (spar) and microbially-mediated (micrite) precipitation during this stage.

5.5.2.3 Destructive stage

As the lake declined, the tufa deposits successively reached the zone above the wave base until they became exposed to the wave-breaking zone, promoting diagenesis under progressively greater flow energy and turbulence. This initially led to crystal size reduction (degrading recrystallization) of the Mg-calcite spar, as suggested by the textural relationships observed in shrubs showing internal spar that grades to zones of mixed micrite/microspar (Fig. 25B-C-G-M, 27F and 28B) and

massive micrite (Fig. 27K and 28C). Notably, although some clotted micrite is likely primary (Fig. 25B and 28D), either formed due to encrustation of coccoid cyanobacteria or calcification of heterogeneous EPSs/organo-matrixes (Riding, 2000; Shiraishi *et al.,* 2017; Willmer and Rasser, 2022), in most cases it is a diagenetic product forming at expenses of sparitic shrubs (Fig. 25K-N, 27G-K and 28A).

Diagenetic micrite (pseudomicrite; Flügel, 2010) formation in vadose (sparmicritization; Kahle, 1977) and shallow-marine settings (Reid *et al.,* 1992) can result by the activity of endolithic organisms, degradation of organic matrices (Kahle, 1977; Reid and Macintyre, 1998), or concomitant dissolution-precipitation due the circulation of fluids with variable carbonate saturation though the pore system (Kahle, 1977). Biotic processes did contribute to the micritization in Lago Sarmiento but are inferred play secondary roles compared to the hydrodynamic effects. This interpretation is supported by theoretical and experimental data showing that at greater flow velocity and turbulence the mass transfer kinetics at the solid-liquid interface in porous media is increased, thus enhancing carbonate dissolution and precipitation rates (Buhmann and Dreybrodt, 1985; Dreybrodt and Buhmann, 1991; Liu and Dreybrodt, 1997), and is consistent with greater micritization in shallow-marine sub-environments of higher energy (Reid and Macintyre, 1998).

Wave-breaking zone exposure of the deposits leads to the erosion and abrasion of the tufa framework as evidenced by reworked intraclast observed at outcrop (Fig. 21D) and thin section (Fig. 28E-H) scales. This results in pore enlargement and formation of vugs and intercrystalline secondary pores which were subsequently filled by internal sediments (Fig. 26). The microtextural relationships between erosion/dissolution surfaces and internal sedimentation (Fig. 28E to G) are similar to those described in ancient thrombolites (Bosence and Gallois, 2022), while the peloids infilling the primary (Fig. 11I) and secondary pores (Fig. 11A-F) resemble the “internal micrite” described as pores infill in marine limestones from high-energy settings (Reid *et al.,* 1990). These features could serve as diagnostic indicators of high-energy lacustrine environments, characteristic of wind-exposed, large lakes like Lago Sarmiento where long fetch amplifies wave action.

Subsequent subaerial exposure to relatively high amplitude daily thermal oscillations generated *in situ* micro-brecciated textures compose of unrotated clast (Fig. 26G-H) (Armenteros, 2010) without significant meteoric cementation, consistent with the cold semi-arid climate in the area.

5.5.3 Interpretation of stable isotopes

5.5.3.1 Controls on $\delta^{13}C$-DIC composition

Limnological data reveal stable physicochemical conditions (pH, temperature, DO, ion concentrations) up to 100 m-depth in Lago Sarmiento (Campos *et al.,* 1994a), suggesting absence of seasonal stratification as in Lago Toro (Fig. 18C) and other deep lakes in Patagonia (Campos *et al.,* 1994b and references therein). This suggests minimal lake turnover effects on euphotic zone DIC/nutrient dynamics where calcification occurs. While sinking organic matter ($\delta^{13}C$: -30 to -25‰; Villa-Martínez and Moreno, 2007; Roberts *et al.,* 2022) could explain $\delta^{13}C$-DIC values in local open lakes (-3 to -1‰) or closed lakes of the TdPB (-4‰; Moy *et al.,* 2008), it cannot account for Lago Sarmiento's positive values (ca. 1.5‰; Fig. 22B).

Conversely, the DIC of Lago Sarmiento, predominantly composed of bicarbonate (avg. pH of 8.6), exhibit $\delta^{13}C$ values consistent with those expected for DIC near isotopic equilibrium with atmospheric CO_2 (Leng and Marshall, 2004; Zhang *et al.,* 1995). This is evaluated by calculating the theoretical $\delta^{13}C_{HCO3}$ in equilibrium with atmospheric CO_2 (modern $\delta^{13}C_{CO2}$ = -8.4; Graven *et al.,* 2017), using the isotope fractionation factor proposed by Mook *et al.* (1974):

$$1000\ln\alpha(HCO_{3(l)}^{-} - CO_{2(g)}) = 9.522 \times (1000/T) - 24.1,$$

where T is expressed in K. Considering field temperature (10°C), the theoretical $\delta^{13}C$-DIC (1.1‰) is slightly lower than measured (1.6‰) (Fig. 31A), likely reflecting turbulence-driven $^{12}CO_2$ degassing effects on DIC pool. This indicates near-equilibrium between lake DIC and atmospheric CO_2. It is inferred that rapid and persistent winds in Patagonia and relatively large surface area of Lago Sarmiento (Bade *et al.,* 2004) promote the efficient lake-atmosphere gas exchange at present, as well as during Holocene. This is supported by ubiquitous calcified *Rivularia* in the fossil deposits, which suggest long-term nutrient limitation (Mateo *et al.,* 2015; Whitton and Mateo, 2012) and thus low impact of respiration on $\delta^{13}C$-DIC.

FIGURE 31 – PALEOTEMPERATURE ESTIMATES

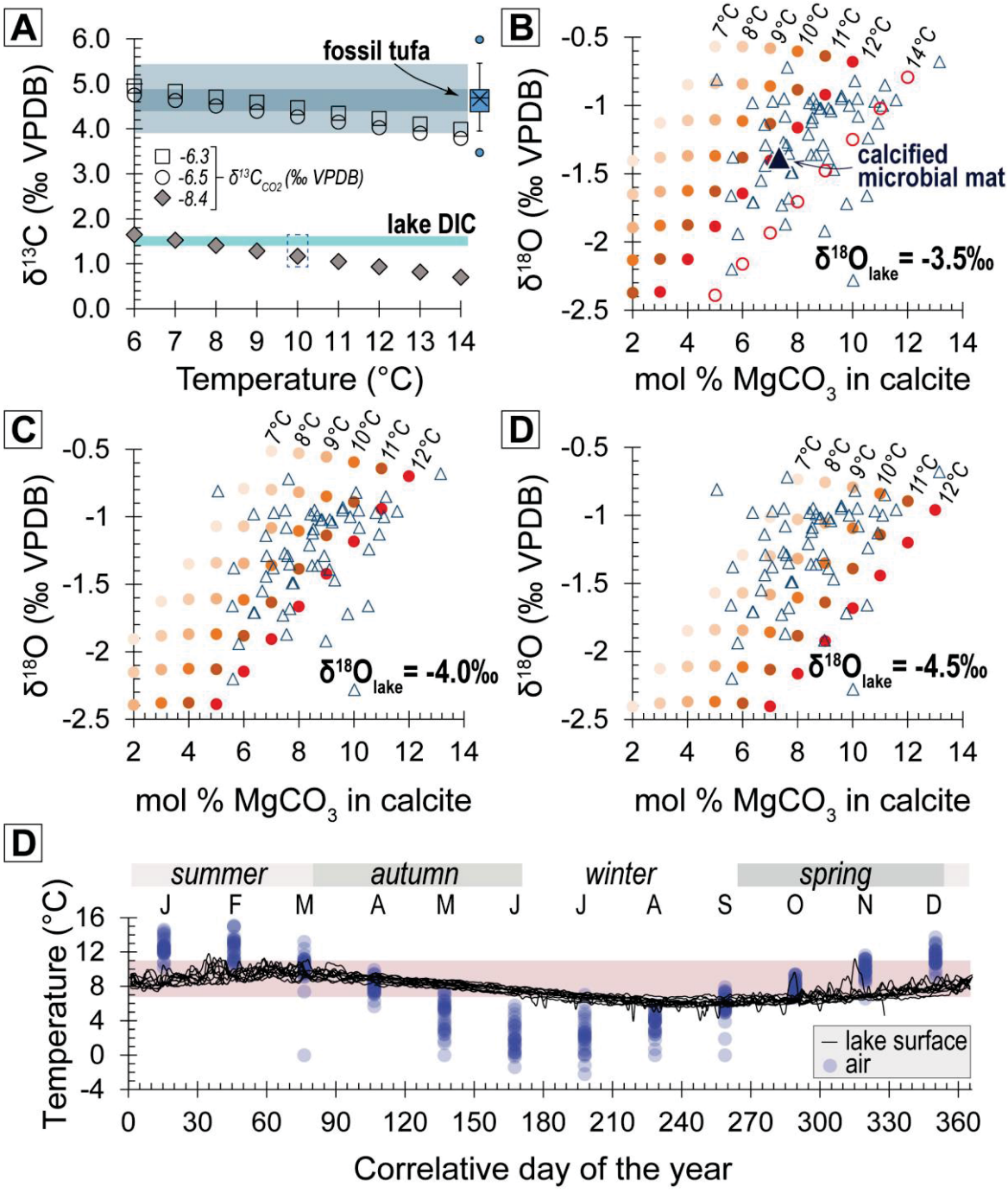

SOURCE: This work

LEGEND: A) Theoretical estimates of the $\delta^{13}C$ of dissolved bicarbonate in isotopic equilibrium with modern atmospheric CO_2 (grey diamonds), and the $\delta^{13}C$ of calcite in isotopic equilibrium with middle to late Holocene atmospheric CO_2 (open circles and squares). The range of $\delta^{13}C$-DIC and $\delta^{13}C$ of the fossil tufa is indicated. Details on the calculations in the text. B) to D) Theoretical estimates of the $\delta^{18}O$ of Mg-calcite calculated for a fixed lake water oxygen isotope composition ($\delta^{18}O_{lake}$) and variable temperatures and Mg contents (circles). The theoretical values are compared with those of the fossil tufa data (open triangles). The microbial mat is only plotted for water composition as the modern ($\delta^{18}O_{lake}$ = -3.5 ‰). Details on the calculations in the text. D) Variation of the average monthly air temperature between 1985 and 2015 (circles) and average daily lake surface temperature between 2010 and 2021 (black lines). Data was obtained from stations 12284009-3 (Lago Sarmiento) and

12286001-9 (Torres del Paine) from the Dirección General de Aguas (General Water Directorate) website (https://dga.mop.gob.cl/).

5.5.3.2 Diagenetic overprint?

No large variation in $\delta^{13}C$-$\delta^{18}O$ exist between the diagenetically modified and the more pristine deposits, i.e., between the tufa build-ups and the tufa crusts, respectively (Fig. 30A). The trend of increasing $\delta^{18}O$ in the top of the TP3 site profile (level T3d) likely show evaporative effects as supported by its positive covariance with $\delta^{13}C$ (R^2=0.77; Fig. 30C) (Talbot, 1990). Such $\delta^{18}O$ variation is similar to that in the entire dataset (ca. 1 ‰) (Fig. 30A-C), suggesting narrow temperature and lake $\delta^{18}O$ variations between deposition and diagenesis (e.g., Rainey and Jones, 2007) instead of significant isotopic homogenization (cf., De Boever *et al.,* 2017).

5.5.3.3 Paleotemperature estimates

Theoretical estimates of $\delta^{13}C$ for calcite in isotopic equilibrium with pre-industrial atmospheric CO_2 ($\delta^{13}C_{CO2}$ between ca. -6.5 to -6.3‰ for the middle and late Holocene) (Elsig *et al.,* 2009) were calculated using the isotopic fractionation factor proposed by Romanek *et al.* (1992):

$$1000\ln\alpha(\text{calcite - } CO_{2(g)}) = 11.98 - 0.12 \times T,$$

where T is expressed in °C. Compositions as those exhibited by the fossil tufa ($\delta^{13}C$ mostly between 4.0 and 4.9 ‰) are reproduced at 7-12°C (Fig. 31A). $\delta^{13}C$ values above 4.9‰ are associated to more positive $\delta^{18}O$ compositions (Fig. 30A-C), suggesting evaporative ^{13}C-enrichment (Horton *et al.,* 2016) and/or $^{12}CO_2$ degassing. Conversely, higher $\delta^{13}C$ of the calcified microbial mat (5.6‰; Fig. 30A) likely reflects photosynthetic uptake of isotopically light bicarbonate (Merz, 1992) in the small pond where calcification occurs.

For oxygen isotopes, depending on the magnesium content, the $\delta^{18}O$ of Mg-calcite deviates towards more positive values compared to pure calcite (Jiménez-López *et al.,* 2004; Tarutani *et al.,* 1969). The incorporation of Mg in calcite can depends on the Mg/Ca ratio of the fluids and/or the precipitation rates (De Choudens-Sánchez and Gonzalez, 2009; Mucci and Morse, 1983) but appears to be independent of temperature in freshwater microbially-influenced carbonates (Rogerson *et al.,* 2008; Saunders *et al.,* 2014). This allows the use of the isotopic

fractionation factor between Mg-calcite (6 to 32 mol % $MgCO_3$) and water proposed by Mavromatis *et al.,* (2012):

$$1000\ \ln\alpha_{Mg\text{-}calcite–H2O} = 18030/T - 32.42 + (6 \times 10^8/T^3 - 5.47 \times 10^6/T^2 + 16780/T - 17.21) \times C_{Mg},$$

where T refers to the temperature in Kelvin and C_{Mg} to the mol % $MgCO_3$. Although this parametrization is based on experiments conducted at higher temperatures (Mavromatis *et al.,* 2012), its strong correlation and the lack of available calibration for lower temperatures justify its use.

For the modern water composition ($\delta^{18}O_{lake}$ of 3.5‰) the $\delta^{18}O$ value of the calcified microbial mat (-1.4 ‰) is reproduced at *ca.* 12°C, while >12°C are needed to match most of the fossil tufa deposits (Fig. 31B). However, during fossil tufa deposition the lake-levels were higher and thus the $\delta^{18}O_{lake}$ more negative than at present. Under this assumption, theoretical estimates between 9 and 12 °C and 7 and 10 °C are obtained for $\delta^{18}O_{lake}$ of -4 ‰ and -4.5 ‰, respectively (Fig. 31C-D).

Daily surface water temperatures in Lago Sarmiento (2010–2021) averaged 6–11°C (Fig. 31E). This is a reasonable range for past warm/dry periods, like the currently prevailing (Moreno *et al.,* 2014), while lower temperatures are expected during cold/wet phases. The good agreement between these temperatures and the theoretical estimates calculated independently from $\delta^{13}C$ and $\delta^{18}O$ (7–12°C) (Fig. 31A-C-D) supports previous interpretations regarding (paleo-)lake dynamics while confirming carbonate precipitation under relatively cold conditions as earlier suggested (Solari *et al.,* 2010).

5.5.4 Paleoenvironmental significance: a record of lacustrine stability amid climate fluctuations

The extensive tufa deposition in Lago Sarmiento suggests protracted favorable intrinsic and extrinsic conditions for microbially-mediated precipitation. In such setting, the degree of vertical and lateral development of the deposits within each studied site is likely influenced by accommodation space (Pollier *et al.,* 2024) and lake-level stability, while variations among different sites reflect local controls (*e.g.,* sediment input, substrate type and topography) (Airo, 2010). Under these assumptions, it is interpreted that build-ups in the upper terraces (T3d, T4c, T5c-d and T7c; Fig. 20B-D-F and 21B-G) formed during prolonged highstand conditions,

allowing development of taller, closely spaced to amalgamated, tufa edifices in the sublittoral zone. Such phase is estimated to have lasted >2300 ± 420 yr considering a 3.7 m-tall build-up (Fig. 21G) and *Rivularia* calcification rates of 1.60 ± 0.29 mm/yr (Pentecost and Talling, 1987), while onset of deposition should have started >3.5 ka if the minimum age of the uppermost tufa level is considered (*ca.* 1.2 ka; Solari *et al.,* 2010). Conversely, lower-relief build-ups located below reflect shallower deposition and less stable lake-levels, with concave tops marking subaerial exposure (e.g., on terrace T5a; Fig. 21E) (Della Porta, 2015). The crust (Fig. 20A) are interpreted as eulittoral-supralittoral deposits younger than 1.2 ka, formed during high but fluctuating lake-levels that prevented thicker accumulations (Eymard *et al.,* 2019; Vennin *et al.,* 2019).

The tufa's non-laminated mesostructure limits their use as high-resolution paleoclimatic proxies, though $\delta^{13}C$-$\delta^{18}O$ clustering between the upper terrace and those below may express lake's sensitivity to the influence of cold/wet vs. warm/dry periods (Fig. 32A). Cold/wet phases produced more positive $\delta^{13}C$-DIC values through greater bicarbonate-CO_2 fractionation (Mook *et al.,* 1974) and negative $\delta^{18}O_{lake}$ shifts from elevated lake levels, while warm/dry generates the opposite pattern. Upper terraces exhibit lower $MgCO_3$ content, potentially reflecting both diluted Mg/Ca ratios and and/or lower precipitation rates (Saunders *et al.,* 2014) due slower *Rivularia* calcification under colder conditions (Pentecost and Talling, 1987). However, the lake's variable Mg/Ca ratios (1.6-7.1; Campos *et al.,* 1994b) suggest additional controls, making the Mg-calcite formation particularly intriguing since it is more common in microbial lakes with either greater salinities (>19 g/L; Chagas *et al.,* 2016) or floored by mafic bedrock (Zeyen *et al.,* 2021) - neither of which characterize Lago Sarmiento's environment, deserving further investigation.

Although cold/wet-warm/dry oscillations significatively affected local ecosystems (e.g., glacier and vegetation cover; Moreno *et al.,* 2018), and speleothem isotopes (Fig. 32B) (Nehme *et al.,* 2023), Lago Sarmiento's muted $\delta^{13}C$-$\delta^{18}O$ variability (Fig. 32A-B) suggest greater climatic resilience. In comparison, the microbialites in Laguna Amarga, a smaller endorheic lake (< 0.006 km^3) (Fig. 18C), exhibit larger spread and positive isotopic covariance (Fig. 32B) (Solari *et al.,* 2010), reflecting heightened sensitivity to hydroclimatic shifts. It is inferred that due size-effects Lago Sarmiento's buffer environmental variability. Its relatively large volume (ca. 9 km^3) regulates $\delta^{18}O_{lake}$ via stabilizing evaporation/inflow ratios (cf. Solari *et al.,*

2010), while its thermal inertia attenuates air temperature fluctuations throughout the year (Fig. 31E), which maintains consistent bicarbonate-CO_2 isotopic fractionation and thus minimal δ^{13}C-DIC variations (Mook *et al.,* 1974). As result, the isotopic identity of Lago Sarmiento resembles that of open lakes rather than endorheic systems with long residence times (Benson *et al.,* 1996; Leng and Marshall, 2004; Talbot, 1990).

FIGURE 32 – STABLE ISOTOPES AND CLIMATE SHIFTS

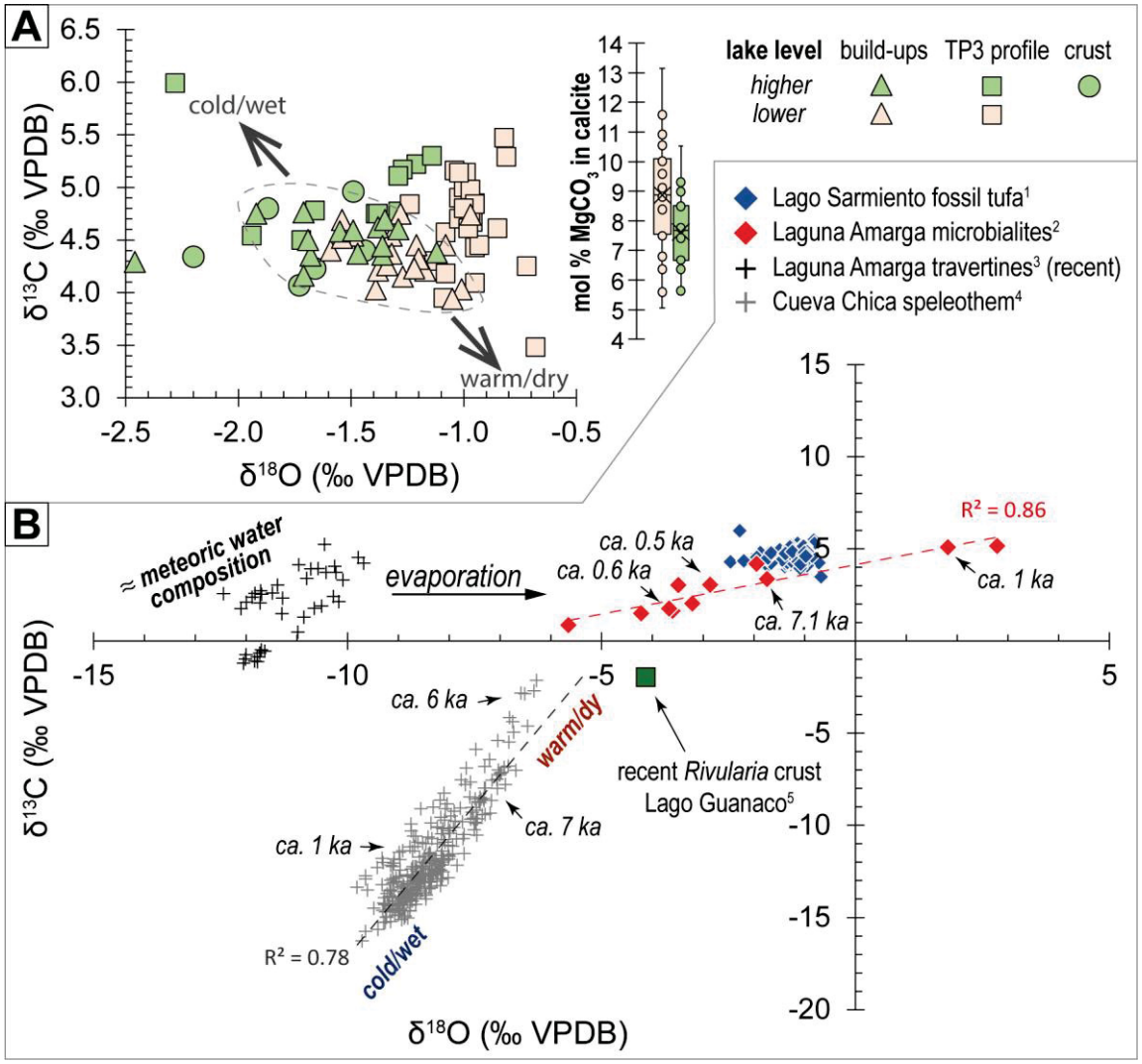

SOURCE: This work

LEGEND: A) Carbon and oxygen isotope composition and mol % $MgCO_3$ content of fossil tufa from Lago Sarmiento. The deposits in the higher terraces (in green) correspond to those in T3d, T4c, T5c, T5d and the two samples at the top of the V-shaped build-up in site TP7 (Fig. 4G). The gray segmented line highlights the composition of most bulk-rock analysis. B) Comparison between the carbon and oxygen isotope composition of Lago Sarmiento[1] (this work), and local carbonate deposits ([2]Solari *et al.,* 2010; [3]Quezada *et al.,* 2024; [4]Nehme *et al.,* 2024; [5]Moy *et al.,* 2008). Note the evaporative ^{18}O-enrichment of Lago Sarmiento compared to the isotope composition of the travertines and speleothem.

Three inferences are derived from Lago Sarmiento's record: (1) Mg-calcite composition might not be a reliable paleo-salinity proxy in non-marine settings, (2) without proxies of meteoric water's paleo-compositions (*e.g.,* spring-related carbonates; Fig. 32B), or other methodological approaches (*e.g.,* clumped isotopes; Horton *et al.,* 2016), ancient systems comparable to Lago Sarmiento could be erroneously interpreted as through-flow lakes, and (3) the lake's buffering of Holocene climate variability likely contributed maintaining suitable conditions for *Rivulariaceae*-rich mats colonization and carbonate precipitation, promoting exceptional tufa formation.

5.6 CONCLUSION

This work provided an integrative perspective on the formation of one of the largest occurrence of Holocene-to-Present freshwater microbial carbonates in the Southern Hemisphere. Our results confirm previous studies regarding the role of cyanobacteria, particularly Rivulariaceae, as the main framework builders (Airo, 2010), while revealing a complex progression of processes shaping the final mineralogy and microstructure of the deposits. This includes: (1) the early induration of photosynthetic microbial substrates through non-classical crystallization pathway, with formation of Sr- and Mg-rich nanoparticles precursors to aragonite and Mg-calcite, respectively; (2) a constructive stage of diagenesis involving aragonite inversion to Mg-calcite, crystal size coarsening, and Mg-calcite cementation; and (3) a later stage of destructive diagenesis leading to micritization, dissolution/erosion of the framework, and internal sedimentation within pores. The constructive stage is nearly syn-depositional and allowed the stabilization of the organosedimentary structures while preserving the microbial textures. Conversely, the destructive stage occurred under higher-energy conditions as the lake-level demise and the deposits faced the wave-breaking zone, leading to the partial-to-total destruction of the microbial textures within the framework.

The calcified rivulariaceans and narrow range of carbon and oxygen stable isotope composition of fossil tufa thrombolite suggests deposition under oligotrophic, relatively cold (≤12°C) and stable conditions throughout Holocene cold/wet to warm/dry climate transitions. In this context extensive tufa deposition resulted from synergic contributions of organomineralization processes (s.l.), promoting carbonate

nucleation within microbial mats, and thermodynamic/hydrodynamic conditions favoring heterogeneous precipitation. Paradoxically, Lago Sarmiento's agitated waters acted as a relevant constructive and destructive force, stimulating lithification and the growth of metric-sized build-ups while leading to the destruction of microbial structures. Nevertheless, the diagenetic microtextural relationships in thrombolites remain diagnostic for identifying ancient high-energy lacustrine settings, which are underrepresented in the geologic record.

6 FINAL CONSIDERATIONS

This doctoral research provided an integrative analysis on the formation of travertines and lacustrine tufa in the Torres del Paine area (Chilean Patagonia – 51°S) offering new insights into the deposition of cold-temperature terrestrial carbonates formed in wind-stressed environments. A synthesis of the main topics addressed in this work are summarized.

6.1 CARBONATE PRECIPITATION

Among the key drivers on carbonate precipitation in the studied systems are physicochemical factors, hydrodynamics effects stimulated by the strong and persistent westerly winds in the area, and biological mediation. However, the preponderance of these varies depending on the sedimentary (sub)environment.

Based on water physiochemistry, both systems exhibit at least periodically favorable thermodynamic conditions for carbonate precipitation ($SI_{calcite}$ >0) although achieved through different processes; water/rock interaction in subsurface is a main control on dissolved ion concentration in the travertine's spring waters emerging at the vent, while evaporative enrichment stands as a significant process for Lago Sarmiento.

The along-stream variations of physiochemical parameters and carbon stable isotope composition of the spring waters are the typical of evasive travertines, indicating that CO_2 outgassing is a key process leading to precipitation. This phenomenon can be passive, due to the above atmospheric CO_2 concentrations in the spring water, as well as enhanced by wind-driven water turbulence. Biotic mediation, on the other hand, is restricted to zones of lower flow energy and mostly involves plants, microbes and EPS serving as substrate for precipitation.

In the case of the lacustrine tufa accretion in Lago Sarmiento the biotic mediation is fundamental. Cyanobacteria, particularly those of family Rivulariaceae, are recognized as the main framework builders of the deposits. Their calcification involves EPS-influenced nucleation of ACC-like particles though diffusion-driven processes within communal EPS secreted by the microbial consortia and/or sheath impregnation, likely reflecting photosynthetically induce precipitation. Following nucleation, it is inferred that favorable thermodynamic and kinetic conditions in the

long-term allowed stabilization and growth of the build-ups, including carbonate supersaturation levels above threshold for heterogeneous precipitation in freshwater systems ($SI_{calcite}$ > 0.48) and wind-driven water agitation and CO_2 degassing.

6.2 THE RECORD OF ENVIRONMENTAL INFLUENCES ACROSS DEPOSITIONAL SYSTEMS

The sedimentological variations along the longitudinal profile of the travertines are similar among both studied sites. There is a greater preponderance of biotic mediation in the deposition of spherulitic carbonates in the sluggish waters at the ponds of the proximal zones, while abiotic precipitation dominates in the flowing waters at the intermediate/distal zone, where crystalline dendrites form under the influence of wind-driven water turbulence. This marked segmentation is also evident in the carbon and oxygen stable isotope composition of both travertines, characterized by higher values in the proximal zone compared to those in the intermediate/distal zones. Such an unusual compositional trend for evasive travertines is interpreted to reflect (1) diachronic precipitation between the proximal and intermediate/distal zones, involving (2) slow CO_2 degassing and photosynthetic uptake of CO_2 during precipitation of the spherulitic carbonates in the vents, and (3) the kinetic effects on oxygen isotope fractionation due to higher precipitation rates and/or disequilibrium between DIC and water during precipitation of the crystalline dendrites downstream. These relationships underscore the relevance of fluid hydrodynamics modulating the sedimentology and isotope composition in low-temperature spring-related carbonate systems.

In Lago Sarmiento, climate-induced variations in the evaporation-to-inflow ratio between cold/wet and warm/dry periods modulates lake's transgressive and regressive phases, respectively. Despite local environmental factors influence the development of the deposits from site to site, at basin scales, the degree of vertical and lateral development of the tufa build-ups is modulated by the accommodation space and lake-level stability. In this sense, the taller and closely spaced to amalgamated build-ups composing the uppermost tufa terrace formed during a relatively long period of lake highstand, while the smaller build-ups at lower altitudes reflect deposition at shallower depths during periods of lower lake-levels. The sparse tufa crust, on the other hand, formed during high but highly unstable lake levels.

The narrow variation in carbon and oxygen stable isotope composition among the deposits formed during lake-levels maxima and those located below is consistent with precipitation under relatively cold (≤12°C) and stable lake conditions despite contrasting cold/wet and warm/dry climatic conditions, respectively. This results due intrinsic and extrinsic factors; the relatively large volume of Lago Sarmiento helps regulate the water oxygen isotope composition via stabilizing evaporation/inflow ratios (Solari *et al.,* 2010), while the persistent westerly winds and relatively large surface area of Lago Sarmiento promotes efficient lake-atmosphere exchange, thus the lake's DIC is buffered by the carbon isotope composition of atmospheric CO_2.

6.3 . ENDOGENIC INFLUENCE IN TRAVERTINE DEPOSITION

Despite both travertines exhibit carbon isotope signatures in the typical range of endogenic travertines (>-1‰) it remains unclear whether there is influence of deep processes on their deposition. Similar sources and a relatively shallow infiltration depth (<500 m) of the meteoric waters are inferred from the oxygen and Sr isotope composition of the travertines. Besides, their small size points to low precipitation rates, which is an uncommon feature of endogenic travertines. Regarding their context, there is a large paucity of thermal springs in Torres del Paine as well as hundreds of kilometers around.

Although this will need further investigation, it is hypothesized that the studied deposits are epigenic in origin and that their relatively high carbon isotope composition is the result of carbonate dissolution at shallow depth involving sulfuric acid derived from pyrite oxidation, similar as observed in groundwaters of catchments floored by black mudstones and shales. Besides, CO_2 outgassing or its uptake by photosynthetic organisms in the vents may also contribute to generating the endogenic-like carbon isotope as documented in this work, while the influence of Previous Calcite Precipitation during the subsurface migration of the fluids can also play a role, although it is complex to address this variable.

6.4 IMPLICATIONS FOR THE ROCK RECORD

Notably, despite similar sedimentological features and common fluid sources, the carbon isotope composition of the travertines in Laguna Amarga exhibit a marked difference in their range of carbon isotope composition, with higher values on the sun-exposed (north-facing) travertine compared to the sun-shaded (south-facing) travertine. This is proposed to reflect the microclimatic zonation resulting from contrasting solar irradiance between both margins, a common phenomenon in mid-latitude mountainous regions with semi-arid climates known as slope aspect. Based on these findings, it is suggested that equatorward-facing and poleward-facing spring-related carbonates might serve as proxies to track biomass fluctuations at (sub-)basin scales in mid-latitude semiarid ecosystems, which are highly susceptible to hydroclimate oscillations.

The tufa thrombolites at Lago Sarmiento, on the other hand, provide insights into the recognition of microbial carbonate deposited under high-energy conditions in the rock record. Their shoreline-parallel distributions are typical of littoral reef-like microbial deposits, while the relatively big size of individual build-ups evidence positive feedback between lithification and fluid energy regime, resembling marine examples formed under high-energy environments. The diagnostic features are the microscale textural relationships associated with early diagenetic processes, including framework micritization, dissolution/erosion features, and internal sedimentation by intraclasts and other authigenic and terrigenous grains.

REFERENCES

AIRO, A. **Biotic and abiotic controls on the morphological and textural development of modern microbialites at Lago Sarmiento, Chile**. 2010. Dissertation (Ph. D in Geology) - Geological and Environmental Sciences Department, Stanford, 2010.

AITKEN, J. D. Classification and environmental significance of cryptalgal limestones and dolomites, with illustrations from the Cambrian and Ordovician of southwestern Alberta. **Journal of Sedimentary Petrology**, v. 37, n. 4, p. 1163–1178, 1967.

AITKEN, J. D.; NARBONNE, G. M. Two occurrences of Precambrian thrombolites from the Mackenzie Mountains, northwestern Canada. **Palaios**, v. 4, n. 4, p. 384–388, 1989.

ALMONACID, L.; PESSACG, N.; DIAZ, B. G.; BONFILI, O.; PERI, P. L. Nueva base de datos reticulada de precipitación para la Provincia de Santa Cruz, Argentina. **Revista Meteorológica**, v. 46, n. 2, p. 26–53, 2021.

ALONSO-ZARZA, A. M.; WRIGHT, V. P. Palustrine carbonates. **Developments in Sedimentology**, v. 61, p. 103–131, 2010.

ALTENBERGER, U.; OBERHÄNSLI, R.; PUTLITZ, B.; WEMMER, K. Tectonic controls and Cenozoic magmatism at the Torres del Paine, Southern Andes (Chile, 51°10′S). **Revista Geológica de Chile**, v. 30, n. 1, p. 65–81, 2003.

AMINOT, A.; KÉROUEL, R. **Hydrologie des écosystèmes marins: paramètres et analyses**. [s.l.] Editions Quae, 2004.

ANDREWS, J. E. Palaeoclimatic records from stable isotopes in riverine tufas: synthesis and review. **Earth-Science Reviews**, v. 75, n. 1–4, p. 85–104, 2006.

ANSELMETTI, F. S.; ARIZTEGUI, D.; DE BATIST, M.; CATALINA GEBHARDT, A.; HABERZETTL, T.; NIESSEN, F.; OHLENDORF, C.; ZOLITSCHKA, B. Environmental history of Southern Patagonia unravelled by the seismic stratigraphy of Laguna Potrok Aike. **Sedimentology**, v. 56, n. 4, p. 873–892, 2009.

ARENAS-ABAD, C.; VÁZQUEZ-URBEZ, M.; PARDO-TIRAPU, G.; SANCHO-MARCÉN, C. Fluvial and associated carbonate deposits. **Developments in Sedimentology**, v. 61, p. 133–175, 2010.

ARMENTEROS, I. Diagenesis of Carbonates in Continental Settings. **Developments in Sedimentology**, v. 62, p. 61–151, 2010.

ARP, G.; THIEL, V.; REIMER, A.; MICHAELIS, W.; REITNER, J. Biofilm Exopolymers control microbialite formation at thermal springs discharging into the alkaline Pyramid Lake , Nevada , USA. **Geomicrobiology Journal** v. 126, p. 159–176, 1999.

ARP, G.; REIMER, A.; REITNER, J. Photosynthesis-induced biofilm calcification and calcium concentrations in Phanerozoic oceans. **Science**, v. 292, n. 5522, p. 1701–

1704, 2001.

ARP, G.; BISSETT, A.; BRINKMANN, N.; COUSIN, S.; DE BEER, D.; FRIEDL, T.; MOHR, K. I.; NEU, T. R.; REIMER, A.; SHIRAISHI, F.; STACKEBRANDT, E.; ZIPPEL, B. Tufa-forming biofilms of German karstwater streams: microorganisms, exopolymers, hydrochemistry and calcification. **Geological Society Special Publication**, v. 336, n. August 2014, p. 83–118, 2010.

ARP, G.; HELMS, G.; KARLINSKA, K.; SCHUMANN, G.; REIMER, A.; REITNER, J.; TRICHET, J. Photosynthesis versus exopolymer degradation in the formation of microbialites on the atoll of Kiritimati, Republic of Kiribati, Central Pacific. **Geomicrobiology Journal**, v. 29, n. 1, p. 29–65, 2012.

ARVIDSON, R. S.; MACKENZIE, F. T. The dolomite problem: control of precipitation kinetics by temperature and saturation state. **American Journal of Science**, v. 299, n. 4, p. 257–288, 1999.

ASTA, M. P.; AUQUÉ, L. F.; SANZ, F. J.; GIMENO, M. J.; ACERO, P.; BLASCO, M.; GARCÍA-ALIX, A.; GÓMEZ, J.; DELGADO-HUERTAS, A.; MANDADO, J. Travertines associated with the Alhama-Jaraba thermal waters (NE, Spain): Genesis and geochemistry. **Sedimentary Geology**, v. 347, p. 100–116, 2017. Available at: <http://dx.doi.org/10.1016/j.sedgeo.2016.11.010>.

BADE, D. L.; CARPENTER, S. R.; COLE, J. J.; HANSON, P. C.; HESSLEIN, R. H. Controls of δ13C-DIC in lakes: geochemistry, lake metabolism, and morphometry. **Limnology and Oceanography**, v. 49, n. 4, p. 1160–1172, 2004.

BECK, W. C.; GROSSMAN, E. L.; MORSE, J. W. Experimental studies of oxygen isotope fractionation in the carbonic acid system at 15°, 25°, and 40°C. **Geochimica et Cosmochimica Acta**, v. 69, n. 14, p. 3493–3503, 2005.

BENSON, L.; WHITE, L. D.; RYE, R. Carbonate deposition, Pyramid Lake subbasin, Nevada: 4. Comparison of the stable isotope values of carbonate deposits (tufas) and the Lahontan lake-level Record. **Palaeogeography, Palaeoclimatology, Palaeoecology**, v. 122, n. 1–4, p. 45–76, 1996.

BERGER, A.; LOUTRE, M. F. Insolation values for the climate of the last 10 million years. **Quaternary Science Reviews**, v. 10, n. 4, p. 297–317, 1991.

BERNHARDT, A.; JOBE, Z. R.; GROVE, M.; LOWE, D. R. Palaeogeography and diachronous infill of an ancient deep-marine foreland basin, Upper Cretaceous Cerro Toro Formation, Magallanes Basin. **Basin Research**, v. 24, n. 3, p. 269–294, 2012.

BERNHARDT, A.; JOBE, Z. R.; LOWE, D. R. Stratigraphic evolution of a submarine channel e lobe complex system in a narrow fairway within the Magallanes Foreland Basin, Cerro Toro. **Marine and Petroleum Geology**, v. 28, n. 3, p. 785–806, 2011. Available at: <http://dx.doi.org/10.1016/j.marpetgeo.2010.05.013>.

BERRENDERO, E.; PERONA, E.; MATEO, P. Genetic and morphological characterization of Rivularia and Calothrix (Nostocales, Cyanobacteria) from running water. **International Journal of Systematic and Evolutionary Microbiology**, v. 58, n. 2, p. 447–460, 2008.

BERTINI, A.; MINISSALE, A.; RICCI, M. Use of quaternary travertines of central-southern Italy as archives of paleoclimate, paleohydrology and neotectonics. **Alpine and Mediterranean Quaternary**, v. 21, n. 1, p. 99–112, 2008.

BISSETT, A.; DE BEER, D.; SCHOON, R.; SHIRAISHI, F.; REIMER, A.; ARP, G. Microbial mediation of stromatolite formation in karst-water creeks. **Limnology and Oceanography**, v. 53, n. 3, p. 1159–1168, 2008a.

BISSETT, A.; REIMER, A.; DE BEER, D.; SHIRAISHI, F.; ARP, G. Metabolic microenvironmental control by photosynthetic biofilms under changing macroenvironmental temperature and Ph conditions. **Applied and Environmental Microbiology**, v. 74, n. 20, p. 6306–6312, 2008b.

BOSENCE, D.; GALLOIS, A. How do thrombolites form? Multiphase construction of lacustrine microbialites, Purbeck Limestone Group, (Jurassic), Dorset, UK. **Sedimentology**, v. 69, n. 2, p. 914–953, 2022.

BRASIER, A. T. Searching for travertines, calcretes and speleothems in deep time: processes, appearances, predictions and the impact of plants. **Earth-Science Reviews**, v. 104, n. 4, p. 213–239, 2011.

BRASIER, A.; WACEY, D.; ROGERSON, M.; GUAGLIARDO, P.; SAUNDERS, M.; KELLNER, S.; MERCEDES-MARTIN, R.; PRIOR, T.; TAYLOR, C.; MATTHEWS, A.; REIJMER, J. A Microbial role in the construction of Mono Lake carbonate chimneys? **Geobiology**, v. 16, n. 5, p. 540–555, 2018.

BROUGHTON, P. L. Microbial EPS-mediated amorphous calcium carbonate–monohydrocalcite–calcite transformations during early tufa deposition. **Depositional Record**, v. 9, n. 3, p. 647–674, 2023.

BUHMANN, D.; DREYBRODT, W. The kinetics of calcite dissolution and precipitation in geologically relevant situations of karst areas. 2. Closed system. **Chemical Geology**, v. 53, n. 1–2, p. 109–124, 1985.

BURNE, R. V.; MOORE, L. S. Microbialites: Organosedimentary deposits of benthic microbial communities. **Palaios**, v. 2, n. 3, p. 241–254, 1987.

CALDERÓN, M.; HERVÉ, F.; MASSONNE, H. J.; TASSINARI, C. G.; PANKHURST, R. J.; GODOY, E.; THEYE, T. Petrogenesis of the Puerto Edén Igneous and Metamorphic Complex, Magallanes, Chile: Late Jurassic syn-deformational anatexis of metapelites and granitoid magma genesis. **Lithos**, v. 93, n. 1–2, p. 17–38, 2007.

CALLAHAN, B. J.; MCMURDIE, P. J.; ROSEN, M. J.; HAN, A. W.; JOHNSON, A. J. A.; HOLMES, S. P. DADA2: High-resolution sample inference from illumina amplicon data. **Nature Methods**, v. 13, n. 7, p. 581–583, 2016.

CAMPOS, H.; SOTO, D.; STEFFEN, W.; PARRA, O.; AGUERO, G.; ZUÑIGA, L. Limnological studies of Lake Sarmiento (Chile): A subsaline lake from Chilean Patagonian. **Archives of Hydrobiology**, v. 1–2, p. 217–234, 1994a.

CAMPOS, H.; SOTO, D.; STEFFEN, W.; AGUERO, A.; PARRA, O.; ZUÑIGA, L. Limnological studies of Lake Del Toro (Chile): Morphometry, physics, chemistry, and

plankton. **Archiv für Hydrobiologie Supplement**, v. 99, p. 199–215, 1994b.

CANTLON, J. E. Vegetation and microclimates on north and south slopes of Cushetunk Mountain , New Jersey. **Ecological Monographs**, v. 23, n. 3, p. 241–270, 1953.

CAPEZZUOLI, E.; GANDIN, A.; PEDLEY, M. Decoding tufa and travertine (fresh water carbonates) in the sedimentary record: The state of the art. **Sedimentology**, v. 61, n. 1, p. 1–21, 2014.

CAPORASO, J. G.; KUCZYNSKI, J.; STOMBAUGH, J.; BITTINGER, K.; BUSHMAN, F. D.; COSTELLO, E. K.; FIERER, N.; PEÑA, A. G.; GOODRICH, J. K.; GORDON, J. I.; HUTTLEY, G. A.; KELLEY, S. T.; KNIGHTS, D.; KOENIG, J. E.; LEY, R. E.; LOZUPONE, C. A.; MCDONALD, D.; MUEGGE, B. D.; PIRRUNG, M.; REEDER, J.; SEVINSKY, J. R.; TURNBAUGH, P. J.; WALTERS, W. A.; WIDMANN, J.; YATSUNENKO, T.; ZANEVELD, J.; KNIGHT, R. Correspondence QIIME allows analysis of high- throughput community sequencing data intensity normalization improves color calling in SOLiD Sequencing. **Nature Publishing Group**, v. 7, n. 5, p. 335–336, 2010. Available at: <http://dx.doi.org/10.1038/nmeth0510-335>.

CAPORASO, J. G.; LAUBER, C. L.; WALTERS, W. A.; BERG-LYONS, D.; HUNTLEY, J.; FIERER, N.; OWENS, S. M.; BETLEY, J.; FRASER, L.; BAUER, M.; GORMLEY, N.; GILBERT, J. A.; SMITH, G.; KNIGHT, R. Ultra-high-throughput microbial community analysis on the Illumina HiSeq and MiSeq Platforms. **ISME Journal**, v. 6, n. 8, p. 1621–1624, 2012.

CASAMATTA, D. A.; HAŠLER, P. Blue-green algae (Cyanobacteria) in rivers. *In*: NECCHI JR, O. **River Algae**. [s.l.] Springer, Cham, 2016. p. 5–34.

CAUDWELL, C.; LANG, J.; PASCAL, A. lamination of swampy-rivulets Rivularia Haematites stromatolites in a temperature climate. **Sedimentary Geology**, v. 143, n. 1–2, p. 125–147, 2001.

CAUMARTIN, J.; BENZERARA, K.; HAVAS, R.; THOMAZO, C.; DUPRAT, E. The chemical conditions necessary for the formation of microbialites**.** ***Geochemical Perspectives Letters***, v. 25, p. 30-35, 2023.

CERLING, T. E.; QUADE, J. Stable carbon and oxygen isotopes in soil carbonates. **Geophysical Monograph Series**, v. 78, p. 217–231, 1993.

CHACÓN-BACA, E.; ROMERO DE LA CRUZ, O.; CHAVEZ-CABELLO, G.; CIENFUEGOS ALVARADO, E.; MORALES-PUENTE, P.; ALBA-ALDAVE, L.; BLANCO LANZA, S. The generation of a clotted peloidal micrite fabric by endolithic cyanobacteria in recent thrombolites from Cuatro Cienegas, Northern Mexico. **Sedimentology**, v. 71, n. 7, p. 2290–2313, 2024.

CHADHA, D. K. A Proposed new diagram for geochemical classification of natural waters and interpretation of chemical data. **Hydrogeology Journal**, v. 7, n. 5, p. 431–439, 1999.

CHAFETZ, H.; RUSH, P. F.; UTECH, N. M. Microenvironmental controls on mineralogy and habit of CaCO3 precipitates: An example from an active travertine

system. **Sedimentology**, v. 38, n. 1, p. 107–126, 1991.

CHAFETZ, H. S.; LAWRENCE, J. R. Stable isotopic variability within modern travertines. **Géographie physique et Quaternaire**, v. 48, n. 3, p. 257–273, 1994.

CHAFETZ, H. S.; GUIDRY, S. A. Bacterial shrubs, crystal shrubs, and ray-crystal shrubs: Bacterial vs. abiotic precipitation. **Sedimentary Geology**, v. 126, n. 1–4, p. 57–74, 1999.

CHAGAS, A. A. P.; WEBB, G. E.; BURNE, R. V.; SOUTHAM, G. Modern lacustrine microbialites: towards a synthesis of aqueous and carbonate geochemistry and mineralogy. **Earth-Science Reviews**, v. 162, p. 338–363, 2016.

CHEN, J.; ZHANG, D. D.; WANG, S.; XIAO, T.; HUANG, R. Factors controlling tufa deposition in natural waters at waterfall sites. **Sedimentary Geology**, v. 166, n. 3–4, p. 353–366, 2004.

CLAES, H.; SOETE, J.; VAN NOTEN, K.; EL DESOUKY, H.; ERTHAL, M. M.; VANHAECKE, F.; ÖZKUL, M.; SWENNEN, R. Sedimentology, three-dimensional geobody reconstruction and carbon dioxide origin of Pleistocene travertine deposits in the Ballık Area (South-West Turkey). **Sedimentology**, v. 62, n. 5, p. 1408–1445, 2015.

COHEN, A. S.; THOUIN, C. Nearshore carbonate deposits in Lake Tanganyika. **Geology,** v. 15, n. 5, p. 414–418, 1987.

COLETTA, P.; PENTECOST, A.; SPIRO, B. Stable isotopes in charophyte incrustations: relationships with climate and water chemistry. **Paleoceanography and Paleoclimatology**, v. 173, n. 1–2, p. 9–19, 2001.

CONRAD, O.; BECHTEL, B.; BOCK, M.; DIETRICH, H.; FISCHER, E.; GERLITZ, L.; WEHBERG, J.; WICHMANN, V.; BÖHNER, J. System for automated geoscientific analyses (SAGA) v. 2.1.4. **Geoscientific Model Development**, v. 8, n. 7, p. 1991–2007, 2015.

COPLEN, T. B. Calibration of the calcite-water oxygen-isotope geothermometer at Devils Hole, Nevada, a natural laboratory. **Geochimica et Cosmochimica Acta**, v. 71, n. 16, p. 3948–3957, 2007.

CROSSEY, L. J.; FISCHER, T. P.; PATCHETT, P. J.; KARLSTROM, K. E.; HILTON, D. R.; NEWELL, D. L.; HUNTOON, P.; REYNOLDS, A. C.; DE LEEUW, G. A. M. Dissected hydrologic system at the Grand Canyon: Interaction between deeply derived fluids and plateau aquifer waters in modern springs and travertine. **Geology**, v. 34, n. 1, p. 25–28, 2006.

DANSGAARD, W. Stable Isotopes in precipitation. **Tellus A: Dynamic Meteorology and Oceanography**, v. 16, n. 4, p. 436–468, 1964.

DAVIES, B. J.; DARVILL, C. M.; LOVELL, H.; BENDLE, J. M.; DOWDESWELL, J. A.; FABEL, D.; GARCÍA, J. L.; GEIGER, A.; GLASSER, N. F.; GHEORGHIU, D. M.; HARRISON, S.; HEIN, A. S.; KAPLAN, M. R.; MARTIN, J. R. V.; MENDELOVA, M.; PALMER, A.; PELTO, M.; RODÉS, Á.; SAGREDO, E. A.; SMEDLEY, R. K.;

SMELLIE, J. L.; THORNDYCRAFT, V. R. The evolution of the Patagonian Ice Sheet from 35 ka to the present day (PATICE)**. Earth-Science Reviews**, v. 204, p. 103152, 2020.

DE BOEVER, E.; BRASIER, A. T.; FOUBERT, A.; KELE, S. What do we really know about early diagenesis of non-marine carbonates?. **Sedimentary Geology**, v. 361, p. 25–51, 2017.

DE CHOUDENS-SÁNCHEZ, V.; GONZALEZ, L. A. Calcite and aragonite precipitation under controlled instantaneous supersaturation: Elucidating the role of CACO3 saturation state and Mg/Ca ratio on calcium carbonate polymorphism. **Journal of Sedimentary Research**, v. 79, n. 6, p. 363–376, 2009.

DE LOS RÍOS, P.; SOTO, D. Estudios limnológicos en lagos y lagunas del Parque Nacional Torres Del Paine (51° S, Chile). **Anales del Instituto de la Patagonia**, v. 37, n. 1, p. 63–71, 2009.

DE YOREO, J. J.; GILBERT, P. U. P. A.; SOMMERDIJK, N. A. J. M.; PENN, R. L.; WHITELAM, S.; JOESTER, D.; ZHANG, H.; RIMER, J. D.; NAVROTSKY, A.; BANFIELD, J. F.; WALLACE, A. F.; MICHEL, F. M.; MELDRUM, F. C.; CÖLFEN, H.; DOVE, P. M. Crystallization by particle attachment in synthetic, biogenic, and geologic environments. **Science**, v. 349, n. 6247, 2015.

DECHO, A. W. Overview of biopolymer-induced mineralization: What goes on in biofilms? **Ecological Engineering**, v. 36, n. 2, p. 137–144, 2010. Available at: <http://dx.doi.org/10.1016/j.ecoleng.2009.01.003>.

DELLA PORTA, G. Carbonate build-ups in lacustrine, hydrothermal and fluvial settings: Comparing Depositional geometry, fabric types and geochemical signature. **Geological Society Special Publication**, v. 418, n. 1, p. 17–68, 2015.

DELLA PORTA, G.; HOPPERT, M.; HALLMANN, C.; SCHNEIDER, D.; REITNER, J. The influence of microbial mats on travertine precipitation in active hydrothermal systems (Central Italy). **Depositional Record**, v. 8, n. 1, p. 165–209, 2022.

DEMOTT, L. M.; SCHOLZ, C. A.; JUNIUM, C. K. 8200-year growth history of a Lahontan-age lacustrine tufa deposit. **Sedimentology**, v. 66, n. 6, p. 2169–2190, 2019.

DEMOTT, L. M.; SCHOLZ, C. A.; AWALEH, M. O. Lacustrine carbonate towers of Lake Abhe, Djibouti: Interplay of hydrologic and microbial processes. **Sedimentary Geology**, v. 424, 2021.

DIETZEL, M.; TANG, J.; LEIS, A.; KÖHLER, S. J. Oxygen Isotopic fractionation during inorganic calcite precipitation - effects of temperature, precipitation rate and pH. **Chemical Geology**, v. 268, n. 1–2, p. 107–115, 2009.

DREYBRODT, W.; BUHMANN, D. A mass transfer model for dissolution and precipitation of calcite from solutions in turbulent motion. **Chemical Geology**, v. 90, n. 1–2, p. 107–122, 1991.

DUPRAZ, C.; REID, R. P.; BRAISSANT, O.; DECHO, A. W.; NORMAN, R. S.;

VISSCHER, P. T. Processes of carbonate precipitation in modern microbial mats. **Earth-Science Reviews**, v. 96, n. 3, p. 141–162, 2009.

ELSIG, J.; SCHMITT, J.; LEUENBERGER, D.; SCHNEIDER, R.; EYER, M.; LEUENBERGER, M.; JOOS, F.; FISCHER, H.; STOCKER, T. F. Stable isotope constraints on Holocene carbon cycle changes from an antarctic ice core. **Nature**, v. 461, n. 7263, p. 507–510, 2009.

ERTHAL, M. M.; CAPEZZUOLI, E.; MANCINI, A.; CLAES, H.; SOETE, J.; SWENNEN, R. Shrub morpho-types as indicator for the water flow energy - Tivoli Travertine case (Central Italy). **Sedimentary Geology**, v. 347, p. 79–99, 2017.

EYMARD, I.; BILMES, A.; ALVAREZ, M. del P.; FEO, R.; HUNGER, G.; VASCONCELOS, C.; ARIZTEGUÍ, D. Growth morphologies and plausible stressors ruling the formation of Late Pleistocene lacustrine carbonate buildups in the Maquinchao Basin (Argentina). **The Depositional Record**, v. 5, n. 3, p. 498–514, 2019.

EYMARD, I.; ALVAREZ, M. D. P.; BILMES, A.; VASCONCELOS, C.; ARIZTEGUI, D. Tracking organomineralization processes from living microbial mats to fossil microbialites. **Minerals**, v. 10, n. 7, p. 1–20, 2020.

EYMARD, I.; DEL PILAR ÁLVAREZ, M.; BILMES, A.; VASCONCELOS, C.; THOMAS, C.; ARIZTEGUI, D. Evolving controls on mineralization in Patagonian microbial mats as inferred by water chemistry, microscopy and DNA signatures. **Latin American Journal of Sedimentology and Basin Analysis**, v. 28, n. 2, p. 133–151, 2021.

FARÍAS, M. E.; VILLAFAÑE, P. G.; LENCINA, A. I. Integral prospection of Andean microbial ecosystem project. *In*: FARÍAS, M. E. (Ed.). **Microbial Ecosystems in Central Andes Extreme Environments: Biofilms, Microbial Mats, Microbialites and Endoevaporites**. Springer, Cham, 2020. p. 245–260.

FILDANI, A.; HESSLER, A. M. Stratigraphic record across a retroarc basin inversion: Rocas Verdes-Magallanes Basin, Patagonian Andes, Chile. **Bulletin of the Geological Society of America**, v. 117, n. 11–12, p. 1596–1614, 2005.

FISHER, A. G. Fossils ,early life , and atmospheric history. **Proceedings of the National Academy of Sciences of the United States of America**, v. 53, n. 6, p. 1205–1213, 1965.

FLECK, R. J.; MERCER, J. H.; NAIRN, A.; PETERSON, D. Chronology of Late Pliocene and Early Pleistocene G. **Earth and Planetary Science Letters**, v. 16, p. 15–22, 1972.

FLÜGEL, E. **Microfacies of carbonate rocks: analysis, interpretation and application**. 2. ed. Berlin: Springer, 2010. v. 976

FOLK, R. L. Petrologie of Sedimentary Rocks. **Hemphll Publishing Company, Austin, Texas**, p. 78703, 1965.

FOLK, R. L. Interaction between bacteria, nannobacteria, and mineral precipitation in

hot springs of Central Italy. **Geographie physique et Quaternaire**, v. 48, n. 3, p. 233–246, 1994.

FORD, T. D.; PEDLEY, H. M. A review of tufa and travertine deposits of the world. **Earth-Science Reviews**, v. 41, n. 3–4, p. 117–175, 1996.

FOSDICK, J. C.; ROMANS, B. W.; FILDANI, A.; BERNHARDT, A.; CALDERÓN, M.; GRAHAM, A.; FOSDICK, J. C.; ROMANS, B. W.; FILDANI, A.; BERNHARDT, A.; CALDERÓN, M.; GRAHAM, S. A. Kinematic evolution of the Patagonian retroarc fold-and-thrust belt and Magallanes foreland basin , Chile and Argentina, 51°30′S. **Geological Society of America Bulletin**, v. 123, n. 9–10, p. 1679–1698, 2011.

FOUKE, B. W.; FARMER, J. D.; DES MARAIS, D. J.; PRATT, L.; STURCHIO, N. C.; BURNS, P. C.; DISCIPULO, M. K. Depositional facies and aqueous-solid geochemistry of travertine-depositing hot springs (Angel Terrace, Mammoth Hot Springs, Yellowstone National Park, U.S.A.). **Journal of Sedimentary Research**, v. 70, n. 3, p. 565–585, 2000.

FOUKE, B. W. Hot-spring systems geobiology: Abiotic and biotic influences on travertine formation at Mammoth Hot Springs, Yellowstone National Park, USA. **Sedimentology**, v. 58, n. 1, p. 170–219, 2011.

FREYTET, P.; VERRECCHIA, E. Freshwater organisms that build stromatolites: A synopsis of biocrystallization by Prokaryotic and Eukaryotic algae. **Sedimentology**, v. 45, n. 3, p. 535–563, 1998.

GAILLARDET, J.; DUPRÉ, B.; ALLÈGRE, C. J.; NÉGREL, P. Chemical and physical denudation in the Amazon River Basin. **Chemical Geology**, v. 142, n. 3–4, p. 141–173, 1997.

GANDIN, A.; CAPEZZUOLI, E. Travertine versus calcareous tufa: Distinctive petrologic features and stable isotopes signatures. **Alpine and Mediterranean Quaternary**, v. 21, n. 1, p. 125–136, 2008.

GANDIN, A.; CAPEZZUOLI, E. Travertine: Distinctive Depositional fabrics of carbonates from thermal spring systems. **Sedimentology**, v. 61, n. 1, p. 264–290, 2014.

GARCÍA, J. L.; KAPLAN, M. R.; HALL, B. L.; SCHAEFER, J. M.; VEGA, R. M.; SCHWARTZ, R.; FINKEL, R. Glacier expansion in Southern Patagonia throughout the Antarctic Cold Reversal. **Geology**, p. 859–863, 2012.

GARCÍA, J.; HALL, B. L.; KAPLAN, M. R.; VEGA, R. M.; STRELIN, J. A. Geomorphology glacial geomorphology of the Torres Del Paine Region (Southern Patagonia): Implications for glaciation , deglaciation and paleolake history. **Geomorphology**, v. 204, p. 599–616, 2014. Available at: <http://dx.doi.org/10.1016/j.geomorph.2013.08.036>.

GARCÍA, J.; HALL, B. L.; KAPLAN, M. R.; GABRIEL, A. G.; POL-HOLZ, R. De; GARCÍA, V. J.; SCHAEFER, J. M.; SCHWARTZ, R. 14C and 10Be dated Late Holocene fluctuations of Patagonian glaciers in Torres Del Paine (Chile, 51°S) and connections to Antarctic climate change. **Quaternary Science Reviews**, v. 246, p.

106541, 2020.

GARREAUD, R.; LOPEZ, P.; MINVIELLE, M.; ROJAS, M. Large-scale control on the Patagonian climate. **Journal of Climate**, v. 26, n. 1, p. 215–230, 2013.

GE, Y.; DELLA PORTA, G.; PEDERSON, C. L.; LOKIER, S. W.; HOFFMANN, R.; IMMENHAUSER, A. Botryoidal and spherulitic aragonite in carbonates associated with microbial mats: Precipitation or diagenetic replacement product? **Frontiers in Earth Science**, v. 9, n. June, p. 1–22, 2021.

GEROY, I. J.; GRIBB, M. M.; MARSHALL, H. P.; CHANDLER, D. G.; BENNER, S. G.; MCNAMARA, J. P. Aspect influences on soil water retention and storage. **Hydrological Processes**, v. 25, n. 25, p. 3836–3842, 2011.

GHIGLIONE, M. C.; LIKERMAN, J.; BARBERÓN, V.; BEATRIZ GIAMBIAGI, L.; AGUIRRE-URRETA, B.; SUAREZ, F. Geodynamic context for the deposition of coarse-grained deep-water axial channel systems in the Patagonian Andes. **Basin Research**, v. 26, n. 6, p. 726–745, 2014.

GIVEN, R. K.; WILKINSON, B. H. Kinetic control of morphology, composition, and mineralogy of abiotic sedimentary carbonates. **Journal of Sedimentary Research**, v. 55, n. 1, p. 109–119, 1985.

GOLUBIC, S.; CAMPBELL, S. E. Biogenically formed aragonite concretions in marine Rivularia. *In*: **Phanerozoic Stromatolites: Case Histories**. Berlin, Heidelberg: Springer Berlin Heidelberg, 1981. p. 209–229.

GÓMEZ-FONTEALBA, C.; FLORES-AQUEVEQUE, V.; ALFARO, S. C. Variability of the Southwestern Patagonia (51°S) winds in the recent (1980–2020) period: Implications for past wind reconstructions. **Atmosphere**, v. 13, n. 2, p. 1–17, 2022.

GONZALES, J.; AYDIN, A. Structural characterization of deep-water deposits in a foreland basin, Silla Syncline (Chilean Patagonia), with applications to depositional processes. **Journal of Structural Geology**, v. 30, n. 9, p. 1095–1108, 2008a.

GONZALES, J.; AYDIN, A. The origin of oriented lakes in the Andean foreland, Parque Nacional Torres Del Paine (Chilean Patagonia). **Geomorphology**, v. 97, n. 3–4, p. 502–515, 2008b.

GRADZIŃSKI, M. Factors controlling growth of modern tufa: Results of a field experiment. **Geological Society Special Publication**, v. 336, p. 143–191, 2010.

GRAHAM, L. E.; KNACK, J. J.; PIOTROWSKI, M. J.; WILCOX, L. W.; COOK, M. E.; WELLMAN, C. H.; TAYLOR, W.; LEWIS, L. A.; ARANCIBIA-AVILA, P. Lacustrine Nostoc (Nostocales) and associated microbiome generate a new type of modern clotted microbialite. **Journal of Phycology**, v. 50, n. 2, p. 280–291, 2014.

GRAVEN, H.; ALLISON, C. E.; ETHERIDGE, D. M.; HAMMER, S.; KEELING, R. F.; LEVIN, I.; MEIJER, H. A. J.; RUBINO, M.; TANS, P. P.; TRUDINGER, C. M.; VAUGHN, B. H.; WHITE, J. W. C. Compiled records of carbon isotopes in atmospheric CO2 for historical simulations in CMIP6. **Geoscientific Model Development**, v. 10, n. 12, p. 4405–4417, 2017.

GUO, L.; RIDING, R. Aragonite laminae in hot water travertine crusts, Rapolano Terme, Italy. **Sedimentology**, v. 39, n. 6, p. 1067–1079, 1992.

GUO, L.; ANDREWS, J.; RIDING, R.; DENNIS, P.; DRESSER, Q. Possible microbial effects on stable carbon isotopes in hot-spring travertines. **Journal of Sedimentary Research**, v. 66, p. 468–473, 1996.

GUO, L.; RIDING, R. Hot-spring travertine facies and sequences, Late Pleistocene, Rapolano Terme, Italy. **Sedimentology**, v. 45, n. 1, p. 163–180, 1998.

GUO, X.; CHAFETZ, H. S. Large tufa mounds, Searles Lake, California. **Sedimentology**, v. 59, n. 5, p. 1509–1535, 2012.

HÄGELE, D.; LEINFELDER, R.; GRAU, J.; BURMEISTER, E. G.; STRUCK, U. Oncoids from the River Alz (Southern Germany): Tiny ecosystems in a phosphorus-limited environment. **Palaeogeography, Palaeoclimatology, Palaeoecology**, v. 237, n. 2–4, p. 378–395, 2006.

HARRISON, L. N.; HURWITZ, S.; PACES, J. B.; WHITLOCK, C.; PEEK, S.; LICCIARDI, J. Travertine records climate-induced transformations of the Yellowstone Hydrothermal System from the Late Pleistocene to the present. **Geological Society of America Bulletin**, n. X, p. 1–14, 2024.

HASHIMOTO, S.; KOMATSU, H. Relationships between soil CO2 concentration and CO2 production, temperature, water content, and gas diffusivity: Implications for field studies through sensitivity analyses. **Journal of Forest Research**, v. 11, n. 1, p. 41–50, 2006.

HENRÍQUEZ, C.; CALDERÓN, M.; CURY, L. F.; ATHAYDE, G.; CARVAJAL, S.; OYARZÚN, P.; BAHNIUK, A. The role of physicochemical and biochemical processes on carbonate precipitation within the Laguna Timone Maar in the Pali Aike Volcanic Field, southernmost extra-Andean Patagonia. **Sedimentary Geology**, v. 439, p. 106216, 2022.

HOLLAND, P. G.; STEYN, D. G. Vegetational responses to latitudinal variations in slope angle and aspect. **Journal of Biogeography**, v. 2, n. 3, p. 179–183, 1975.

HOPPERT, M.; REIMER, A.; SAUTER, K.; REITNER, J. Modern Rivularia freshwater stromatolites as models for formation of laminated stromatolitic crusts. **Geomicrobiology Journal**, v. 40, n. 4, p. 382–398, 2023.

HORTON, T. W.; DEFLIESE, W. F.; TRIPATI, A. K.; OZE, C. Evaporation induced 18O and 13C enrichment in lake systems: A Global perspective on hydrologic balance effects. **Quaternary Science Reviews**, v. 131, p. 365–379, 2016.

JIMÉNEZ-LÓPEZ, C.; ROMANEK, C. S.; HUERTAS, F. J.; OHMOTO, H.; CABALLERO, E. Oxygen isotope fractionation in synthetic magnesian calcite. **Geochimica et Cosmochimica Acta**, v. 68, n. 16, p. 3367–3377, 2004.

JONES, B. Review of calcium carbonate polymorph precipitation in spring systems. **Sedimentary Geology**, v. 353, p. 64–75, 2017a.

JONES, B. Review of aragonite and calcite crystal morphogenesis in thermal spring systems. **Sedimentary Geology**, v. 354, p. 9–23, 2017b.

JONES, B.; RENAUT, R. W. Calcareous spring deposits in continental settings. **Developments in Sedimentology**, v. 61, p. 177–224, 2010.

JONES, B.; RENAUT, R. W.; ROSEN, M. R. Trigonal dendritic calcite crystals forming from hot spring waters at Waikite, North Island, New Zealand. **Journal of Sedimentary Research**, v. 70, n. 3, p. 586–603, 2000.

KAHLE, C. F. Origin of subaerial Holocene calcareous crusts: role of algae, fungi and sparmicritisation. **Sedimentology**, v. 24, n. 3, p. 413–435, 1977.

KANDIANIS, M. T.; FOUKE, B. W.; JOHNSON, R. W.; VEYSEY, J.; INSKEEP, W. P. Microbial Biomass: A catalyst for CaCO3 precipitation in advection-dominated transport regimes. **Bulletin of the Geological Society of America**, v. 120, n. 3–4, p. 442–450, 2008.

KATZ, H. R. Revision of Cretaceous stratigraphy in Patagonian cordillera of Ultima Esperanza, Magallanes Province, Chile. **AAPG Bulletin**, v. 47, n. 3, p. 506–524, 1963.

KAWAGUCHI, T.; DECHO, A. W. A Laboratory investigation of cyanobacterial Extracellular Polymeric Secretions (EPS) in influencing CaCO3 polymorphism. **Journal of Crystal Growth**, v. 240, n. 1–2, p. 230–235, 2002a.

KAWAGUCHI, T.; DECHO, A. W. Isolation and biochemical characterization of Extracellular Polymeric Secretions (EPS) from modern soft marine stromatolites (Bahamas) and its inhibitory effect on CaCO3 precipitation. **Preparative Biochemistry and Biotechnology**, v. 32, n. 1, p. 51–63, 2002b.

KAWANO, M.; OBOKATA, S. Effects of cyanobacteria on precipitation rate and polymorphism of CaCO3 minerals in hot spring water. **Journal of the Clay Science Society of Japan**, v. 46, n. 3, p. 156–128, 2007.

KELE, S.; ÖZKUL, M.; FÓRIZS, I.; GÖKGÖZ, A.; BAYKARA, M. O.; ALÇIÇEK, M. C.; NÉMETH, T. Stable isotope geochemical study of Pamukkale Travertines: New evidences of low-temperature non-equilibrium calcite-water fractionation. **Sedimentary Geology**, v. 238, n. 1–2, p. 191–212, 2011. Avilable at: <http://dx.doi.org/10.1016/j.sedgeo.2011.04.015>.

KELE, S.; BREITENBACH, S.F.M.; CAPEZZUOLI, E.; MECKLER, A.N.; ZIEGLER, M.; MILLAN, I.M.; KLUGE, T.; DE´ AK, J.; HANSELMANN, K.; JOHN, C.M.; YAN, H.; LIU, Z.; BERNASCONI, S.M. Temperature dependence of oxygen- and clumped isotope fractionation in carbonates: a study of travertines and tufas in the 6-95◦C temperature range. **Geochimica et Cosmochimica Acta**, v. 168, p. 172–192, 2015. Available at: https://doi.org/10.1016/j.gca.2015.06.032

KEMPE, S.; KAZMIERCZAK, J. Calcium carbonate supersaturation and the formation of in situ calcified stromatolites. *In*: ITTEKKOT, S. K. V.; MICHAELIS, W.; SPITZY, A. **Facets of Modern Biogeochemistry**. Berlin: Springer, 1990. p. 255–278.

KENNARD, J. M.; JAMES, N. P. Thrombolites and stromatolites: Two distinct types of microbial structures. **Palaios**, v. 1, n. 5, p. 492–503, 1986.

KERSHAW, S.; GUO, L. Pleistocene cyanobacterial mounds in the Perachora Peninsula, Gulf of Corinth, Greece: Structure and applications to interpreting sea-level history and terrace sequences in an unstable tectonic setting. **Palaeogeography, Palaeoclimatology, Palaeoecology**, v. 193, n. 3–4, p. 503–514, 2003.

KRABBENHÖFT, A.; FIETZKE, J.; EISENHAUER, A.; LIEBETRAU, V.; BÖHM, F.; VOLLSTAEDT, H. Determination of Radiogenic and stable strontium isotope ratios (87Sr/86Sr; Δ88/86Sr) by Thermal Ionization Mass Spectrometry Applying an 87Sr/84Sr double spike. **Journal of Analytical Atomic Spectrometry**, v. 24, n. 9, p. 1267–1271, 2009.

KREMER, B.; KAZMIERCZAK, J.; ŁUKOMSKA-KOWALCZYK, M.; KEMPE, S. Calcification and Silicification: Fossilization potential of cyanobacteria from stromatolites of Niuafo'ou's caldera lakes (Tonga) and implications for the early fossil record. **Astrobiology**, v. 12, n. 6, p. 535–548, 2012.

LANDAIS, Amaëlle; STENNI, Barbara. **Water stable isotopes (dD, d18O) from EPICA Dome C ice core (Antarctica) (0-800 ka).** PANGAEA, 2021. Available at: https://doi.org/10.1594/PANGAEA.934094. Access at: 14 jun. 2024.

LENG, M. J.; MARSHALL, J. D. Palaeoclimate interpretation of stable isotope data from lake sediment archives. **Quaternary Science Reviews**, v. 23, n. 7–8, p. 811–831, 2004.

LIU, L.; WU, Y.; HONGXIA, J.; RIDING, R. Calcified rivulariaceans from the Ordovician of the Tarim Basin, northwest China, Phanerozoic lagoonal examples, and possible controlling factors. **Palaeogeography, Palaeoclimatology, Palaeoecology**, v. 448, p. 371–381, 2016. Available at: <http://dx.doi.org/10.1016/j.palaeo.2015.08.034>.

LIU, Z.; DREYBRODT, W. Dissolution kinetics of calcium carbonate minerals in H2O-CO2 solutions in turbulent flow: The role of the diffusion boundary layer and the slow reaction H2O + CO2 → H+ + HCO3−. **Geochimica et Cosmochimica Actamica and**, v. 61, n. 14, p. 2879–2889, 1997.

LIU, Z.; SUN, H.; BAOYING, L.; XIANGLING, L.; WENBING, Y.; CHENG, Z. Wet-Dry Seasonal variations of hydrochemistry and carbonate precipitation rates in a travertine-depositing canal at Baishuitai, Yunnan, SW China: Implications for the formation of biannual laminae in travertine and for climatic reconstruction. **Chemical Geology**, v. 273, n. 3–4, p. 258–266, 2010. Available at: <http://dx.doi.org/10.1016/j.chemgeo.2010.02.027>.

LIU, Z.; SVENSSON, U.; DREYBRODT, W.; DAOXIAN, Y.; BUHMANN, D. Hydrodynamic control of inorganic calcite precipitation in Huanglong Ravine, China: Field measurements and theoretical prediction of deposition rates. **Geochimica et Cosmochimica Acta**, v. 59, n. 15, p. 3087–3097, 1995.

LIU, Z.; ZHANG, M.; LI, Q.; YOU, S. Hydrochemical and isotope characteristics of

spring water and travertine in the Baishuitai Area (SW China) and their meaning for paleoenvironmental reconstruction. **Environmental Geology**, v. 44, n. 6, p. 698–704, 2003.

LUO, L.; CAPEZZUOLI, E.; ROGERSON, M.; VASELLI, O.; WEN, H.; LU, Z. Precipitation of carbonate minerals in travertine-depositing hot springs: Driving forces, microenvironments, and mechanisms. **Sedimentary Geology**, v. 438, 2022.

MANCINI, A.; CORNACCHIA, I.; LAMAL, J.; CAPEZZUOLI, E.; SWENNEN, R.; BRANDANO, M. Using stable isotopes in deciphering climate changes from travertine deposits: The case of the Lapis Tiburtinus succession (Acque Albule Basin, Tivoli, Central Italy). **Frontiers in Earth Science**, v. 12, p. 1355693, 2024.

MANCINI, L. H.; CASAPULA, I.; FERNANDES, D. P.; PEREIRA, A. L.; CURY, L. F.; BAHNIUK, A. M. Implementation of routines for the analysis of the isotopic ratio of C and N in organic matter and for the isotopic ratio of H and O in water. *In*: XII SOUTH AMERICAN SYMPOSIUM ON ISOTOPE GEOLOGY (SSAGI), 2022, Santiago. **Annals** [...]. Santiago, Chile: 2022. p. 39.

MATEO, P.; LEGANÉS, F.; PERONA, E.; LOZA, V.; FERNÁNDEZ-PIÑAS, F. Cyanobacteria as bioindicators and bioreporters of environmental analysis in aquatic ecosystems. **Biodiversity and Conservation**, v. 24, n. 4, p. 909–948, 2015.

MAVROMATIS, V.; SCHMIDT, M.; BOTZ, R.; COMAS-BRU, L.; OELKERS, E. H. Experimental quantification of the effect of mg on calcite-aqueous fluid oxygen isotope fractionation. **Chemical Geology**, v. 310–311, p. 97–105, 2012.

MAYR, C.; LÜCKE, A.; STICHLER, W.; TRIMBORN, P.; ERCOLANO, B.; OLIVA, G.; OHLENDORF, C.; SOTO, J.; FEY, M.; HABERZETTL, T.; JANSSEN, S.; SCHÄBITZ, F.; SCHLESER, G. H.; WILLE, M.; ZOLITSCHKA, B. Precipitation origin and evaporation of lakes in semi-arid Patagonia (Argentina) inferred from stable isotopes (δ18O, δ2H). **Journal of Hydrology**, v. 334, n. 1–2, p. 53–63, 2007.

MAYR, C.; LANGHAMER, L.; WISSEL, H.; MEIER, W.; SAUTER, T.; LAPRIDA, C.; MASSAFERRO, J.; FÖRSTERRA, G.; LÜCKE, A. Atmospheric controls on hydrogen and oxygen isotope composition of meteoric and surface waters in Patagonia [*preprint*]. **Hydrology and Earth System Sciences Discussions**, 15 sept 2023, https://doi.org/10.5194/hess-2018-431.

MCARTHUR, J. M.; HOWARTH, R. J.; SHIELDS, G. A.; ZHOU, Y. **Strontium Isotope Stratigraphy**. *In* Geologic time scale, Elsevier, p. 211–238, 2020.

MERCEDES-MARTÍN, R.; ROGERSON, M.; PRIOR, T. J.; BRASIER, A. T.; REIJMER, J. J. G.; BILLING, I.; MATTHEWS, A.; LOVE, T.; LEPLEY, S.; PEDLEY, M. Towards a morphology diagram for terrestrial carbonates: Evaluating the impact of carbonate supersaturation and alginic acid in calcite precipitate morphology. **Geochimica et Cosmochimica Acta**, v. 306, p. 340–361, 2021.

MERZ-PREISS, M.; RIDING, R. Cyanobacterial tufa calcification in two freshwater streams: Ambient environment, chemical thresholds and biological processes. **Sedimentary Geology**, v. 126, p. 103–124, 1999.

MERZ, M. U. E. The biology of carbonate precipitation by Cyanobacteria. **Facies**, v. 26, n. 1, p. 81–101, 1992.

MEZA DABACENS, F. **Análisis de la variación de caudales río las Chinas — río Serrano. Región de Magallanes y Antártica Chilena**. [s.l: s.n.]. Avilable at: https://bibliotecadigital.ciren.cl/handle/20.500.13082/32734. Accessed in: 23 nov. 2023.

MOESLUND, J. E.; ARGE, L.; BØCHER, P. K.; DALGAARD, T.; SVENNING, J. C. Topography as a driver of local terrestrial vascular plant diversity patterns. **Nordic Journal of Botany**, v. 31, n. 2, p. 129–144, 2013.

MOHAMMADI, Z.; CAPEZZUOLI, E.; CLAES, H.; ALIPOOR, R.; MUCHEZ, P.; SWENNEN, R. Substrate geology controlling different morphology, sedimentology, diagenesis and geochemistry of adjacent travertine bodies: A case study from the Sanandaj-Sirjan zone (western Iran). **Sedimentary Geology**, v. 389, p. 127–146, 2019. Available at: <https://doi.org/10.1016/j.sedgeo.2019.06.005>.

MONNIN, E. **EPICA Dome C high resolution carbon dioxide concentrations**. PANGAEA, 2006. Available at: https://doi.org/10.1594/PANGAEA.472488. Access at: 19 jun. 2024.

MOOK, W. G.; BOMMERSON, J. C.; STAVERMAN, W. H. Carbon isotope fractionation between dissolved bicarbonate and gaseous carbon dioxide. **Earth and Planetary Science Letters**, v. 22, n. 2, p. 169–176, 1974.

MOORE, L. S.; BURNE, R. V. The modern thrombolites of Lake Clifton, western Australia. *In*: BERTRAND-SARFATI, J.; MONTY, C. **Phanerozoic Stromatolites II**. [s.l.] Springer, Dordrecht, 1994. p. 3–29.

MORENO, P. I.; KAPLAN, M. R.; FRANÇOIS, J. P.; VILA-MARTÍNEZ, R.; MOY, C. M.; STERN, C. R.; KUBIK, P. W. Renewed glacial activity during the Antarctic Cold Reversal and persistence of cold conditions until 11.5 Ka in southwestern Patagonia. **Geology**, v. 37, n. 4, p. 375–378, 2009.

MORENO, P. I.; VILANOVA, I.; VILLA-MARTÍNEZ, R.; GARREAUD, R. D.; ROJAS, M.; DE POL-HOLZ, R. Southern Annular Mode-like changes in Southwestern Patagonia at centennial timescales over the last three millennia. **Nature Communications**, v. 5, 2014.

MORENO, P. I.; VILANOVA, I.; VILLA-MARTÍNEZ, R.; DUNBAR, R. B.; MUCCIARONE, D. A.; KAPLAN, M. R.; GARREAUD, R. D.; ROJAS, M.; MOY, C. M.; DE POL-HOLZ, R.; LAMBERT, F. Onset and evolution of Southern Annular Mode-like changes at centennial timescale. **Scientific Reports**, v. 8, n. 1, p. 1–9, 2018.

MORS, R. A.; GOMEZ, F. J.; ASTINI, R. A.; MLEWSKI, E. C.; GÉRARD, E. Physico-chemical and biological controls in a travertine system in the high Andes of northwestern Argentina. **Sedimentary Geology**, v. 439, 2022.

MOY, C. M.; DUNBAR, R. B.; MORENO, P. I.; FRANCOIS, J. P.; VILLA-MARTÍNEZ, R.; MUCCIARONE, D. M.; GUILDERSON, T. P.; GARREAUD, R. D. Isotopic evidence for hydrologic change related to the westerlies in SW Patagonia, Chile,

during the last millennium. **Quaternary Science Reviews**, v. 27, n. 13–14, p. 1335–1349, 2008.

MUCCI, A.; MORSE, J. W. The incorporation of Mg2+ and Sr2+ into calcite overgrowths : Influences of growth rate and solution composition. **Geochimica et Cosmochimica Acta**, v. 47, p. 217–233, 1983.

MÜLLER, G.; IRION, G.; FÖRSTNER, U. Formation and diagenesis of inorganic Ca-Mg carbonates in the lacustrine environment. **Die Naturwissenschaften**, v. 59, n. 4, p. 158–164, 1972.

NAHIDAN, S.; NOURBAKHSH, F.; MOSADDEGHI, M. R. Variation of soil microbial biomass c and hydrolytic enzyme activities in a rangeland ecosystem: are slope aspect and position effective? **Archives of Agronomy and Soil Science**, v. 61, n. 6, p. 797–811, 2015.

NEHME, C.; TODISCO, D.; BREITENBACH, S. F. M.; COUCHOUD, I.; MARCHEGIANO, M.; PERAL, M.; VONHOF, H.; HELLSTROM, J.; TJALLINGI, R.; CLAEYS, P.; BORRERO, L.; MARTIN, F. Holocene hydroclimate variability along the Southern Patagonian Margin (Chile) reconstructed from Cueva Chica speleothems. **Global and Planetary Change**, v. 222, p. 1–20, 2023.

OBST, M.; DYNES, J. J.; LAWRENCE, J. R.; SWERHONE, G. D. W.; BENZERARA, K.; KARUNAKARAN, C.; KAZNATCHEEV, K.; TYLISZCZAK, T.; HITCHCOCK, A. P. Precipitation of amorphous CaCO3 (aragonite-like) by Cyanobacteria : A STXM study of the influence of EPS on the nucleation process. **Geochimica et Cosmochimica Acta**, v. 73, n. 14, p. 4180–4198, 2009. Available at: <http://dx.doi.org/10.1016/j.gca.2009.04.013>.

OKUMURA, T.; TAKASHIMA, C.; KANO, A. Textures and processes of laminated travertines formed by unicellular Cyanobacteria in Myoken hot spring, southwestern Japan. **Island Arc**, v. 22, n. 3, p. 410–426, 2013.

OKUMURA, T.; TAKASHIMA, C.; SHIRAISHI, F.; AKMALUDDIN; KANO, A. Textural transition in an aragonite travertine formed under various flow conditions at Pancuran Pitu, Central Java, Indonesia. **Sedimentary Geology**, v. 265–266, p. 195–209, 2012. Available at: <http://dx.doi.org/10.1016/j.sedgeo.2012.04.010>.

OOMS, M. D.; DINH, C. T.; SARGENT, E. H.; SINTON, D. Photon management for augmented photosynthesis. **Nature Communications**, v. 7, 2016.

OSMAN, J. R.; VIEDMA, P.; MENDOZA, J.; COTORAS, D. Bacterial and geochemical composition of thrombolites from Lake Sarmiento, Torres Del Paine National Park of Chilean Patagonia. **Geomicrobiology Journal**, v. 37, n. 4, p. 376–388, 2020. Available at: <https://doi.org/10.1080/01490451.2019.1709107>.

PACE, A.; BOURILLOT, R.; BOUTON, A.; VENNIN, E.; GALAUP, S.; BUNDELEVA, I.; PATRIER, P.; DUPRAZ, C.; THOMAZO, C.; SANSJOFRE, P.; YOKOYAMA, Y.; FRANCESCHI, M.; ANGUY, Y.; PIGOT, L.; VIRGONE, A.; VISSCHER, P. T. Microbial and diagenetic steps leading to the mineralisation of Great Salt Lake microbialites. **Scientific Reports**, v. 6, n. April, p. 1–12, 2016.

PACTON, M.; HUNGER, G.; MARTINUZZI, V.; CUSMINSKY, G.; BURDIN, B.; BARMETTLER, K.; VASCONCELOS, C.; ARIZTEGUI, D. Organomineralization processes in freshwater stromatolites: A living example from eastern Patagonia. **Depositional Record**, v. 1, n. 2, p. 130–146, 2015.

PANICHI, C.; TONGIORGI, E. Carbon isotopic composition of CO2 from springs, fumaroles, mofettes, and travertines of central and southern Italy: a preliminary prospection method of geothermal area. *In*: PROC. 2ND U. N. SYMPOSIUM ON THE DEVELOPMENT AND USE OF GEOTHERMAL ENERGY, 1976, San Francisco. **Annals** [...]. San Francisco: 1976. p. 815–825.

PARKHURST, D. L.; APPELO, C. a. J. Description of Input and examples for PHREEQC Version 3 — A Computer program for speciation , batch-reaction , one-dimensional transport , and inverse geochemical calculations. U.S. Geological Survey Techniques and Methods, Book 6, Chapter A43, 497 P. **U.S. Geological Survey Techniques and Methods, book 6, chapter A43**, p. 6- 43A, 2013.

PEDLEY, H. M. Classification and environmental models of cool freshwater tufas. **Sedimentary Geology**, v. 68, n. 1–2, p. 143–154, 1990.

PEDLEY, H. M.; ROGERSON, M. In vitro investigations of the impact of different temperature and flow velocity conditions on tufa microfabric. **Geological Society Special Publication**, v. 336, p. 193–210, 2010.

PEDLEY, M. Tufas and travertines of the Mediterranean region: A testing ground for freshwater carbonate concepts and developments. **Sedimentology**, v. 56, n. 1, p. 221–246, 2009.

PEDLEY, M.; ROGERSON, M.; MIDDLETON, R. Freshwater calcite precipitates from in vitro mesocosm flume experiments: A case for biomediation of tufas. **Sedimentology**, v. 56, n. 2, p. 511–527, 2009.

PEDLEY, M. The morphology and function of thrombolitic calcite precipitating biofilms: A universal model derived from freshwater mesocosm experiments. **Sedimentology**, v. 61, n. 1, p. 22–40, 2014.

PENG, X.; JONES, B. Patterns of biomediated CaCO3 crystal bushes in hot spring deposits. **Sedimentary Geology**, v. 294, p. 105–117, 2013.

PENTECOST, A.; TALLING, J. F. Growth and calcification of the freshwater cyanobacterium Rivularia Haematites. **Proceedings of the Royal Society of London. Series B. Biological Sciences**, v. 232, n. 1266, p. 125–136, 1987.

PENTECOST, A. Growth and calcification of Calothrix—dominated oncolites from Northern England. *In*: **Origin, Evolution, and Modern Aspects of Biomineralization in Plants and Animals**. Boston, MA: Springer US, 1989. p. 443–454.

PENTECOST, A.; VILES, H. A Review and reassessment of travertine classification. **Géographie physique et Quaternaire**, v. 48, n. 3, p. 305–314, 1994.

PENTECOST, A. **Travertine**. [s.l.] Springer Berlin Heidelberg, 2005. 445 p.

PENTECOST, A.; COLETTA, P. The role of photosynthesis and CO2 evasion in travertine formation: A quantitative investigation at an important travertine-depositing hot spring, Le Zitelle, Lazio, Italy. **Journal of the Geological Society**, v. 164, n. 4, p. 843–853, 2007.

PENTECOST, A.; FRANKE, U. photosynthesis and calcification of the stromatolitic freshwater cyanobacterium Rivularia. **European Journal of Phycology**, v. 45, n. 4, p. 345–353, 2010.

PERRI, E.; MANZO, E.; TUCKER, M. E. Multi-scale study of the role of the biofilm in the formation of minerals and fabrics in calcareous tufa. **Sedimentary Geology**, v. 263–264, n. July, p. 16–29, 2012.

PETRYSHYN, V. A.; JUNKINS, E. N.; STAMPS, B. W.; BAILEY, J. V.; STEVENSON, B. S.; SPEAR, J. R.; CORSETTI, F. A. Builders, tenants, and squatters: The origins of genetic material in modern stromatolites. **Geobiology**, v. 19, n. 3, p. 261–277, 2021.

PLANAVSKY, N.; GINSBURG, R. N. Taphonomy of modern marine bahamian microbialites. **Palaios**, v. 24, n. 1–2, p. 5–17, 2009.

POLLIER, C. G. L.; GUERRERO, A. N.; RABASSA, J.; ARIZTEGUI, D. The hidden biotic face of microbialite morphogenesis – a case study from Laguna de Los Cisnes, southernmost Patagonia (Chile). **Sedimentology**, v. 71, n. 5, p. 1615–1638, 2024.

PORTMAN, C.; ANDREWS, J. E.; ROWE, P. J.; LEEDER, M. R.; HOOGEWERFF, J. Submarine-spring controlled calcification and growth of large Rivularia bioherms, Late Pleistocene (MIS 5e), Gulf of Corinth, Greece. **Sedimentology**, v. 52, n. 3, p. 441–465, 2005.

PRADO-PÉREZ, A. J.; HUERTAS, A. D.; CRESPO, M. T.; SÁNCHEZ, A. M.; PÉREZ DEL VILLAR, L. Late Pleistocene and Holocene mid-latitude palaeoclimatic and palaeoenvironmental reconstruction: An approach based on the isotopic record from a travertine formation in the Guadix-Baza Basin, Spain. **Geological Magazine**, v. 150, n. 4, p. 602–625, 2013.

QUAST, C.; PRUESSE, E.; YILMAZ, P.; GERKEN, J.; SCHWEER, T.; YARZA, P.; PEPLIES, J.; GLÖCKNER, F. O. The SILVA ribosomal RNA Gene Database Project: Improved data processing and web-based tools. **Nucleic Acids Research**, v. 41, n. D1, p. 590–596, 2013.

QUEZADA, P.; FADEL CURY, L.; CALDERÓN, M.; HENRÍQUEZ, C.; MANCINI, L.; MICHELETTO, J.; BARBOSA ATHAYDE, G.; BAHNIUK RUMBELSPERGER, A. Similar sources but distinct δ13C signatures in adjacent low-temperature travertines from Laguna Amarga (Southern Patagonian Andes). **Sedimentary Geology**, v. 473, p. 106758, 2024.

RAINEY, D. K.; JONES, B. Rapid cold water formation and recrystallization of relict bryophyte tufa at the Fall Creek Cold Springs, Alberta, Canada. **Canadian Journal of Earth Sciences**, v. 44, n. 7, p. 889–909, 2007.

RAINEY, D. K.; JONES, B. Abiotic versus biotic controls on the development of the

Fairmont Hot Springs carbonate deposit, British Columbia, Canada. **Sedimentology**, v. 56, n. 6, p. 1832–1857, 2009.

RAINEY, D. K.; JONES, B. Preferential soft-tissue preservation in the Hot Creek carbonate spring deposit, British Columbia, Canada. **Sedimentary Geology**, v. 227, n. 1–4, p. 20–36, 2010.

RAMÍREZ DE ARELLANO, C.; CALDERÓN, M.; RIVERA, H.; VALENZUELA, M.; FANNING, C. M.; PAREDES, E. Neogene patagonian magmatism between the rupture of the Farallon Plate and the Chile Ridge subduction. **Journal of South American Earth Sciences**, v. 110, n. February, 2021.

REID, R. P.; MACINTYRE, I. G.; JAMES, N. P. Internal precipitation of microcrystalline carbonate: A fundamental problem for sedimentologists. **Sedimentary Geology**, v. 68, n. 3, p. 163–170, 1990.

REID, R. P.; MACINTYRE, I. G.; POST, J. E. Micritized skeletal grains in northern Belize Lagoon: A major source of Mg-calcite mud. **Journal of Sedimentary Petrology**, v. 62, n. 1, p. 145–156, 1992.

REID, R. P.; MACINTYRE, I. G. Carbonate recrystallization in shallow marine environments: A widespread diagenetic process forming micritized grains. **Journal of Sedimentary Research**, v. 68, n. 5, p. 928–946, 1998.

REID, R. P.; SUOSAARI, E. P.; OEHLERT, A. M.; POLLIER, C. G. L.; DUPRAZ, C. Microbialite accretion and growth: Lessons from Shark Bay and the Bahamas. **Annual Review of Marine Science**, v. 16, n. January, p. 487–511, 2024.

RICKETTS, J. W.; MA, L.; WAGLER, A. E.; GARCIA, V. H. Global travertine deposition modulated by oscillations in climate. **Journal of Quaternary Science**, v. 34, n. 7, p. 558–568, 2019.

RIDING, R. Calcified Plectonema (Blue-Green Algae), a recent example of Girvanella from Aldabra Atoll. **Palaeontology**, v. 20, n. 1, p. 33–46, 1977. Available at: <http://www.palass.org/publications/palaeontology-journal/archive/20/1/article_pp33-46>.

RIDING, R.; BRAGA, J. C.; MARTIN, J. M. Oolite stromatolites and thrombolites, Miocene, Spain: Analogues of recent Giant Bahamian Examples. **Sedimentary Geology**, v. 71, n. 3–4, p. 121–127, 1991.

RIDING, R. Microbial Carbonates: The geological record of calcified bacterial–algal mats and biofilms. **Sedimentology**, v. 47, n. 1, p. 179–214, 2000.

RIDING, R. Microbialites, stromatolites, and thrombolites. *In*: REITNER, J.; THIEL, V. **Encyclopedia of Geobiology**. [s.l: s.n.], 2011. p. 635–654.

RIDING, R.; LIANG, L.; LEE, J. H.; VIRGONE, A. Influence of dissolved oxygen on secular patterns of marine microbial carbonate abundance during the Past 490 Myr. **Palaeogeography, Palaeoclimatology, Palaeoecology**, v. 514, p. 135–143, 2019.

ROBERTS, S. J.; MCCULLOCH, R. D.; EMMINGS, J. F.; DAVIES, S. J. Late glacial

and Holocene palaeolake history of the Última Esperanza Region of Southern Patagonia. **Frontiers in Earth Science**, v. 10, p. 813396, 2022.

ROGERSON, M.; PEDLEY, H. M.; WADHAWAN, J. D.; MIDDLETON, R. New insights into biological influence on the geochemistry of freshwater carbonate deposits. **Geochimica et Cosmochimica Acta**, v. 72, n. 20, p. 4976–4987, 2008.

ROGERSON, M.; PEDLEY, H. M.; MIDDLETON, R. Microbial influence on macroenvironment chemical conditions in alkaline (tufa) streams: Perspectives from in vitro experiments. **Geological Society Special Publication**, v. 336, p. 65–81, 2010.

ROGERSON, M.; PEDLEY, H. M.; KELHAM, A.; WADHAWAN, J. D. Linking mineralisation process and sedimentary product in terrestrial carbonates using a solution thermodynamic approach. **Earth Surface Dynamics**, v. 2, n. 1, p. 197–216, 2014.

ROMANEK, C. S.; L., G. E.; W., M. J. Carbon isotopic fractionation in synthetic aragonite and calcite: Effects of temperature and precipitation rate. **Geochimica et Cosmochimica Acta**, v. 56, p. 419–430, 1992.

ROSEN, M. R.; AREHART, G. B.; LICO, M. S. Exceptionally fast growth rate of <100-yr-old tufa, Big Soda Lake, Nevada: Implications for using tufa as a paleoclimate proxy. **Geology**, v. 32, n. 5, p. 409–412, 2004.

ROZANSKI, K.; ARAGUÁS-ARAGUÁS, L.; GONFIANTINI, R. Isotopic patterns in modern global precipitation. *In*: **Climate Change in Continental Isotopic Records**. [s.l: s.n.]p. 1–36, 1993.

SÁNCHEZ-CAÑETE, E. P.; BARRON-GAFFORD, G. A.; CHOROVER, J. A considerable fraction of soil-respired CO2 is not emitted directly to the atmosphere. **Scientific Reports**, v. 8, n. 1, p. 2–11, 2018.

SÁNCHEZ, A.; DE SAINT-BLANQUAT, M.; HERVÉ, F.; POLVÉ, M.; MORATA, D.; DE PARSEVAL, P.; BENOIT, M. Geochemistry of Cenozoic plutonic rocks in the extra-Andean Southern Patagonia as evidence for a magmatic arc migration process. **Andean Geology**, v. 48, n. 3, p. 359–402, 2021.

SÁNCHEZ ZURANO, A.; GÓMEZ SERRANO, C.; ACIÉN-FERNÁNDEZ, F. G.; FERNÁNDEZ-SEVILLA, J. M.; MOLINA-GRIMA, E. Modeling of photosynthesis and respiration rate for microalgae–bacteria consortia. **Biotechnology and Bioengineering**, v. 118, n. 2, p. 952–962, 2021.

SANTANA, A.; OLAVE, C.; BUTOROVIC, N. Estudio climatológico con registros de alta resolución temporal en campamento posesión (Enap): Magallanes, Chile. **Anales del Instituto de la Patagonia**, v. 38, n. 1, p. 5–34, 2010.

SAUNDERS, P.; ROGERSON, M.; WADHAWAN, J. D.; GREENWAY, G.; PEDLEY, H. M. Mg/Ca ratios in freshwater microbial carbonates: Thermodynamic, kinetic and vital effects. **Geochimica et Cosmochimica Acta**, v. 147, p. 107–118, 2014. Disponível em: <http://dx.doi.org/10.1016/j.gca.2014.10.014>.

SCHMITT, Jochen et al. **Measurements of stable carbon isotope ratios of CO2 over the last 24000 years and CO2 concentration measurements on Antarctic ice cores using three different methods**. PANGAEA, 2012. Available at: https://doi.org/10.1594/PANGAEA.772713. Access at: 14 jun. 2024.

SCHWIKOWSKI, M.; SCHLÄPPI, M.; SANTIBAÑEZ, P.; RIVERA, A.; CASASSA, G. Net accumulation rates derived from ice core stable isotope records of Pío XI Glacier, Southern Patagonia Icefield. **Cryosphere**, v. 7, n. 5, p. 1635–1644, 2013.

SEGAL, M.; OOKOUCHI, Y.; PIELKE, R. . On the effect of steep slope orientation on the intensity of daytime upslope flow. **Journal of Atmospheric Sciences**, v. 44, n. 23, p. 3587–3592, 1987.

SHAPIRO, R. S. A comment on the systematic confusion of thrombolites. **Palaios**, v. 15, p. 166–169, 2000.

SHIRAISHI, F.; BISSETT, A.; DE BEER, D.; REIMER, A.; ARP, G. Photosynthesis, respiration and exopolymer calcium-binding in biofilm calcification (Westerhöfer and Deinschwanger Creek, Germany). **Geomicrobiology Journal**, v. 25, n. 2, p. 83–94, 2008a.

SHIRAISHI, F.; REIMER, A.; BISSETT, A.; DE BEER, D.; ARP, G. Microbial effects on biofilm calcification, ambient water chemistry and stable isotope records in a highly supersaturated setting (Westerhöfer Bach, Germany). **Palaeogeography, Palaeoclimatology, Palaeoecology**, v. 262, n. 1–2, p. 91–106, 2008b.

SHIRAISHI, F.; HANZAWA, Y.; OKUMURA, T.; TOMIOKA, N.; KODAMA, Y.; SUGA, H.; TAKAHASHI, Y.; KANO, A. Cyanobacterial exopolymer properties differentiate microbial carbonate fabrics. **Scientific Reports**, v. 7, n. 1, p. 1–8, 2017. Available at: <http://dx.doi.org/10.1038/s41598-017-12303-9>.

SHIRAISHI, F.; ENO, Y.; NAKAMURA, Y.; HANZAWA, Y.; ASADA, J.; BAHNIUK, A. M. Relative Influence of biotic and abiotic processes on travertine fabrics, Satono-Yu Hot Spring, Japan. **Sedimentology**, v. 66, n. 2, p. 459–479, 2019.

SHIRAISHI, F.; OMORI, T.; TOMIOKA, N.; MOTAI, S.; SUGA, H.; TAKAHASHI, Y. Characteristics of CaCO3 nucleated around Cyanobacteria: Implications for calcification process. **Geochimica et Cosmochimica Acta**, v. 285, p. 55–69, 2020.

SHIRAIWA, T.; KOHSHIMA, S.; UEMURA, R.; YOSHIDA, N.; MATOBA, S.; UETAKE, J.; GODOI, M. A. High net accumulation rates at Campo de Hielo Patagónico Sur, South America, revealed by analysis of a 45.97 m long ice core. **Annals of Glaciology**, v. 35, p. 84–90, 2002.

SIHVONEN, L. M.; LYRA, C.; FEWER, D. P.; RAJANIEMI-WACKLIN, P.; LEHTIMÄKI, J. M.; WAHLSTEN, M.; SIVONEN, K. Strains of the cyanobacterial genera Calothrix and Rivularia isolated from the Baltic Sea display cryptic diversity and are distantly related to Gloeotrichia and Tolypothrix. **FEMS Microbiology Ecology**, v. 61, n. 1, p. 74–84, 2007.

SINGH, Y.; KUMAR, A. Studies on species of Rivularia : A cyanobacterium. **Biochemical and Cellular Archivess**, v. 9, p. 67–72, 2009.

SMITH, R. B.; EVANS, J. P. Orographic precipitation and water vapor fractionation over the Southern Andes. **Journal of Hydrometeorology**, v. 8, n. 1, p. 3–19, 2007.

SOLARI, M. A.; HERVÉ, F.; LE ROUX, J. P.; AIRO, A.; SIAL, A. N. Paleoclimatic significance of lacustrine microbialites: A stable isotope case study of two lakes at Torres Del Paine, Southern Chile. **Palaeogeography, Palaeoclimatology, Palaeoecology**, v. 297, n. 1, p. 70–82, 2010. Available at: <http://dx.doi.org/10.1016/j.palaeo.2010.07.016>.

SOLARI, M. A.; ROUX, J. P. Le; HERVÉ, F.; AIRO, A.; CALDERÓN, M. Evolution of the Great Tehuelche Paleolake in the Torres Del Paine National Park of Chilean Patagonia during the Last Glacial Maximum and Holocene. **Andean Geology**, v. 39, n. 1, p. 1–21, 2012.

SPIRO, B.; PENTECOST, A. One Day in the life of a stream—a diurnal inorganic carbon mass balance for a travertine-depositing stream (Waterfall Beck, Yorkshire). **Geomicrobiology Journal**, v. 9, n. 1, p. 1–11, 1991.

STRELIN, J. A.; KAPLAN, M. R.; VANDERGOES, M. J.; DENTON, G. H.; SCHAEFER, J. M. Holocene Glacier History of the Lago Argentino Basin, Southern Patagonian Icefield. **Quaternary Science Reviews**, v. 101, p. 124–145, 2014.

SUN, H.; LIU, Z. Wet-dry seasonal and spatial variations in the δ13C and δ18O values of the modern endogenic travertine at Baishuitai, Yunnan, SW China and their paleoclimatic and paleoenvironmental implications. **Geochimica et Cosmochimica Acta**, v. 74, n. 3, p. 1016–1029, 2010.

SUN, H.; LIU, Z.; YAN, H. Oxygen isotope fractionation in travertine-depositing pools at Baishuitai, Yunnan, SW China: Effects of deposition rates. **Geochimica et Cosmochimica Acta**, v. 133, p. 340–350, 2014. Available at: <http://dx.doi.org/10.1016/j.gca.2014.03.006>.

SUOSAARI, E. P.; PAMELA REID, R.; OEHLERT, A. M.; PLAYFORD, P. E.; STEFFENSEN, C. K.; ANDRES, M. S.; SUOSAARI, G. V.; MILANO, G. R.; EBERLI, G. P. Stromatolite provinces of Hamelin Pool: Physiographic Controls on stromatolites and associated lithofacies. **Journal of Sedimentary Research**, v. 89, n. 3, p. 207–226, 2019.

TALBOT, M. R. A review of the palaeohydrological interpretation of carbon and oxygen isotopic ratios in primary lacustrine carbonates. **Chemical Geology: Isotope Geoscience Section**, v. 80, n. 4, p. 261–279, 1990.

TANNER, L. H. Chapter 4 Continental Carbonates as indicators of paleoclimate. **Developments in Sedimentology**, v. 62, p. 179-214, 2010.

TARUTANI, T.; CLAYTON, R. N.; MAYEDA, T. K. The effect of polymorphism and magnesium substitution on oxygen isotope fractionation between calcium carbonate and water. **Geochimica et Cosmochimica Acta**, v. 33, n. 8, p. 987–996, 1969.

TEBOUL, P. A.; DURLET, C.; GAUCHER, E. C.; VIRGONE, A.; GIRARD, J. P.; CURIE, J.; LOPEZ, B.; CAMOIN, G. F. Origins of elements building travertine and tufa: New perspectives provided by isotopic and geochemical tracers. **Sedimentary**

Geology, v. 334, p. 97–114, 2016. Available at: <http://dx.doi.org/10.1016/j.sedgeo.2016.01.004>.

TERRA, J. G. S.; SPADINI, A. R.; FRANÇA, A. B.; LEITE, C.; ZAMBONATO, E. E.; COSTA, L.; ARIENTI, L. M.; ERTHAL, M. M.; BLAUTH, M.; FRANCO, M. P.; MATSUDA, N. S.; GOULART, N.; AUGUSTO, P.; JUNIOR, M.; FRANCISCO, R. S.; AVILA, D.; SOUZA, R. S. De; TONIETTO, S. N.; MARIA, S. Classificações clássicas de rochas carbonáticas. **B. Geoci. Petrobras, Rio de Janeiro**, v. 18, n. 1, p. 9–29, 2010.

VASCONCELOS, C.; MCKENZIE, J. A. Microbial mediation of modern dolomite precipitation and diagenesis under anoxic conditions (Lagoa Vermelha, Rio de Janeiro, Brazil. **Journal of Sedimentary Research**, v. 67, n. 3, p. 378–390, 1997.

VENNIN, E.; BOUTON, A.; BOURILLOT, R.; PACE, A.; ROCHE, A.; BRAYARD, A.; THOMAZO, C.; VIRGONE, A.; GAUCHER, E. C.; DESAUBLIAUX, G.; VISSCHER, P. T. The lacustrine microbial carbonate factory of the successive Lake Bonneville and Great Salt Lake, Utah, USA. **Sedimentology**, v. 66, n. 1, p. 165–204, 2019.

VEYSEY, J.; FOUKE, B. W.; KANDIANNIS, M. T.; SCHICKEL, T. J.; JOHNSON, R. W.; GOLDENFELD, N. Reconstruction of water temperature, pH, and flux of ancient hot springs from travertine depositional facies. **Journal of Sedimentary Research**, v. 78, n. 2, p. 69–76, 2008.

VILLA-MARTÍNEZ, R.; MORENO, P. I. Pollen evidence for variations in the southern margin of the Westerly Winds in SW Patagonia over the Last 12,600 Years. **Quaternary Research**, v. 68, n. 3, p. 400–409, 2007.

WALTER, M. R.; HEYS, G. R. Links between the rise of the metazoa and the decline of stromatolites. **Precambrian Research**, v. 29, p. 149–174, 1985.

WALTER, M. R.; DES MARAIS, D. J. Preservation of Biological Information in Thermal Spring Deposits: Developing a Strategy for the Search for Fossil Life on Mars. **Icarus**, v. 101, n. 1, p. 129–143, 1993.

WANG, H.; YAN, H.; LIU, Z. Contrasts in variations of the carbon and oxygen isotopic composition of travertines formed in pools and a ramp stream at Huanglong Ravine, China: Implications for paleoclimatic interpretations. **Geochimica et Cosmochimica Acta**, v. 125, p. 34–48, 2014. Available at: <http://dx.doi.org/10.1016/j.gca.2013.10.001>.

WANG, Z.; YIN, J. J.; CHENG, H.; NING, Y.; MEYER, M. C. Climatic controls on travertine deposition in southern Tibet during the Late Quaternary. **Palaeogeography, Palaeoclimatology, Palaeoecology**, v. 589, n. January, p. 110852, 2022. Available at: <https://doi.org/10.1016/j.palaeo.2022.110852>.

WARDEN, J. G.; COSHELL, L.; ROSEN, M. R.; BREECKER, D. O.; RUTHROF, K. X.; OMELON, C. R. The importance of groundwater flow to the formation of modern thrombolitic microbialites. **Geobiology**, v. 17, n. 5, p. 536–550, 2019.

WATKINS, J. M.; NIELSEN, L. C.; RYERSON, F. J.; DEPAOLO, D. J. The influence of kinetics on the oxygen isotope composition of calcium carbonate. **Earth and**

Planetary Science Letters, v. 375, p. 349–360, 2013. Disponível em: <http://dx.doi.org/10.1016/j.epsl.2013.05.054>.

WATKINS, J. M.; HUNT, J. D.; RYERSON, F. J.; DEPAOLO, D. J. The influence of temperature, pH, and growth rate on the δ18O composition of inorganically precipitated calcite. **Earth and Planetary Science Letters**, v. 404, p. 332–343, 2014. Disponível em: <http://dx.doi.org/10.1016/j.epsl.2014.07.036>.

WATKINS, J. M.; HUNT, J. D. A Process-based model for non-equilibrium clumped isotope effects in carbonates. **Earth and Planetary Science Letters**, v. 432, p. 152–165, 2015.

WHITTON, B. A.; MATEO, P. Rivulariaceae. *In*: WHITTON, B. **Ecology of Cyanobacteria II: their diversity in space and time**. [s.l.] Springer, Dordrecht, 2012. p. 561–591.

WILLMER, B. J.; RASSER, M. W. Calcification patterns of Rivularia-type Cyanobacteria: Examples from the Miocene of the North Alpine foreland basin. **Facies**, v. 68, n. 4, p. 16, 2022.

WILSON, T. J. Transition from back-arc to foreland basin development in the southernmost Andes: Stratigraphic record from the Ultima Esperanza District, Chile. **Geological Society of America Bulletin**, v. 103, n. 1, p. 98–111, 1991.

WRIGHT, V. P. Lacustrine carbonates in rift settings: The interaction of volcanic and microbial processes on carbonate deposition. **Geological Society Special Publication**, v. 370, n. 1, p. 39–47, 2012.

XIA, Z.; BUTOROVIC, N.; YU, Z. The influence of synoptic weather types and moisture transport pathways on precipitation isotopes in southern Patagonia. **Atmosphere**, v. 11, n. 5, 2020.

YAN, H.; SUN, H.; LIU, Z. Equilibrium vs. kinetic fractionation of oxygen isotopes in two low-temperature travertine-depositing systems with differing hydrodynamic conditions at Baishuitai, Yunnan, SW China. **Geochimica et Cosmochimica Acta**, v. 95, n. October, p. 63–78, 2012.

YAN, H.; LIU, Z.; SUN, H. Effect of in-stream physicochemical processes on the seasonal variations in δ13C and δ18O values in laminated travertine deposits in a mountain stream channel. **Geochimica et Cosmochimica Acta**, v. 202, p. 179–189, 2017. Available at: <http://dx.doi.org/10.1016/j.gca.2016.12.031>.

YAN, H.; DREYBRODT, W.; BAO, H.; PENG, Y.; WEI, Y.; MA, S.; MO, B.; SUN, H.; LIU, Z. The influence of hydrodynamics on the carbon isotope composition of inorganically precipitated calcite. **Earth and Planetary Science Letters**, v. 565, 2021.

YANG, J.; EL-KASSABY, Y. A.; GUAN, W. The effect of slope aspect on vegetation attributes in a mountainous dry valley, southwest china. **Scientific Reports**, v. 10, n. 1, p. 1–11, 2020. Available at: <https://doi.org/10.1038/s41598-020-73496-0>.

ZEEBE, R. E. An explanation of the effect of seawater carbonate concentration on

foraminiferal oxygen isotopes. **Geochimica et Cosmochimica Acta**, v. 63, n. 13–14, p. 2001–2007, 1999.

ZEYEN, N.; BENZERARA, K.; BEYSSAC, O.; DAVAL, D.; MULLER, E.; THOMAZO, C.; TAVERA, R.; LÓPEZ-GARCÍA, P.; MOREIRA, D.; DUPRAT, E. Integrative analysis of the mineralogical and chemical composition of modern microbialites from ten Mexican lakes: What do we learn about their formation? **Geochimica et Cosmochimica Acta**, v. 305, p. 148–184, 2021.

ZHANG, C.; YIN, L.; OU, Y.; YANG, G.; HUANG, L.; LI, F. Contribution of selective bacterial extracellular polymeric substances to the polymorphism and morphologies of formed Ca/Mg carbonates. **International Biodeterioration and Biodegradation**, v. 160, n. January, p. 105213, 2021. Available at: <https://doi.org/10.1016/j.ibiod.2021.105213>.

ZHANG, D. D.; ZHANG, Y.; ZHU XING CHENG, A. N. Physical mechanisms of river waterfall tufa (travertine) formation. **Journal of Sedimentary Research**, v. 71, n. 1, p. 205–216, 2001.

ZHANG, J.; QUAY, P. D.; WILBUR, D. O. Carbon isotope fractionation during gas-water exchange and dissolution of CO2. **Geochimica et Cosmochimica Acta**, v. 59, n. 1, p. 107–114, 1995.

APPENDIX 1 – SPRING WATER ANALYSIS OF LAGUNA AMARGA TRAVERTINES

Table SF1.1. Physical-chemical parameters of the spring waters and Laguna Amarga

Date	*Location*	*Sampling site*	*pH* ±0.1 pH	*T (°C)* 0.01°C*	*ORP (mV)* ±15 mV	*DO (mg/L)* ± 0.5 mg/L	*EC (µS/cm)* ±1%	*Salininy (ppt)* ±3 ppt	$T_{south\ vent} - T_{north\ vent}$ (°C)	$T_{south\ lake} - T_{north\ lake}$ (°C)
17-10-2017	North-facing travertine	TP11A	7.0	12.8			1290			
		TP11C	7.8	13.1			1240			
		TP11F	7.5	9.8			1115			
		Laguna Amarga	8.6	8.2						
07-10-2018	South-facing travertine	TP9A	6.7	12.8	108.0	12.8	1290	0.6	5.0	2.1
		TP9C	7.9	11.9	68.0	19.3	1410	0.7		
		Laguna Amarga	9.0	12.5						
	North-facing travertine	TP11A	6.8	17.8	53.0	8.3	2020	1.0		
		TP11B	7.3	18.7	70.0	14.0	1840	0.9		
		TP11C	8.1	18.3	228.0	13.7	1280	0.6		
		TP11D	7.8	15.4	227.0	13.7	1870	1.0		
		TP11G	8.0	15.6	269.0	35.1	1590	0.8		
		Laguna Amarga	9.0	14.7						
10-10-2022	South-facing travertine	TP9A	8.3	12.95	13.0	15.5	1580	1.0	1.0	2.0
		Laguna Amarga	8.9	10.8						
	North-facing travertine	TP11A	6.6	13.9	15.0	13.4	1690	1.7		
		Laguna Amarga	9.0	12.79						
19-02-2024	South-facing travertine	TP9A	6.8	13.87	-53	41.4	3550	1.9	2.2	3.1
		Laguna Amarga	7.9	17.2						
	North-facing travertine	TP11A	6.2	16.08	-3	28.18	1670	0.8		
		Laguna Amarga	7.6	20.3						

*Instrumental precision is indicated below of each measured parameter. *In the case of temperature, the resolution is indicated*

Table SF1.2. Chemical composition of the spring waters of the North-facing travertine

Sample location		TP11A	TP11A	TP11A
	date	17/10/2017	07/10/2018	10/10/2022
	$T_{(°C)}$	12.8	17.8	13.9
	pH	7.62	6.76	6.58
	Cond $_{(\mu S/cm)}$	1072	2020	1560
	TDS	697	1292.8	981
Anions	HCO_3	690.01	450.91	919.6
	CO_3	0	2.64	0
	Cl	94.39	1.4	32
	SO_4	0	176	14
	NO_3	0	0	2
Cations	Ca	112	121.91	263.2
	Mg	40.5	79.06	49.98
	Na	61	264	64
	K	5	7.6	4
	Fe	0	15.96	0
	SiO_2	0	19.48	130
	Mg/Ca*	0.60	1.07	0.31
	Ca/HCO_3^*	0.25	0.41	0.44
	$\log_{10}(pCO_2)$	-1.89	-1.19	-0.73
Mineral saturation indexes	Ar	0.62	-0.36	0.04
	Cc	0.77	-0.22	0.18
	Sd		1.09	
	$Fe(OH)_3$		2.2	
	Gth		7.83	
	Hm		17.63	
	Qz		0.27	1.16

Ar: aragonite, Cc: calcite, Dol: dolomite, Sd: siderite, Gth: goethite, Hm: hematite, Qz: quartz

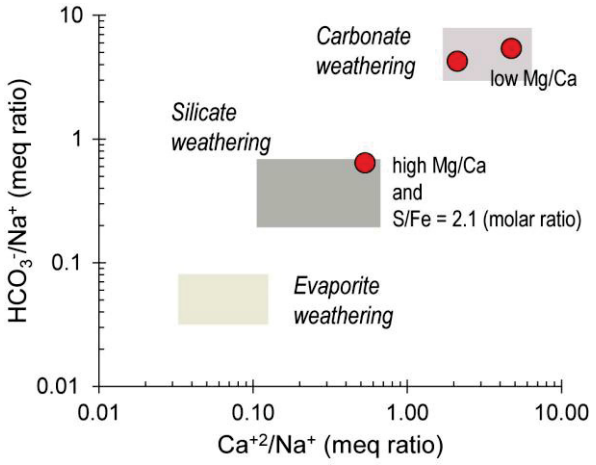

Figure S1. Ca^{+2}/Na^{+} vs HCO_3^{-}/Na^{+} chemical relationship of spring waters from the north-facing travertine, based on Gaillardet et al. (1997).

Table SF1.3. Isotope composition of the analyzed waters

	Sampling site	*Date*	*$\delta^{18}O$ (‰ VSMOW)*	*$\delta^{2}H$ (‰ VSMOW)*	*d-excess* (‰)*	*$\delta^{13}C$-DIC (‰ VPDB) 0.2 mL*	*0.5 mL*	*mean*
Spring waters								
South-facing travertine	TP9A	09-10-2022	-13.7	-104	5.1	-3.4	-3.4	-3.4
	TP9D		-13.5	-105	3.1	-1.9	-1.8	-1.9
	TP9F		-13.2	-104	1.8	-0.6	-0.5	-0.6
North-facing travertine	TP11A	09-10-2022	-14.4	-109	6.2	-4.7	-4.5	-4.6
	TP11A	11-04-2023	-14.5	-110	5.9	1.6	1.5	1.6
	TP11A		-14.4	-108	7.0	1.4	1.6	1.5
	TP11A	01-02-2023	-14.3	-111	3.6	4.6	4.2	4.4
South-facing travertine	TP9A	19-02-2024	-13.5	-107	1.2	-	-5.3	-5.3
North-facing travertine	TP11A		-14.5	-113	2.7	-	-4.1	-4.1
Open lakes and rivers								
Open lake	Lago Nordensjold	09-10-2022	-13.1	-96.0	8.5			
	Lago Grey	19-02-2024	-12.7	-94.5	6.9			
	Laguna Torres del Paine	12-04-2023	-14.1	-111.4	1.0			
River	drainage of the Laguna Torres del Paine		-14.1	-109.5	3.1			

** d-excess = $\delta^{2}H - 8*\delta^{18}O$ (Dansgaard, 1964)*

APPENDIX 2 – ROCK ANALYSIS OF LAGUNA AMARGA TRAVERTINES

Table SF2.1. XRD and O-C data of the travertines

	Depositional zone	*Sampling site*	*Sample code*	Bulk- rock (b) / Subsample (s)	Facies / *Fabric*	X-ray Diffraction (XRD) Semiquantitative content (%) (Low-Mg) Calcite	Ar	Qz	Other terr*	Hl	Ar%*	calcite mol % $MgCO_3$	IRMS (‰ VPDB) $\delta^{13}C$	$\delta^{18}O$
South-facing travertine	proximal zone	TP9A	040/22-125	b	Phyto-boundstone	100					0.0	**0.9**	1.5	-11.3
			040/22-125_P1	s	*Microstromatolite*	100					0.0	0.0	4.7	-9.7
			040/22-126	b	Spherulitic/laminated boundstone	100					0.0	0.0	1.9	-10.5
			040/22-126_P1	s	*spherulitic calcite*	100					0.0	0.0	1.3	-10.9
			040/22-126_P2	s	*Micro-laminated calcite*	100					0.0	0.0	1.8	-10.7
	intermediate zone	TP9B	040/22-127	b	Crystalline dendrite	99					0.0	**0.8**	-1.0	-12.0
		TP9C	040/22-128	b	Spherulitic/laminated boundstone	98.8	1.1	0.1			1.1	**1.9**	0.5	-11.0
		TP9C	040/22-129	b	Crystalline dendrite	100					0.0	**2.4**	-0.6	-11.6
			040/22-129_P1	s	*Feather-like calcite*	100					0.0	0.0	-1.2	-12.1
			040/22-129_P2	s	*Feather-like calcite*	100					0.0	0.0	-1.1	-11.8
		TP9D	040/22-130	b	Crystalline dendrite	98.3	1.7				1.7	**0.3**	-1.1	-11.8
		TP9E	040/22-131	b	Crystalline dendrite	98.1	1.9				1.9	0.0	-0.7	-11.7
			040/22-131_P1	s	*Feather-like calcite*	96.9		3.1			0.0	0.0	-0.9	-11.8
			040/22-131_P2	s	*Feather-like calcite*	100					0.0	0.0	-0.7	-12.0
	distal zone	TP9F	040/22-132	b	Crystalline dendrite	98.1	1.9				1.9	0.0	-0.5	-11.7
Reworked trav.	*proximal zone?*		108/18-01	*b*	Spherulite/dendrite boundstone	*66.6*	*33.4*				*33.4*	***0.3***	*4.4*	*-10.6*
			108/18-03	*b*	Spherulite/dendrite boundstone	*44.6*	*55.1*			*0.3*	*55.3*	***0.2***	*4.9*	*-10.2*
			040/22-116_P1	*s*	*Feather-like calcite*	*79*	*19.6*	*0.6*			*19.9*	*0.0*	*3.5*	*-10.4*
			040/22-116_P2	*s*	*Aragonite spherulites*	*47.9*	*52.1*				*52.1*	*0.0*	*4.5*	*-10.4*
travertine	proximal zone	TP11A	060/18-01	b	Spherulite/dendrite boundstone	42.2	57.8				57.8	**0.3**	5.3	-10.5
	intermediate zone	TP11B	060/18-02	b	Crystalline dendrite	92.6	6.5	0.9			6.6	**0.2**	4.1	-11.0
			040/22-109_P1	s	*Microstromatolite*	28.1	71.9				71.9	0.0	11.2	-6.0

		040/22-109_P2	s	*white calcite cement*						3.9	-10.7
	TP11C	060/18-03	b	Crystalline dendrite	98.6	1.2	0.3		1.2	**0.5**	3.0	-11.4
		060/18-04	b	Crystalline dendrite	92.9	7.1			7.1	**0.4**	2.6	-11.5
	TP11D	040/22-111_P1	s	*Micro-laminated calcite*	77.2	22.8			22.8	0.0	2.6	-11.8
		040/22-111_P2	s	*Micro-laminated calcite*	100				0.0	0.0	2.5	-11.7
		040/22-111_P3	s	*Micro-laminated calcite*	88.2	11.8			11.8	0.0	2.1	-12.0
		040/22-111_P4	s	*Feather-like calcite*	92.4	7.2	0.3		7.2	0.0	2.7	-11.7
		040/22-111_P5	s	*Micro-laminated calcite*	92.1	7.9			7.9	0.0	2.4	-11.9
		040/22-111_P6	s	*Micro-laminated calcite*	100				0.0	0.0	1.8	-12.1
		040/22-111_P7	s	*Feather-like calcite*	100				0.0	0.0	2.6	-12.4
		060/18-05	b	Crystalline dendrite	97.7	1.6	0.7		1.6	**0.9**	3.7	-10.2
	TP11E	040/22-112_P1	s	*Microstromatolite*	93.1	6.9			6.9	0.0	5.4	-10.0
		040/22-137_P1	s	*Microstromatolite*	60.1	39.9			39.9	0.0	9.1	-7.9
	TP11F	060/18-06	b	Crystalline dendrite	99.1	0.5	0.5		0.5	**1.1**	3.4	-10.8
		060/18-07	b	Phyto-boundstone	98.8	0	1.2		0.0	**0.8**	3.9	-10.6
	TP11G	060/18-07_P1	s	Phyto-boundstone	99.7	0.3			0.3	0.0	2.1	-11.7
distal zone		060/18-07_P2	s	*white calcite cement*	99.2		0.8		0.0	**0.6**	2.3	-11.3
		060/18-07_P3	s	*green calcite cement*	99.5		0.5		0.0	**1.3**	4.1	-10.3
		060/18-07_P4	s	Phyto-boundstone	97.6	0.3	2.1		0.3	0.0	3.3	-10.1
		060/18-07_P5	s	*phreatic to vadose cement*	41.3	10.8	20	27.9	20.7	0.0	4.2	-8.7
	Loose granular facies/ components	040-22-195	b	*spherulitic calcite*					0.0		3.7	-10.4
Intermediate to distal zone		040-22-196	b	*spherulitic calcite*	100				0.0	0.0	4.2	-9.7
		040-22-197	s	Oncoid rim	100				0.0	0.0	2.4	-10.3
		040-22-197_P1	s	Oncoid core	72.9	27.1			27.1	0.0	4.5	-9.8
		040-22-198	b	Oncoid	100				0.0	0.0	2.1	-10.2

Ar: aragonite, Qz: quartz, Other terr: terrigenous grains other than quartz (mostly albite and chlinoclore), Hl: halite.*

Ar: aragonite fraction. Percentage of aragonite content calculated according to Ar* = 100*Ar /(Cc + Ar), Ar: aragonite, Cc: calcite.*

Table SF2.2. O-C data of sedimentary carbonates composing the bedrock of the study area

Unit / Type	*Location (lat/long) or depth*		*Sample code*	*Description*	IRMS (‰ VPDB) $\delta^{13}C$	IRMS (‰ VPDB) $\delta^{18}O$
Upper Zapata Fm (Toro-1B well core)	140 - 150 m		040-22-93	calcite-bearing mudstone	0.2	-14.1
			040-22-93_P1	calcite vein	-1.5	-12.3
	200 - 205 m		040-22-94	calcite-bearing mudstone	-2.8	-14.0
	255 - 260 m		040-22-95	calcite-bearing mudstone	-3.9	-14.1
	ca. 305 m		040-22-96	calcite-bearing mudstone	-0.3	-14.3
	ca. 340 m		040-22-97	calcite-bearing mudstone	0.3	-14.2
			040-22-97_P1	calcite vein	-0.4	-14.1
	ca. 340 m		040-22-98	calcite-bearing mudstone	-0.9	-14.2
	455 - 460 m		040-22-99	calcite-bearing mudstone	-1.1	-14.4
				Average value	***-1.1***	***-14.0***
Cerro Toro Fm	-50.9421	-72.7937	040/22-073	fresh calcitic sedimentary concretion	-11.9	-13.8
	-50.9801	-72.8002	040-22-50	dolostone	-5.5	-13.1
	-50.9801	-72.8002	040-22-51_P1	calcite cement in dolostone	-6.5	-14.4
	-50.9801	-72.8002	040-22-51_P3	dolostone	-6.5	-12.8
	-50.9695	-72.7474	040/22-074	weathered fossiliferous sedimentary concretion	-17.4	-13.0
	-51.0625	-72.9244	040/22-070	marlstone	-10.9	-15.3
	-51.0422	-72.8795	040-22-71	marlstone	-8.8	-14.7
	-51.0344	-72.7586	040/22-072	marlstone	-10.0	-13.4
				Average value	***-9.7***	***-13.8***

APPENDIX 3 – WATER ANALYSIS OF LAGO SARMIENTO

Table SF3.1. Compilation of water data of Lago Sarmiento and local open lakes

	Location		Date	Depth	T	pH	O_2	C_{25}	TDS	Salinity*	δ^2H	$\delta^{18}O$	$\delta^{13}C$-DIC	d-excess**
	Lat	Long		(m)	*(°C)*		*(mg/l)*	*(µS/cm)*	*(g/l)*	*(g/l)*	(‰ VSMOW)	(‰ VSMOW)	(‰ VPDB)	(‰ VSMOW)
Lago Sarmiento														
	-51.00	-72.69	oct-17	0.0	9.9	8.6		1340		0.96	-42	-3.7		-12
	-51.00	-72.69	oct-17	0.0							-47	-4.3		
	-51.01	-72.62	oct-17	0.0	6.7	8.5		1349		1.06	-40	-3.4		-12
	-51.04	-72.67	oct-17	0.0	5.7	8.1		1363		1.10	-37	-3.5		-8
This work	-51.06	-72.92	nov-18	0.0	7.7	8.8	26.5	1310	0.63	1.00				
	-51.05	-72.92	nov-18	0.0	7.9	8.8	23.5	1300	0.64	0.99				
	-51.05	-72.92	oct-19	0.0	6.8	8.6	> 50	1493	0.86	1.18	-40	-3.6		-11
	-51.05	-72.92	oct-22	0.0	10.1	8.8	17.8	1390	0.89	0.99	-40	-3.4	1.6	-13
	-51.04	-72.66	apr-24	0.0							-43	-3.1	1.4	-19
Campos *et al.* (1994a)			sept-88	0.0	7.2	8.7	12.2	1000		0.76				
			jan-89	0.0	9.5	8.4	11.4	965		0.69				
			may-89	0.0	8.6	8.7	11.5	770		0.56				
			oct-89	30.0	6.1	8.6	8.3	618		0.48				
				100.0	6.0	8.7	9.7	618		0.48				
			jan-90	0.0	6.2	8.3	10.5	622		0.48				
				0.0	8.9	8.3	12.6	891		0.64				
				0.1	9.6	8.5	13.7	2720		2.04				
Solari *et al.* (2010)			jan-07								-43	-3.5		-15
			jan-07								-45	-3.4		-18
			jan-07								-43	-3.5		-16
			jan-07								-43	-3.4		-16
Mayr *et al.* (2018)			mar-13								-43	-3.6		-14
Open lakes (this work)														
Laguna Sofía	-51.54	-72.6	apr-24								-67	-6.8	-1.0	-13

Laguna Base Torres	-50.94	-72.95	apr-24	-112	-14.3	-1.9	3
Lago Grey			feb-24	-94	-12.7	-3.0	7

* Calculated based on Aminot and Kérouel (2024); ** Calculated based on Dansgaard (1964)

APPENDIX 4 – ROCK ANALYSIS OF TUFA THROMBOLITES FROM LAGO SARMIENTO

Table SF4.1 Compilation of

					Semiquantitative mineral content (%)											IRMS (‰ VPDB)		Petrography	
					Authigenic carbonates				*Silicate components*										
Site	Laboratorial sample code	Size	Terrace	Position*	Mg-calcite	Ar	MHC	Dol	Qz	Plg	Px	Others	Total detrital	d_{104}-spacing calcite (A)	mol % MgCO3	$\delta^{13}C$	$\delta^{18}O$	Thin section	SEM
TP3	198/19-005	Tall columns	**T3d**	base	96				1	3			4	3.01131	8.5	4.4	-1.1		x
	198/19-006			top	90	2			4	4			8	3.01713	6.4	4.8	-1.7		x
	198/19-007	Lower relief columns and mounds	T3c	base	95				3	3			5	3.01339	7.7	4.5	-1.3		x
	198/19-008			top	88	4			3	6			8	3.01094	8.6	4.8	-1.3		x
	198/19-009		T3b	base	92	5			2	2			3	3.01227	8.2	4.5	-1.5		x
	198/19-010			top	95				2	3			5	3.01465	7.3	4.4	-1.6		x
	198/19-011		T3a	base	60				11	19	7	2	40	3.02853	2.2	4.0	-1.0		x
	040/22-83			top	86				5	7		2	14	3.01086	8.7	4.7	-1.0		x
TP4	198/19-004	Tall columnar build-ups	**T4c**	top	88				4	8		1	12	3.01358	7.7	4.4	-1.7		
	198/19-003			middle	95				2	3			5	3.01360	7.7	4.7	-1.4		
	198/19-002			middle	68				9	13	10		32	3.01136	8.5	4.4	-1.4		
	198/19-001			base	55			2	19	23		2	44	3.00910	9.3	4.4	-1.5		
	514/17-G	lower relief mounds and columns	T4b		92				4	4			8	3.01000	9.0	4.8	-1.9	x	
	514/17-F				90		5		3	2			5	3.01918	5.6	4.6	-1.4	x	
	514/17-E				98				2				2	3.01198	8.3	4.0	-1.4		
	514/17-D				98				2				2	3.00927	9.2	3.9	-1.1		
	514/17-C				91	7			2				2	3.00890	9.4	4.7	-1.5	x	
	514/17-B		T4a		94	3			2			1	3	3.01040	8.8	4.2	-1.3	x	
TP5	064/18-001	Big-sized domes	**T5d**		99				2				2	3.01605	6.8	4.3	-2.5	x	
	064/18-002				86				6	7			14	3.01684	6.5	4.5	-1.7	x	
	064/18-004		**T5c**		84				8	8			16	3.01083	8.7	4.4	-1.4	x	
	064/18-005				94				3	3			6	3.01591	6.8	4.6	-1.3	x	
	064/18-006				94				3	3			6	3.01634	6.7	4.6	-1.6	x	

	064/18-007	Low-relief build-ups	T5b		99		1			1	3.01163	8.4	4.5	-1.5	x	
	064/18-008		T5a		97		2	1		3	3.01110	8.6	4.5	-1.2	x	
	064/18-009				99		1			1	3.01058	8.8	4.2	-1.4	x	
TP7	064/18-017	V-shaped build-up	T7c	**top**	94		4	2	0	6	3.01719	6.4	4.2	-1.7	x	x
	064/18-016			**3.7**	72		14	13	1	28	3.01322	7.8	4.6	-1.5	x	x
	064/18-015			2	81		11	8	1	19	3.01618	6.7	4.2	-1.2	x	x
	064/18-014			1.8	87		6	6		13	3.01413	7.5	4.3	-1.3	x	x
	064/18-013			1.6	88		6	5		12	3.01371	7.6	4.3	-1.2	x	x
	064/18-012			0.9	89		6	5		11	3.01005	9.0	4.4	-1.3	x	x
	064/18-011			0.3	89		6	5		11	3.00870	9.5	4.5	-1.1	x	x
	064/18-010			base	90		6	4		10	3.00709	10.0	4.2	-1.2	x	x
LS2	040/22-79	calcified mat			75	25				0	3.01455	7.3	5.6	-1.4		x
	040/22-80	crust			98		2			2	3.01335	7.8	5.0	-1.5	x	x
	040/22-81	crust			100					0	3.01392	7.6	4.8	-1.9	x	x
north shore	040/22-01	crust			90	9	1			1	3.01597	6.8	4.4	-1.4	x	x
	040/22-03	crust			99		1			1	3.01927	5.6	4.3	-2.2	x	
	040/22-04	crust			96	3	1			1	3.01428	7.4	4.1	-1.7	x	
	040/22-05	crust			95		2	3		5	3.00576	10.5	4.2	-1.7	x	
TP3	040-22-139		T3d	7.6	100					0	3.01868	5.8	4.5	-1.9		
	040-22-140			7.4	96		4			4	3.00715	10.0	6.0	-2.3		
	040-22-142			7.2	100					0	3.00782	9.8	4.5	-1.7		
	040-22-143			7.0	100					0	3.01933	5.6	4.8	-1.7		
	040/22-144			6.8	97		3			3	3.01381	7.6	4.8	-1.3		
	040/22-145			6.6	98		2			2	3.00963	9.1	4.8	-1.4		
	040/22-146			6.4	98		2			2	3.01163	8.4	5.2	-1.2		
	040/22-147			6.2	99		2			2	3.01599	6.8	5.3	-1.1		
	040/22-148			6.0	100					0	3.0141	7.5	5.2	-1.3		
	040/22-149			5.8	99		1			1	3.01015	8.9	5.1	-1.3		

040/22-150		5.6	100					0	3.01523	7.1	4.8	-1.4
040/22-151		5.4	90	10				0	3.00698	10.1	5.5	-0.8
040/22-152		5.2	99		2			2	3.01373	7.6	4.3	-0.7
040/22-154		5.0	98		2			2	3.00961	9.1	4.9	-1.0
040/22-155		4.8	100					0	3.00834	9.6	4.4	-1.0
040/22-156		4.6	98		2			2	3.00936	9.2	5.2	-1.0
040/22-157		4.4	97		2	1		3	3.00671	10.2	4.1	-1.0
040/22-158	T3c	4.2	96		2		2	4	3.00831	9.6	4.5	-0.9
040/22-159		4.0	92		2		7	8	3.02076	5.1	5.3	-0.8
040/22-160		3.8	97		3			3	3.01151	8.4	4.7	-1.0
040/22-161		3.6	94		6			6	3.01394	7.5	4.6	-1.1
040/22-162		3.4	97		3			3	3.01113	8.6	4.9	-1.0
040/22-163		3.0	99		1			1	3.00286	11.6	4.7	-1.0
040/22-164		2.8	98			2		2	3.00467	10.9	4.3	-1.1
040/22-165		2.6	99		1			1	3.0042	11.1	5.0	-1.0
040/22-166		2.4	99		1			1	3.01084	8.7	5.1	-1.0
040/22-167		2.2	96		1		3	4	3.00567	10.6	4.8	-1.2
040/22-168	T3b	2.0	97		3			3	3.01519	7.1	4.7	-1.0
040/22-169		1.8	97		3			3	3.00399	11.2	4.6	-0.9
040/22-170		1.6	99		1			1	3.00499	10.8	5.0	-1.0
040/22-171		1.4	92		5		3	8	3.01038	8.8	5.1	-1.0
040/22-172		1.2	99		1			1	3.01122	8.5	4.0	-1.1
040/22-173		1.0	98		2			2	3.01046	8.8	4.7	-1.0
040/22-175		0.8	96		3		2	5	3.01406	7.5	4.8	-1.0
040/22-176		0.6	97		3			3	3.00755	9.9	4.8	-1.0
040/22-177	T3a	0.4	98		2			2	3.00665	10.2	4.2	-1.1
040/22-178		0.2	98		2			2	3.0172	6.4	4.6	-1.0
040/22-179		0.0	78		12	10		22	2.99854	13.2	3.5	-0.7

Mg-calcite composition calculated based on Arvidson and McKenzie (1999); *Absolute positions are indicated in meters.